

Stony Brook University



OFFICIAL COPY

The official electronic file of this thesis or dissertation is maintained by the University Libraries on behalf of The Graduate School at Stony Brook University.

© All Rights Reserved by Author.

Recombination of Charge Carriers in Low Dielectric Constant Organic Solvent

A Dissertation Presented

by

Hung Cheng Chen

to

The Graduate School

in Partial Fulfillment of the

Requirements

for the Degree of

Doctor of Philosophy

in

Materials Science and Engineering

Stony Brook University

December 2014

Stony Brook University
The Graduate School

Hung Cheng Chen

We, the dissertation committee for the above candidate for the
Doctor of Philosophy degree, hereby recommend
acceptance of this dissertation.

Dissertation Advisor

Dr. John R. Miller

Senior Chemist, Chemistry Department, Brookhaven National Laboratory
Adjunct Professor, Department of Materials Science and Engineering

Chairperson of Defense

Dr. Miriam Rafailovich

Distinguished Professor, Department of Materials Science and Engineering

Dr. David O. Welch

Adjunct Professor, Department of Materials Science and Engineering

Dr. James F. Wishart

Senior Chemist and LEAF Facility Supervisor, Chemistry Department,
Brookhaven National Laboratory

This dissertation is accepted by the Graduate School

Charles Taber
Dean of the Graduate School

Abstract of the Dissertation
Recombination of Charge Carriers in Low Dielectric Constant Environment
by
Hung Cheng Chen
Doctor of Philosophy
in
Materials Science and Engineering
Stony Brook University
2014

This dissertation consists of three projects:

- (1) Escape of Anions from Geminate Recombination due to Charge Delocalization.
- (2) Charge Separation of Electron-Hole Pairs (Exciplexes) Enhanced by Charge Delocalization.
- (3) Energies of Radical Anions Measured by Bimolecular Electron Transfer Equilibria Method.

The first project studies geminate recombination of 23 radical anions ($M^{\bullet-}$) with solvated protons (RH_2^+) in tetrahydrofuran (THF). The recombination has two steps: (1) Diffusion of $M^{\bullet-}$ and RH_2^+ together to form intimate (contact and solvent separated) ion pairs, driven by Coulomb attraction; (2) Annihilation of anions due to proton transfer (PT) from RH_2^+ to $M^{\bullet-}$. The kinetic analyses find that intimate ion pairs are formed in ~ 8 ns while the subsequent PT step can range from much faster (< 0.5 ns) to as slow as 50 ns. A free ion yield $G_{fi} = 0.69 \pm 0.06$ per 100 eV, comprising $\sim 29\%$ of the total, was formed. This yield of “Type I” free ions is independent of the PT rate because it arises entirely by escape from the initial distribution of ion pair distances without forming intimate ion pairs. For 20 of the 23 molecules studied this is the only measurable source of free ions: once these anions enter intimate ion pairs the PT process annihilates all of them within detection limits. The three exceptions were anions of oligo(9,9-dihexyl)fluorenes, $F_n^{\bullet-}$ ($n=2-4$). These three have PT rates similar to the slowest of the other 20 molecules, and have increased free ion yields. For these charge-delocalized anions, intimate ion-pairs are able to escape to form an additional yield of free ions, which may be termed “Type II” free ions. Protons attach to C and O atoms with a wide variety of PT rates providing opportunities to examine PT models, which discuss PT rate in terms of ΔG^0 , PT coupling and the reorganization energy. While the Coulomb-bound ion pairs seem to offer an excellent vehicle for study of PT rates, the free energy correlation is scattered because different factors affect the rates and because knowledge of ΔG^0 is inaccurate. An important observation is that no reaction transferring a proton to a C atom of $M^{\bullet-}$ is diffusion controlled. The most important finding is the effect of low charge densities in highly charge-delocalized anions on PT rates and free ion yields.

Based on the above findings, the influence of the charge delocalization on charge separation and potential energy of electron-hole pairs were studied with F_n ($n=1-6$). Because charge delocalization of ions results in weak Coulomb attraction between opposite ions, potential energy of electron-hole pair increases with decreasing charge density. This weak Coulomb attraction also results in preference of solvent separated radical ion pair for electron-hole pairs. The

recombination of electron-hole pair is an electron transfer (ET) reaction. In a simple two-state ET model, the rate of ET exponentially decreases with increasing r so the lifetime of electron-hole pair is increased. Due to the weak Coulomb attraction and long lifetime of electron-hole pair, the charge separation of electron-hole pair (the free ion yield) is enhanced.

Reduction potentials (E_{red}) of molecules were measured by combination of the bimolecular ET equilibria method and pulse radiolysis, which is capable of measuring E_{red} for high reduction potential molecules and molecules with unstable anions. Pulse radiolysis is capable of rapidly reducing molecules in many solvent. The bimolecular ET method provides a window to estimate the equilibrium constant (K_{eq}) of ET reactions. With K_{eq} and E_{red} of the reference molecule, E_{red} of the subject molecule can be estimated.

Table of Contents

Chapter 1. Introduction	p.1
Chapter 2. Backgrounds	
2.1 Pulse Radiolysis	p.5
2.2 Time-Dependent Onsager Problem	p.7
2.3 Electron Transfer Theory	p.11
2.4 Proton Transfer Model	p.15
Chapter 3. Laser Electron Accelerator Facility	p.20
Chapter 4. Escape of Anions from Geminate Recombination due to Charge Delocalization	
4.1 Introduction	p.23
4.2 Experimental	p.26
4.3 Results	p.26
4.4 Estimations of Standard Free Energy Change for the PT Reaction	p.32
4.5 Discussion	p.37
4.5.1 Kinetics of the geminate recombination and PT Reaction	p.38
4.5.2 Capture of Electrons	p.39
4.5.3 Kinetic Analysis	p.39
4.5.4 The CIP-SSIP Picture	p.41
4.5.5 Theoretical Fraction of Free Ions	p.44
4.5.6 Proton Transfer Model	p.45
4.6 Conclusion and Summaries	p.46
Chapter 5. Charge Separation of Electron-Hole Pairs (Exciplexes) Enhanced by Charge Delocalization.	
5.1 Introduction	p.48
5.2 Experiments	p.50
5.3 Results	p.50
5.4 Discussion	p.61
5.4.1 Kinetic Analysis	p.61
5.4.2 Influence of The Low Charge Density	p.64
5.4.3 Transformation between CRIP and SSRIP	p.65
5.4.4 Influence of Charge Density in Electron Transfer Reaction	p.66
5.4.5 Potential Energy of Radical Ion Pair	p.68
5.5 Conclusion and Summaries	p.71
Chapter 6. Energies of Radical Anions Measured by Electron Transfer Equilibria Method.	
6.1 Introduction	p.73
6.2 Experiments	p.73

6.3 Bimolecular Electron Transfer Equilibria Method	p.74
6.4 Results	p.76
6.5 Discussion	p.80
6.6 Summary	p.82
Chapter 7. Summary	p.84
Appendix A. Chemical Structures	
A1. Chemical Structures in Chapter 4	p.89
A2. Chemical Structures in Chapter 5	p.92
A3. Chemical Structures in Chapter 6	p.93
Appendix B. Supporting Information for Chapter 4	p.94
B1. Extinction coefficients of radical anions of benzophenone and oligofluorenes ($F_{n,n=1-4}$)	p.108
B2. Estimation for Difference of Hydrogen Atom Affinity ($\Delta\Delta G_8^0$)	p.110
B3. Measuring the Maximum Observed $G(t)$ and G_{fi} Values of Benzophenone Radical Anions	p.111
B4. The Fraction of Captured Electrons for Benzophenone (BPhO)	p.114
Appendix C. Supporting Information for Chapter 5	p.116
C1. Estimation of Extinction Coefficients for Tetracene Radical Anion and Cation, Oligofluorene Radical Cations, F_n^{*+} ($n=1-6$).	p.117
References	p.120

Table of Tables

TABLE 4.1 ELECTRON ATTACHMENT RATE CONSTANTS (k_{ATT}), EXTINCTION COEFFICIENTS (E) OF THE RADICAL ANIONS AND DIFFUSION COEFFICIENTS (D).....	27
TABLE 4.2 EXTINCTION COEFFICIENTS (E OF $F_N H^+$ ($N=2-4$) AND OSCILLATOR STRENGTH (F) FOR THE STRONGEST BANDS OF $F_N H^+$ ($N=1-4$).....	28
TABLE 4.3 MEASURED PROTON TRANSFER RATE CONSTANTS ($k_{MPT}=K_{EQ}k_{PT}$), REDUCTION POTENTIALS (E_{RED} VS. SCE), HYDROGEN ATOM AFFINITIES (ΔG_8^0), THE CALCULATED STANDARD FREE ENERGY CHANGE (ΔG^0) FOR THE PROTON TRANSFER REACTION, AND THE NUMBER OF ATOMS (NA) OVER WHICH CHARGE IS DISTRIBUTED IN THE ANIONS AND THE ACCEPTING ATOM (AA).....	33
TABLE 4.4 EXPERIMENTAL AND COMPUTED ΔG_8^0 OF BENZENE IN GAS PHASE.....	36
TABLE 4.5 G_{FI} VALUES, TYPE II FREE ION YIELDS (G_{FI}^{II}) AND ESCAPE RATE CONSTANTS (K_{ESC}).....	40
TABLE 4.6 K_{ESC} OF THE (NA^+, PY^-) AND ($RH_2^+, MEPY^-$) ION PAIRS.....	41
TABLE 4.7 LIST OF VARIABLES AFFECTING THE FRACTION OF FREE IONS (F_H) BASED ON THE THEORETICAL FRACTION OF FREE IONS (F_H^{THEORY}).....	44
TABLE 5.1 EXTINCTION COEFFICIENTS OF ANION (E_A) AND CATION (E_C).....	52
TABLE 5.2 LIST OF OXIDATION (E_{OX} VS. SCE) AND REDUCTION (E_{RED} VS. SCE) POTENTIALS, ENERGY OF SINGLET (E_S) AND TRIPLET (E_T) EXCITED STATES AND LIFETIMES OF SINGLET EXCITED STATES (T_S).....	53
TABLE 5.3 GEMINATE RECOMBINATION RATES (K_R), CHARGE SEPARATION RATES (K_{CS}), THE FREE ION PAIR YIELD (G_{FI}), THE TYPE II FREE ION PAIR YIELD (G_{FI}^{II}) AND THE NUMBER OF THE ATOMS (NA).....	55
TABLE 5.4 GROWTH RATE CONSTANTS OF TRIPLET EXCITED STATES (K_G) AND DECAY RATES OF SINGLET EXCITED STATES (K_D) FOR $F_N(N=1-6)$	60
TABLE 5.5 THE COULOMB POTENTIAL ENERGIES OF CRIP AND SSRIP RELATIVE TO THAT OF FREE IONS FOR $F_N(N=1-6)$ IN 2,3-DIHYDROBENZOFURAN (DF) AND TETRAHYDROFURAN (THF).....	69
TABLE 6.1 REDUCTION POTENTIALS (E_{RED}), EQUILIBRIUM CONSTANTS (K_{EQ}), AND BIMOLECULAR ELECTRON TRANSFER RATE CONSTANTS (K_{ET}).....	79
TABLE 6.2 LIST OF ABSORPTION ENERGIES OF P_2 BANDS AND ENTROPIC CONTRIBUTIONS ($-\Delta ST$) FOR $F_N^+(N=5-10)$	82

Table of Figures

FIGURE 1.1 DIAGRAM FOR BULK HETEROJUNCTION SOLAR CELL WHERE AN EXCITON IS GENERATED BY THE ELECTRON DONOR ABSORBING LIGHT THEN IT DIFFUSE TO THE INTERFACE WITH THE ELECTRON ACCEPTOR TO FORM ELECTRON-HOLE PAIR AS CHARGE TRANSFER (CT) STATE. THIS ELECTRON-HOLE PAIR EITHER SEPARATES FROM EACH OTHER TO BE COLLECTED BY THEIR RESPECTIVE ELECTRODES, OR THEY RECOMBINE WITH EACH OTHER. ...1	1
FIGURE 1.2 CHEMICAL STRUCTURES OF (A) POLY(3-HEXYLTHIOPHENES) AND (B) POLY(9,9-DIOCTYLFLUORENE- <i>ALT</i> -BENZOTHIADIAZOLE).2	2
FIGURE 1.3 SCHEMAS OF (A) PHOTOINDUCED ELECTRON TRANSFER (PCT) REACTION AND (B) CHARGE RECOMBINATION (CR) PROCESSES FOR PULSE RADIOLYSIS IN ORGANIC SOLVENT. THE MOST IMPORTANT DIFFERENCE BETWEEN TWO SCHEMAS IS IN FORMATION OF THE CT STATE. IN PCT SYSTEM, FORMATION OF THE CT STATE IS DUE TO ELECTRON TRANSFER REACTION. FOR PULSE RADIOLYSIS, FORMATION OF THE CT STATE IS DUE TO DIFFUSION UNDER INFLUENCE OF THE COULOMB ATTRACTION. D_E IS THE ELECTRON DONOR, A_E IS THE ELECTRON ACCEPTOR, CT IS CHARGE TRANSFER AND CS IS CHARGE SEPARATION STATES, PRIP IS PRIMARY RADICAL ION PAIR CREATED BY PULSE RADIOLYSIS. K_{CT} IS CHARGE TRANSFER RATE AND K_{CR} IS CHARGE RECOMBINATION RATE, K_{CS} IS CHARGE SEPARATION RATE AND K_A IS RATE CONSTANT FOR PRIP DIFFUSION TOGETHER TO BECOME CT STATE.3	3
FIGURE 1.4 CHEMICAL STRUCTURES FOR (A) TETRAHYDROFURAN AND (B) 2,3-DIHYDROBENZOFURAN (C) OLIGO(9,9-DIHEXYL)FLUORENES, ($F_N, N=1-6$).4	4
FIGURE 2.1 AFTER ELECTRON PULSE, (A) TIME SCALE AND (B) THERMALIZATION PROCESSES ADAPTED FROM REFERENCE 14 FOR ELECTRONS GENERATED BY ENERGETIC ELECTRON PULSE. k_B IS THE BOLTZMANN CONSTANT, T IS TEMPERATURE, S IS THE SOLVENT MOLECULE, $^1(S^{++}+E^-)$ AND $^3(S^{++}+E^-)$ REPRESENT SINGLET AND TRIPLET SPIN CONFIGURATIONS, RESPECTIVELY, eloc – IS LOCALIZED ELECTRONS, AND es – IS SOLVATED ELECTRONS.6	6
FIGURE 2.2 SCHEME OF THE TIME-DEPENDENT ONSAGER PROBLEM. R_c IS THE ONSAGER RADIUS WHERE $k_B T = V(R)$; $V(R)$ IS THE COULOMB POTENTIAL, AND T IS TEMPERATURE.8	8
FIGURE 2.3 SCHEMATIC ILLUSTRATION OF THE RADIATION BOUNDARY CONDITION.9	9
FIGURE 2.4 A SCHEMATIC DEPICTION FOR THE MARCUS THEORY (ADAPT FROM REFERENCE 24 AND 25). TWO LOCALIZED ELECTRONIC STATES REPRESENT THE ELECTRON ACCEPTOR (A_E) AND DONOR (D_E), WHERE $-\Delta G^0$ IS THE STANDARD FREE ENERGY CHANGE, λ_s IS THE REORGANIZATION ENERGY, E_A IS THE ACTIVATION ENERGY. THE INSERT ILLUSTRATES SPLITTING OF THE TWO POTENTIAL ENERGY SURFACES WITH THE ENERGY GAP $2V_{fi}$, WHERE V_{fi} IS THE ELECTRON COUPLING MATRIX ELEMENT, FOR A STRONGLY ELECTRONIC COUPLING SYSTEM. 12	12
FIGURE 2.5 THE WELL-KNOWN MARCUS CURVE SHOWS A BELL-SHAPE RELATION BETWEEN ELECTRON TRANSFER RATE (k_{ET}) AND THE STANDARD FREE ENERGY CHANGE (ΔG^0), WHERE k_{ET} IS MAXIMAL AT $-\Delta G^0$ EQUALING TO THE REORGANIZATION ENERGY (λ_s). THE NORMAL REGION IS WHERE k_{ET} INCREASES WITH INCREASING THE MAGNITUDE OF $-\Delta G^0$, AND THE INVERTED REGION IS WHERE k_{ET} DECREASES WITH DECREASING THE MAGNITUDE OF $-\Delta G^0$13	13
FIGURE 2.6 SCHEMATIC REPRESENTATION OF THE PROTON TRANSFER MODEL PROPOSED BY BORGIS AND HYNES (AFTER REFERENCE 47). A_p IS THE PROTON ACCEPTOR, D_p IS THE PROTON DONOR, Q IS THE INTERMOLECULAR COORDINATE DEFINED BY DISTANCE BETWEEN A_p AND D_p , Q IS A COORDINATE DEFINED BY DISTANCE BETWEEN PROTON (H^+) AND D_p , AND S IS THE SOLVENT COORDINATE. SOLVENT MOLECULE IS AN OVAL WITH A DIPOLE AND MASS M_s . DOUBLE-HEAD ARROWS MEAN FLUCTUATIONS.15	15
FIGURE 2.7 (A) POTENTIAL ENERGY (PE) LANDSCAPES OF PROTON TRANSFER (PT) PROPOSED BY BORGIS AND HYNES WITH S AND Q COORDINATES. (B) THE PE PROFILE ALONG THE COORDINATE Q DEFINED BY THE PROTON DONOR-ACCEPTOR DISTANCE. (C) THE PE PROFILE ALONG SOLVENT COORDINATE S FOR THE WEAKLY PROTONIC COUPLING SYSTEM. THE FREE ENERGY OF REACTION ΔG_s^0 AND REORGANIZATION ENERGY λ_s ARE SHOWN. THE INSERT SHOWS THE PE PROFILE IN THE CROSSING POINT FOR THE STRONGLY PROTONIC COUPLING SYSTEM. (D) TWO DOUBLE WELLS AT DIFFERENT S VALUE, WHERE Q IS THE DISTANCE BETWEEN D_p AND H^+ . THE UPPER PANEL SHOWS THAT THE PROTON POTENTIAL IS LOWER THAN THE POTENTIAL BARRIER. THE PROTON TUNNELING OCCURS AT SOLVENT CONFIGURATION S_T IN THE WEAKLY PROTONIC COUPLING SYSTEM. THE LOWER PANEL IS THAT PROTON POTENTIAL IS GREATER THAN THE POTENTIAL BARRIERS IN THE STRONGLY COUPLING SYSTEM. (THESE FOUR FIGURES ARE AFTER REFERENCE 47)17	17
FIGURE 2.8 (A) TOP VIEW OF FIGURE 2.7(A) WITH THE DIRECTION OF THE ENERGY GAP COORDINATE ΔH INDICATED, WHERE R AND P ARE REACTANT AND PRODUCT STATES. (B) POTENTIAL SURFACE (PE) ALONG ΔH (THESE TWO	

FIGURES ARE AFTER REFERENCE 45). THE INSERT SHOWS THE PROTON COUPLING C_0 (AT THE TRANSITION STATE) PRODUCING AN ADIABATIC PE SURFACE.....	19
FIGURE 3.1 OPERATION SCHEMATIC OF THE LASER ELECTRON ACCELERATOR FACILITY (LEAF) LOCATED IN BROOKHAVEN NATIONAL LABORATORY. THE DURATION OF THE ELECTRON PULSE IS DEPENDENT ON THE EXPERIMENTAL END STATION. e_s^- IS SOLVATED ELECTRON S^{++} IS SOLVENT RADICAL CATION, AND S^* IS EXCITED SOLVENT MOLECULE. M IS SOLUTE MOLECULE, M^{++} AND M^- ARE , SOLUTE CATION AND ANION, RESPECTIVELY.	20
FIGURE 3.2 SCHEMATIC ILLUSTRATION OF THE LASER SYSTEM AND OPTICAL PATH IN LEAF. (THIS ILLUSTRATION IS REDRAWING WITH THE PERMISSION FROM DR. ANDREW COOK FROM BROOKHAVEN NATIONAL LABORATORY.)	21
FIGURE 4.1 A SCHEMATIC RELATION BETWEEN THE ION POPULATION, $P(R_i)$, OF INITIAL SEPARATION DISTANCE, R_i , AND THE KINETIC TRACE OF ION RECOMBINATION, WHERE R_c IS ONSAGER RADIUS, $V(R)$ IS COULOMB POTENTIAL. F_H IS THE FRACTION OF FREE (HOMOGENOUS) IONS, WHICH IS G_{FI}/G_{MAX} , AND F_G IS THE FRACTION OF GEMINATE IONS, WHICH IS $(G_{MAX}-G_{FI})/G_{MAX}$, SO $F_H+F_G=1$; G_{FI} IS THE G VALUE OF FREE IONS AND G_{MAX} IS THE MAXIMUM OBSERVED $G(T)$ VALUE OF IONS. THE KINETIC TRACE IN THIS FIGURE IS NOT ACTUAL DATA.	25
FIGURE 4.2 TRANSIENT SPECTRA OF $F_N^{\bullet-}$ ($N=1-4$) WITH 50, 20, 10 AND 5 mM, RESPECTIVELY, CREATED BY PULSE RADIOLYSIS IN THF. THE SPECTRA ARE COLLECTED AT TIMES, $t=10, 50, 100, 500$ AND 1000 NS.....	27
FIGURE 4.3 NORMALIZED KINETIC TRACES OF BENZOPHENONE (BPHO 50 mM AT 800 NM), FLUORANTHENE (FA 60 mM AT 450 NM), 1-METHYLPYRENE (MEPY 40 mM AT 490 NM), DIBENZOFURAN (DBF 50 mM AT 680 NM), <i>P</i> -TERPHENYL (<i>PT</i> 50 mM AT 950 NM), <i>O</i> -TERPHENYL (<i>oT</i> 50 mM AT 600 NM), F_1 (50 mM AT 650 NM), F_2 (30 mM AT 530 NM), F_3 (30 mM AT 570 NM) AND F_4 (20 mM AT 570 NM). THE ABSORBANCE TRACES WERE MULTIPLIED BY FACTORS OF 14.7, 30.1, 17.4, 27.0, 9.53, 15.6, 16.3, 8.4, 3.3 AND 8.2, RESPECTIVELY. SMALL CONTRIBUTIONS OF TRIPLET ABSORBANCE TO THE KINETIC TRACES OF FA AND F_N ($N=2-4$) HAVE BEEN DETERMINED AND SUBTRACTED (SEE TEXT). THE INSERT SHOWS KINETIC TRACES OF $BPhO^{\bullet-}$, $DBF^{\bullet-}$ AND $F_1^{\bullet-}$, WHERE GEMINATE DECAY OF $BPhO^{\bullet-}$ IS THE FASTEST.	29
FIGURE 4.4 NORMALIZED KINETIC TRACES OF RADICAL ANIONS OF BENZOPHENONE ($BPhO^{\bullet-}$ AT 800 NM), 2,3-DICHLORO-5,6-DICYANO- <i>P</i> -BENZOQUINONE ($DDQ^{\bullet-}$ AT 600 NM) AND 4-CYANO-4'- <i>N</i> -PENTYL- <i>P</i> -TERPHENYL ($CNTP^{\bullet-}$ AT 900 NM), WHICH ARE CREATED BY PULSE RADIOLYSIS WITH 50 mM OF THE NEUTRAL SOLUTES IN THF. THE TRACES ARE NORMALIZED BY FACTORS OF $BPhO^{\bullet-}$, $DDQ^{\bullet-}$ AND $CNTP^{\bullet-}$ ARE 14.7, 17.5 AND 6.89, RESPECTIVELY. THE INSERT SHOWS ALMOST IDENTICAL GEMINATE DECAYS FOR $t < 100$ NS AFTER THE ELECTRON PULSE. THE F_H IS 0.36 ± 0.03 FOR THESE THREE ANIONS (SEE TEXT). THE HOMOGENOUS DECAY OF $DDQ^{\bullet-}$ IS DIFFERENT FROM OTHER ANIONS BECAUSE $DDQ^{\bullet-}$ REACTS WITH SMALL AMOUNT OF IMPURITY (TRANSIENT SPECTRA OF $DDQ^{\bullet-}$ IN FIGURE B9 OF APPENDIX B SHOW THE INFLUENCE OF THE IMPURITIES TO $DDQ^{\bullet-}$ IN THE HOMOGENOUS STAGE).	30
FIGURE 4.5 KINETIC TRACES OF 4-NITRO- <i>P</i> -TERPHENYL (NTP 1 mM) AT 720 NM IN THF SOLUTIONS WITH WITH HIGH CONCENTRATIONS OF F_3 (30 mM), BENZOPHENONE (BPHO 50 mM), FLUORANTHENE (FA 60 mM) AND 1-METHYLPYRENE (MEPY 40 mM). AFTER ~ 150 NS, $NTP^{\bullet-}$ IS THE ONLY REMAINING RADICAL ANION, AND THE ONLY ABSORBING SPECIES. FOR $F_3 + NTP$, $\sim 50\%$ MORE $NTP^{\bullet-}$ IONS ARE FORMED THAN FOR THE OTHER THREE SOLUTES.	31
FIGURE 4.6 A PLOT OF MEASURED PROTON TRANSFER RATE CONSTANT ($K_{MPT}=K_{EQ}K_{PT}$) VS. THE ESTIMATED STANDARD FREE ENERGY CHANGE (ΔG^0). THE SYMBOL LEGENDS ARE GIVEN IN TABLE 3. THE UP ARROWS MEAN THAT ONLY LOWER LIMITS WERE DETERMINED, AND DOWN ARROWS MEAN THAT NO PROTON TRANSFER (PT) REACTION WAS OBSERVED.....	35
FIGURE 4.7 EXAMPLES OF DATA AND FITS FOR BENZOPHENONE (BPHO) AND F_N ($N=1-4$), WHERE THE DASHED LINES ARE FITS. THE INSERT SHOWS THAT A SUM OF TWO EXPONENTIAL DECAYS IS SUFFICIENT TO DESCRIBE DIFFUSION-CONTROLLED GEMINATE RECOMBINATION OF $BPhO^{\bullet-}$. THE FITTING PROCEDURE EXTRACTS K_{MPT} AND K_{ESC} FROM DATA, WITH F_H^1 , K_{R1} AND K_{R2} HELD FIXED.	38
FIGURE 4.8 A PLOT OF K_{MPT} VS. THE NUMBER OF ATOMS (NA) OVER WHICH THE NEGATIVE CHARGE IS DISTRIBUTED FOR THE CARBON ACCEPTING ANIONS. THE PLOT SHOWS THAT HIGH CHARGE DENSITY HELPS THE RECOMBINATION OF RADICAL ANIONS WITH SOLVATED PROTONS IN THF. THE LEGENDS OF SYMBOLS ARE GIVEN IN TABLE 4.3.	42
FIGURE 4.9 SCHEMATIC ILLUSTRATION OF ION PAIR POTENTIAL, $U(R)$, VS. SEPARATION DISTANCE, R , WHERE SPHERES ARE IONS AND OVALS ARE SOLVENT MOLECULE WITH A DIPOLE. CIP AND SSIP ARE CONTACT AND SOLVENT SEPARATED ION PAIRS, RESPECTIVELY.	43

FIGURE 4.10 COMPARISON OF THE SPATIAL EXTENT OF F_2 (BEHIND, DARK BLUE) AND PYRENE (FOREGROUND, LIGHT BLUE).....	44
FIGURE 5.1 DIAGRAMS OF CONTACT RADICAL ION PAIR (CRIP) AND SOLVENT SEPARATED RADICAL ION PAIR (SSRIP), WHERE IONS ARE SPHERE, AND SOLVENT MOLECULES ARE OVAL.....	48
FIGURE 5.2 (A) KINETIC TRACES FROM PULSE RADIOLYSIS OF 4,4'-DIMETHYLBIPHENYL (DMBP), <i>P</i> -TERPHENYL (<i>P</i> T), TERTHIOPHENE (T_3) AND FLUORANTHENE (FA) IN 2,3-DIHYDROBENZOFURAN (DF) SOLUTIONS, WHERE CONCENTRATIONS OF ALL SOLUTES ARE 50 mM. (B) KINETIC TRACES OF THESE FOUR MOLECULES AT EARLY TIME.....	51
FIGURE 5.3 KINETIC TRACES FROM PULSE RADIOLYSIS OF $F_N(N=1-6)$ AT OBSERVATION WAVELENGTH IN 2,3-DIHYDROBENZOFURAN WHERE CONCENTRATIONS OF $F_N(N=1-6)$ ARE 50, 50, 40, 30, 20 AND 20 mM, RESPECTIVELY.	52
FIGURE 5.4 KINETIC TRACES FROM PULSE RADIOLYSIS OF (A) $F_N(N=1-3)$ AND (B) F_1 , 4,4'-DIMETHYLBIPHENYL (DMBP), <i>P</i> -TERPHENYL (<i>P</i> T), TERTHIOPHENE (T_3) AND FLUORANTHENE (FA) AT 830 NM IN 2,3-DIHYDROBENZOFURAN WITH 0.5 mM OF TETRACENE (TC). THE CONCENTRATIONS OF $F_N(N=3,4)$ ARE 40 AND 30 mM, RESPECTIVELY, AND THE CONCENTRATIONS OF OTHER MOLECULES ARE 50 mM. THE KINETIC TRACE OF F_3+TC IS CORRECTED FOR ABSORPTION OF ${}^3F_3^*$ AT 830 NM.	54
FIGURE 5.5 BASED ON KINETIC TRACES FROM PULSE RADIOLYSIS OF $F_N(N=3-6)$ SHOWN IN FIGURE 5.3 AND 4,4'-DIMETHYLBIPHENYL (DMBP) SHOWN IN FIGURE 5.2(B), PLOTS OF CONCENTRATIONS OF $F_N(N=3-6)$ AND DMBP RADICAL ION PAIRS (RIP) VS. TIME AT (A) LONGER AND (B) EARLY TIME. THE CONCENTRATIONS OF $F_N(N=3-6)$ IN 2,3-DIHYDROBENZOFURAN SOLUTIONS ARE 40, 30, 20 AND 20 mM, RESPECTIVELY. THE CONCENTRATIONS OF $F_N(N=3-6)$ ION PAIRS ARE ESTIMATED BY THE EXTINCTION COEFFICIENTS OF $F_N(N=3-6)$ AND DMBP RADICAL IONS GIVEN IN TABLE 5.1 WITH PATH LENGTH 5 MM. UNCERTAINTY FOR THE CONCENTRATION OF RIP IS $\sim 13\%$	56
FIGURE 5.6 (A) KINETIC TRACES FROM PULSE RADIOLYSIS OF (A) 4,4'-DIMETHYLBIPHENYL (DMBP) RADICAL IONS AT 680 NM (B) TRIPLET EXCITED STATES OF DMBP (${}^3DMBP^*$) AT 390 NM IN 2,3-DIHYDROBENZOFURAN (DF) WITH DIFFERENT CONCENTRATIONS OF DMBP. THE INSERT OF FIGURE 5.6(A) SHOWS THE KINETIC TRACES OF DMBP RADICAL IONS AT EARLY TIME. THE KINETIC TRACES OF ${}^3DMBP^*$ ARE CORRECTED FOR ABSORPTION OF DMBP RADICAL IONS AT 390 NM.	57
FIGURE 5.7 KINETIC TRACES FROM 397 NM PHOTOLYSIS OF (A) F_3 IONS (F_3^- AND F_3^{++}) AT 1500 NM AND (B) ${}^3F_3^*$ AT 640 NM WHERE THE PATH LENGTHS ARE 0.5 MM WITH DIFFERENT CONCENTRATIONS OF F_3 IN THF. THE INSERT OF (A) SHOWS THE DECAYS OF F_3 IONS AT EARLY TIME. FORMATION OF F_3 IONS IS DUE TO ELECTRON TRANSFER FROM ${}^1F_3^*$, EXCITED BY 397 NM LIGHT, TO F_3 . AT 640 NM, THE INSTANT ABSORPTION IS DUE TO THE INTERSYSTEM CROSSING AND ${}^1F_3^*$, AND THE SLOW GROWTH OF ABSORPTION IS DUE TO THE RECOMBINATION OF F_3 IONS.....	59
FIGURE 5.8 KINETIC TRACES FROM PULSE RADIOLYSIS OF $F_N(N=1-6)$ TRIPLET EXCITED STATES, ${}^3F_N^*(N=1-6)$, AT THEIR MAXIMUM ABSORPTION WAVELENGTHS IN 2,3-DIHYDROBENZOFURAN. THE CONCENTRATIONS OF $F_N(N=1-6)$ ARE 50,50,40,30,20 AND 20 mM, RESPECTIVELY.	60
FIGURE 5.9 TRANSIENT EMISSION FROM PULSE RADIOLYSIS OF $F_N(N=1-6)$ AT THEIR MAXIMUM EMISSION INTENSITY WAVELENGTHS IN 2,3-DIHYDROBENZOFURAN. THE CONCENTRATIONS OF $F_N(N=1-6)$ ARE 50, 50, 40, 30, 20 AND 20 mM, RESPECTIVELY. THE INSERT SHOWS THE TRANSIENT EMISSION OF F_1	61
FIGURE 5.10 THE FREE ENERGY (E) DIAGRAMS OF CHARGE SEPARATION PROCESSES FOR ION PAIRS CREATED BY (A) PHOTOEXCITATION AND (B) PULSE RADIOLYSIS. CS IS CHARGE SEPARATION AND CT IS CHARGE TRANSFER STATES. PRIP IS THE PRIMARY RADICAL ION PAIR CREATED BY PULSE RADIOLYSIS. THE CT STATES COMPRISE OF CONTACT AND SOLVENT SEPARATED RADICAL ION PAIRS.	62
FIGURE 5.11 A PLOT OF THE TYPE II FREE ION PAIR YIELD (G_{FI}^{II}) VS. THE NUMBER OF THE ATOMS (NA). RELATION BETWEEN CHARGE DENSITY AND NA IS RECIPROCAL.....	64
FIGURE 5.12 SCHEMATIC DIAGRAM FOR CALCULATING COULOMB POTENTIAL ENERGY BETWEEN TWO IRREGULAR CHARGED OBJECTS. P_A IS CHARGE DENSITY OF THE ACCEPTOR AND P_D IS CHARGE DENSITY OF THE DONOR. V_A IS VOLUME OF THE ACCEPTOR AND V_D IS THE VOLUME OF THE DONOR.	67
FIGURE 5.13 A PLOT OF GEMINATE RECOMBINATION RATE (k_R) VS. THE NUMBER OF THE ATOMS (NA). RELATION BETWEEN CHARGE DENSITY AND NA IS RECIPROCAL. THE UP ARROW MEANS THE LOWER LIMIT.	68

FIGURE 6.1 (A) TRANSIENT SPECTRA OF TRIMETHYLPHENYLSILANE RADICAL ANIONS (TMPS) IN THF WITH 5 mM OF TMPS. (B) KINETIC TRACES AT 1507 NM IN THF WITHOUT AND WITH TMPS.	76
FIGURE 6.2 KINETIC TRACES AT 650 NM OF $F_1^{\cdot-}$ WITH AND WITHOUT PHENANTHRENE (PHE) IN THF, WHERE THE CONCENTRATIONS ARE 100 mM F_1 , 100 mM $F_1 + 0.8$ mM PHE AND 48 mM PHE IN THF SOLUTIONS CONTAINING 10 mM OF SODIUM TETRAPHENYLBORATE (NABPH ₄). $F_1^{\cdot-}$ WITHOUT NABPH ₄ (RED, 100 mM OF F_1) DECAYS MUCH FASTER THAN $F_1^{\cdot-}$ WITH NABPH ₄ (BLUE).	77
FIGURE 6.3 KINETIC TRACES OF (A) SOLVATED ELECTRONS (E_s^-) AND <i>TRANS</i> -STILBENE (ES) WITH AND WITHOUT F_8 AT 710 NM, AND (B) E_s^- AND TETRAPHENYLMETHANE (TPM) WITH AND WITHOUT FLUOROBENZENE (FBZ) AT 900 NM IN THF. ES AND FBZ WERE USED AS THE ELECTRON DONOR FOR CAPTURING E_s^- WITHOUT ELECTROLYTE. E_{RED} OF F_8 WAS ESTIMATED BY USING E_{RED} OF ES AS A REFERENCE, AND E_{RED} OF TPM WAS ESTIMATED BY USING E_{RED} OF FBZ AS REFERENCES; K_{EQ} OF THE ELECTRON TRANSFER REACTIONS WERE DETERMINED BY THE BIMOLECULAR ELECTRON TRANSFER EQUILIBRIA METHOD.	78
FIGURE 6.4 A PLOT OF THE REDOX POTENTIAL OF F_N ($N=1-10$) VS. REPEAT UNITS (N), WHERE E_{RED} IS REDUCTION POTENTIAL AND E_{OX} IS OXIDATION POTENTIAL. THE E_{OX} OF F_N ($N=2-7$) ARE TAKEN FROM TABLE 1 OF THIS REFERENCE ¹⁵⁵ ARE REPORTED VS. $AgNO_3/Ag$ AND CONVERTED INTO VS. SCE WITH E_{OX} OF FERROCENE, 0.232 V (VS. $AgNO_3/Ag$) ¹⁵⁵ AND 0.53 V (VS. SCE). ⁹⁷ FIT RESULTS ARE $E_{OX}=1.16+0.53(1/N)$ AND $E_{RED}=-1.91-0.63(1/N)$, WHICH ARE RED AND BLUE LINES, RESPECTIVELY.	80
FIGURE 6.5 MOLECULAR ORBITAL DIAGRAM FOR NEUTRAL AND CHARGED CONJUGATED OLIGOMERS. FOR THE ANION OF CONJUGATED OLIGOMERS, SOMO IS DUE TO THAT ADDITIONAL ELECTRON DISTORTS THE ENERGY LEVEL OF LUMO. SOMO IS THE SINGLY OCCUPIED MOLECULAR ORBITAL, LUMO IS THE LOWEST UNOCCUPIED MOLECULAR ORBITAL, AND HOMO IS THE HIGHEST OCCUPIED MOLECULAR ORBITAL. THE P_1 AND P_2 ARE ABSORPTION BANDS OF POLARON. THE VN IS THE VESTIGIAL NEUTRAL BAND IN NEUTRAL CONJUGATED OLIGOMERS.	81

List of Schemes

- SCHEME 4.1** KINETIC OF GEMINATE ION RECOMBINATION IN THF, WHERE ANNIHILATION OF RADICAL ANIONS ($M^{\cdot-}$) IS DUE TO THE PT REACTION (SEE TEXT). CIP AND SSIP ARE CONTACT AND SOLVENT SEPARATED ION PAIRS, RESPECTIVELY. THE EFFECTIVE PT RATE CONSTANT IS THE MEASURED PT RATE CONSTANT ($K_{MPT} = K_{EQ}K_{PT}$). F_H^I AND F_H^{II} ARE THE FRACTIONS OF TYPE I AND TYPE II FREE IONS, RESPECTIVELY.....37
- SCHEME 5.1 KINETICS OF CHARGE SEPARATION (CS) PROCESSES, WHERE CRIP IS CONTACT RADICAL ION PAIR AND SSRIP IS SOLVENT SEPARATED RADICAL ION PAIRS, K_{ET} IS ELECTRON TRANSFER (ET) RATE CONSTANT, K_{-ET} IS REVERSED ET RATE CONSTANTS, K_{SOLV} IS SOLVATION RATE CONSTANT, K_{-SOLV} IS REVERSED SOLVATION RATE CONSTANTS, K_{CS} IS CS RATE CONSTANT, K_{DISS} IS DISSOCIATION RATE CONSTANT ($K_{DISS} = K_{SOLV}K_{CS}$), K_{SOLV} IS EQUILIBRIUM CONSTANT BETWEEN CRIP AND SSRIP ($K_{SOLV} = K_{SOLV}/K_{-SOLV}$ OR $[SSIP]/[CRIP]$), WHICH IS RECIPROCAL TO K_{EQ} FROM SCHEME 4.1, K_R IS THE RECOMBINATION RATE CONSTANT OF IONS. K_{LET} IS LONG RANGE ET RATE CONSTANT AND K_{-LET} IS REVERSED LONG RANGE ET RATE CONSTANTS.....62
- SCHEME 5.2 KINETICS OF GEMINATE RECOMBINATION FOR IONS CREATED BY PULSE RADIOLYSIS. PRIP IS PRIMARY RADICAL ION PAIRS, CT STATE IS CHARGE TRANSFER STATE, WHICH CONSISTS OF SOLVENT SEPARATED AND CONTACT RADICAL ION PAIRS, AND CS STATE IS CHARGE SEPARATED STATE. K_{A1} AND K_{A2} ARE ASSOCIATION RATE CONSTANTS, K_R IS GEMINATE RECOMBINATION RATE CONSTANT AND K_{CS} IS THE CHARGE SEPARATION RATE CONSTANT.63

List of Abbreviations

A_e : Electron Acceptor
 A_p : Proton Acceptor
AO: acetophenone
AQ: Anthraquinone
BH Model: Borgis and Hynes Model
BHJ: Bulk Heterojunction
BP: biphenyl
BPhO: Benzophenone
CIP: Contact Ion Pair
CNTP: 4-cyano-4'-*n*-pentyl-*p*-terphenyl
CR: Charge Recombination
CRIP: Contact Radical Ion Pair
CS: Charge Separation
CT: Charge Transfer
DBF: Dibenzofuran
 D_e : Electron Donor
DNB: Dinitrobenzene
DMP: 2,3-dimethylphenta-3-one
DMF: Dimethylformamide
 D_p : Proton Donor
DF: 2,3-dihydrobenzofuran
DS equation: Debye-Smoluchowski equation
E.A.: Electron Affinity
EC: Electron Capture
ET: Electron Transfer
 e_s^- : Solvated Electrons
ES: trans-Stilbene
FA: Fluoranthene
FBz: Fluorobenzene
 F_{esc} : The Fraction the Free Ion Yield from Photoexcitation Data
 F_h : The Fraction of the Free Ion Yield
 F_h^I : The Fraction of the Type I Free Ion Yield
 F_h^{II} : The fraction of the Type II Free Ion Yield
 F_n : oligo(9,9-dihexyl)fluorenes
 G_{fi} : The Free Ion Yield
 G_{fi}^I : The Type I Free Ion Yield
 G_{fi}^{II} : The Type II Free Ion Yield
HOMO: Highest Occupied Molecular Orbital
IPE: Ideal Polarisable Electrode

IRIP: Intimate Radical Ion Pair
LUMO: Lowest Unoccupied Molecular Orbital
MePy: 1-methylpyrene
NaBPh₄: Sodium Tetraphenylborate
NaPF₆: Sodium Hexafluorophosphate
NBz: nitrobenzene
NTP: 4-nitro-*p*-terphenyl
*o*T: *o*-Terphenyl
PCT: Photoinduced Charge Transfer
Phe: Phenanthrene
PRIP: Primary Radical Ion Pair PT: Proton Transfer
*p*T: *p*-Terphenyl
*p*Xy: *p*-Xylene
RIP: Radical Ion Pair
SOMO: Singly Occupied Molecular Orbital
SSIP: Solvent Separated Ion Pair
SSRIP: Solvent Separated Radical Ion Pair
T₃: Terthiophene
TC: tetracene
TCB: 1,2,4,5-tetracyanobenzene
TBAPF₆: Tetrabutylammonium Hexafluorophosphate
TCNE: Tetracyanoethylene
THF: Tetrahydrofuran
TMPS: Trimethylphenylsilane
TPM: Tetraphenylmethane
VN: Vestigial Neutral

Chapter 1. Introduction

Due to the energy crisis and global warming, needs for renewable energy have increased in the last decade. One of most promising renewable energy resources, organic solar cells, has attracted high attention. Generally, there are two types of organic solar cells, dye-sensitized and bulk heterojunction (BHJ) solar cells. Due to low cost processing techniques capable of fabricating solar cells with large area, BHJ solar cells remain of interest. A simplified photovoltaic process of BHJ solar cells is illustrated in Figure 1.1. An exciton is created by absorption of a photon within the electron donor (D_e). The exciton then transfers to an interface with an electron acceptor (A_e). Once the exciton diffuses to the interface, it forms a charge transfer (CT) state, where an electron resides A_e and hole resides D_e . If the Coulombic attraction of the CT state can be overcome, the electron and hole will separate and become free charges. If this binding energy cannot be overcome, electron recombines with hole. Eventually, these free charges are collected at their respective electrodes to create available electricity if the electron and hole are separated. For BHJ solar cells, the energy efficiency is dependent on the yield of the free charges. For a charge to be “free”, there are two criteria: (1) the two opposite-charge carriers, negative and positive, are separated from each other at least a critical distance, r_c , which is usually referred as the Onsager¹ radius where $k_B T = V(r_c)$, k_B is the Boltzmann constant, T is temperature and $V(r_c)$ is the mutual Coulomb potential at r_c ; (2) recombination of the charged species is bimolecular.

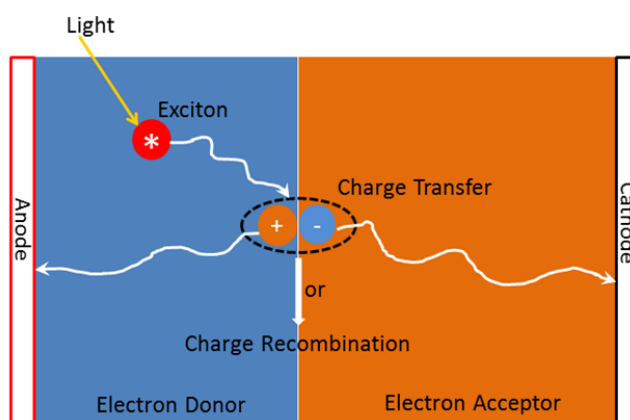


Figure 1.1 Diagram for bulk heterojunction solar cell where an exciton is generated by the electron donor absorbing light then it diffuses to the interface with the electron acceptor to form electron-hole pair as charge transfer (CT) state. This electron-hole pair either separates from each other to be collected by their respective electrodes, or they recombine with each other.

Organic solvents provide an excellent “sandbox” to study charge recombination (CR) of BHJ solar cells. The most common conjugated polymers for the BHJ solar cells are typically poly(3-hexylthiophenes) and poly(9,9-dioctylfluorene-*alt*-benzothiadiazole), illustrated in Figure 1.2, which are amorphous and have low dielectric constant ($\epsilon_d \sim 3-4$). In polar organic solvents such

as acetonitrile ($\epsilon_d=37.5$), photoinduced charge transfer (PCT) reactions illustrated in Figure 1.3 (a) have been well studied by many groups²⁻¹² by flash photolysis. In general, the D_e is excited by light then an electron transfers from D_e^* to A_e with CT rate constant k_{CT} to produce the CT state, where pairing between $A_e^{\bullet-}$ and $D_e^{\bullet+}$ is due to the Coulombic attraction. The CT state may separate into free charges or charge separation (CS) state, if the Coulombic attraction is overcome, or collapse by CR with a rate k_{CR} . From Figure 1.1 and Figure 1.3 (a), the PCT reactions are almost identical with photovoltaic effects in the BHJ solar cells. With pulse radiolysis rapidly creating electrons and holes, a high concentration of solute is capable of capturing the electrons and holes to become charge carriers. For pulse radiolysis, CR processes in organic solvent are illustrated in Figure 1.3 (b). The difference of CT state between the flash photolysis and pulse radiolysis is in formation. The CT state created by flash photolysis is due to ET from D_e^* to A_e , and the CT state created by pulse radiolysis is due to two opposite-ions diffuse together under influence of the mutual Coulombic attraction.

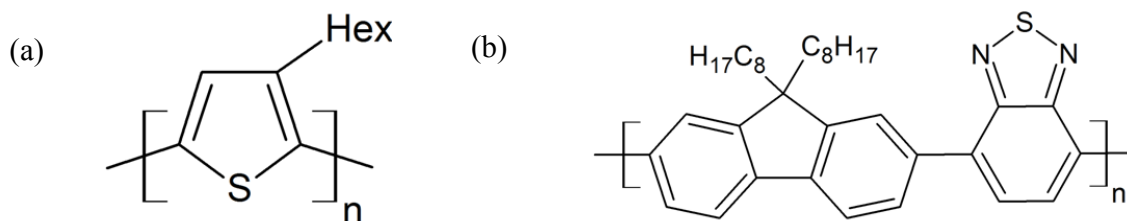


Figure 1.2 Chemical Structures of (a) Poly(3-hexylthiophenes) and (b) Poly(9,9-dioctylfluorene-*alt*-benzothiadiazole).

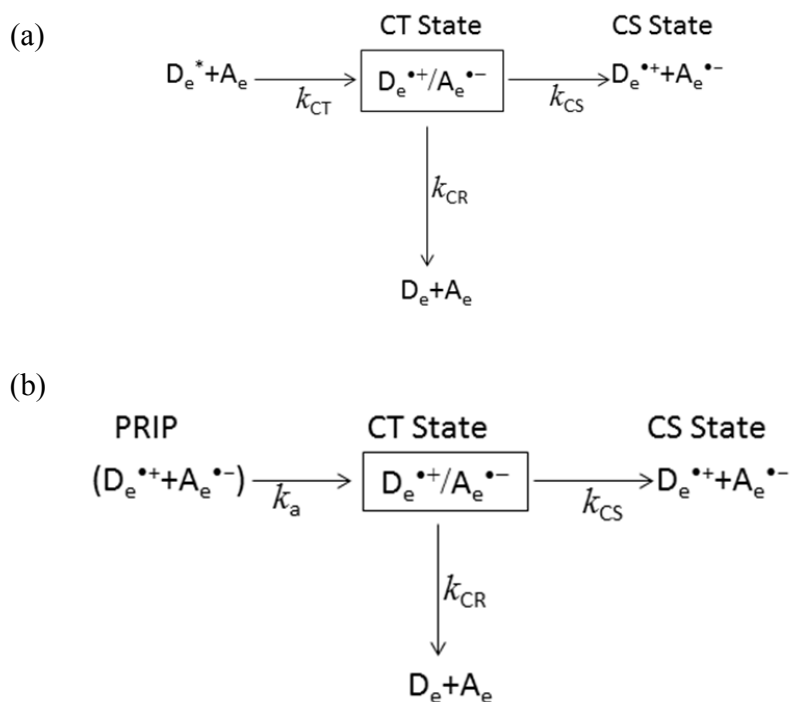


Figure 1.3 Schemas of (a) photoinduced electron transfer (PCT) reaction and (b) charge recombination (CR) processes for pulse radiolysis in organic solvent. The most important difference between two schemas is in formation of the CT state. In PCT system, formation of the CT state is due to electron transfer reaction. For pulse radiolysis, formation of the CT state is due to diffusion under influence of the Coulomb attraction. D_e is the electron donor, A_e is the electron acceptor, CT is charge transfer and CS is charge separation states, PRIP is primary radical ion pair created by pulse radiolysis. k_{CT} is charge transfer rate and k_{CR} is charge recombination rate, k_{CS} is charge separation rate and k_a is rate constant for PRIP diffusion together to become CT state.

A pioneer, Albert Weller,⁸⁻¹¹ studying PCT in organic solvents concluded that the yield of the CS state was dependent on the Coulomb potential, solvation (polarization) energy and interaction between two charge carriers such as electronic spin configuration of radical ion pair (RIP). Based on this conclusion, this thesis consists of three projects:

- (1) Escape of Anions from Geminate Recombination due to Charge Delocalization (Chapter 4).
- (2) Charge Separation of Electron-Hole Pairs (Exciplexes) Enhanced by Charge Delocalization (Chapter 5).
- (3) Energies of Radical Anions Measured by Electron Transfer Equilibria Method (Chapter 6).

The purpose of first two projects is to understand the influence of charge delocalization in recombination kinetics of charge carriers in low dielectric constant organic solvents such as tetrahydrofuran (THF, $\epsilon_d=7.48$) and 2,3-dihydrobenzofuran (DF, $\epsilon_d=4.33$)¹³ illustrated in Figure 1.4 (a) and (b), respectively, with pulse radiolysis. The purpose of the last project is to measure

reduction potential of $F_n(n=1-6)$ anion for estimating potential energy of $F_n(n=1-6)$ ion pair in THF. In conjugated polymer, ion's degree of charge delocalization is dependent on the conjugated length of π -orbital, which is related to the repeat units (n), therefore ions of oligomers with different n have different degrees of charge delocalization. In this thesis, oligo(9,9-dihexyl)fluorenes (F_n , $n=1-6$) as illustrated in Figure 1.4 (c) are used to varied degree of charge delocalization. Influence of charge delocalization in CR reactions, proton transfer in THF and electron transfer reactions in DF will be systemically studied in this thesis. This information about CR with different degree of charge delocalization in these organic solvents can provide insight useful for the improving energy efficiency of the BHJ solar cells.

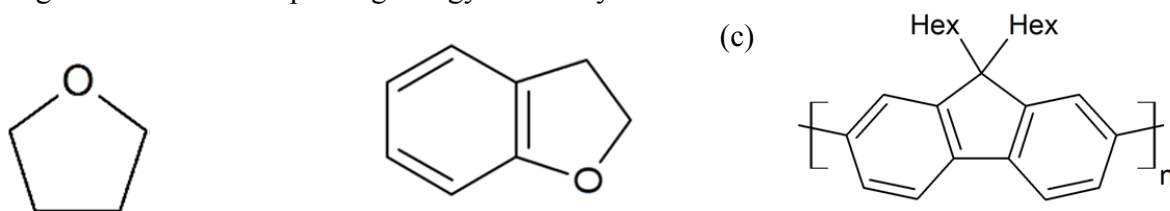


Figure 1.4 Chemical Structures for (a) Tetrahydrofuran and (b) 2,3-Dihydrobenzofuran (c) oligo(9,9-dihexyl)fluorenes, (F_n , $n=1-6$).

Chapter 2. Background

Recombination of charge carriers are studied in organic solvent with $F_n(n=1-6)$ ions with different charge density by pulse radiolysis. The CR reactions in THF and DF are the ET and PT reactions. Therefore, this chapter will briefly introduce pulse radiolysis, the time-dependent Onsager problem, the Marcus theory (ET theory) and PT model. In organic solvent, the recombination proceeds by the anion and cation diffusing together under influence of the Coulombic attraction followed by charge annihilation each other. In the following subsections, the Onsager time-dependent problem describing diffusion under influence of the Coulomb attraction between anion and cation will be introduced. The ET theory and the PT model will be introduced subsequently.

2.1 Introduction to Pulse Radiolysis

Pulse radiolysis, the initiation of reactions by energetic particles, such as electrons and protons, or an ionizing photon pulse, is a powerful technique for studying chemical reactions. The energetic particles or photons transfer their energy to the medium due to inelastic collisions that ionize or excite the medium's molecules. The rate of energy transfer is dependent on the energies of particles and photons, the type of particles and the density of the medium. Radiolysis reactions likely occur in the area around the path of the particle pulse, where the number of molecular fragments is high. Outside the path, the medium molecules are unperturbed. Ionizations of medium frequently result secondary electrons with enough energy to induce further excitations or ionizations within their own paths or "spurs". The cross section of medium's molecule decides distribution of ionizations and excited medium molecules, which cross-react to yield solvated electrons, ions, radicals, excited molecules and molecular products. These primary products can react with solutes to form transient species of interest.

The common energetic photons are such as X-rays and γ -rays, and the common energetic particles are such as electrons, neutrons, protons and other atomic nuclei. In relative terms, energy deposition depth is large for X-rays and γ -rays, and moderate for electrons. For more massive and more highly charged particles, the deposition depth is short because the stopping power is high. The yield of the final products of radiolysis is increased with increasing the density of interactions for the cross reactions between initial radiolysis products. It is important to remember that different types of the radiation result in different distributions of products. Nevertheless, this section will only focus on radiolysis reactions initiated by the electron pulse.

High energy electrons, referred to as primary and secondary electrons, are created by the Compton effect while the medium molecules are ionized by the electron pulse, and the time scale is shown in Figure 2.1 (a).¹⁴ These electrons interact with the medium molecules to ionize or excite them. These interactions mainly result in the low energy electrons (<10 eV) which lose their energy in exciting electronic transitions and vibrational states of the medium molecules.

When the energy of the electrons is below 50 meV, they are referred to localized electrons (e_{loc}^-), which are thermalized but not solvated by the medium yet. Eventually, when the energy of electrons drops to ~ 30 meV, they are referred to solvated electrons (e_s^-). During the thermalization of the electrons shown in Figure 2.1 (b), the distance between cation (hole) and electron increases and e_{loc}^- might leave spurs and possibly also the mutual Coulomb potential. However, they can eventually recombine with charge annihilation.

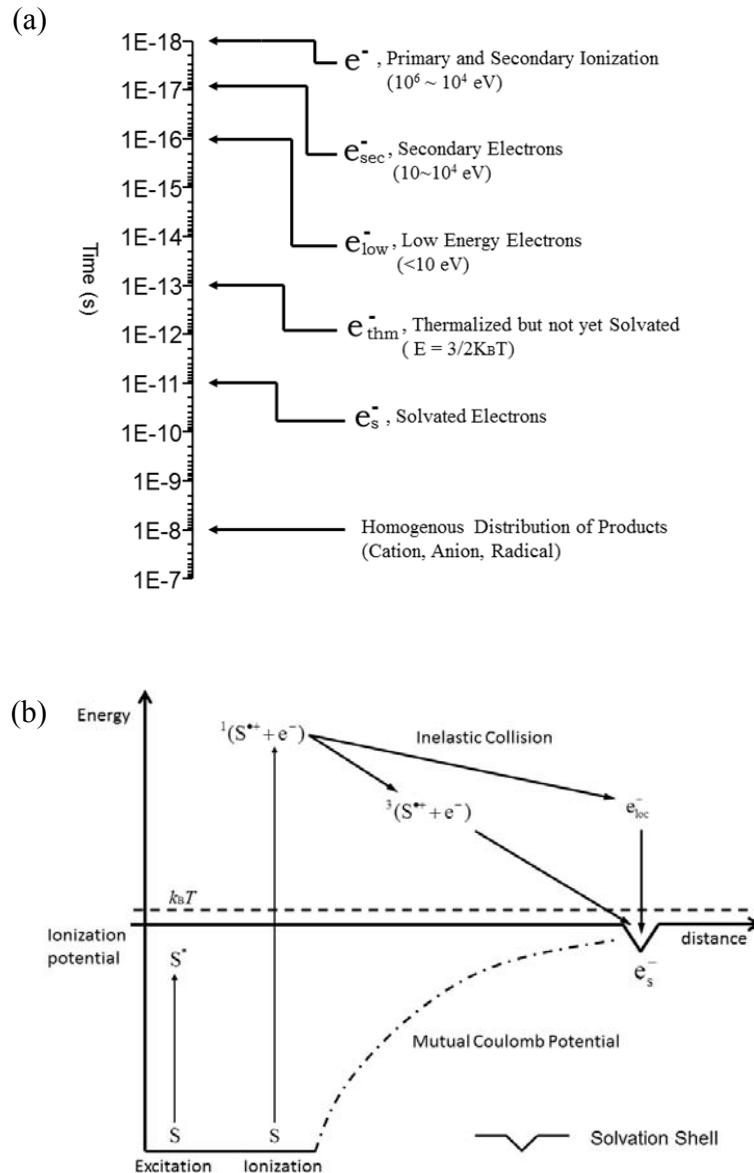


Figure 2.1 After electron pulse, (a) time scale and (b) thermalization processes adapted from reference 14 for electrons generated by energetic electron pulse. k_B is the Boltzmann constant, T is temperature, S is the solvent molecule, $^1(S^{*+} + e^-)$ and $^3(S^{*+} + e^-)$ represent singlet and triplet spin

configurations, respectively, $\mathbf{e}_{\text{loc}}^-$ is localized electrons, and \mathbf{e}_{s}^- is solvated electrons.

2.2 Time-dependent Onsager Problem

Onsager¹ employed the Debye-Smoluchowski (DS) equation¹⁵ with the assumption that the ion recombination was instant upon contact (diffusion-controlled recombination) to estimate the probability of paired ion escapes from each other as illustrated in Figure 2.2. Debye¹⁵ used the DS equation to calculate ion recombination rates under influence of the Coulomb attraction between anion and cation with two assumptions, uniform spatial distribution of ions and annihilation of ions happening upon contact. The DS equation describing Brownian motion of one particle under the influence of the mutual Coulomb attraction is:

$$\frac{\partial \rho}{\partial t} - \nabla \cdot (D \nabla \rho + \rho \mathbf{v}) = 0 \quad (2.2.1a)$$

and

$$\mathbf{v} = -\mu \frac{q}{4\pi\epsilon_0\epsilon r^2} \hat{\mathbf{r}} \quad (2.2.1b),$$

where t is time, $\rho(r, \mu, t)$ is the distribution function of the ion pairs, r is the separation distance (center to center) of ion pair, D is the mutual diffusion coefficient, μ is the mutual ion mobility, q is charge of the ion and ϵ is dielectric constant, with polar coordinates. For the recombination occurring upon contact, the boundary condition is

$$\frac{\partial \rho}{\partial t} = -\infty \text{ for } r = r_- + r_+ \quad (2.2.2a)$$

$$\frac{\partial \rho}{\partial t} = 0 \text{ for } r > r_- + r_+ \quad (2.2.2b),$$

where r_- and r_+ are the radius of anion and cation, respectively. The initial, δ -functional distribution of ion pairs is:

$$\rho(r, \mu, t | r_i, \mu_i, 0) = \frac{1}{2\pi \cdot r_i^2} \delta(r - r_i) \delta(\mu - \mu_i) \quad (2.2.3),$$

where μ_i is the initial mobility of ion. To solve the DS equation with these initial and boundary conditions. With Green's function of equation (2.2.2), Onsager solved the DS equation analytically. The ultimate escape probability (P_{esc}) given by Onsager is:

$$P_{\text{esc}} = \exp\left(-\frac{r_c}{r_i}\right) \quad (2.2.4),$$

where r_c is the critical distance usually referred as Onsager radius where $k_B T = V(r_c)$, and r_i is the initial separation distance of ion pair. $V(r)$ is the mutual Coulomb potential at r_c .

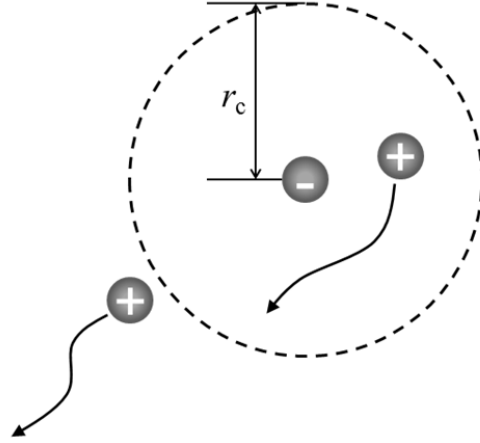


Figure 2.2 Scheme of the Time-dependent Onsager Problem. r_c is the Onsager radius where $k_B T = V(r)$; $V(r)$ is the Coulomb potential, and T is temperature.

Many scientists¹⁶⁻²⁰ extended the work of Onsager with the assumption that the ion recombination was not instant upon contact (non-diffusion controlled recombination) to estimate the probability of paired ions escape from each other. Hong¹⁶⁻¹⁷ and Noolandi^{16-17, 20-21} solved the DS equation with the radiation boundary condition as illustrated in Figure 2.3. This boundary describes a partly absorbing and partly reflecting sphere with radius $r = r_m$. The effective radius (r_m) represents the distance where some of the ion pairs approach one another and then separate again. Therefore, the boundary condition for solving the DS equation is:

$$j_r = -k_r \cdot r_m \cdot \rho \quad (2.2.5),$$

at $r = r_m$, where j_r is the current density in the surface of the sphere surfaces and k_r is the recombination rate.

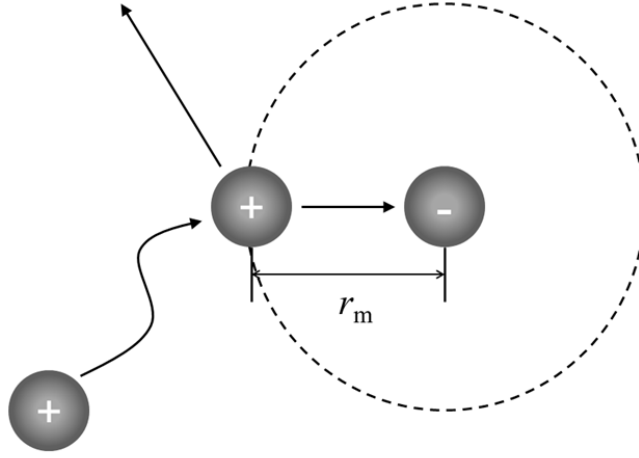


Figure 2.3 Schematic illustration of the radiation boundary condition.

A brief description for solving the DS equation with the radiation boundary condition will be given in the following. To simplify equation (2.2.1) for solving it, a new function $h(r, \mu, t)$ is introduced. With taking $r_c/2$ as unit length and $r_c^2/4D$ as unit time, the relation between ρ and h is:

$$\rho(r, \mu, t | r_i, \mu_i) = \frac{1}{4\pi\sqrt{r_i r}} \exp\left(-\frac{r-r_i}{r_i r}\right) h(r, \mu, t | r_i, \mu_i) \quad (2.2.6)$$

so the initial distribution function and equation (2.2.1) are rewritten as:

$$\rho(r, \mu, t | r_i, \mu_i) = \frac{h(r, \mu, t | r_i, \mu_i)}{2\pi\sqrt{r_i \cdot r}} \exp\left[-\frac{1}{2}\left(\frac{r_c}{r_i} - \frac{r_c}{r}\right)\right] \quad (2.2.7)$$

and

$$\frac{\partial h}{\partial t} = \frac{\partial^2 h}{\partial r^2} + \frac{1}{r} \frac{\partial h}{\partial r} - h \cdot \left(\frac{1}{4r^2} + \frac{1}{r^4}\right) + \frac{1}{r^2} \frac{\partial}{\partial \mu} \left[(1-\mu^2) \frac{\partial h}{\partial \mu} \right] \quad (2.2.8),$$

respectively; the corresponding initial and boundary conditions are written as:

$$h(r, \mu, 0 | r_i, \mu_i) = \frac{1}{r_i} \delta(r - r_i) \delta(\mu - \mu_i) \quad (2.2.9)$$

and

$$\frac{\partial h}{\partial t} = \left(\frac{1}{r_m^2} + \frac{1}{2r_m} + k_r \cdot r_m \right) h(r, \mu, t | r_m) \quad (2.2.10).$$

After introducing $h(r, \mu, t)$, the equation (2.2.8) is separable and similar to the time-dependent Schrödinger equation for a particle moving in a dipole-type potential field with an inverse fourth-power repulsive core, which has been solved by Bühring.²² With this similarity, the solution of equation (2.2.8) can be written as series solution that is:

$$h(r, \mu, t | r_i, \mu_i) = \sum_{l=0}^{\infty} R_l(r, \mu, t | t_i) P_l(\mu) P_l(\mu_i) \quad (2.2.11),$$

where $P_l(\mu)$ and $P_l(\mu_i)$ are the generating Legendre functions that satisfy the equation,

$$\frac{\partial}{\partial \mu} \left[(1 - \mu^2) \frac{\partial P_l}{\partial \mu} \right] + \lambda_l P_l = 0 \quad (2.2.12)$$

and λ_l are the eigenvalues for the angular components of the solution; With the series solution, the equation (2.2.8) is

$$\frac{\partial R_l}{\partial t} = \frac{\partial^2 R_l}{\partial r^2} + \frac{1}{r} \frac{\partial R_l}{\partial r} - R_l \cdot \left(\frac{1}{4r^2} + \frac{\lambda_l}{r^2} + \frac{1}{r^4} \right) \quad (2.2.13)$$

and the boundary condition is:

$$R_l(r, 0 | r_i) = \frac{1}{r_i} \delta(r - r_i) \quad (2.2.14).$$

The Laplace transform of R_l is

$$\tilde{R}_l(r, s | r_i) = L[R_l(r, t | r_i)] = \int_0^{\infty} dt e^{-st} R_l(r, t | r_i) \quad (2.2.15)$$

that satisfies

$$\frac{d^2 \tilde{R}_l}{dr^2} + \frac{1}{r} \frac{d\tilde{R}_l}{dr} - \tilde{R}_l \left(s + \frac{1}{4r^2} + \frac{\lambda_l}{r^2} + \frac{1}{r^4} \right) = -\frac{1}{r_i} \delta(r - r_i) \quad (2.2.16).$$

The solution of equation (2.2.1) can be represented by two linear independent solutions to the homogenous equation corresponding to equation (2.2.16), which are in terms of a series of modified Bessel function products.²² The solutions consisting of appropriate linear combinations

of these Bessel functions for $r > r_i$ and $r < r_i$ are determined by the continuity of the particle density and the discontinuity in the derivatives of $h(r, \mu, t)$ at r_i , and the boundary condition, equation (2.2.5).

The purpose of this research is to study the free ion yield. For the long-time behavior of the ion recombination, the Laplace transform of the solution for the DS equation with boundary condition equation (2.2.5) is:

$$U(r) = \exp\left(-\frac{r_c}{r}\right) + \left(\frac{D \cdot r_c}{k_r \cdot r_m^3} - 1\right) \exp\left(-\frac{r_c}{r_m}\right) \quad (2.2.17),$$

where k_r is the recombination rate. The definition of “long-time” given by Hong and Noolandi¹⁶⁻¹⁷ is that $Dt \gg r^2, r_i^2$ and r_c^2 . P_{esc} that ion escaping from ion recombination is:

$$P_{\text{esc}} = \frac{U(r_i)}{U(\infty)} \quad (2.2.18).$$

For k_r or $r_m \rightarrow 0$ equation (2.2.17) gives $P_{\text{esc}} = \exp(-r_c/r_i)$ which is identical with the ultimate escape probability given by Onsager.¹

2.3 Electron Transfer Theory

In molecular systems, the motion of electrons are correlated due to their Coulomb and energy exchange interactions. However, many reactions produce a change in the equilibrium position of just a small number of these electrons, so it is useful to formulate physical pictures and rate theories for the electron transfer (ET). To formulate theories of ET reactions, it is expedient to separate the dynamics of ET from the nuclear degrees of freedom. With the Born-Oppenheimer approximation,²³ electronic and nuclear motions are separated. ET can be visualized as Figure 2.4 showing this separation that where two localized electronic states representing potential energies of A_e and D_e that depend on the nuclear coordinates. ET occurs at the crossing point of the two potential energy surfaces and driven by interactions between A and D_e . The weakly electronic coupling (adiabatic) between A_e and D_e result in non-adiabatic ET via overlaps of wave functions for electrons on A_e and D_e . The insert of Figure 2.4 shows that the strong interactions (non-adiabatic) between A_e and D_e result in an avoided crossing point of the two potential surfaces and splitting into two levels with an energy gap.

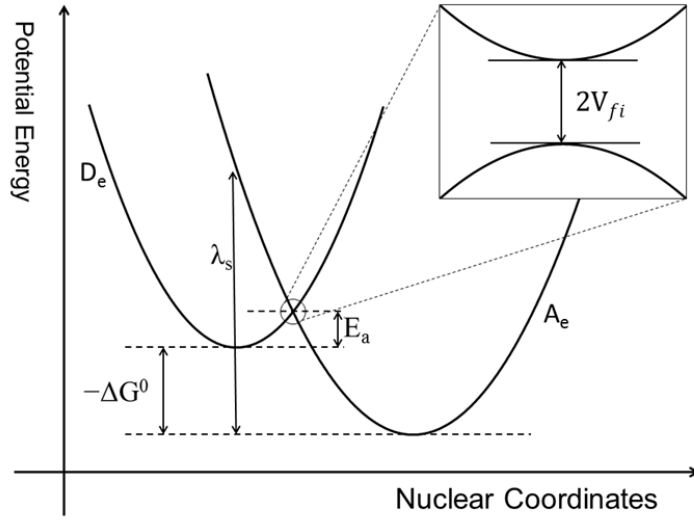


Figure 2.4 A Schematic Depiction for the Marcus Theory (adapt from reference 24 and 25). Two localized electronic states represent the electron acceptor (A_e) and donor (D_e), where $-\Delta G^0$ is the standard free energy change, λ_s is the reorganization energy, E_a is the activation energy. The insert illustrates splitting of the two potential energy surfaces with the energy gap $2V_{fi}$, where V_{fi} is the electron coupling matrix element, for a strongly electronic coupling system.

For a weakly electronic coupling system, first-order perturbation theory, a standard quantum mechanical approach, is applied to describe the probability of ET from a reactant state ψ_i to a product state ψ_f . This probability is:

$$P_{fi} = \frac{1}{\hbar^2} |\langle \psi_i | H | \psi_f \rangle|^2 \left[\frac{\sin(\omega_{fi}/2)}{\omega_{fi}/2} \right]^2 \quad (2.3.1),^{26}$$

where $\langle \psi_i | H | \psi_f \rangle = V_{fi}$ is corresponding electronic coupling matrix element, H is the electronic Hamiltonian, $\hbar\omega_{fi}$ is the transition energy between electronic states ψ_i and ψ_f . For a continuous distribution of final electronic states, the density of final states, $\rho(E_f)$, is introduced to calculate the transition probability. With summation of all probability density and assuming $|V_{fi}|^2 \rho(E_f)$ slowly changed with energy, the ET rates or transition probability per unit time is:

$$k_{fi} = \frac{2\pi}{\hbar} |V_{fi}|^2 \rho(E_f) \quad (2.3.2),^{26}$$

which has form of the Fermi's Golden Rule. The physical meaning of $|V_{fi}|^2$ is to describe overlaps of the wave functions for the electron on A_e and D_e at the contact distance R_0 . When there is a separation distance (r) between A_e and D_e , the overlapping of wave functions for electrons on A_e and D_e falls exponentially with distance beyond R_0 so the electronic coupling matrix element term can be replaced by:

$$V(r) = V(R_0) \exp\left(-\frac{r-R_0}{a}\right) \quad (2.3.3),$$

where $V(R_0)=|V_{fi}|^2$ and a is the attenuated length, 0.5~1.0 Å for reactions of radical ions,²⁷ due to interaction between the electron and surrounding medium such as solvent molecules.

To accounting vibrational motions driving the reaction coordinates from the reactants to products, Franck-Condon principle²⁸⁻³⁰ is applied to describe $\rho(E_f)$ by Franck-Condon weighted density (FCWD) of states :

$$\text{FCWD} = \sqrt{\frac{1}{4\pi\lambda_s k_B T}} \exp\left[-\frac{(\Delta G + \lambda_s)^2}{4\lambda_s k_B T}\right] \quad (2.3.4),$$

where $-\Delta G$ is the standard energy change of the ET reaction and λ is the reorganization energy affecting by differences between bond lengths and bond angles in the reactants and products.^{25, 31-33} Therefore, a classical expression of ET rates developed by Marcus³¹⁻³³ is:

$$k_{ET} = \frac{2\pi}{\hbar} |V_{fi}|^2 \text{FCWD} \quad (2.3.5),$$

which gives well-known Marcus curves showing pendulum relation between k_{ET} and $-\Delta G^0$ as illustration in Figure 2.5.

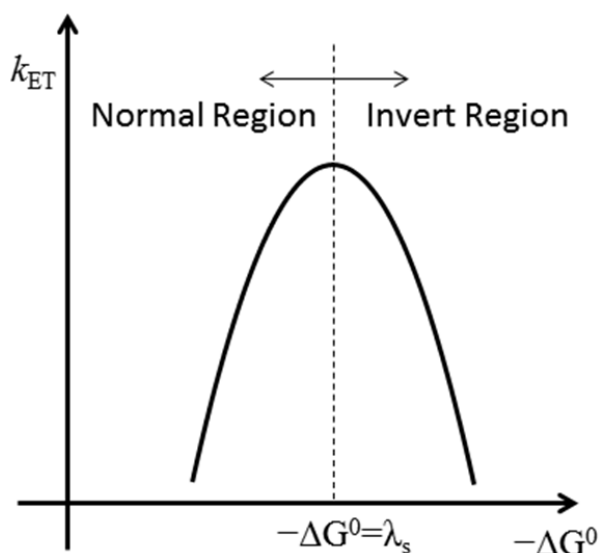


Figure 2.5 The well-known Marcus curve shows a bell-shape relation between electron transfer rate (k_{ET}) and the standard free energy change (ΔG^0), where k_{ET} is maximal at $-\Delta G^0$ equaling to the reorganization energy (λ_s). The normal region is where k_{ET} increases with increasing the magnitude of $-\Delta G^0$, and the inverted region is where k_{ET} decreases with decreasing the magnitude of $-\Delta G^0$.

The FCWD is sensitive to differences between bond lengths and bond angles in the reactants and products.^{25, 33-35} ET from D_e to A_e rearranges vibrational modes of the system such as low frequency (<100 cm⁻¹) polarization modes of solvents and high frequency (~500-3000 cm⁻¹) intramolecular vibrations of the A_e and D_e, which strongly affect the FCWD in λ_s. To account for these rearrangements of vibrational modes, the method used by Bixon³⁴ and Jortner³⁴⁻³⁵ treating rearranged vibrational modes as displaced harmonic oscillators is applied. The low frequency modes of solvents are treated classically, which is appropriate for ħω << k_BT. The high frequency modes can be represented by an average frequency with the assumption that these modes have a narrow range of frequency. The ET rate is rewritten as:

$$k_{ET} = \frac{2\pi}{\hbar} V(r) \frac{1}{\sqrt{4\pi\lambda_s k_B T}} \sum_{n=0}^{\infty} \frac{s^n e^{-s}}{n!} \exp\left[-\frac{(\Delta G^0 + \lambda_s + n\hbar\omega)^2}{4\lambda_s k_B T}\right] \quad (2.3.6),$$

where λ_s is the reorganization energy of the solvent and s=λ_v/ħω is the electron-vibration coupling strength where λ_v is the reorganization energy of A_e and D_e motions and ω is the average frequency of the high frequency modes. Therefore, λ=λ_s+λ_v and:

$$\lambda_s = \sum \Delta_n^2 \hbar \omega_n \quad (2.3.7)$$

summed over all vibrational modes of solvent molecules,

$$\lambda_v = \sum \Delta_n^2 \hbar \omega_n \quad (2.3.8)$$

summed over all high frequency modes, where Δ_n=(μ_nω_n/2ħ)ΔR_n. μ_n is the displacement in configuration space, and ΔR_n is the reduce mass for the n_{th} normal vibration mode.

For a strongly electronic coupling system, the ET rate is dependent on the rearrangement of the system and independent from the environment.²⁶ By “Strongly”, it means that the molecular orbitals of A_e and D_e are well spatial overlap between them in interaction. With increasing electronic coupling and thus increasing level splitting showing in the insert of Figure 2.4, reactant and product states can no longer be regarded as two separate states but become a single potential energy surface. The reactant and product states are treated as two nuclear configurations of the ET system where the electronic wave function is mainly localized at the A_e and D_e. For λ_s>>λ_v, the nuclear relaxation time of the solvent molecules limits the upper limit of the ET rate.³⁶⁻³⁷ This nuclear relaxation time is usually approximated by the longitudinal dielectric relaxation of the solvent molecules.

2.4 Proton Transfer Model

Proton transfer (PT) models are proposed by many groups.³⁸⁻⁴⁹ Borgis and Hynes⁴⁵⁻⁴⁹ (BH) developed a dynamical theory for the PT in a partially adiabatic regime characterized by an electronic coupling that is large compared to $k_B T$ and a vibrational coupling small compared to $k_B T$. The central assumptions of the BH model are the following: (1) The PT occurs along a linear $D_p-H^+-A_p$ bond under influence of the D_p-A_p stretching vibration; D_p is the proton donor and A_p is the proton acceptor. (2) The overall PT in the solvent is non-adiabatic tunneling, and the reaction can be described as a transition between two well defined reactant and product states at any instant. (3) The PT is electronically adiabatic, and the electrons of the system instantaneously adjust to any proton position change. To describe PT from D_p to A_p , BH model uses three coordinates: (1) Q , the intermolecular coordinate defined by distance between the A_p and D_p . (2) S , solvent coordinates. (3) q is a coordinate defined by distance between D_p and H^+ . A simple picture illustrating the PT within a weakly bounded molecular complex comprised of a proton (H^+), the A_p and D_p is shown in Figure 2.6.

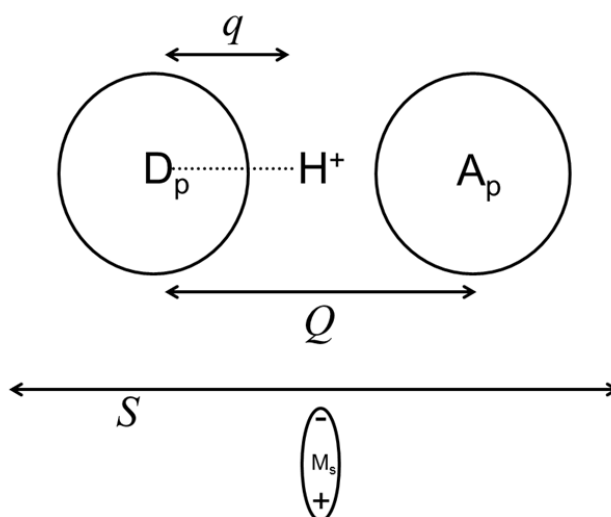


Figure 2.6 Schematic representation of the proton transfer model proposed by Borgis and Hynes (after reference 47). A_p is the proton acceptor, D_p is the proton donor, Q is the intermolecular coordinate defined by distance between A_p and D_p , q is a coordinate defined by distance between proton (H^+) and D_p , and S is the solvent coordinate. Solvent molecule is an oval with a dipole and mass M_s . Double-head arrows mean fluctuations.

Borgis and Hynes described the PT in terms of a two-state quantum mechanical system corresponding to the reactant and product states, respectively. The potential energy (PE) landscapes corresponding to the reactant and product states are illustrated in Figure 2.7 (a) that shows the PT occurs in a multidimensional potential surface. The cross section of the PE

surfaces along the Q and S coordinates are illustrated in Figure 2.7 (b) and (c), respectively. The Q coordinate is characterized by reduced mass M of A_P and D_P and vibrational frequency ω_Q . The S coordinate is characterized by mass M_s of solvent molecule and vibrational frequency ω_s . The reorganization energy along Q coordinate is $\lambda_Q=1/2M\omega_Q^2\Delta Q^2$, and that along the S coordinate is $\lambda_S=1/2M_s\omega_s^2\Delta S^2$; $\Delta Q=Q_P-Q_R$ is displacement from reactant state to product state along Q coordinate, and $\Delta S=S_P-S_R$ is displacement from reactant state to product state along the S coordinate. For a weakly protonic coupling system such as intramolecular PT reaction, the main solvent contribution is to provide an asymmetry interaction with respect to the reactant and product position of the proton. As illustrated in the upper panel of Figure 2.7 (d), which in a solvent dielectric continuum model is related to the orientational polarization, a suitable fluctuation in S coordinates, can restore the symmetry and allow proton tunneling to occur.

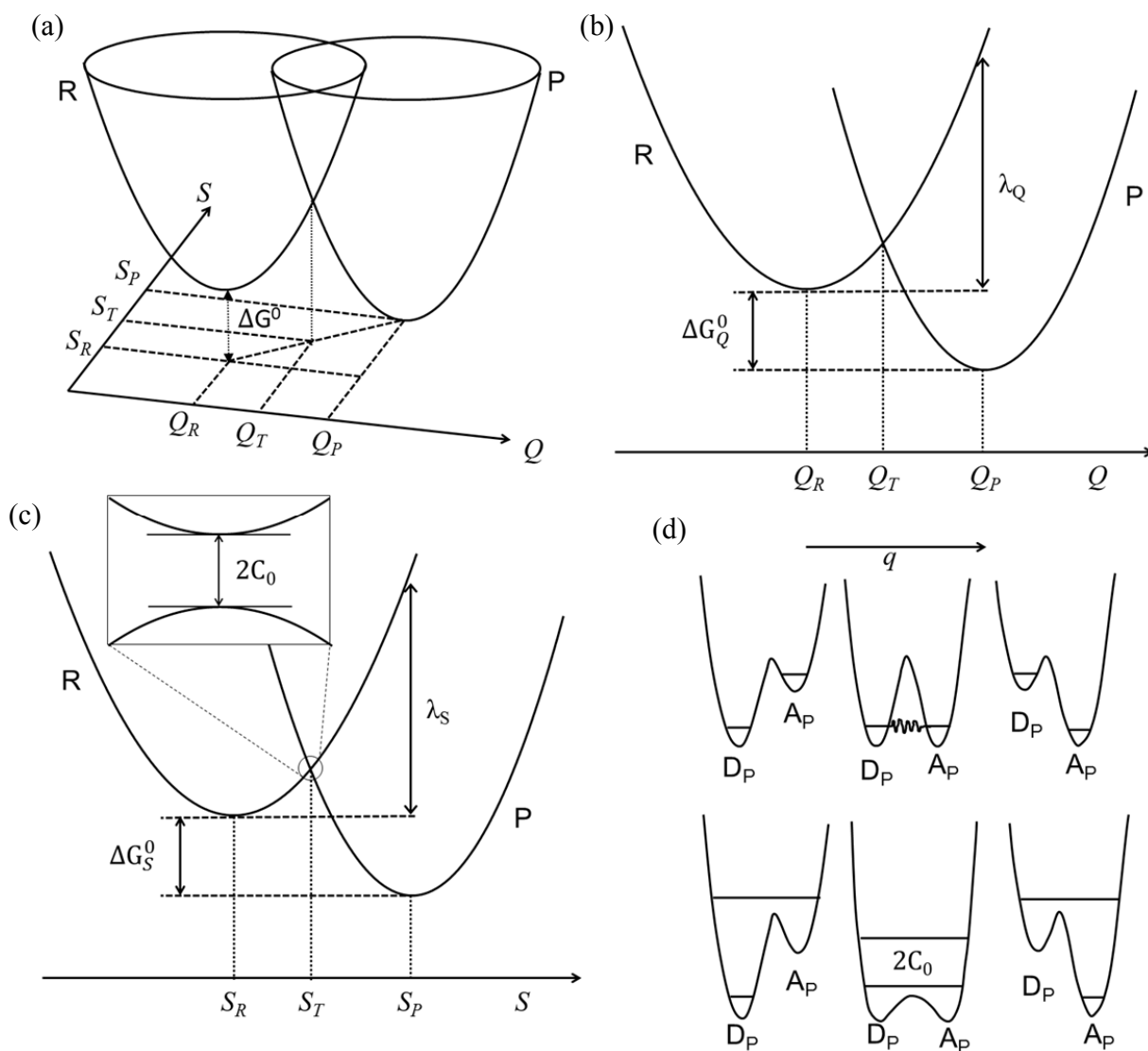


Figure 2.7 (a) Potential energy (PE) landscapes of Proton Transfer (PT) proposed by Borgis and Hynes with S and Q coordinates. (b) The PE profile along the coordinate Q defined by the proton donor-acceptor distance. (c) The PE profile along solvent coordinate S for the weakly protonic coupling system. The free energy of reaction ΔG_S^0 and reorganization energy λ_S are shown. The insert shows the PE profile in the crossing point for the strongly protonic coupling system. (d) Two double wells at different S value, where q is the distance between D_p and H^+ . The upper panel shows that the proton potential is lower than the potential barrier. The proton tunneling occurs at solvent configuration S_T in the weakly protonic coupling system. The lower panel is that proton potential is greater than the potential barriers in the strongly coupling system. (These four figures are after reference 47)

As shown in Figure 2.7(a), the PT occurs in a multidimensional PE surface. Borgis and Hynes used the energy gap variable ΔH illustrated in Figure 2.8(a) to render the PT model from multidimensional to one-dimensional⁴⁵ shown in Figure 2.8 (b), where

$$\Delta H = \Delta G_S^0 + \Delta G_Q^0 + \lambda_S + \lambda_Q - \sqrt{2M_S\omega_S^2\lambda_S}\delta S - \sqrt{2M_Q\omega_Q^2\lambda_Q}\delta Q \quad (2.4.1).$$

$\delta S = S - S_R$ and $\delta Q = Q - Q_R$ are displacements from the oscillator equilibrium position along S and Q coordinates, respectively, in the reactant state. Based on this one-dimensional picture, Borgis and Hynes⁴⁵ formulated the rate of PT (k_{PT}) for the weakly and strongly protonic coupling systems with Landau-Zener curve crossing approach.⁵⁰ The intramolecular PT attributes to the weakly protonic coupling system, and the intermolecular PT attributes to the strongly protonic coupling system.⁴⁵ The proton coupling, C , is calculated for fixed Q and S coordinates by focusing on the corresponding asymmetric proton double wells shown in Figure 2.7(d). Because S coordinates appears only to have a minor influence on the proton coupling, the coupling term can be simplified into $C(Q)$. For a weakly protonic coupling system, the $C(Q)$ is

$$C(Q) = C_0 \exp(-\alpha\delta Q) \quad (2.4.2),$$

where C_0 is the PT matrix element and α is the decay parameter in the range 25~30 \AA^{-1} .⁴⁷ For a strongly protonic coupling system, the behavior of $C(Q)$ is no longer exponential, and can be described by a polynomial law such as the Laguerre polynomial with C_0 and α .⁵¹ The general formolism of k_{PT} for the intramolecular PT is:

$$k_{PT} = \frac{2\pi}{\hbar} \langle C(Q)^2 \rangle_{\Delta H=0} \sqrt{\frac{1}{4\pi k_B T (\lambda_Q + \lambda_S)}} \exp\left[-\frac{(\Delta G^0 + \lambda_S + \lambda_Q)^2}{4k_B T (\lambda_S + \lambda_Q)}\right] \quad (2.4.3)$$

and the k_{PT} for intermolecular PT is:

$$k_{PT} = \frac{1}{2\pi} \sqrt{\frac{\omega_S^2\lambda_S + \omega_Q^2\lambda_Q}{\lambda_S - \lambda_Q - 2\lambda_S\lambda_Q C_2}} \exp\left(-\frac{E_a}{k_B T}\right) \quad (2.4.4a)$$

$$E_a = \frac{(\Delta G^0 + \lambda_S + \lambda_Q)^2}{4(\lambda_S + \lambda_Q)} - C_0 \left[1 - \frac{1}{2} \left(\frac{\lambda_S\lambda_Q\Delta G^0}{\lambda_S + \lambda_Q} - \frac{\lambda_S C_1}{\lambda_S + \lambda_Q - C_2} \right)^2 \right] - \frac{C_1^2}{\lambda_S + \lambda_Q - 2C_2} \quad (2.4.4b)$$

where $\Delta G^0 = \Delta G_S^0 + \Delta G_Q^0$ and $C_n = d^n C / d\Delta H_Q^n$. ΔH_Q is the energy gap variable along Q coordinates.

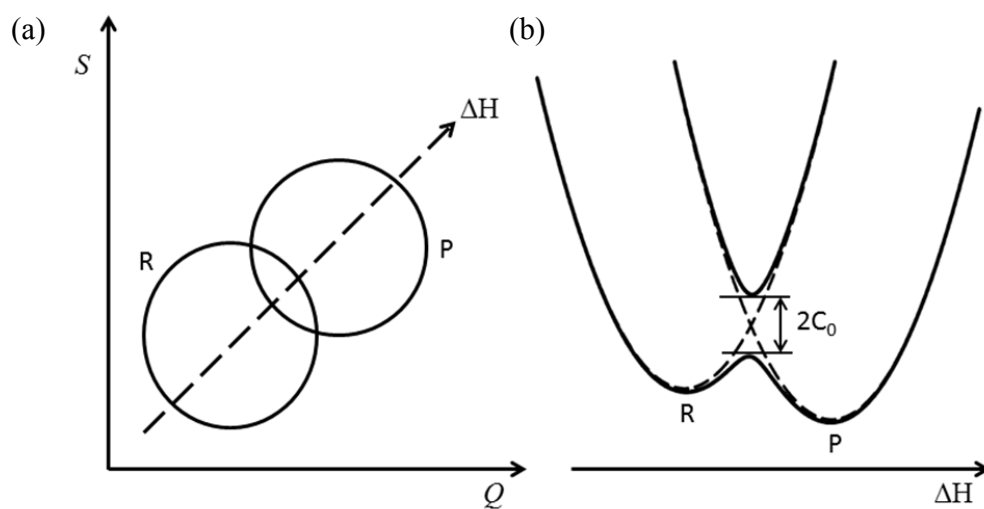


Figure 2.8 (a) Top view of Figure 2.7(a) with the direction of the energy gap coordinate ΔH indicated, where R and P are reactant and product states. (b) Potential surface (PE) along ΔH (These two figures are after reference 45). The insert shows the proton coupling C_0 (at the transition state) producing an adiabatic PE surface.

Chapter 3. Experiments

3.1 Laser Electron Accelerator Facility (LEAF)⁵²

LEAF located at Brookhaven National Laboratory is a laser pulsed photocathode, radio frequency (RF) electron accelerator. This type of accelerator has been developed as electron beam source for experimental physics facilities and free electron laser development since the mid-1980s. The LEAF is one of prototypes used for pulse radiolysis to examine the dynamics and reactivity of chemical species on the picosecond time scale. It is capable of generating ~ 5 ps pulses of 9 MeV electrons for pulse radiolysis experiments. A simple diagram illustrating the principle of operation of LEAF is shown in Figure 3.1.

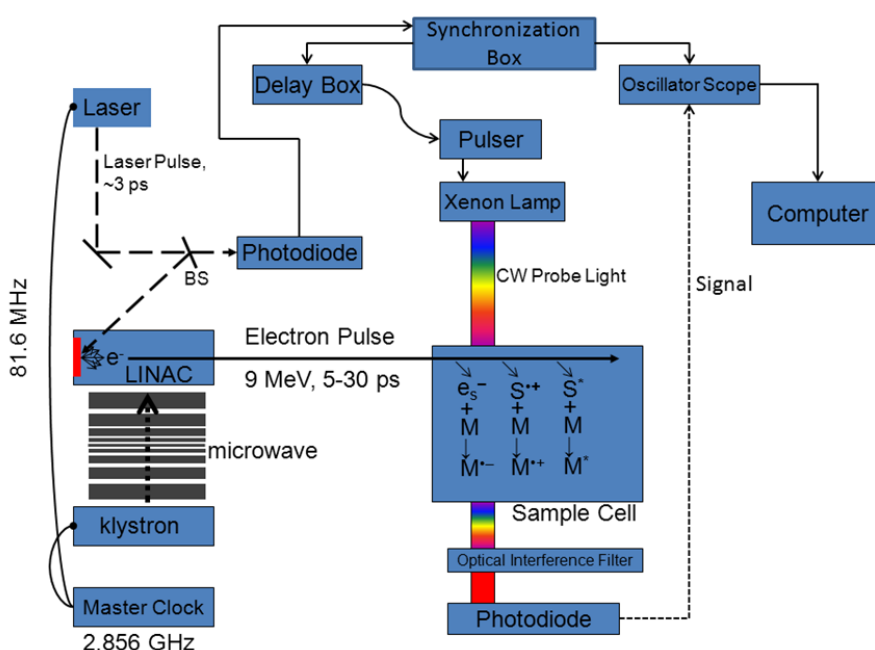


Figure 3.1 Operation Schematic of the Laser Electron Accelerator Facility (LEAF) located in Brookhaven national laboratory. The duration of the electron pulse is dependent on the experimental end station. e_s^- is solvated electron $S^{+\bullet}$ is solvent radical cation, and S^* is excited solvent molecule. M is solute molecule, $M^{+\bullet}$ and $M^{-\bullet}$ are , solute cation and anion, respectively.

The accelerator system of the LEAF is a RF photocathode electron linear accelerator. It is a 3.5 cell, 2856 MHz resonant cavity structure composed of oxygen free high thermal conductivity cooper. Each cell of the gun is equipped copper slug mounted on an actuator for adjusting the resonant frequency, and a RF pick-up loop to measure the instantaneous microwave power. A 6 mm diameter magnesium plug is pressed into the back plate of the gun to serve as the photocathode. The 266 nm laser pulse that excites the photocathode is entering through a Suprasil vacuum window in the horizontal plane of the photocathode and 65° from normal incidence with respect to the cathode surface.

Microwave power for the acceleration is provided by an *S*-band klystron, which generates 15 MW peak power and a pulse width of 2.5 μ s. The modulator contains an 8-element pulse forming network powered by a 6 kVA, 40 kV high voltage power supply (General Atomics) and triggered by an LS-3229 thyatron (Perkin-Elmer). It is important to provide phase-synchronized signals to both microwave frequency and laser system to drive the photocathode. At LEAF, the master reference oscillator operates at 81.6 MHz to supply the Ti:Sapphire oscillator laser with a reference signal for cavity length stabilization. A phase-locked loop is employed to generate the 35th harmonic (2856 MHz), which is amplified to 500 W before seeding the klystron. The *S*-band waveguide after the klystron incorporates a microwave circulator for isolation, followed by a microwave window connecting to the vacuum section of waveguide leading to the gun.

To produce photoelectrons, frequency tripling the 800 nm output of a 10 Hz, chirped pulse amplified Ti:Sapphire laser system is employed. The core of the laser system is the frequency stabilized Ti:Sapphire oscillator (Spectra Physics Lock-to-Lock Tsunami). The lock-to-lock unit adjusts the oscillator's cavity length to match the master reference frequency (81.6 MHz) to provide synchronized, amplified, and frequency tripled 266 nm, 100 fs laser pulses. These pulses can consistently excite the photocathode at the correct point in the microwave cycle for proper acceleration of the photoelectrons. The timing jitter is on the order of a picosecond.

Figure 3.2 shows the schematic of the laser system and optical path. The Tsunami Ti:Sapphire oscillator is pumped at 523 nm by a 5 W Spectra Physics Millennia-Vi diode pumped Nd:YVO₄ laser. The 800 nm oscillator output passes into a Spectra Physics Spitfire Ace amplifier pump at 527 nm by two 10 Hz Nd:YLF lasers (Spectra Physics Empower 45). The 3 ps, 8 nJ oscillator pulses are regeneratively amplified to 16 mJ. A beam splitter directs half of the beam to Spitfire Ace internal stretcher to stretch to \sim 250 ps then goes to an external compressor that compresses the pulse to 5 ps. The 5 ps pulse directs to homemade frequency tripler that produces the 266 nm beam used to excite photoelectrons from magnesium photocathode on the accelerator.

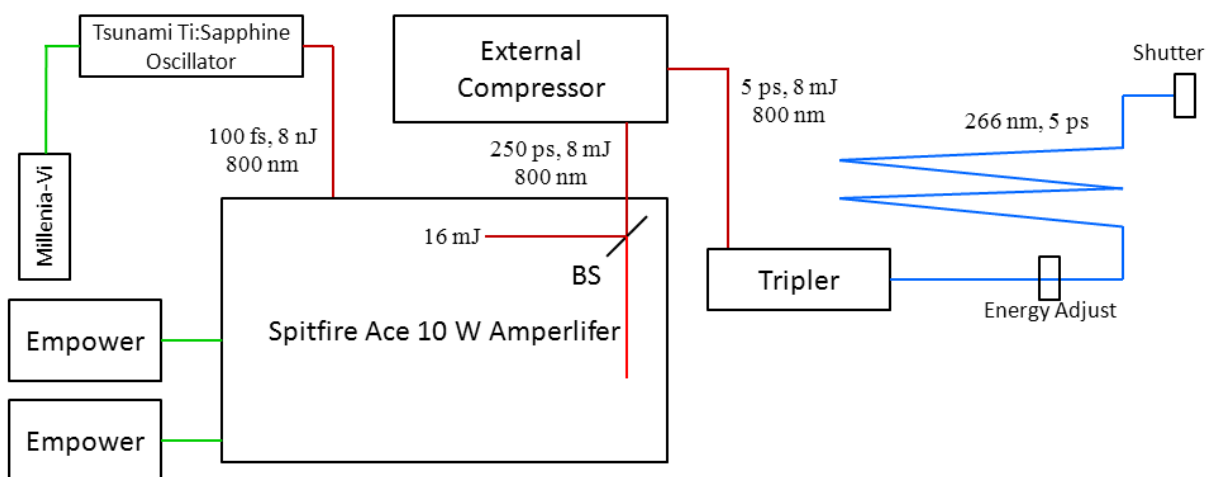


Figure 3.2 Schematic Illustration of the Laser System and Optical Path in LEAF. (This illustration is redrawing with the permission from Dr. Andrew Cook from Brookhaven National

Laboratory.)

The beam transport system consists of a straight section leading to three arms (lines A, B, and C), selected by three bending magnets for individual beam line. The A line is for the optical fiber single shot (OFSS)⁵³ experiment, the B line is for the transient digitizer (TD)⁵² experiment, and the C line is for time-resolved vibration spectroscopy. This thesis only employed the A and B line. The following paragraphs will introduce the TD briefly because most experimental results is obtained by TD experiment in this study.

Briefly, the electrons were injected into quartz cells with an optical length of 20 mm, or 5 mm, containing THF solutions of the molecules under study in purified THF, and prepared under Argon atmosphere. The monitoring light source is a pulsed Xenon arc lamp. The wavelength is selected by 10 or 40 nm bandpass interference filters. Transient absorption signals are detected by either a silicon photodiode (EG&G FND-100, 2 ns response time), an InGaAs Photodiode (GDP Optoelectronics GAP-500L, 2 ns response time), a Germanium photodiode (GDP Optoelectronics GEP-600L, 6 ns response time) or a phototube (Hamamatsu Photonic, R1328U-03, 65 ps response time) and digitized by LeCroy 8620A, HRO 66Zi or 640Zi oscilloscopes.

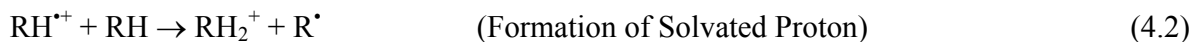
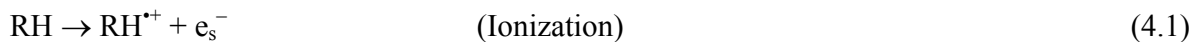
Chapter 4. Escape of Anions from Geminate Recombination in THF due to Charge Delocalization

4.1 Introduction

Ion recombination within amorphous materials, e.g., organic solvents or polymers, is an old but not well understood problem. In 1938, Onsager¹ applied the Debye-Smoluchowski (DS) equation to the case in which positive and negative ions annihilate upon contact (infinite annihilation rate: ion annihilation is diffusion-controlled) based on his earlier work.⁵⁴ He discussed ion recombination under the influence of the Coulomb potential, predicted the fraction of free ions (F_h) as a function of initial separation distance, and defined a critical radius (r_c). The F_h can be written in terms of G_{fi}/G_{max} , where G_{fi} is the G value of free ions and G_{max} is the maximum observed $G(t)$ value of ions. t is the time. The r_c is now often called the Onsager radius, at which the attractive Coulomb potential energy, $V(r_c)$, equals the thermal energy, $V(r_c)=k_B T$. An ion thermalized at r_c from its geminate counter ion has a 37% probability of escape to become a free ion and a 63% probability of recombine. For geminate ion pairs, the probabilities of escape and recombination change with the initial distance. We will refer to the F_h arising from escape by diffusion from their initial separation distances, as envisaged in Onsager's theory, as the fraction of the Type I free ions ($F_h^I=G_{fi}^I/G_{max}$, where G_{fi}^I is the G value of the Type I free ions). Many scientists^{16, 18-19, 55-56} extended Onsager's work to solve the DS equation for the case in which the rate of annihilation upon contact was not infinite, and suggested that an additional contribution to F_h could arise from ion-pairs that escape after coming together. We will refer to this additional contribution as the fraction of Type II free ions ($F_h^{II}=G_{fi}^{II}/G_{max}$, where G_{fi}^{II} is the G_{fi} value of the Type II free ions).

The kinetics of the ion recombination in nonpolar organic solvents where the F_h is almost entirely Type I have been investigated by several groups.^{4, 57-66} De Waele⁶⁷ and Martini⁶⁸ studied recombination of solvated electrons in THF using pulse radiolysis and multiphoton ionization, respectively. Van den Ende⁶⁹ employed pulse radiolysis to study ion recombination in CCl_4 . They found that the free ion yield was Type I, and that geminate ions decayed with time t as $\tau^{-0.6}$ for $\tau < 32$ where $\tau=Dt/r_c^2$, and D was the sum of diffusion coefficients of the anion and the cation. This is slightly different from the theoretical prediction $\tau^{-0.5}$. In polar solvents like acetonitrile,^{3, 70} octanenitrile,⁷⁰ water⁷¹ and 1,2-dichloroethane,⁷² geminate ions can escape from the recombination and become the Type II free ions. Masuhara,⁷² Zhou²⁻³ and Zhong¹² reported that solvent separated ion pairs (SSIP) had crucial impact on F_h^{II} in polar solvents such as 1,2-dichloroethane.

The present work uses pulse radiolysis to study the ion recombination in THF, for which r_c is 7.3 nm at 298 K. Unlike photoexcitation, which initially creates excited states, the pulse radiolysis ionizes the medium to initially create ions, providing for rapid injection of charge into molecules. Pulse radiolysis reactions for a molecule M in THF=RH solution are:⁷³



Ionization of THF produces solvated electrons (e_s^-) and THF radical cations ($\text{RH}^{\bullet+}$) which react with other THF molecules to create the solvated protons (RH_2^+).⁷⁴ Reactions (4.1) and (4.2) occur in less 1 ps.⁶⁸ Because the solute anions ($\text{M}^{\bullet-}$) are strong bases the recombination of $\text{M}^{\bullet-}$ with RH_2^+ , reaction (4.4), might be expected to be diffusion-controlled, but this has not been investigated in detail. Annihilation of anions and cations is usually due to the proton transfer (PT) reaction (4.4a) in THF. Electron transfer to RH_2^+ , reaction (4.4b), is probably thermodynamically unfavorable and would give rates correlated with redox potentials alone, which is not observed. It will be neglected in the discussion below.

We observe time evolution of transient absorption of anions to study kinetics of the ion recombination. Figure 4.1 illustrates that pulse radiolysis creates primary ion pairs with an initial separation distance distribution, $\rho(r_i)$, where r_i is the initial separation distance. It also depicts the relation between $\rho(r_i)$ and the kinetic trace of ion recombination. Whether they begin at $r_i > r_c$ or escape from shorter distance, we will refer to the ions, that escape to become free (or homogenous ions) as F_h comprised of F_h^I and F_h^{II} .

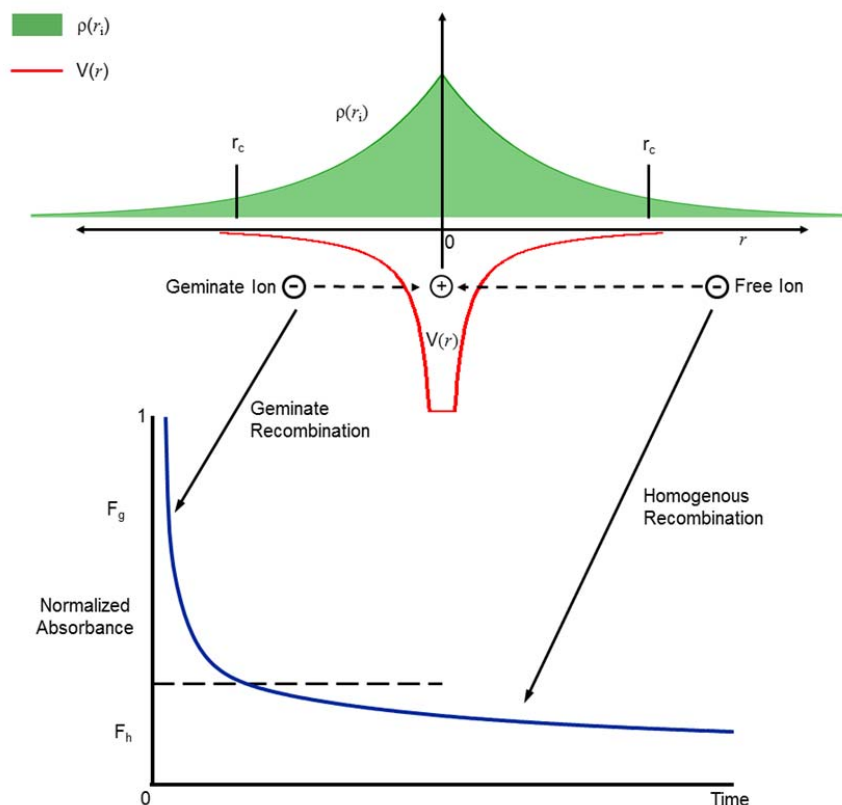


Figure 4.1 A schematic relation between the ion population, $\rho(r_i)$, of initial separation distance, r_i , and the kinetic trace of ion recombination, where r_c is Onsager radius, $V(r)$ is Coulomb potential. F_h is the fraction of free (homogenous) ions, which is G_{fi}/G_{max} , and F_g is the fraction of geminate ions, which is $(G_{max}-G_{fi})/G_{max}$, so $F_h+F_g=1$; G_{fi} is the G value of free ions and G_{max} is the maximum observed $G(t)$ value of ions. The kinetic trace in this figure is not actual data.

The results below demonstrate that, in most cases, the free ion yield in THF is Type I, which is independent of the nature of the solute; any Type II free ion yield is too small to measure. In a few exceptional cases, substantial Type II free ion yield was observed. The geminate recombination of small anions such as F_1 radical anion ($F_1^{\bullet-}$), benzophenone radical anions ($BPhO^{\bullet-}$) and dibenzofuran radical anion ($DBF^{\bullet-}$) is extremely fast. Within the limits of the present observations the recombination rate is controlled only by diffusion, so that all observed small anions are the Type I free ions. Larger oligofluorene radical anions, $F_n^{\bullet-}$ ($n=2-4$), for which the recombination reaction is not diffusion-controlled, form long-lived ion pairs with RH_2^+ despite the large thermodynamic driving force of the PT reactions, and the presence of long-lived radical ion pairs also increases the Type II free ion yield. The experimental results reported below, along with computed chemistry, will examine these reactions and provide information regarding their energetics, and place them in context with several similar ion-recombination reactions.

4.2 Experimental

Observations of the ion recombination were carried out using the Laser Electron Accelerator Facility (LEAF) with 9 MeV electron pulse at Brookhaven National Laboratory; methods of measurement are reported elsewhere.⁵² Briefly, the electrons were injected into quartz cells with an optical path length of 20 or 5 mm containing THF solutions of the molecules under study in purified THF under Argon. The monitor light source is a pulsed Xenon arc lamp. The probe wavelengths were selected by 10 nm bandpass optical interference filters. Transient absorption signals are detected by a silicon photodiode (EG&G FND-100, 2 ns response time) and digitized by LeCroy 8620A or 640Zi oscilloscopes.

2,3-dicyano-*p*-benzoquinone, (CN)₂BQ, was purchased from BioTechnology Corporation of America, and other chemicals were purchased from Aldrich or Alfa-Aesar. The preparation of oligo(9,9-dihexyl)fluorenes, F_n(n=1-4), has been described,⁷⁵ 4-nitro-*p*-terphenyl (NTP), *p*-dinitrobenzene (DNB) and tetracyanoethene (TCNE) were sublimed under vacuum; other chemicals were used as received. Chemical structures are given in Appendix B.

4.3 Results

Attachment of e_s⁻ to F_n(n=1-4) in THF creates F_n^{•-}(n=1-4) having intense absorptions between 400-750 nm. Transient absorption spectra of F_n^{•-}(n=1-4) are shown in Figure 4.2. Reported extinction coefficients (ε) of F_n^{•-}(n=1-4)⁷⁶ are given in Table 4.1. The method of determining extinction coefficients is given in section B1 of Appendix B. Small absorption bands near 560, 640 and 700 nm in the transient spectra of F_n^{•-}(n=2-4), respectively, are triplet-triplet absorptions.⁷⁷ Data at lower concentrations than used in Figure 4.2 gave rate constants for electron attachment, which are reported in Table 4.1 along with those for other representative solutes. In the transient spectra F₂^{•-}, the decay of anions is accompanied by an increase of absorbance at 440 nm. An isosbestic point at 450 nm also suggests that reaction (4.4a) produces F₂H[•] as the anions decay. Similar growing bands and isosbestic points are seen at 460 and 470 nm for F₃^{•-} and F₄^{•-}, respectively. Figure B1 of Appendix B, shows that similar transient spectra of F₂H[•] are created when HCl protonates F₂^{•-}, supporting the above assignment for F₂H[•]. In Figure 3, F₂^{•-} absorbance at 530 nm decreased by ~2/3 from 10 to 1000 ns. Over the same period, absorbance at 440 nm grows. Assuming that each anion decaying produced one F₂H[•], ε of F₂H[•] was estimated from the growth after correction for the decay of F₂^{•-} absorbance at 440 nm. ε of F₃H[•] and F₄H[•] were estimated by the same method. The extinction coefficients are compared with absorption bands of F_nH[•](n=2-4) computed by time-dependent density functional theory with B3LYP/6-31G(d) in THF with the polarizable continuum model (PCM) in Table 4.2.

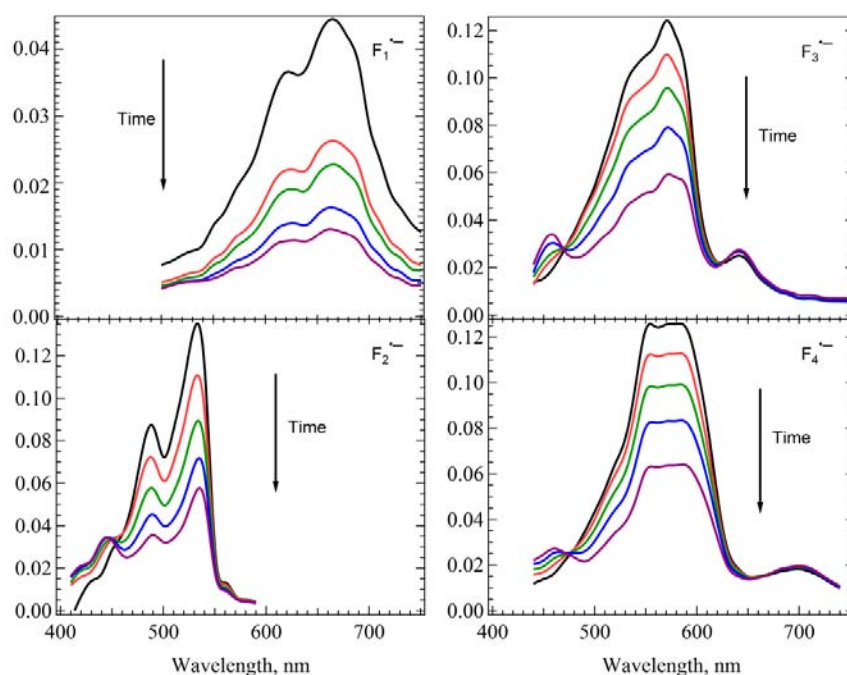


Figure 4.2 Transient spectra of $F_n^{\bullet-}$ ($n=1-4$) with 50, 20, 10 and 5 mM, respectively, created by pulse radiolysis in THF. The spectra are collected at times, $t=10, 50, 100, 500$ and 1000 ns.

Table 4.1 Electron Attachment Rate Constants (k_{att}), Extinction Coefficients (ϵ) of the Radical Anions and Diffusion Coefficients (D).

Name	$^{75}k_{\text{att}} \text{ (M}^{-1}\text{s}^{-1}\text{)}$	$^{\text{Ref}}\epsilon \text{ (M}^{-1}\text{cm}^{-1}\text{) of } M^{\bullet-}$	$^{\text{Ref}}D \text{ (cm}^2\text{/s)}$
F_1	$^{75}5.88 \times 10^{10}$	$^a8.18 \times 10^3$ at 650 nm	$^d9.85 \times 10^{-6}$
F_2	$^{75}6.62 \times 10^{10}$	$^a4.81 \times 10^4$ at 530 nm	$^d6.50 \times 10^{-6}$
F_3	$^{75}6.15 \times 10^{10}$	$^a4.82 \times 10^4$ at 570 nm	$^d5.10 \times 10^{-6}$
F_4	$^{75}1.09 \times 10^{11}$	$^a4.97 \times 10^4$ at 580 nm	$^d4.29 \times 10^{-6}$
benzophenone	$^b6.40 \times 10^{10}$	$^a9.00 \times 10^3$ at 800 nm	$^{78}1.65 \times 10^{-5}$
dibenzofuran	$^b6.90 \times 10^{10}$	$^{79}3.50 \times 10^4$ at 687 nm	-
1-methylpyrene	$^b7.68 \times 10^{10}$	$^c2.43 \times 10^4$ at 490 nm	-
fluoranthene	$^b5.60 \times 10^{10}$	$^{80}1.70 \times 10^4$ at 450 nm	-

^aThe method of determining ϵ is given in section B1 of Appendix B, and the uncertainty is $\sim 6\%$. ^b k_{att} is obtained by observing decay of solvated electrons in THF solution directly. ^cDetails of determining ϵ are available in Figure B2 of Appendix B. ^dThe diffusion coefficients of the oligofluorenes were estimated as $D=1.13 \times 10^{-5} (0.75n/0.6)^{-0.6} \text{ cm}^2\text{/s}$, where n is the number of repeat units. This empirical equation based on the model found in Figure 5 of reference⁸¹ interpolates the measured values from Table 1 of this reference.⁸¹

Table 4.2 Extinction coefficients (ϵ of F_nH^\bullet ($n=2-4$) and Oscillator Strength (f) for the Strongest Bands of F_nH^\bullet ($n=1-4$).

Name	ϵ ($M^{-1}cm^{-1}$)	$^a\lambda(f)$
F_1H^\bullet		b313 nm (0.5951)
F_2H^\bullet	1.5×10^4 at 440 nm	c431 nm (0.7124)
F_3H^\bullet	1.7×10^4 at 460 nm	d472 nm (0.5128)
F_4H^\bullet	1.4×10^4 at 460 nm	e443 nm (0.5305)

^aComputed by time-dependent density functional theory in THF with B3LYP/6-31G(d) and the polarizable continuum model. ^b λ_3 ; $\lambda_1(f_1) = 465$ nm (0.0090), $\lambda_2(f_2) = 322$ nm (0.0797). ^c λ_3 ; $\lambda_1(f_1) = 522$ nm (0.0545), $\lambda_2(f_2) = 467$ nm (0.0329). ^d λ_2 ; $\lambda_1(f_1) = 550$ nm (0.1043), $\lambda_3(f_3) = 412$ nm (0.3006). ^e λ_3 ; $\lambda_1(f_1) = 557$ nm (0.1263), $\lambda_2(f_2) = 489$ nm (0.2927).

In Figure 4.3, decays of radical anions during the first 200 ns display large variations with solute. The insert of Figure 4.3 shows that the decay of $BPhO^{\bullet-}$ is the fastest among these anions. The kinetic traces of anions show two things: (1) The fast decay rates of $F_n^{\bullet-}$ ($n=2-4$) decrease for the longer oligofluoroenes; (2) For other anions in Figure 4.3, rates of fast decays are different from each other but their F_h , estimated by G_{fi}/G_{max} , are close to each other. This procedure might overestimate F_h if G_{max} is not similar for all of the anions, which might occur if we do not intercept all electrons. From Figure B3 of Appendix B, we find $\sim 1\%$ difference between peak absorbances seen in solutions 21.4-50 mM of F_2 . The concentrations of solutes used in this study are at least 20 mM so they can capture most e_s^- in less 2 ns for the electron attachment rate constants (k_{att}) of $BPhO$, DBF , 1-methylpyrene ($MePy$), fluoranthene (FA) and F_n ($n=1-4$) reported in Table 4.1.

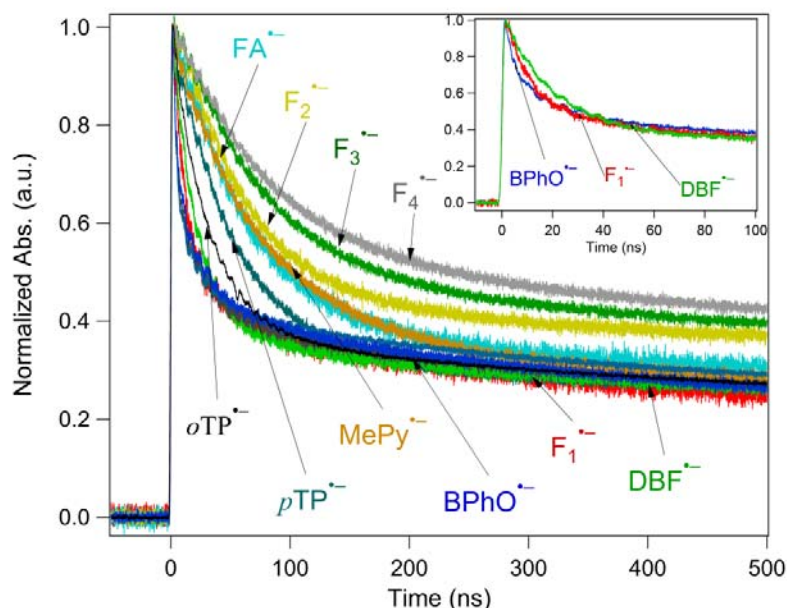


Figure 4.3 Normalized kinetic traces of benzophenone (BPhO 50 mM at 800 nm), fluoranthene (FA 60 mM at 450 nm), 1-methylpyrene (MePy 40 mM at 490 nm), dibenzofuran (DBF 50 mM at 680 nm), *p*-terphenyl (*p*T 50 mM at 950 nm), *o*-terphenyl (*o*T 50 mM at 600 nm), F₁ (50 mM at 650 nm), F₂ (30 mM at 530 nm), F₃ (30 mM at 570 nm) and F₄ (20 mM at 570 nm). The absorbance traces were multiplied by factors of 14.7, 30.1, 17.4, 27.0, 9.53, 15.6, 16.3, 8.4, 3.3 and 8.2, respectively. Small contributions of triplet absorbance to the kinetic traces of FA and F_n(*n*=2-4) have been determined and subtracted (see text). The insert shows kinetic traces of BPhO^{•-}, DBF^{•-} and F₁^{•-}, where geminate decay of BPhO^{•-} is the fastest.

For some solutes, triplet states contribute to the absorption. Pulse radiolysis may directly generate a triplet excited state of a solute molecule by direct ionization or excitation of the solute rather than the solvent. In most cases, the triplet excited states of the solute do not absorb at observation wavelengths of anions. In a few cases, triplet-triplet (T-T) absorption of the solute will contribute at the observation wavelengths of anions. T-T absorbance of FA and F_n(*n*=2-4) contributed 3.8%, 3.1%, 3%, and 3.3% of absorbance of the observation wavelengths for FA^{•-} and F_n^{•-} (*n*=2-4), respectively, at *t*=2 ns (details of determining the fraction of ³FA* and ³F_n* (*n*=2-4) are in Figure S5-S8 of the SI). This T-T absorbance was subtracted from kinetic traces of FA^{•-} and F_n^{•-} (*n*=2-4) so that Figure 4 shows only the absorbance due to radical anions. Normalized kinetic traces without the corrections are shown in Figure B4(b) of Appendix B.

In Figure 4.4, normalized kinetic traces of BPhO^{•-}, 4-cyano-4'-*n*-pentyl-*p*-terphenyl radical anion (CNTP^{•-}) and 2,3-dichloro-5,6-dicyano-*p*-benzoquinone radical anion (DDQ^{•-}) in THF show that their slowly-decaying fractions (*t*>100 ns) are almost identical with each other. Transient spectra of DDQ^{•-} in Figure S9 show that the absorption peak of DDQ^{•-} shifts with time so slight differences between slow decays of DDQ^{•-} and BPhO^{•-} may be due to reactions with impurities. The *F_h* of the above three anions were 0.36±0.03 determined by the *G_{fi}* and *G_{max}*

values of $\text{BPhO}^{\bullet-}$ in THF, which are obtained from 50 mM of BPhO in this study. The inset of Figure 4.4 shows that they have nearly identical decays at short time, which we will refer to as geminate decays, although their chemical structures and reduction potentials (E_{red}) are different. These findings strongly suggest that their geminate decays are diffusion-controlled. The kinetic analyses indicate that for the geminate decays these solutes have an average decay time to decrease to $1/e$ of $\sim 8 \pm 1$ ns.

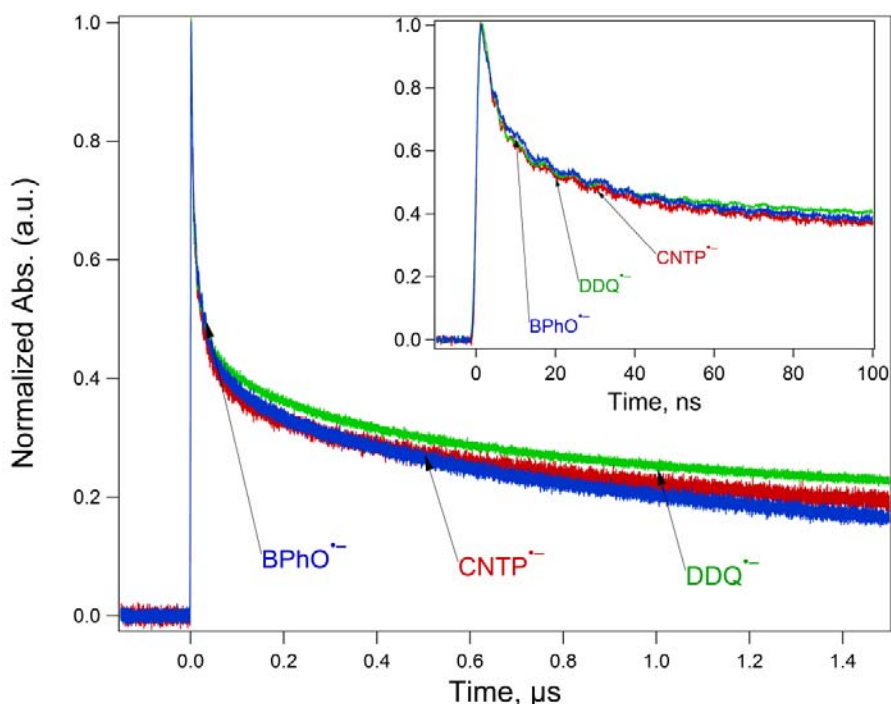


Figure 4.4 Normalized kinetic traces of radical anions of benzophenone ($\text{BPhO}^{\bullet-}$ at 800 nm), 2,3-dichloro-5,6-dicyano-*p*-benzoquinone ($\text{DDQ}^{\bullet-}$ at 600 nm) and 4-cyano-4'-*n*-pentyl-*p*-terphenyl ($\text{CNTP}^{\bullet-}$ at 900 nm), which are created by pulse radiolysis with 50 mM of the neutral solutes in THF. The traces are normalized by factors of $\text{BPhO}^{\bullet-}$, $\text{DDQ}^{\bullet-}$ and $\text{CNTP}^{\bullet-}$ are 14.7, 17.5 and 6.89, respectively. The insert shows almost identical geminate decays for $t < 100$ ns after the electron pulse. The F_h is 0.36 ± 0.03 for these three anions (see text). The homogenous decay of $\text{DDQ}^{\bullet-}$ is different from other anions because $\text{DDQ}^{\bullet-}$ reacts with small amount of impurity (transient spectra of $\text{DDQ}^{\bullet-}$ in Figure B9 of Appendix B show the influence of the impurities to $\text{DDQ}^{\bullet-}$ in the homogenous stage).

An alternative method to study the free ions is to employ a free-ion indicator to capture the free ions. Anions of a good free-ion indicator undergo fast geminate decay, annihilating rapidly upon contact with a RH_2^+ . The indicator should have a less negative reduction potential than the target molecule so that the indicator can capture electrons from free anions. The average geminate decay of 4-nitro-*p*-terphenyl radical anions ($\text{NTP}^{\bullet-}$) is fast, ~ 8 ns, as determined by two exponential function from data shown in Figure B10 of Appendix B, and E_{red} of NTP given in Table 4.3 is less negative than for FA and MePy.

In Figure 4.5, kinetic traces of high concentrations of BPhO, F₃, FA and MePy, each mixed with 1 mM of NTP, were collected at the 720 nm absorption peak of NTP^{•-}. Most solvated electrons are initially captured by the highly concentrated solutes, which then transfer electrons to NTP in ~100 ns. Any geminate electrons transferring to NTP disappear rapidly, leaving only free-ions. Kinetic traces of FA and F₃ with NTP grow with rates 1.38×10^7 and 1.03×10^7 s⁻¹, respectively, which are reasonable rates for diffusion-controlled electron transfer reactions to 1 mM of NTP. For BPhO, MePy and F₃, there is substantial initial absorbance because anions of these highly concentrated solutes absorb light at 720 nm. No observable growth is seen for BPhO and MePy indicating that ϵ of BPhO^{•-} and MePy^{•-} are close to ϵ of NTP^{•-} at 720 nm.

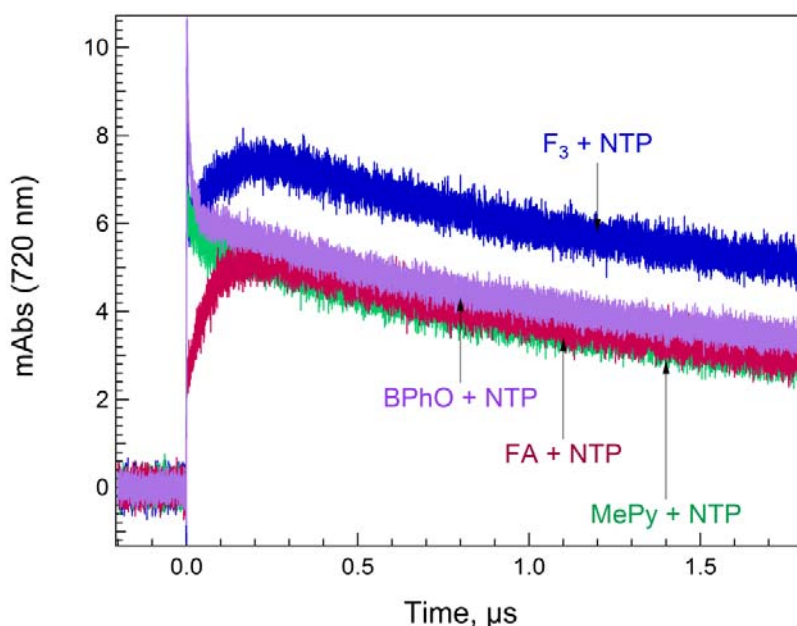
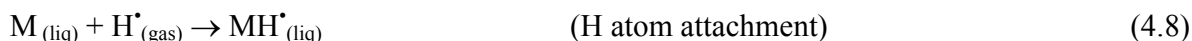
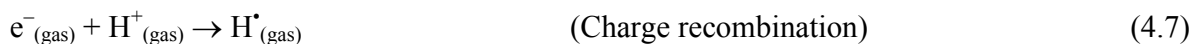
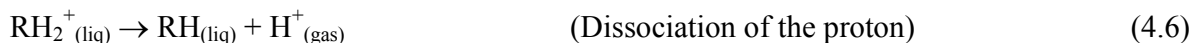
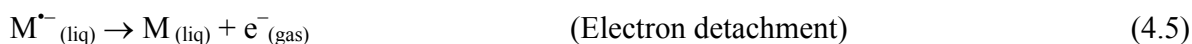


Figure 4.5 Kinetic traces of 4-nitro-*p*-terphenyl (NTP 1 mM) at 720 nm in THF solutions with with high concentrations of F₃ (30 mM), benzophenone (BPhO 50 mM), fluoranthene (FA 60 mM) and 1-methylpyrene (MePy 40 mM). After ~150 ns, NTP^{•-} is the only remaining radical anion, and the only absorbing species. For F₃ + NTP, ~50% more NTP^{•-} ions are formed than for the other three solutes.

After ~150 ns, the electron transfer is complete so that only NTP^{•-} remains. These remaining anions are clearly free ions, which decay slowly. For $t > 150$ ns, almost identical absorbance of NTP^{•-} indicate that the free ion yields of BPhO^{•-}, FA^{•-} and MePy^{•-} are nearly identical, but the free ion yield of F₃^{•-} is $50 \pm 5\%$ larger than the other three anions. The above findings agree with the measurements in Figure 4.4, where the long-lived fraction of F₃^{•-} is greater than that of BPhO^{•-} and MePy^{•-}. This result supports the conclusion that a substantial number of F₃^{•-} escape from (F₃^{•-}, RH₂⁺) ion pairs to become free ions.

4.4 Estimations of the Standard Free Energy Change (ΔG^0) for the PT reaction

Diffusion together of anions and protons is expected to occur with roughly similar rates for all molecules because the mutual diffusion coefficient is will always have a constant contribution from the solvated proton, assuming that its diffusion coefficient is similar to the self-diffusion coefficient of THF, $1.3 \times 10^{-5} \text{ cm}^2/\text{s}$.⁸² Therefore, the wide variation of geminate decay rates seen in Figure 4.3 implies a range of rates for the PT reaction, reaction (4.4a). To examine whether the decay rates of anions reflect energetics, estimations of standard free energy change (ΔG^0) for the PT reaction are collected here. While there is no obvious direct measurement of ΔG^0 for the PT reaction, we combine E_{red} and computations to estimate ΔG^0 ; the computations were performed by Gaussian 09 B.01.⁸³ The PT reaction is separated into four half-reactions shown below:



ΔG^0 for the PT reaction is the sum of ΔG_i^0 ($i=5-8$). ΔG_i^0 ($i=5-8$) are the standard free energy changes of reactions 4.5-4.8, respectively. Calculated ΔG^0 are given in Table 4.3. Figure 4.6 plots the measured PT rate constants (k_{MPT}) vs. ΔG^0 , where k_{MPT} given in Table 4.3 are determined by the fitting procedure described in the discussion section from data. Plots of k_{MPT} vs. ΔG_8^0 and E_{red} are in Figure B11 (a) and (b) of Appendix B, respectively.

Table 4.3 Measured Proton Transfer Rate Constants ($k_{\text{MPT}}=K_{\text{eq}}k_{\text{PT}}$), Reduction Potentials (E_{red} vs. SCE), Hydrogen Atom Affinities (ΔG_8^0), the Calculated Standard Free Energy Change (ΔG^0) for the Proton Transfer Reaction, and the Number of Atoms (NA) over which charge is distributed in the anions and the Accepting Atom (AA).

Symbol	Name (AA) ^b	^c k_{MPT} (s ⁻¹)	E_{red} (V) ^{Ref}	ΔG_8^0 (eV)	ΔG^0 (eV)	^d NA
F ₁	F ₁ (C)	1.98(±0.06)×10 ⁸	-2.628 ⁷⁶	-0.695	-1.607	11.1
F ₂	F ₂ (C)	2.02(±0.08)×10 ⁷	-2.333 ⁷⁶	-0.714	-1.332	21.5
F ₃	F ₃ (C)	1.52(±0.20)×10 ⁷	-2.218 ⁷⁶	-0.715	-1.216	32.0
F ₄	F ₄ (C)	1.17(±0.06)×10 ⁷	-2.165 ⁷⁶	-0.714	-1.164	42.4
C1	dibenzofuran (C)	9.55(±0.15)×10 ⁷	-2.503 ^{84,k,t}	-0.779	-1.566	6.0
C2	fluoranthene (C)	2.52(±0.04)×10 ⁷	-1.78 ^{85,t}	-1.150	-1.214	6.9
C3	phenanthrene (C)	9.49(±0.38)×10 ⁷	-2.47 ^{85,r,t}	-0.841	-1.595	7.5
C4	1-methylpyrene (C)	1.83(±0.08)×10 ⁷	-2.08 ^{85,s,t}	-1.182	-1.546	9.7
C5	biphenyl (C)	1.49(±0.07)×10 ⁸	-2.60 ^{85,s,t}	-0.583	-1.467	9.6
C6	<i>p</i> -terphenyl (C)	2.72(±0.06)×10 ⁷	-2.37 ^{86,m,t}	-0.720	-1.288	11.2
C7	terthiophene (C)	4.67(±0.48)×10 ⁷	-2.115 ^{87,n}	-0.536	-0.849	7.6
C8	fluorobenzene (C)	1.68(±0.33)×10 ⁸	-3.207 ^{88,o}	-0.515	-1.92	3.9
C9	<i>o</i> -terphenyl (C)	5.67(±0.01)×10 ⁷	-2.55 ^{86,m,t}	-0.570	-1.318	11.6
CN	4-cyano-4'- <i>n</i> -pentyl- <i>p</i> -terphenyl (N) ^g	≥ 5.00×10 ⁹	-1.838 ^e	-0.788 ^h	-0.824 ^h	3.9
O1	<i>p</i> -dinitrobenzene (O)	≥ 5.00×10 ⁹	-0.645 ^{89,p,t}	-1.370	-0.213	5.3
O2	benzophenone (O)	≥ 5.00×10 ⁹	-1.926 ^{84,k,t}	-1.021	-1.231	1.9
O3	anthraquinone (O)	1.29(±1.17)×10 ⁹	-0.897 ^{89,p,t}	-1.389	-0.484	3.3
O4	tetrachloro- <i>p</i> -benzoquinone (O)	3.12(±0.72)×10 ⁷	0.14 ^{90,q,t}	-2.283	-0.427	8.7
O5	acetophenone (O)	3.63(±0.78)×10 ⁸	-1.96 ^{91,r,t}	-0.789	-1.033	2.0
O6	^a DDQ (O)	≥ 5.00×10 ⁹	0.608 ^{90,q,t}	-2.422	-0.097	5.4
O7	4-nitro- <i>p</i> -terphenyl (O)	≥ 5.00×10 ⁹	-1.14 ^{92,s,t}	-1.322	-0.746	3.7
O8	2,3-dicyano- <i>p</i> -benzoquinone (O)	^j ≥ 8.05×10 ⁷	0.383 ^{90,q,t}	-2.477	-0.377	5.2
N	tetracynaoethene (N)	^f N.R.	0.18 ^{93,s,t}	-1.112	0.87	3.9

All footnotes of this table are in the next page.

Footnotes of Table 4.3:

^a2,3-dicyano-5,6-dichloro-*p*-benzoquinone

^bThe accepting atom (see text) ^c k_{MPT} are determined by the fitting procedure from the data with F_{h}^{I} , k_{r1} and k_{r2} held as 0.36, $1.28 \times 10^8 \text{ s}^{-1}$ and $1.27 \times 10^7 \text{ s}^{-1}$.

^dThe Number of the Atoms (NA) containing 80% of the negative charge of anion (see text).

^eMeasured by bimolecular electron transfer equilibria method in THF with acetophenone (AO) as the electron donor; the reduction potential difference $\Delta E_{\text{red}}(\text{CNTP-AO})=122 \pm 14 \text{ mV}$, and the reduction potential (E_{red}) of AO is given in Table III; CNTP: 4-cyano-4'-*n*-pentyl-*p*-terphenyl.

^f"N.R." means that no proton transfer reaction occurred.

^hFor the scenario that proton transfer from RH_2^+ to the C atom.

ⁱFor the scenario that proton transfer from RH_2^+ to the N atom.

^jDetermined by fitting to a two exponential function from data of $\text{CN}_2\text{BQH}^{\bullet}$. Because absorption bands of $\text{CN}_2\text{BQ}^{\bullet-}$ are weak and well overlapped with those of $\text{CN}_2\text{BQH}^{\bullet}$, it is difficult to extract

k_{MPT} from the data of $\text{CN}_2\text{BQ}^{\bullet-}$. Transient spectra of $\text{CN}_2\text{BQ}^{\bullet-}$ are in Figure S12 of the SI; $\text{CN}_2\text{BQH}^{\bullet}$: semi-2,3-dicyano-*p*-benzoquinone radicals. ^kReported E_{red} vs. Ag/AgCl (-0.045 V vs. SCE)⁹⁴ in dimethylformamide (DMF).

^lReported E_{red} vs. Hg pool (-0.55 V vs. SCE)⁸⁵ in DMF with tetra-*n*-butylammonium iodide (TBAI).

^mReported E_{red} vs. Ag/AgNO₃ in DMF; the values are converted into vs. SCE with $E_{\text{red}}(\text{biphenyl})=-2.60 \text{ V}^{\text{85}}$ (vs. SCE.), $\Delta E_{\text{red}}(\text{pTP-biphenyl})=0.24 \text{ V}$,⁸⁶ and $\Delta E_{\text{red}}(\text{oTP-biphenyl})=0.01 \text{ V}$;⁸⁶ *p*TP: *p*-terphenyl; *o*TP: *o*-terphenyl.

ⁿReported E_{red} vs. Ag/AgCl (-0.045 V vs. SCE)⁹⁴ in dimethylamine (DMA) with tetra-*n*-butylammonium bromide (TBABr). Because the dielectric constants of DMA and THF are similar, the E_{red} measured in DMA is close to that measured in THF.

^oBased on $\Delta E_{\text{red}}(\text{FBz-benzene})=0.173 \text{ V}$ in THF⁹⁵ and $E_{\text{red}}(\text{benzene})=-3.38 \text{ V}$ (vs. SCE).⁹⁶

^pFrom this publication,⁸⁹ the E_{red} of DNB, AQ and oxidation potential (E_{ox}) of ferrocene (Fc) are -0.124, -0.125, and 1.332 V (vs. cobaltocenium/cobaltocene) in THF with tetra-*n*-butylammonium hexafluorophosphate (TBAPF₆). Therefore, with $E_{\text{ox}}(\text{Fc})=0.56 \text{ V}^{\text{97}}$ vs. SCE in THF with TBAPF₆, the E_{red} of DNB and AQ can be converted into vs. SCE.

^qReported E_{red} vs. SCE in DMF with tetra-*n*-butylammonium tetrafluoroborate.

^rReported E_{red} vs. SCE in DMF with TBAI.

^sReported E_{red} vs. SCE in DMF with tetra-*n*-butylammonium perchlorate.

^tThe E_{red} measured in THF may be ~0.11-0.15 V more negative than that measured in DMF.^{89, 97}

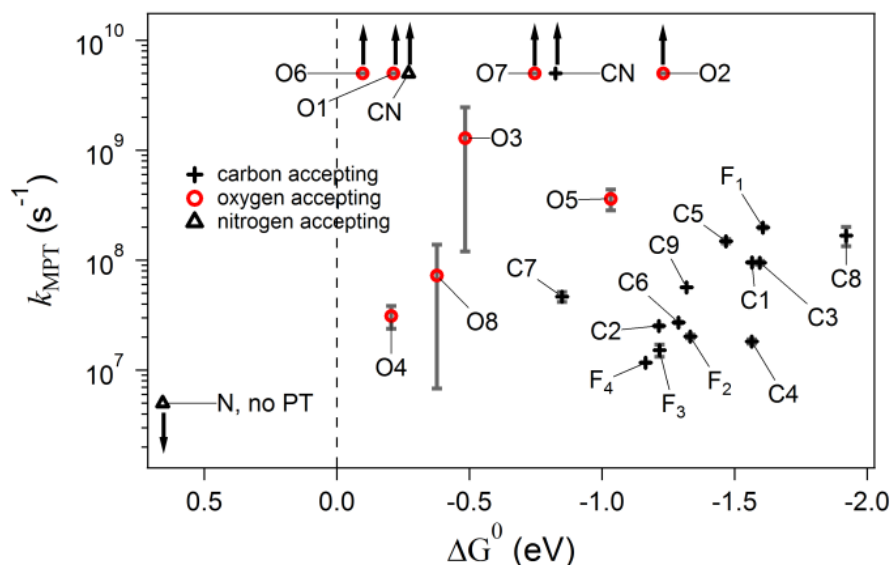


Figure 4.6 A Plot of measured proton transfer rate constant ($k_{\text{MPT}}=K_{\text{eq}}k_{\text{PT}}$) vs. the estimated standard free energy change (ΔG^0). The symbol legends are given in Table 3. The up arrows mean that only lower limits were determined, and down arrows mean that no proton transfer (PT) reaction was observed.

In the scheme to estimate ΔG^0 for the PT reaction, ΔG_5^0 is E_{red} value subtracting the Fermi level of the reference electrode in the liquid state. ΔG_5^0 of solutes are given in Table 4.3 with the E_{red} reported by Zaikowski.⁷⁶ ΔE_{red} given in Table 4.3 are versus the saturated calomel electrode (SCE) for which the Fermi level is -4.71 eV.⁹⁸ The standard free energy change of electron-proton recombination (ΔG_7^0) in vacuum is -13.61 eV.⁹⁹⁻¹⁰⁰ ΔG_6^0 and ΔG_8^0 were calculated as described in the following paragraphs.

The single point energy of the solvated proton complex was computed by RMP2/6-31G(d) with the optimized geometry computed by B3LYP/6-31G(d) in THF with PCM and corrected for basis set superposition error (BSSE). Because the solvated proton is a weakly bound molecular complex, its computed geometry may be affected by BSSE leading to an artificial shortening of intermolecular distance. The solvation energy of the solvated proton complex was calculated by B3LYP/6-31G(d) in THF with and without the PCM.

The solvated proton complex might contain one, two or more THF molecules. For most PT reactions, the calculated ΔG_6^0 for the complex where two THF molecules stabilize the proton makes most the reactions endoergic in disagreement with the experimental results that show occurrence of PT reactions. While this disagreement may be related to errors in the calculated quantities, we utilize calculated $\Delta G_6^0=2.9$ eV for the complex in which one THF molecule stabilizes the proton. Possible structures of solvated proton complexes where the proton is stabilized by one and two THF molecules are shown in Figure B13 of Appendix B.

ΔG_8^0 was estimated by computation. Benzene was used as reference to select a reliable computation method to calculate ΔG_8^0 because an experimental value, $\Delta G_8^0 = -0.67$ eV, for benzene in gas phase has been reported;¹⁰¹ We are not aware of reports of ΔG_8^0 for other molecules. Optimized geometries of benzene and benzene-H radical (BzH[•]) were calculated by B3LYP/6-31G(d). The optimized geometry of BzH[•] is shown in Figure S14(a) of Appendix B. The single point energies were computed by HF/6-31G(d), B3LYP/6-31G(d), and ROMP2/6-31G(d) in vacuum with the above optimized geometries. The G3 method was also employed to calculate ΔG_8^0 of benzene in gas phase. The calculated values of ΔG_8^0 for benzene in gas phase are given in Table 4.4. The wide variations signal the possibility of large errors. We chose ROMP2/6-31G(d) to estimate the ΔG_8^0 of solutes given in Table 4.3. While this method gave the best agreement with experiment it does differ by 0.17 eV, signaling that the computed estimates of ΔG_8^0 are likely to contain errors.

Table 4.4 Experimental and Computed ΔG_8^0 of Benzene in Gas Phase.

method	Experimental	^a ROMP2	^a B3LYP	^a HF	G3
ΔG_8^0 (benzene)	-0.67 eV ¹⁰¹	-0.499 eV	-1.222 eV	-1.318 eV	-1.009 eV

^aBasis sets are 6-31G(d).

The single point energies of neutral molecules were calculated by ROMP2/6-31G(d), and that of MH[•] were computed by ROMP2/6-31G(d) in vacuum with their optimized geometry computed by B3LYP/6-31G(d) in THF with the PCM. Examples of optimized geometries for F₂H[•] and BPhO ketyl radical are available in Figure B14 (b) and (c) of Appendix B. The solvation energies of neutral molecules and MH[•] estimated from differences of single point energies computed by B3LYP/6-31G(d) in THF with and without the PCM. The calculated ΔG_8^0 are given in Table 4.3.

The uncertainty of ΔG_8^0 is roughly estimated to be ~0.3 eV from comparison of calculated $\Delta \Delta G_8^0 = 0.309$ eV between BPhO^{•-} and AQ^{•-} in water. This calculated difference can be compared to $\Delta \Delta G_8^0 = 0.50$ eV in water based on pKa's¹⁰² of BPhO ketyl radicals and semi-anthraquinone radicals and E_{red}^{102} of BPhO and AQ. Details are in the section S2 of the SI. The above check shows a 0.191 eV of difference between computed and experimental $\Delta \Delta G_8^0$. The uncertainty of is not well tested or understood; again the uncertainty of ~0.3 eV is a rough estimate.

The lowest computed single point energy of MH[•] was employed to predict the accepting atom (AA) to which the proton may transfer. The computed results and the possible AA are given in Table 4.3. This criterion assumes that the most stable product is formed, but, this might not be always correct. In molecules, where C, N or O atoms might accept the proton, PT to an N or O

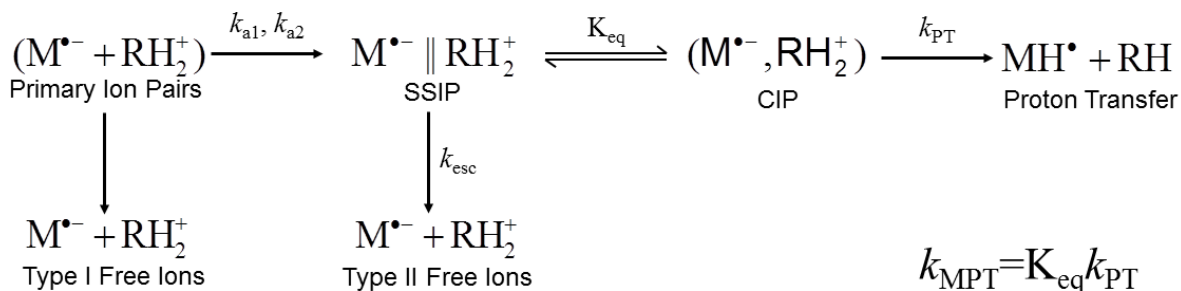
atom might be faster than PT to a C atom, which requires greater geometry change, even if the energetics to the C atom are more favorable. For the case of CNTP⁻, the Mulliken¹⁰³ charge distribution computed by B3LYP/6-31G(d) in vacuum predicts that most charge localizes around the C≡N group. The solvated proton probably prefers to approach the lone electronic pair of the N atom that makes PT to the N atom easier than that to a C atom. Therefore, the AA of CNTP⁻ may not be a C of the *p*-terphenyl group but the N atom of the C≡N group. The calculated ΔG_8^0 and ΔG^0 of CNTP⁻ are reported in two different scenarios, the C accepting and the N accepting, and given in Table 4.3.

Estimates of ΔG^0 for the PT reactions are plausibly uncertain by ~ 0.4 eV based on estimated uncertainties of ΔG_8^0 and smaller uncertainties for E_{red} . The estimated ΔG^0 for the PT reaction is favorable, $\Delta G^0 = -0.097$ eV for DDQ⁻ in agreement with the observed fast geminate decay, and is unfavorable, $\Delta G^0 = 0.87$ eV for TCNE in agreement with the absence of decay of TCNE⁻ as shown in Figure B15 of the SI, which points to formation of stable (TCNE⁻, RH₂⁺) ion-pairs.

4.5 Discussion

The kinetics of the geminate recombination are illustrated in Scheme 4.1. That scheme includes two well established types of ion pairs,¹⁰⁴⁻¹¹⁰ contact ion pairs (CIP) and solvent separated ion pairs (SSIP), based on the CIP-SSIP picture.¹¹¹ SSIP and CIP are also called loose and tight ion pairs, respectively. The Type II free ions have been proposed in many theoretical works such as works of Hong and Noolandi,¹⁶ and we will apply their works to examine F_h. PT is assumed to occur only in CRIP and to be described by PT models such as those of Borgis and Hynes.⁴⁵⁻⁴⁹

Scheme 4.1 Kinetic of geminate ion recombination in THF, where annihilation of radical anions (M⁻) is due to the PT reaction (see text). CIP and SSIP are contact and solvent separated ion pairs, respectively. The effective PT rate constant is the measured PT rate constant ($k_{\text{MPT}} = K_{\text{eq}} k_{\text{PT}}$). F_h^I and F_h^{II} are the fractions of Type I and Type II free ions, respectively.



4.5.1 Kinetics of Geminate Recombination and PT Reaction

Based on Scheme 4.1, a fitting procedure was developed to extract kinetic information from the data. The Coulomb-driven diffusion recombination to form SSRIPs is described by a two exponential function. Diffusion-controlled geminate recombination can be described by a three exponential function,¹¹² but a two exponential function is sufficient to describe the present observations as seen in Figure 4.7 and this reference.⁷⁵ SSIPs can become CIPs, or the associated ions can escape from each other to become Type II free ions. Here, the transformation between SSIP and CIP is described by an equilibrium constant ($K_{\text{eq}}=[\text{CIP}]/[\text{SSIP}]$). This approximation, which yields a relatively simple solution to the differential equations of Scheme 1, assumes that transformation between these two types of ion pairs is much faster than the other reactions. The primary ion pairs may diffuse together as CIP and little or no SSIP if K_{eq} is sufficiently large. Dissociation of SSIP to form the Type II free ions is described by an escape rate constant k_{esc} . After forming of CIP, the proton will transfer from RH_2^+ to M^- with a proton transfer rate constant k_{PT} . The fitting procedure also uses a single exponential to describe decays of free ions, which may be due to recombination with RH_2^+ , R^* and impurities. Scheme 4.1 describes the geminate decay and does not include this part.

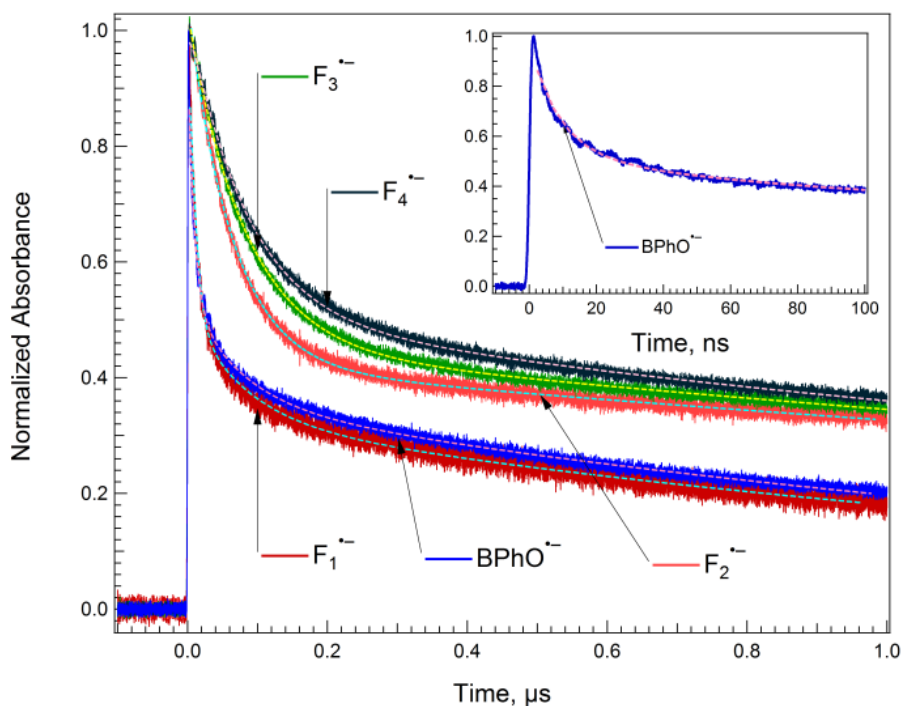


Figure 4.7 Examples of data and fits for benzophenone (BPhO) and F_n ($n=1-4$), where the dashed lines are fits. The insert shows that a sum of two exponential decays is sufficient to describe diffusion-controlled geminate recombination of $\text{BPhO}^{\bullet-}$. The fitting procedure extracts k_{MPT} and k_{esc} from data, with $\text{F}_h^{\bullet-}$, k_{r1} and k_{r2} held fixed.

4.5.2 Capture of Electrons

In this study, our measurements gave the free ion yield, $G_{fi}=0.69\pm 0.06$ per 100 eV of $BPhO^{\bullet-}$ for 50 mM of BPhO in THF. The above result is near the upper end of a range of reported G_{fi} values, 0.205~0.72 per 100 eV, in THF.^{61, 67, 113-117} The method of measuring the G_{fi} value of $BPhO^{\bullet-}$ in THF is in the section B3 of Appendix B.

To study geminate ion recombination, high concentrations of electron scavengers (solutes), 50 and 200 mM of BPhO, were used to capture the electrons. BPhO captures e_s^- with a rate constant of $6.4\times 10^{10} M^{-1}s^{-1}$ given in Table 1. It also captures presolvated electrons in a “step capture” process¹¹⁸⁻¹¹⁹ during pulse radiolysis. “Step capture” is a mechanism in which presolvated electrons are captured rapidly ($\ll 20$ ps) by solute molecules during pulse radiolysis.¹¹⁸⁻¹¹⁹ The step capture fraction of the presolvated electrons of BPhO is estimated by $1-\exp(-q[s])$,¹²⁰⁻¹²¹ where q is a quenching coefficient and $[s]$ is solute’s concentration with $q=11.5 M^{-1}$ from measurements on biphenyl (BP),¹¹⁸ which has similar size to BPhO. The estimated step capture fraction of 50 mM BPhO is ~43.7% and that of 200 mM BPhO is ~89.9%. The step capture process does not change yields of geminate and homogenous ions.¹¹⁹ De Waele⁶⁷ reported that the deconvolved $G(t=0)$ value of e_s^- was 2.89 per 100 eV in THF. In this study, the maximum observed $G(t)$ values of $BPhO^{\bullet-}$ of 50 mM BPhO is 2.41 per 100 eV at $t=280$ ps, and that of 200 mM BPhO is 3.16 per 100 eV at 60 ps. These maximum $G(t)$ values are in reasonable agreement with the deconvolved $G(t=0)$ value of e_s^- in THF reported by De Waele.⁶⁷ Details for estimation of maximum observed $G(t)$ values are in the section B3 of the SI. In THF the estimated fractions of the captured electrons for 50 and 200 mM BPhO are ~94% and ~99%, respectively, based on the electron attachment with k_{att} of BPhO and “step capture” with q of BP. The above estimations are available in the section B4 of the SI. Based on the above estimations and measurements, 50 mM of BPhO captures ~90% of the electrons, and other solutes in the current study probably capture similar fractions of the electrons.

4.5.3 Kinetic Analysis

For each anion, the fitting procedure extracts k_{MPT} and k_{esc} from data, over the time period from 2 ns to 1 μs , with F_h^I , k_{a1} and k_{a2} held fixed. Examples of data and fits to obtain k_{MPT} and k_{esc} are given in Figure 4.7. The fitting procedure can only extract a combination of K_{eq} and k_{PT} , called k_{MPT} , from the data because the measurements have not been able to distinguish between SSIP and CIP. The relation between k_{MPT} , F_h^{II} and k_{esc} is

$$F_h^{II} = \frac{k_{esc}}{k_{esc} + k_{MPT}} (1 - F_h^I) \quad (4.9a)$$

and the fitting procedure obtains k_{esc} from data by

$$k_{\text{esc}} = \frac{k_{\text{MPT}} \cdot F_{\text{h}}^{\text{II}}}{1 - F_{\text{h}}} \quad (4.9b),$$

where $F_{\text{h}} = F_{\text{h}}^{\text{I}} + F_{\text{h}}^{\text{II}}$. F_{h}^{II} for each anion is estimated by equation (4.9a). Nearly identical decays of $\text{BPhO}^{\bullet-}$, $\text{CNTP}^{\bullet-}$ and $\text{DDQ}^{\bullet-}$ shown in Figure 4.5 suggest that their geminate decays are diffusion controlled, and their $F_{\text{h}} = 0.36 \pm 0.03$ are entirely F_{h}^{I} . $\text{BPhO}^{\bullet-}$ is used to obtain $k_{\text{a1}} = 1.28 \times 10^8$ and $k_{\text{a2}} = 1.27 \times 10^7 \text{ s}^{-1}$, and the first and second fractions of geminate association are $F_{\text{g1}} = 0.45$ and $F_{\text{g2}} = 0.19$, respectively. F_{h}^{I} is calculated by $G_{\text{fi}}/G_{\text{max}}$ with $G_{\text{fi}} = 0.69 \pm 0.06$ per 100 eV and G_{max} is $G(t=2 \text{ ns}) = 1.92$ per 100 eV. Details for estimation of $G(t=2 \text{ ns})$ value of $\text{BPhO}^{\bullet-}$ are available in section S3 of the SI. By holding F_{h}^{I} , k_{a1} and k_{a2} fixed, we found that the lower limits of k_{MPT} for $\text{BPhO}^{\bullet-}$, $\text{CNTP}^{\bullet-}$ and $\text{DDQ}^{\bullet-}$ were $5.0 \times 10^9 \text{ s}^{-1}$. From Figure 4.3, F_{h} of $\text{FA}^{\bullet-}$, $\text{MePy}^{\bullet-}$, $\text{oTP}^{\bullet-}$ and $\text{pTP}^{\bullet-}$ are similar to F_{h} of $\text{BPhO}^{\bullet-}$, but their geminate decays are much slower than $\text{BPhO}^{\bullet-}$. The above four anions with fast PT show that there is little or no F_{h}^{II} . The k_{MPT} of anions are given in Table 4.3, and $G_{\text{fi}}^{\text{II}}$ and k_{esc} for anions in Figure 4.3 are given in Table 4.5, where $G_{\text{fi}}^{\text{II}} = G_{\text{fi}} - G_{\text{fi}}^{\text{I}}$.

Table 4.5 G_{fi} values, Type II Free Ion Yields ($G_{\text{fi}}^{\text{II}}$) and Escape Rate Constants (k_{esc}).

Name	^{a,b} G_{fi}	^a $G_{\text{fi}}^{\text{II}}$	$k_{\text{esc}} (\text{s}^{-1})$
[†] F_1	0.71	≤ 0.02	$\leq 3.00 \times 10^6$
[†] F_2	^c 0.84	^c 0.15	^b $2.04(\pm 0.80) \times 10^6$
[†] F_3	^c 0.93	^c 0.24	^b $2.56(\pm 0.42) \times 10^6$
[†] F_4	^c 1.05	^c 0.36	^b $3.28(\pm 0.19) \times 10^6$
^{‡,d} BPhO	0.69	≤ 0.02	$\leq 1.00 \times 10^7$
^{†,e} DBF	0.69	≤ 0.02	$\leq 3.00 \times 10^6$
^{†,f} FA	^c 0.69	^c ≤ 0.06	^c $\leq 1.00 \times 10^6$
^{†,g} MePy	0.69	≤ 0.02	$\leq 7.85(\pm 3.08) \times 10^5$
^{†,h} pTP	0.69	≤ 0.02	$\leq 1.00 \times 10^6$
^{†,i} oTP	0.69	≤ 0.02	$\leq 1.00 \times 10^6$

[†]Carbon Accepting Anion [‡]Oxygen Accepting Anion ^aThe unit is number of ions per absorbing 100 eV. ^b $G_{\text{fi}} = G_{\text{fi}}^{\text{I}} + G_{\text{fi}}^{\text{II}}$, where G_{fi}^{I} is from the G_{fi} values of $\text{BPhO}^{\bullet-}$, 0.69 ± 0.06 per 100 eV. ^cObtained by the fitting procedure from the kinetic trace with correction for T-T absorbance. ^dBenzophenone ^eDibenzofuran ^fFluoranthene ^g1-Methylpyrene ^h*p*-Terphenyl ⁱ*o*-Terphenyl

For most molecules studied, F_h^{II} is too small to measure so the fitting procedure can only estimate an upper limit of k_{esc} . A check of this estimate compares it to k_{esc} calculated by $k_{\text{esc}}=k_aK_{\text{diss}}$, where k_a is the association rate and K_{diss} is the dissociation equilibrium constant. We can estimate k_{esc} for the $(\text{Na}^+, \text{MePy}^-)$ ion pair and compare it to the upper limit of k_{esc} determined here for the solvated $(\text{RH}_2^+, \text{MePy}^-)$ ion pair. Calculations of k_{esc} of Py^- are based on K_{diss} of the $(\text{Na}^+, \text{Py}^-)$ ion pairs,¹²² and k_a of the $(\text{Na}^+, \text{BPhO}^-)$ ion pairs¹¹³ with the assumption that k_a of these two ion-pairs are similar. The estimated k_{esc} for Py^- and MePy^- are given in Table 4.6. We compare k_{esc} of Py^- to that of MePy^- with the assumption that k_a for the $(\text{Na}^+, \text{Py}^-)$ ion pair and for the $(\text{RH}_2^+, \text{MePy}^-)$ ion pair are similar. The comparison finds that k_{esc} of the $(\text{Na}^+, \text{Py}^-)$ ion pair is 25% larger than the upper limit for k_{esc} of the $(\text{RH}_2^+, \text{MePy}^-)$ ion pair. This finding that k_{esc} is smaller for the solvated proton seems reasonable. Because k_{esc} is observable for F_2 , a molecule just slightly larger than MePy , it may be that the actual k_{esc} of the $(\text{RH}_2^+, \text{MePy}^-)$ ion pair is just slightly below the observed limit.

Table 4.6 k_{esc} of the $(\text{Na}^+, \text{Py}^-)$ and $(\text{RH}_2^+, \text{MePy}^-)$ ion pairs.

Ion Pair	k_{esc} (s^{-1})	Estimation Method
$(\text{Na}^+, \text{Py}^-)$	1.01×10^6	^a $k_{\text{esc}}=k_aK_{\text{diss}}$
$(\text{RH}_2^+, \text{MePy}^-)$	$\leq 7.85(\pm 3.08) \times 10^5$	^b From Data

^aIn THF at 298 K, K_{diss} of the $(\text{Na}^+, \text{Py}^-)$ ion pairs¹²² is 6.75×10^{-6} M, and k_a of the $(\text{Na}^+, \text{BPhO}^-)$ ion pairs¹¹³ is $1.5 \times 10^{11} \text{ M}^{-1}\text{s}^{-1}$. ^bDetermined by the fitting procedure from data.

Other limits on k_{esc} may be well above the actual rates. The fitting procedure may estimate a high upper limit of k_{esc} if the k_{MPT} is large and F_h^{II} is small. For example, BPhO^- has large k_{MPT} and little or no F_h^{II} . The upper limit of k_{esc} of BPhO^- , $1.0 \times 10^7 \text{ s}^{-1}$, given in Table 4.5, is greater than that of MePy^- . It seems reasonable to suspect that k_{esc} for BPhO^- is well below that limit determined from the present measurements.

4.5.4. The CIP-SSIP Picture

The equilibrium in Scheme 4.1 between contact and solvent-separated ion pairs is probably influenced by the negative charge density of the anion. Here we estimate the anion's charge density by the number of the atoms (NA) that contain 80% of the negative charge using Mulliken¹⁰³ charges with hydrogens summed into heavy atoms computed by B3LYP/6-31G(d) in vacuum. The NA of anions is $\#_{\text{tot}} \times 0.8 / C_{\text{tot}}$, where $\#_{\text{tot}}$ is total number for atoms that have C_{tot} of negative charge. For the example of BPhO^- , the computed Mulliken¹⁰³ charges indicate that 84% of the negative charge resides on the C=O, which give $\#_{\text{tot}}=2$ and $C_{\text{tot}}=0.84$, so NA of BPhO^- is 1.9. In F_1^- , 86% of the negative charge is evenly distributed in the two six-membered rings, which give $\#_{\text{tot}}=12$ and $C_{\text{tot}}=0.86$, so NA of F_1^- is 11.2. The NA's of other anions are given in Table 4.3. From Figure 4.8, k_{MPT} of the C accepting anions decrease with decreasing

charge density as reflected in increasing the NA. The above finding supports the role of charge density in k_{MPT} .

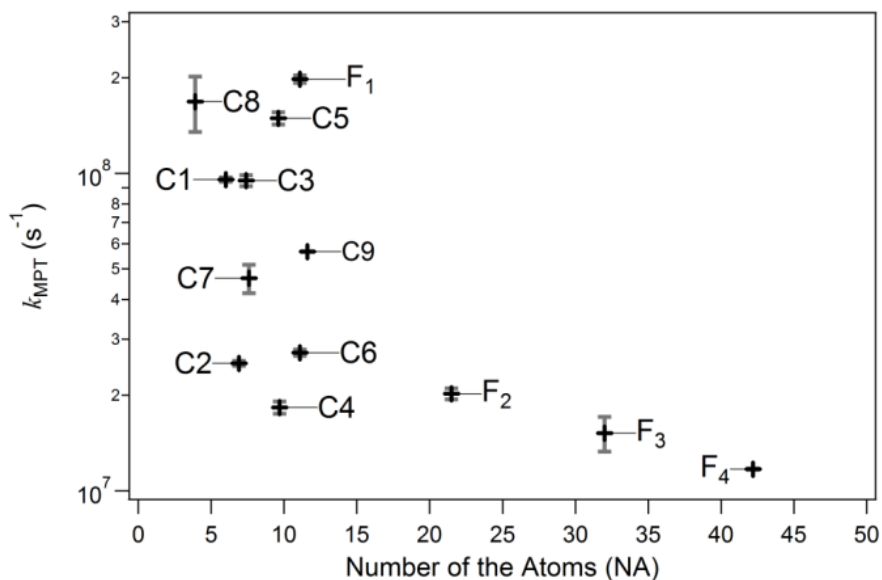


Figure 4.8 A Plot of k_{MPT} vs. the Number of Atoms (NA) over which the negative charge is distributed for the carbon accepting anions. The plot shows that high charge density helps the recombination of radical anions with solvated protons in THF. The legends of symbols are given in Table 4.3.

The CIP-SSIP picture¹¹¹ proposes that K_{eq} between CIP and SSIP is affected by the dielectric constant of environment and the lengths of the ion and solvent molecules. The above picture treats the ion's charge as uniformly spread over the whole molecule. Many experimental results^{104-106, 108} showed that K_{eq} decreased with increasing size of the cation: large cations disfavor CIP. K_{eq} is a result of the competition between two energies: (1) The Coulomb potential between anion and cation, U_c , which is driving force of forming CIP and; (2) The ion-dipole interaction energy between ion and solvent molecules, U_{id} , which is the driving force for forming SSIP. The above two energies create two local minima in the ion pair potential surface for CIP and SSIP, separately. The difference between CIP and SSIP is in that SSIP has at least one solvent molecule between anion and cation, but CRIP does not, so the separation distance (center to center), r , of SSIP is longer. Therefore, the Coulombic interaction of SSIP is weaker than that of CIP. A plot of the ion pair potential, $U(r)$, vs. r is illustrated in Figure 4.9.

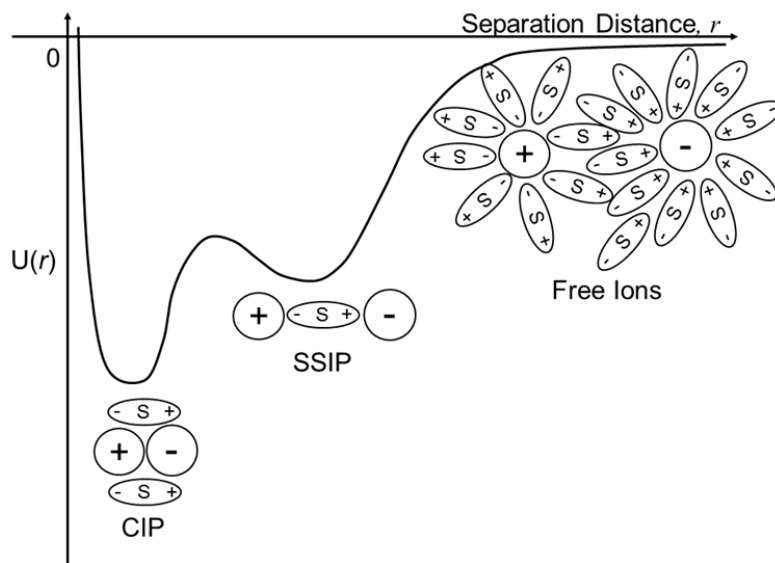


Figure 4.9 Schematic illustration of ion pair potential, $U(r)$, vs. separation distance, r , where spheres are ions and ovals are solvent molecule with a dipole. CIP and SSIP are contact and solvent separated ion pairs, respectively.

Here we add to the CIP-SSIP picture the assumption that K_{eq} is dependent on the ion's charge density, estimated through NA, as an alternative to the classical CIP-SSIP picture in which the anion's charge is uniformly spread over whole molecule. Anions with high charge density are more likely to couple with cations as CIP than are anions with low charge density.

Scheme 4.1 proposes that K_{eq} , k_{PT} and k_{esc} are three major factors affecting F_{h}^{II} . Zhong¹² reported that the Type II free ions were mainly produced from SSRIP in polar solvents such as 1,2-dichloroethane. Because the Coulombic attraction of SSRIP is weaker than that of CIP, SSIP may be expected to dissociate from each other to become free ions. In Table 4.5, the F_{h}^{II} and k_{esc} of $F_{\text{n}}^{\cdot-}$ ($n=2-4$) greater than those of other anions. These findings suggest that $F_{\text{n}}^{\cdot-}$ ($n=2-4$) prefer to pair with opposite-ions as SSIP because of their low charge densities as reflected in the NA's of anions given in Table 4.3. These findings also support proposal of Scheme 4.1 that k_{MPT} and k_{esc} are crucial to F_{h}^{II} .

While $F_{\text{n}}^{\cdot-}$ ($n=2-4$) are special in giving large enough escape rates to produce free ions by escape, their k_{MPT} are not as different from other molecules. For example $F_2^{\cdot-}$ and $\text{MePy}^{\cdot-}$ both contain four benzoid rings and both have k_{MPT} near $2 \times 10^{-7} \text{ s}^{-1}$ (Table 4.3), but k_{esc} is at least 2.5 time larger for $F_2^{\cdot-}$ in Table 4.5. The enhanced escape for $F_2^{\cdot-}$ can be understood in terms of the greater spatial extent of the delocalized electron as illustrated by the comparison to Py in Figure 4.10. Charge in the two outer rings of F_2 is farther from a proton near the center of the anion.

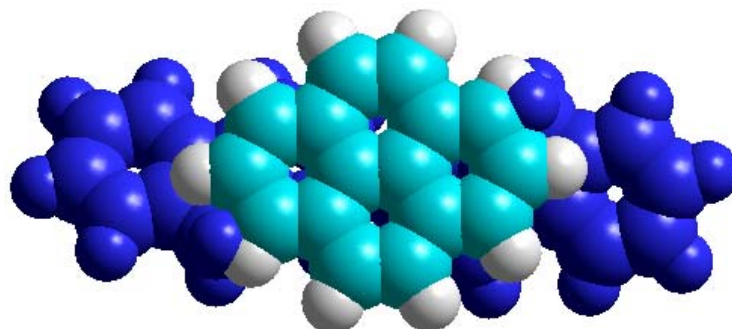


Figure 4.10 Comparison of the spatial extent of F_2 (behind, dark blue) and pyrene (foreground, light blue).

4.5.5. Theoretical Fraction of Free Ions

Hong and Noolandi¹⁶ proposed that F_h was controlled by five factors given in Table 4.7. They estimated a theoretical fraction of free ions (F_h^{theory}) based on the DS equation with the partially reflective boundary condition on a partly absorbing, partly reflecting sphere of radius r_m (effective radius). As mention before, pulse radiolysis creates a distribution of initial separation distances of the primary ion pairs, $\rho(r_i, t=0)$, which is a delta function. r_i are separation distances of the primary ion pairs at $t=0$. Several groups^{4, 69, 112, 123-126} have studied $\rho(r_i, t=0)$ in different solvents with pulse radiolysis, but $\rho(r_i, t=0)$ is still not well understood.

Table 4.7 List of Variables affecting the Fraction of Free Ions (F_h) based on the Theoretical Fraction of Free Ions (F_h^{theory}).

variable	meaning
r_c	Onsager Radius: 7.3 nm.
r_i	Separation distance of the Primary Ion Pairs at $t=0$.(see text)
r_m	The Effective Radius
D	Sum of Diffusion Coefficients of Anion and RH_2^+
k_{MPT}	The Measured Proton Transfer Rate Constant ($k_{\text{MPT}}=K_{\text{eq}}k_{\text{PT}}$)

r_i and r_c are not varied in the current study because THF is the only solvent, and $\rho(r_i, t=0)$ is dependent on the cross section of the solvent molecule and the energy of the electron pulse.⁶⁹ The diffusion coefficient of RH_2^+ is greater than those of anions. Therefore, D for the varied ($M^{\bullet-}, RH_2^+$) ion pairs are likely to be similar within a factor of two, and k_{MPT} and r_m are two factors of F_h^{theory} , which are different for each radical ion pair in the current study.

From Table 4.3 and Table 4.5, $F_n^{\bullet-}$ ($n=2-4$) have higher F_h^{II} and much smaller k_{MPT} than other anions. The above findings agree with the prediction of F_h^{theory} that k_{MPT} is one of the factors affecting F_h . k_{MPT} and F_h^{II} of $MePy^{\bullet-}$ and $F_2^{\bullet-}$ suggest a critical k_{MPT} , between 1.83 and 2.02×10^7 s^{-1} , to form obvious F_h^{II} . In the current study, it is difficult to measure or estimate r_m , which is different from r_m of partly absorbing and partly reflecting sphere proposed by Hong and Noolandi,¹⁶ so we are unable to tell how r_m affects F_h . Hong and Noolandi¹⁶ predicted that F_h would be increased with increasing r_m .

4.5.6 Proton Transfer Model

Theories of PT such as those of Brogiis and Hynes⁴⁵⁻⁴⁹ describe PT between the proton donor and the proton acceptor within a weakly bound complex (WBC) under influence of solvent molecules. The above model suggests that k_{PT} is determined by three principal factors: (1) ΔG^0 of the PT reaction and (2) the reorganization energy in the reaction coordinate, E_R ; (3) the proton coupling term, $C(Q,S)$, where Q is the general vibration coordinate and S is and the solvent coordinate. Because the RH_2^+ is the only proton donor in the current study, the influences of RH_2^+ on these three factors are constant. Therefore, differences of these three factors between each WBC are due to the anion in the current study.

From Figure 4.6, we have three findings: (1) k_{MPT} of the O and N accepting anions are generally greater than that of the C accepting anions. (2) k_{MPT} for the C accepting anions are not diffusion controlled, and the fastest PT rates to C accepting anions are more than a decade slower than fast PT to O or N accepting anions. (3) The rates are so scattered that they provoke the question: Is there any relation between k_{MPT} and ΔG^0 ? At the best, the rates to C atoms or to O atoms considered separately suggest a very rough trend. By contrast observations of both the normal and inverted regions of rate vs. ΔG^0 were reported by Andrieux¹²⁷ for PT to C atoms of carbanions and by Heeb¹²⁸ for PT to O atoms. Such free energy relations work well to reveal the effect of ΔG^0 when other important factors are approximately constant. Edwards and coworkers¹²⁹ however, found no theoretical basis for an inverted region for PT and proposed that observed decreases of rates at high driving force might be due to other factors.

In Figure 4.6, O3 to O5 and O8 seem to show a bell shape relation between k_{MPT} and ΔG^0 , but plot of rate vs. ΔG^0 shows scatter for other anions. Noting the rough trend seen we suggest that in addition to ΔG^0 two major factors, E_R and charge densities, impact the rates. Charge densities based on NA given in Table 4.3, clearly affect the rates to C atoms. Effects on rates to O and N accepting anions are not obvious partly because k_{MPT} is too fast to determine for most of them. For the O accepting anions, Figure B16 of Appendix B suggests no correlation between k_{MPT} and charge density. A plausible hypothesis that could explain the scattered nature of Figure 4.6 is widely varying E_R for the present reactants. In particular, E_R may be relatively small for PT to O and N atoms, and large for PT to C atoms. Figure S14 of Appendix B depicts molecular

geometries of radicals formed by proton addition to a C atom in two molecules and to attachment to an O atom to form BPhO ketyl radical.

4.6 Summary and Conclusions

For most molecules examined geminate recombination of radical anions with solvated protons was nearly diffusion controlled. The kinetic analysis indicates two things: (1) It takes an average of $\sim 8 \pm 1$ ns in a non-exponential process for geminate ion pairs to diffuse together to become intimate ion pairs and; (2) The free ion yield for anions, $G_{fi} = 0.69 \pm 0.06$ per 100 eV. That yield, which may be called the Type I free ion yield (G_{fi}^I), is due to escape from the distribution of initial separation distances of primary ion pairs to become free ions. For those anions with diffusion controlled recombination, the effective proton transfer rate constants, k_{MPT} are $> 5.0 \times 10^9$ s⁻¹. The $\sim 8 \pm 1$ ns required for the ions to diffuse together limits observation of faster rates.

The 50 mM solutions concentration usually used here captured $\sim 76\%$ of electrons produced by pulse radiolysis by comparison between the maximum observed $G(t)$ values of BPhO⁻ from 50 and 200 mM BPhO solutions. From the G_{fi} value of BPhO⁻, $\sim 29\%$ of anions escape from geminate recombination to become the Type I free ions.

For several of the anions, geminate recombination, and therefore k_{MPT} , was slower but there was no measureable change in the fraction of free ions (F_h) compared to anions for which geminate recombination is diffusion controlled. Despite the long-lived ion pairs, no detectable fraction of these anions escaped from the pairs to become free ions. Three anions, $F_n^{\bullet-}$ ($n=2-4$), were exceptions. For these anions, which have low charge densities, geminate decays were much slower and F_h increased measurably. The increase of G_{fi} is due to escape from intimate ion pairs comprised of CIP and SSIP to become the Type II free ions and may be called the Type II free ion yield (G_{fi}^{II}). Observations in the current study provide examples described by the theoretical diffusion model of Hong and Noolandi¹⁶⁻¹⁷ including long-lived ion pairs and the possibility that geminate ions may escape from intimate pairs to become free ions, in contrast to the Onsager model.¹ The low charge density of anions can: (1) reduce the Coulombic attraction of radical ion pairs and (2) give a preference for SSIP, coupling with cations, (3) increase k_{esc} to yield type II free ions and (4) slow down k_{PT} . Low charge density is thus crucial to the Type II free ions. While we attribute the escape yields for these fluorene oligomers to low charge densities, we do not exclude the possibility that the hexyl side chains might have some influence.

In the current study, a wide variety of k_{PT} in the radical ion pairs provides opportunities to examine theory of PT,^{38-41, 45-49, 130-132} which discuss k_{PT} in terms of ΔG^0 , $C(Q,S)$ and E_R . In this study, no PT reaction of the C accepting anions is diffusion controlled, but many PT reactions to the O accepting anions are. These findings may reflect large variations in E_R , which is usually being larger for protonation at C atoms. Whatever the reason, correlation of rate with ΔG^0 is

poor. k_{PT} are affected by two factors: (1) degree of charge delocalization in the anion and (2) the type of atom receiving the proton.

The most important finding of this study is effect of low charge density to the free ion yield. In anions with highly delocalized charges, k_{MPT} decrease and G_{fi}^{II} increases. While G_{fi}^{II} was measurable only for $F_n^{\bullet-}$ ($n=2-4$), it is reasonable to assume that delocalization generally increases G_{fi}^{II} . The observed enhancement of escape of radical ion pairs to form free ions could be important for improvement of the energy efficiency for BHJ organic solar cell.¹³³⁻¹³⁴

Chapter 5. Charge Separation of Electron-Hole Pairs (Exciplexes) Enhanced by Charge Delocalization.

5.1 Introduction

The energy efficiency of photoinduced electron transfer (PET) systems as a solar cell^{133, 135} depend on yield of charge separation (CS). In PET system, an electron transfers from a photoexcited charge donor (D_e^*) to a charge acceptor (A_e) to create a radical ion pair (RIP) of $A_e^{\bullet-}$ and $D_e^{\bullet+}$, referred to as charge transfer (CT) states, which either dissociate into CS states to provide electricity or recombine with each other. By CS, we mean that: (1) $A_e^{\bullet-}$ and $D_e^{\bullet+}$ are separated away from each other at least longer than a critical distance (r_c), often referred to as the Onsager radius,¹ at which the attractive Coulomb potential equals $k_B T$, where k_B is the Boltzmann constant, and T is temperature; (2) Recombination of CS state is bimolecular.

In the current study, CT states are contact radical ion pairs (CRIP), and exciplexes are excited complexes, $(A_e^{\delta-}/D_e^{\delta+})^*$. Some publications referred CRIP to as exciplexes^{5, 136-140} with pure CT character¹⁴¹ and exciplexes as excited molecular complexes.^{8, 10-11, 142} The lifetimes of CRIPs reported by Gould¹⁴⁰ and Mataga¹⁴³⁻¹⁴⁴ were varied from 64 ps to 20 ns in acetonitrile with different charge recombination energy (Δ_{CR}) of electron transfer (ET) reaction, -0.61 to -2.89 eV. Δ_{CR} can be estimated by difference between the reduction potential (E_{red}) and oxidation potential (E_{ox}) of D_e with the Coulomb potential term, which may be negligible in high dielectric constant (ϵ_d) solvent such as acetonitrile.¹⁴⁰ Koch¹⁴⁵ reported the lifetime of the CRIP of phthalic anhydride/9-cyanoanthracene (A_e/D_e) as 510 ps in THF with $\Delta_{CR} = -2.9$ eV. Generally, it is a bell shape relation between Δ_{CR} and lifetime of CRIP.

The dielectric constant of the solvent has a substantial influence on CS processes, which results in yield of CS species (Y_{cs}). There are two steps to CS processes: (1) Solvation from CRIP to solvent separated radical ion pairs (SSRIP) and (2) Charges separate from SSRIP to CS states. The difference between CRIP and SSRIP shown in Figure 5.1 is that the SSRIP has at least one solvent molecule between the anion and the cation, but the CRIP do not. Many groups^{2, 72, 136, 143, 146-148} reported that CS states are favorable states of RIP in polar organic solvents such as acetonitrile.

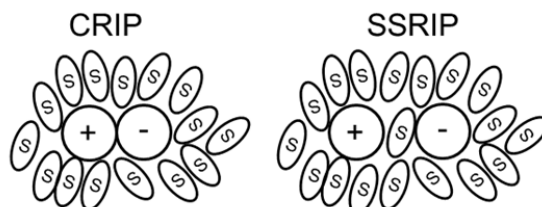
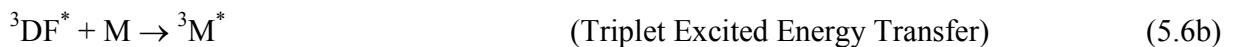
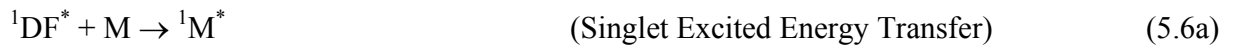
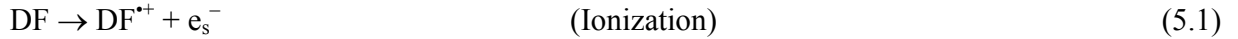


Figure 5.1 Diagrams of contact radical ion pair (CRIP) and solvent separated radical ion pair (SSRIP), where ions are sphere, and solvent molecules are oval.

The purpose of this study is to explore the influence of charge delocalization on the yield of CS species (Y_{cs}) and the energy level of the radical ion pair (RIP). Weller¹⁰ proposed that Y_{cs} was affected by three things: the mutual Coulomb potential, solvation energy and interaction between $A_e^{\bullet-}$ and $D_e^{\bullet+}$. Changing the first two factors can be achieved by the changing charge densities of ion. Bakulin¹⁴⁹ increased the population of CS states by reducing the Coulomb potential of electron-hole pair in a BHJ solar cell by decreasing the charge density of holes using multiphoton excitation method. It is known that the electron densities of oligo(9,9-dihexyl)fluorene anions ($F_n^{\bullet-}$, $n=1-6$) decrease with increasing numbers of repeat units (n).¹⁵⁰ We will observe ion recombination of F_n ($n=1-6$) and other small molecules such as 4,4'-dimethylbiphenyl (DMBP), to study the influence of charge delocalization with pulse radiolysis and photoexcitation.

We studied the ion recombination in 2,3-dihydrobenzofuran (DF) with pulse radiolysis, which is capable of rapidly creating ions, because DF is a good solvent for F_n ($n=1-6$). The dielectric constant (ϵ_d) of DF is 4.33, which is an estimated value from the ϵ_d of anisole ($\epsilon_d=4.33$). Due to similarity between DF and anisole in chemical structure, the ϵ_d of DF is expected to be close to the ϵ_d of anisole. The viscosity (η) of DF is and 1.97 cP,¹⁵¹ and r_c of DF is 12.6 nm in 298 K. Radiation chemistry of DF with solute molecule (M) is given in the below:



where ${}^1DF^*$ and ${}^3DF^*$ are singlet and triplet excited states of DF.

To study the geminate ion recombination in DF, we observed the time evolution of transient absorption of RIP $\sim 1 \mu s$ after the electron pulse. Pulse radiolysis creates the primary radical ion pairs (PRIP) with an initial separation distance distribution, $\rho(r_i)$, where r_i is initial separation distance from center to center and maybe shorter and longer than r_c . The PRIP with $r_i \leq r_c$ usually diffuse together to become intimate radical ion pair (IRIP) in short time, and their recombination is geminate. This IRIP is comprised of SSRIP and CRIP, which both RIP can be referred to as CT states. The escape probability of PRIP to CS states can be estimated by

$1 - \exp(-r_c/r_i)$ given by Onsager.¹ Whether they begin at $r_i > r_c$ or escape from shorter distance, we will refer to them as CS states.

5.2 Experiments

Our measurements were carried out at the Laser Electron Accelerator Facility (LEAF) at Brookhaven National Laboratory with 9 MeV, <15 ps, electron pulse ; methods of measurement are reported elsewhere.⁵² Briefly, the electrons were injected into quartz cells with an optical path length of 5 mm, containing solutions of the molecules under study. The probe light source is a pulsed Xenon arc lamp. The wavelength of the probing light is selected by optical interference filters with either 10 or 40 nm bandpass. Transient absorption and fluorescence are detected by a silicon photodiode (EG&G FND-100, 2 ns response time), an InGaAs photodiode (GPD Optoelectronics GAP-500L, 2 ns response time) or a phototube (Hamamatsu, R1328U-03, 65 ps response time); data are digitized by LeCroy 8620A, 640Zi or HRO 66Zi oscilloscopes.

The photoexcitation experiments were used Raman shifted 397 nm, 100 ps, as pumping light and a Xenon arc lamp to provide probe light. The 397 nm pumping light was generated by the Raman scattering with 355 nm light passing through a pressurized chamber containing 120 psi of D₂. Selection of the probe light and digitization of data were described in the previous paragraph. The samples were in quartz cells, 0.5 mm path length.

All samples were prepared in purified solvents under argon atmosphere. THF was purified by THF purifier (Vacuum Atmosphere Company, VAC 104427) to remove oxygen and water. 2,3-dihydrobenzofuran was passed through silica gel to remove water and impurities. Other chemicals were purchased from Aldrich or Alfa-Aesar and used as received. The synthesis of F_n (n=1-6) has been described.⁷⁵ Chemical structures are given in Appendix A.

5.3 Results

After reduction and oxidization of solute molecules by e_s⁻ and solvent radical cation, respectively, the solute radical anions (M^{-•}) recombine with solute radical cations (M^{+•}) via electron transfer reactions. Kinetic traces from pulse radiolysis of radical ions for small molecules are shown in Figure 5.2 and that of F_n(n=1-6) ions are shown in Figure 5.3. They were collected at observed wavelengths of the radical ions of each molecule by LEAF in DF solution. Extinction coefficients (ϵ) of ions for F_n(n=1-6) and 4,4'-dimethylbiphenyl (DMBP) are given in Table 5.1. Details of estimations for ϵ of cations are in section C1 of Appendix C. From Figure 5.2 and Figure 5.3, decays of radical ions during the first 200 ns display large variations with solute. Figure 5.2 (b) shows that the decay of DMBP ions is the fastest among molecules given in Table 5.3. From Figure 5.3, the fast decay rates of F_n (n=1-6) radical ions decrease for the longer oligofluoroenes.

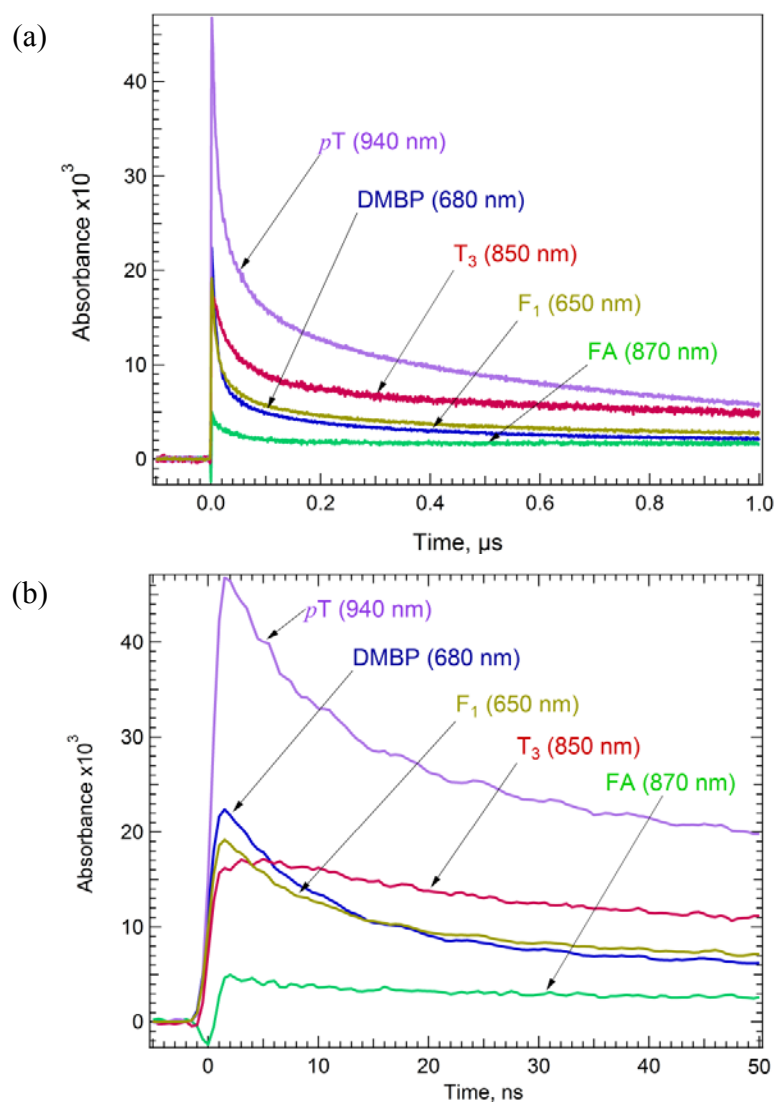


Figure 5.2 (a) Kinetic traces from pulse radiolysis of 4,4'-dimethylbiphenyl (DMBP), *p*-terphenyl (*p*T), terthiophene (T₃) and fluoroanthene (FA) in 2,3-dihydrobenzofuran (DF) solutions, where concentrations of all solutes are 50 mM. (b) Kinetic traces of these four molecules at early time.

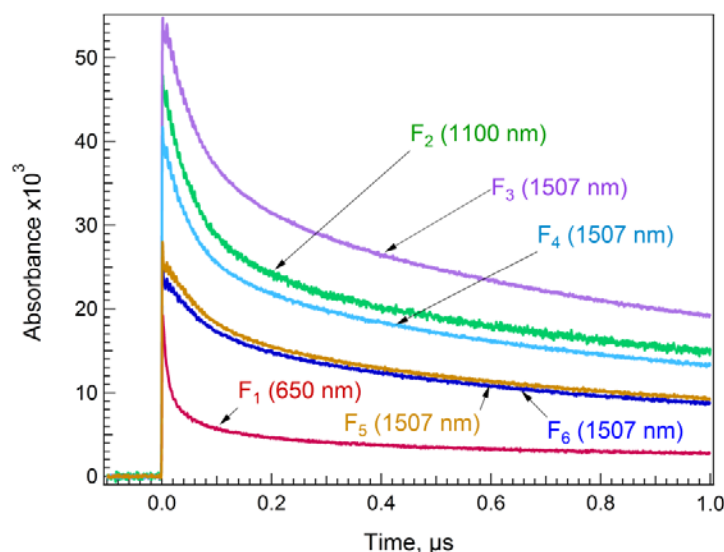


Figure 5.3 Kinetic traces from pulse radiolysis of F_n ($n=1-6$) at observation wavelength in 2,3-dihydrobenzofuran where concentrations of F_n ($n=1-6$) are 50, 50, 40, 30, 20 and 20 mM, respectively.

Table 5.1 Extinction Coefficients of Anion (ϵ_a) and Cation (ϵ_c)

name	ϵ_a ($M^{-1}cm^{-1}$)	ϵ_c ($M^{-1}cm^{-1}$)
F_1	8.18×10^3 (650 nm) ^c	8.82×10^3 (680 nm) ^e
F_2	2.64×10^4 (1100 nm) ⁷⁶	3.71×10^4 (1250 nm) ^e
F_3	2.54×10^4 (1507 nm) ⁷⁶	3.17×10^4 (1507 nm) ^f
F_4	2.46×10^4 (1507 nm) ⁷⁶	1.36×10^4 (1507 nm) ^e
F_5	1.82×10^4 (1507 nm) ⁷⁶	8.23×10^3 (1507 nm) ^e
F_6	1.58×10^4 (1507 nm) ⁷⁶	9.60×10^3 (1507 nm) ^e
^a DMBP	1.10×10^4 (680 nm) ¹¹⁸	1.45×10^4 (680 nm) ¹⁵²
^b TC	1.61×10^4 (830 nm) ^d	3.87×10^4 (830 nm) ^d

^a4,4'-dimethylbiphenyl ^btetracene ^cEstimated in THF, and the details of the estimation are in the section B1 of Appendix B. ^dEstimated in THF with ϵ_a of biphenyl⁻ as reference. The details of the estimations are in the section C1 of Appendix C. ^eEstimated in nitrobenzene, and the details of the estimations for ϵ_c are in section C1 of Appendix C. Uncertainty of ϵ_c is 13%. ^fPersonal communication with Dr. Tomoyasu Mani of Chemistry Department of Brookhaven National Lab.

The recombination of DMBP radical ion in DF is diffusion controlled. From the section 4.3, mean lifetime of fast decay is $\sim 8 \pm 1$ ns in THF for anions with diffusion controlled recombination. DF is more viscous than THF so diffusion controlled recombination may be slightly slower in DF compared with THF. Fitting results of a three exponential function to the kinetic traces of DMBP radical ions in Figure 5.2 show that the mean lifetime of the fast decay is $\sim 9 \pm 1$ ns. This finding suggests that fast decay of DMBP radical ions is diffusion controlled.

To estimate the G_{fi} values, a free-ion indicator is introduced to intercept the free ions. For this indicator, there are two criteria: (1) Low reduction and oxidation potentials (E_{red} and E_{ox}) compared with the target molecule, and (2) Well-separated absorption spectra of radical ions for the indicator. From Table 5.2, redox potentials of tetracene (TC) are well below the redox potentials of other molecules, and the absorption spectra of TC radical ions are well separated from these most of molecules given in Table 5.2. Therefore, TC was used as the indicator to intercept the free ions.

Table 5.2 List of oxidation (E_{ox} vs. SCE) and reduction (E_{red} vs. SCE) potentials, energy of singlet (E_S) and triplet (E_T) excited states and lifetimes of singlet excited states (τ_s).

Name	E_{ox} (V)	E_{red} (V)	$ E_{red}-E_{ox} $ (V)	E_S (eV)	τ_s (ns)	E_T (eV)
F ₁	1.80 ^{150,d}	-2.531 ^{76,f}	4.331	4.08 ⁷⁷	10 ¹⁵³	2.94 ¹⁵⁴
F ₂	1.438 ^{155,e}	-2.238 ^{76,f}	3.676	3.495 ¹⁵⁶	0.79 ¹⁵⁴	2.495 ^c
F ₃	1.328 ^{155,e}	-2.124 ^{76,f}	3.452	3.225 ⁷⁷	0.66 ¹⁵⁴	2.31 ¹⁵⁴
F ₄	1.288 ^{155,e}	-2.074 ^{76,f}	3.362	3.08 ¹⁵⁶	0.58 ¹⁵⁴	2.263 ^c
F ₅	1.238 ^{155,e}	-2.013 ^g	3.251	3.05 ¹⁵⁴	0.549 ¹⁵⁴	2.25 ¹⁵⁴
F ₆	1.258 ^{155,e}	-1.999 ^g	3.257	3.01 ^b	0.520 ¹⁵⁴	2.20 ^b
<i>p</i> -terphenyl	1.78 ⁹²	-2.25 ⁸⁶	4.03	3.95 ¹⁵⁷	1.08 ¹⁵⁸	2.53 ¹⁵⁹
fluoranthene	1.67 ¹⁶⁰	-1.80 ¹⁶⁰	3.47	3.254 ¹⁶¹	53 ¹⁶²	2.29 ¹⁶¹
terthiophene	0.91 ¹⁶³	-2.15 ¹⁶³	3.06	3.05 ¹⁶⁴	0.16 ²⁴	2.70 ¹⁶⁵
^a DMBP	1.56 ¹⁶⁶	-3.04 ¹⁶⁷	4.60	4.33 ¹⁶⁸	16 ¹⁶⁸	2.78 ¹⁶⁹
tetracene	0.72 ¹⁷⁰	-1.57 ⁸⁷	2.29	2.63 ¹⁵³	6.4 ¹⁷¹	1.27 ¹⁷²

^a4,4'-dimethylbiphenyl ^bEstimated by $E_S = 2.80 + 1.23(1/n)$ eV found in this reference,¹⁵⁴ where n is the number of repeat units. ^cEstimated by $E_T = 2.05 + 0.89(1/n)$ eV found in this reference,¹⁵⁴ where n is the number of repeat units. ^d E_{red} vs. $Fc^{+/0}$ in CH_3CN converted into vs. SCE with $Fc^{+/0} = 0.56$ vs. SCE in THF.⁹⁷ ^e E_{ox} vs. $AgNO_3/Ag$ in dichloromethane ($\epsilon_d = 8.93$) with 0.1 M of $TBAPF_6$ and converted into vs. SCE with $Fc^{+/0} = 0.56$ vs. SCE in THF⁹⁷ and $Fc^{+/0} = 0.232$ V vs. $AgNO_3/Ag$.¹⁵⁵ ^f E_{red} vs. $Fc^{+/0}$ in THF and converted into vs. SCE with $Fc^{+/0} = 0.56$ vs. SCE in THF.⁹⁷ ^gMeasured in THF by bimolecular electron transfer equilibria method with a reference, *trans*-stilbene^{0/-} ($ES^{0/-}$) = -2.31 V vs. SCE in dimethylformamide.⁸⁰ $ES^{0/-} - F_5^{0/-} = 123 \pm 13$ meV and $ES^{0/-} - F_6^{0/-} = 137 \pm 11$ meV.

In Figure 5.4, kinetic traces from pulse radiolysis of highly concentrated solutes with 0.5 mM of TC were collected at 830 nm absorption peak of TC radical ions. Most solvated electrons (e_s^-) and DF^{*+} are captured by the highly concentrated solutes, which then completely transfer electrons and holes to TC in $\sim 2 \mu\text{s}$. Any geminate electrons and holes transferring to TC disappear rapidly, leave only free ions. The average growth rate constant is $2.6(\pm 0.8) \times 10^9 \text{ M}^{-1} \text{ s}^{-1}$, which may be a reasonable rate for diffusion-controlled charge transfer reaction for 0.5 mM of TC based on that η of DF is 1.97 cP, for kinetic traces from pulse radiolysis of F_n ($n=1-3$), terthiophene (T_3) and DMBP with TC. A typical geminate, diffusion-controlled ET reaction rate constant in THF ($\eta=0.48 \text{ cP}$) is $\sim 1.2 \times 10^{10} \text{ M}^{-1} \text{ s}^{-1}$. From kinetic trace of fluoranthene (FA) with TC shown in Figure 5.4 (b), the growth is slower than others. This slow growth may be due to slow ET because E_{red} of FA and TC are close. Therefore, the electron transfer rate from $FA^{\cdot-}$ to TC is slow.

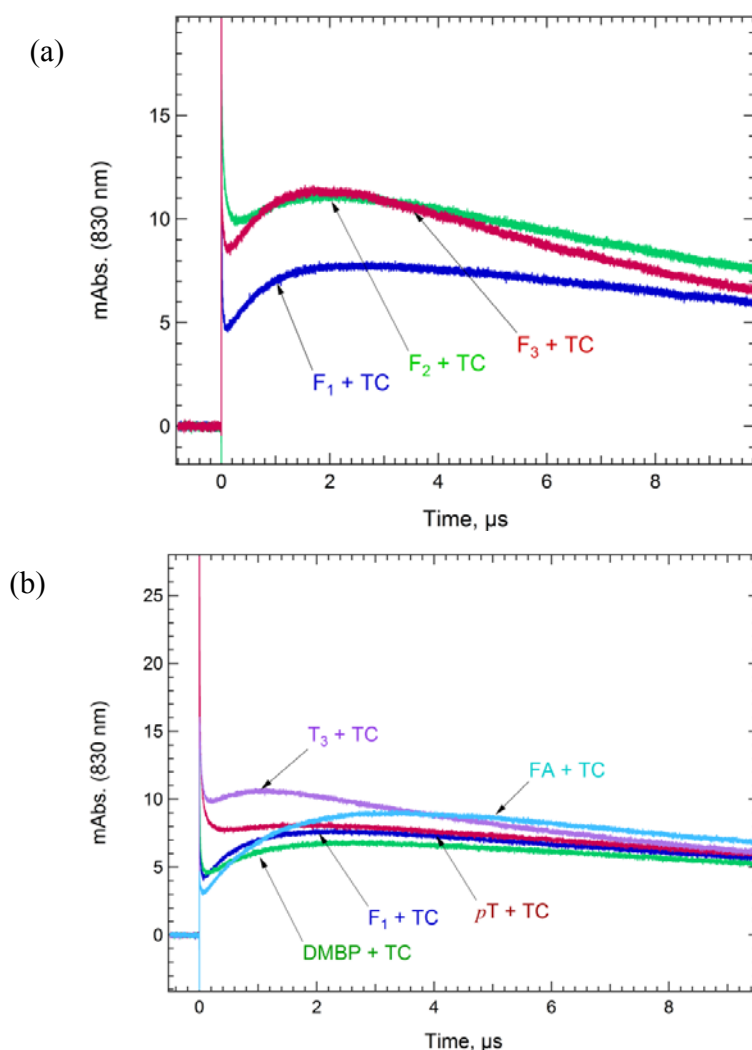


Figure 5.4 Kinetic traces from pulse radiolysis of (a) F_n ($n=1-3$) and (b) F_1 , 4,4'-dimethylbiphenyl (DMBP), *p*-terphenyl (*pT*), terthiophene (T_3) and fluoranthene (FA) at 830 nm in 2,3-dihydrobenzofuran with 0.5 mM of tetracene (TC). The concentrations of F_n ($n=3,4$) are 40 and 30 mM, respectively, and the concentrations of other molecules are 50 mM. The kinetic trace of $F_3 + \text{TC}$ is corrected for absorption of ${}^3F_3^*$ at 830 nm.

After $\sim 2 \mu\text{s}$, the electron and hole transfers are complete so only TC radical ions remain. These remaining ions are clearly free ions, which decay slowly. For $t > 4 \mu\text{s}$, Y_{cs} of F_2 and F_3 are larger than F_1 from Figure 5.4(a), and almost identical absorbance of TC radical ions indicate that the Y_{cs} of F_1 , DMBP and *p*-terphenyl (*p*T) are nearly identical from Figure 5.4(b). In this chapter, Y_{cs} is reported as G value of free ion pairs (G_{fi}) per 100 eV of energy absorbed. The G_{fi} values of F_n ($n=1-6$) and small molecules are given in Table 5.3. The strong absorption of ${}^3F_n^*$ ($n=4-6$) at 830 nm make the free-ion indicator method difficult to estimate the G_{fi} values for F_n ($n=4-6$). An alternative method to estimate the G_{fi} values for F_n ($n=4-6$) is to directly estimate Y_{cs} from kinetic traces of F_n ($n=4-6$) shown Figure 5.3 with ε of F_n ($n=4-6$) ions. In Figure 5.5, a plot of concentrations of F_n ($n=3-6$) radical ion pairs vs. time, shows almost identical decays that suggests almost identical G_{fi} values for F_n ($n=3-6$).

Table 5.3 Geminate Recombination Rates (k_r), Charge Separation Rates (k_{cs}), the Free Ion Pair Yield (G_{fi}), the Type II Free Ion Pair Yield ($G_{\text{fi}}^{\text{II}}$) and the Number of the Atoms (NA).

Name	k_r (s^{-1})	k_{cs} (s^{-1})	${}^eG_{\text{fi}}$	${}^hG_{\text{fi}}^{\text{II}}$	${}^i\text{NA}$
F_1	$2.02(\pm 0.41) \times 10^9$	$< 1.00 \times 10^8$	$0.17(\pm 0.02)$	≤ 0.02	11.1
F_2	$1.08(\pm 0.15) \times 10^7$	$9.73(\pm 1.36) \times 10^6$	$0.25(\pm 0.02)$	0.10	21.5
F_3	$8.10(\pm 0.58) \times 10^6$	$8.77(\pm 0.66) \times 10^6$	$0.27(\pm 0.02)$	0.12	32.0
F_4	$9.65(\pm 0.65) \times 10^6$	$9.66(\pm 0.57) \times 10^6$	$0.27(\pm 0.02)^g$	0.12	42.4
F_5	$6.34(\pm 0.15) \times 10^6$	$7.56(\pm 0.43) \times 10^6$	$0.27(\pm 0.02)^g$	0.12	53.1
F_6	$5.89(\pm 0.17) \times 10^6$	$7.95(\pm 0.39) \times 10^6$	$0.27(\pm 0.02)^g$	0.12	63.5
${}^a\text{DMBP}$	$> 5.00 \times 10^9$	$< 1.00 \times 10^8$	$0.15(\pm 0.01)$	≤ 0.02	9.6
${}^b\text{pT}$	$2.31(\pm 0.22) \times 10^8$	$2.82(\pm 1.31) \times 10^7$	$0.17(\pm 0.02)$	≤ 0.02	11.2
${}^c\text{T}_3$	$2.17(\pm 0.18) \times 10^7$	$1.33(\pm 0.19) \times 10^7$	$0.22(\pm 0.02)$	0.05	7.6
${}^d\text{FA}$	$2.11(\pm 0.20) \times 10^7$	$1.37(\pm 0.34) \times 10^7$	$0.22(\pm 0.02)$	0.05	6.9

a 4,4'-dimethylbiphenyl b *p*-terphenyl c terthiophene d fluoranthene e tetracene f The unit is number of free ion pairs per 100 eV of energy absorbed, and $G_{\text{fi}} = G_{\text{fi}}^{\text{I}} + G_{\text{fi}}^{\text{II}}$. g From Figure 5.5, the G_{fi} values of F_n ($n=3-6$) are almost identical (see text). h The $G_{\text{fi}}^{\text{II}}$ values is estimated by $G_{\text{fi}}^{\text{II}} = G_{\text{fi}} - G_{\text{fi}}^{\text{I}}$ where G_{fi} and $G_{\text{fi}}^{\text{I}} = 0.15$ per 100 eV are estimated by the free-ion indicator. i The Number of the Atoms is used to represent charge density of ions (see text).

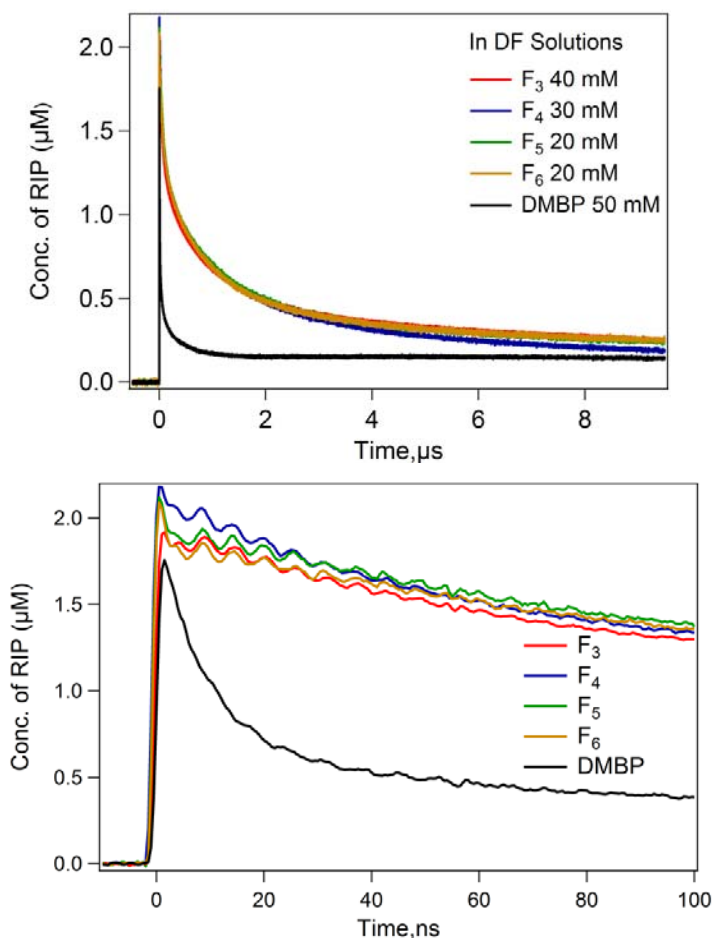


Figure 5.5 Based on kinetic traces from pulse radiolysis of F_n ($n=3-6$) shown in Figure 5.3 and 4,4'-dimethylbiphenyl (DMBP) shown in Figure 5.2(b), plots of concentrations of F_n ($n=3-6$) and DMBP radical ion pairs (RIP) vs. time at (a) longer and (b) early time. The concentrations of F_n ($n=3-6$) in 2,3-dihydrobenzofuran solutions are 40, 30, 20 and 20 mM, respectively. The concentrations of F_n ($n=3-6$) ion pairs are estimated by the extinction coefficients of F_n ($n=3-6$) and DMBP radical ions given in Table 5.1 with path length 5 mm. Uncertainty for the concentration of RIP is $\sim 13\%$.

Kinetic traces of DMBP radical ions and triplet excited states of DMBP (${}^3\text{DMBP}^*$) shown in Figure 5.6 were collected in DF solution with different concentrations of DMBP. Kinetic traces of ${}^3\text{DMBP}^*$ at 390 nm shown in Figure 5.6(b) are corrected because DMBP radical ions also absorb at 390 nm. To form ${}^3\text{DMBP}^*$, there are two possible mechanisms, ion recombination of DMBP radical ions (reaction 5.4) and triplet excited energy transfer from DF to DMBP (reaction 5.6b). The rate of the former reaction is independent of the concentration of DMBP and the latter reaction is concentration dependent. Regardless of the concentration of DMBP, the mean lifetimes for fast decay of DMBP radical ions and fast growth of ${}^3\text{DMBP}^*$ are $\sim 9 \pm 1$ ns. This

finding suggests that growths of ${}^3\text{DMBP}^*$ absorption are due to ${}^3\text{DMBP}^*$ generated from the ion recombination.

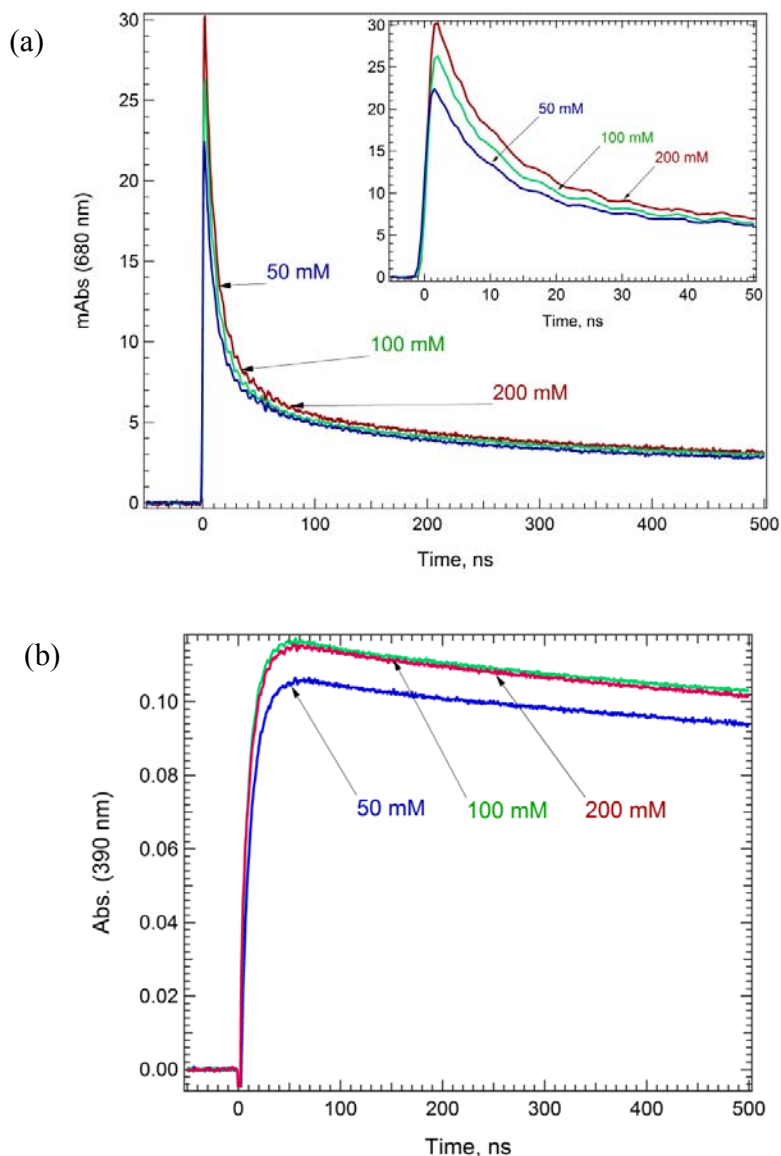


Figure 5.6 (a) Kinetic traces from pulse radiolysis of (a) 4,4'-dimethylbiphenyl (DMBP) radical ions at 680 nm (b) triplet excited states of DMBP (${}^3\text{DMBP}^*$) at 390 nm in 2,3-dihydrobenzofuran (DF) with different concentrations of DMBP. The insert of Figure 5.6(a) shows the kinetic traces of DMBP radical ions at early time. The kinetic traces of ${}^3\text{DMBP}^*$ are corrected for absorption of DMBP radical ions at 390 nm.

From Figure 5.6, the yield is 0.98 ± 0.02 for geminate RIP of DMBP recombining with each other to generate ${}^3\text{DMBP}^*$. Details of estimation for this yield are in section C2 of Appendix C. This finding suggests that potential energy of RIP for DMBP is below the energy of singlet excited state of DMBP. The number of geminate RIP of DMBP and ${}^3\text{DMBP}^*$ generated from geminate

ion recombination are estimated from data shown in Figure 5.6 by a three exponential function with ϵ of ${}^3\text{DMBP}^*$, $3.42 \times 10^4 \text{ M}^{-1}\text{cm}^{-1}$ at 390 nm ¹⁷³ and ϵ of DMBP radical ions given in Table 5.1.

Photoexcitation was also applied to study geminate ion recombination. Kinetic traces from 397 nm photolysis of F_3 radical ions at 1500 nm are shown in Figure 5.7 (a), and that of ${}^3\text{F}_3^*$ at 640 nm are shown in Figure 5.7 (b). In Figure 5.7, F_3 is excited by a 397 nm , 100 ps laser pulse, in THF with different concentrations of F_3 . Due to the small extinction coefficient (ϵ) of F_3 at 397 nm , $1.2 \times 10^3 \text{ M}^{-1}\text{cm}^{-1}$,⁷⁶ ${}^1\text{F}_3^*$ are uniformly created across the cell by using 397 nm light as the excitation. There is significant absorption of F_3 ions in 20 and 40 mM solutions and little absorption of F_3 ions in 5 and 10 mM solutions. The mechanism of forming F_3 radical ions is that F_3 and ${}^1\text{F}_3^*$ diffuse together, and then an electron transfer from ${}^1\text{F}_3^*$ to F_3 occurs to create a F_3 radical ion pair. For F_3 ion pairs created by photoexcitation, the escape probability is ~ 0.18 in THF, as determined by a three exponential function from data. Most geminate F_3 ion pairs created by photoexcitation is CRIP. These fitting results are in Table C1 of Appendix C. For ${}^1\text{F}_3^*$, the bimolecular quenching rate constant (k_q) measured in the current study is $1.60(\pm 0.53) \times 10^9 \text{ M}^{-1}\text{s}^{-1}$ in THF with F_3 as quencher. Lifetime of ${}^1\text{F}_3^*$ is short, 663 ps ,¹⁵⁴ therefore low concentration F_3 solutions such as 5 and 10 mM solutions a little or no F_3 ions may be form before ${}^1\text{F}_3^*$ decaying to the ground state. Because ${}^1\text{F}_3^*$ also absorbs light at 640 nm , the fast decay of the kinetic traces at 640 nm is due to relaxation of ${}^1\text{F}_3^*$. This fast relaxation also suggests that slow growths are not due to intersystem crossing. Therefore, slow growths of kinetic traces at 640 nm suggest that ${}^3\text{F}_3^*$ is likely produced from recombination of free F_3 ions.

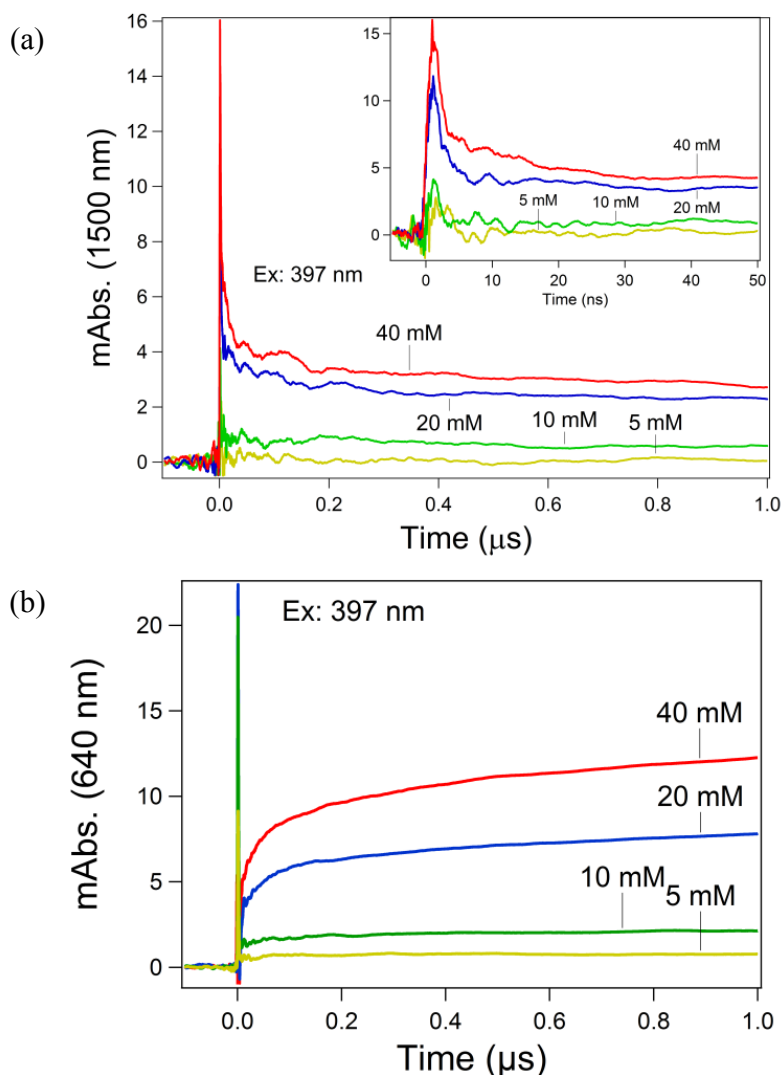


Figure 5.7 Kinetic traces from 397 nm photolysis of (a) F_3 ions ($F_3^{\cdot-}$ and $F_3^{\cdot+}$) at 1500 nm and (b) ${}^3F_3^*$ at 640 nm where the path lengths are 0.5 mm with different concentrations of F_3 in THF. The insert of (a) shows the decays of F_3 ions at early time. Formation of F_3 ions is due to electron transfer from ${}^1F_3^*$, excited by 397 nm light, to F_3 . At 640 nm, the instant absorption is due to the intersystem crossing and ${}^1F_3^*$, and the slow growth of absorption is due to the recombination of F_3 ions.

Figure 5.8 shows kinetic traces from pulse radiolysis of F_n ($n=1-6$) at wavelengths mainly absorbed by triplet excited states of oligofluorenes (${}^3F_n^*$, $n=1-6$). For F_1 , the growth corresponding to the decay of F_1 radical ions shown in Figure 5.3 suggests that a part of ${}^3F_1^*$ is generated by ion recombination of F_1 ions. Because absorption bands of F_2 radical ions and ${}^3F_2^*$ are well overlapped, it is difficult to tell whether F_2 ion recombination generates ${}^3F_2^*$ or not. For F_n ($n=3-6$), no obvious growth corresponding to the decays of F_n ($n=3-6$) ions seen in Figure 5.3

that suggests no triplet excited states are produced from the ion recombination in pulse radiolysis experiments. The fast growth rates of ${}^3F_n^*$ ($n=2-6$) show concentration dependence suggesting that kinetic traces are due to energy transfer from ${}^3DF^*$, (reaction 5.6b), with an average rate constant, $3.72(\pm 0.75)\times 10^9 \text{ M}^{-1}\text{s}^{-1}$. The growth rates are given in Table 5.4 and determined by a two exponential function for accounting growth and decay of triplet excited states from data over the time period from 2 ns to 1 μs .

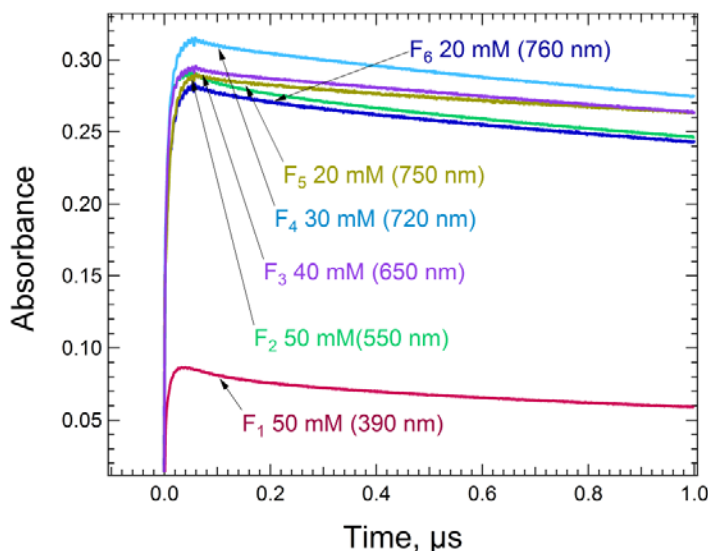


Figure 5.8 Kinetic traces from pulse radiolysis of F_n ($n=1-6$) triplet excited states, ${}^3F_n^*$ ($n=1-6$), at their maximum absorption wavelengths in 2,3-dihydrobenzofuran. The concentrations of F_n ($n=1-6$) are 50,50,40,30,20 and 20 mM, respectively.

Table 5.4 Growth Rate Constants of Triplet Excited States (k_g) and Decay Rates of Singlet Excited States (k_d) for F_n ($n=1-6$)

Name (Conc.)	${}^a k_g (\text{M}^{-1}\text{s}^{-1})$	${}^b k_d (\text{s}^{-1}) / \tau_f (\text{ns})$
F ₁ (50 mM)	2.40×10^9	$1.31 \times 10^8 / 7.63$
F ₂ (50 mM)	2.78×10^9	$5.70 \times 10^8 / 1.76$
F ₃ (40 mM)	3.20×10^9	$7.32 \times 10^8 / 1.38$
F ₄ (30 mM)	3.43×10^9	$7.01 \times 10^8 / 1.42$
F ₅ (20 mM)	4.31×10^9	$7.28 \times 10^8 / 1.37$
F ₆ (20 mM)	4.55×10^9	$7.64 \times 10^8 / 1.31$

^aDetermined by three exponential function, $A_0 + A_1 \exp(-k_g t) + A_2 \exp(-k_2 t)$, from kinetic traces from pulse radiolysis shown in Figure 5.8. A_i ($i=0-2$) are absorbance for exponential decays and t is time. ^bDetermined by a single exponential function from kinetic traces from pulse radiolysis shown in Figure 5.9.

For $F_n(n=1-6)$, the absorption spectra of singlet and triplet excited states are well overlapped. Instead of observing absorption for singlet excited states, observing fluorescence is an alternative way to study them. Figure 5.9 shows no sign of delayed fluorescence corresponding to the ion recombination of $F_n(n=1-6)$ radical ions shown in Figure 5.3. The fluorescence lifetimes were determined by single exponential fitting and given in Table 5.4.

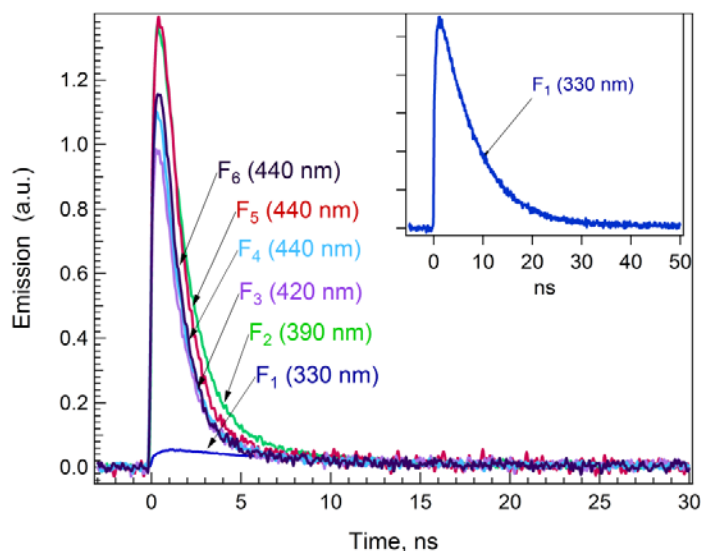


Figure 5.9 Transient emission from pulse radiolysis of $F_n(n=1-6)$ at their maximum emission intensity wavelengths in 2,3-dihydrobenzofuran. The concentrations of $F_n(n=1-6)$ are 50, 50, 40, 30, 20 and 20 mM, respectively. The insert shows the transient emission of F_1 .

5.4 Discussion

From our observations, there are four major findings: (1) For $F_n(n=1-6)$, G_{fi} increases with increasing the number of the repeat units (n) in DF from the pulse radiolysis data. (2) k_r of $F_n(n=1-6)$ decrease with increasing n in DF from the pulse radiolysis data. (3) There are triplet excited states generate by CR in THF from the photoexcitation data. (4) Little or no triplet and singlet excited states generated by CR in DF from the pulse radiolysis data. The first finding is related to the CRIP-SSRIP picture with the correction and the electron transfer (ET) theory.³¹⁻³³ The recombination of RIP generating excited states or not is related to potential energy of RIP. The following discussion will introduce the kinetics of the CS processes and discuss the influence of charge density in ET and potential energy of RIP in reference of free ions.

5.4.1 Kinetic Analysis

Based on the reports of Arnold,¹⁴⁶ Koch¹⁴⁵ and Zhong,¹² a scheme of CS processes is illustrated in Scheme 5.1, and a potential energy diagram for the photoinduced electron transfer (PET) system is illustrated in Figure 5.10 (a). Scheme 5.1 proposes two things: (1) The CRIP acts as a

trap and (2) CS states are produced from SSRIP. Transformation from CRIP to SSRIP is described by solvation rate constant (k_{solv}) or equilibrium constant between CRIP and SSRIP ($K_{\text{solv}}=k_{\text{solv}}/k_{-\text{solv}}$). The CS is described by CS rate constant (k_{cs}) or dissociation rate constant ($k_{\text{diss}}=K_{\text{eq}}k_{\text{cs}}$) for IRIP comprising of CRIP and SSRIP. Experimental results have shown that Y_{cs} , k_{solv} , K_{solv} and k_{diss} increase with increasing dielectric constant.

Scheme 5.1 Kinetics of charge separation (CS) processes, where CRIP is contact radical ion pair and SSRIP is solvent separated radical ion pairs, k_{ET} is electron transfer (ET) rate constant, $k_{-\text{ET}}$ is reversed ET rate constants, k_{solv} is solvation rate constant, $k_{-\text{solv}}$ is reversed solvation rate constants, k_{cs} is CS rate constant, k_{diss} is dissociation rate constant ($k_{\text{diss}}=K_{\text{solv}}k_{\text{cs}}$), K_{solv} is equilibrium constant between CRIP and SSRIP ($K_{\text{solv}}=k_{\text{solv}}/k_{-\text{solv}}$ or $[\text{SSRIP}]/[\text{CRIP}]$), which is reciprocal to K_{eq} from Scheme 4.1, k_{r} is the recombination rate constant of ions. k_{LET} is long range ET rate constant and $k_{-\text{LET}}$ is reversed long range ET rate constants.

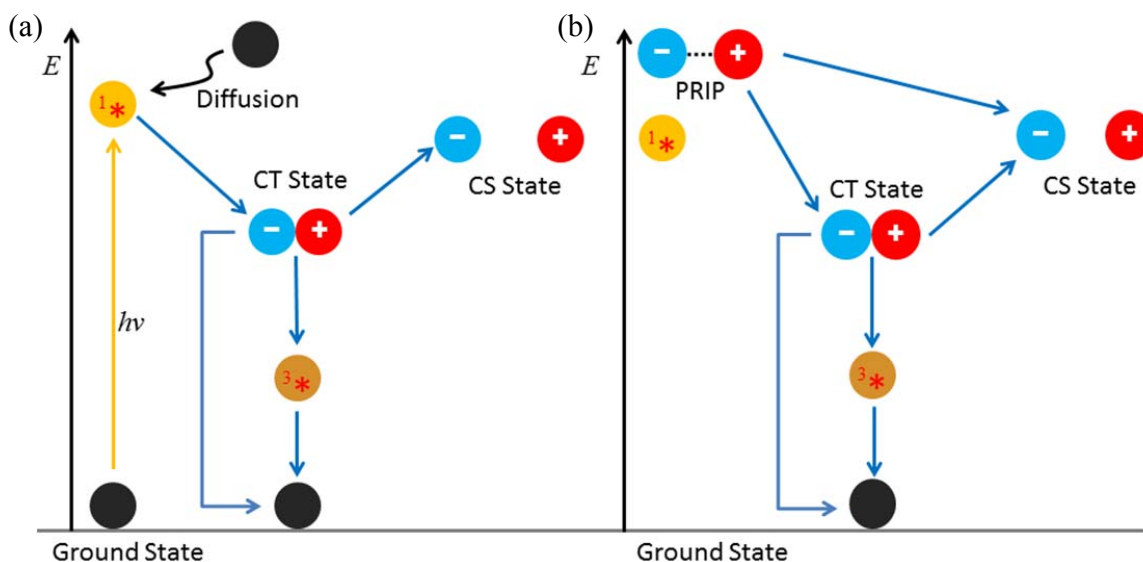
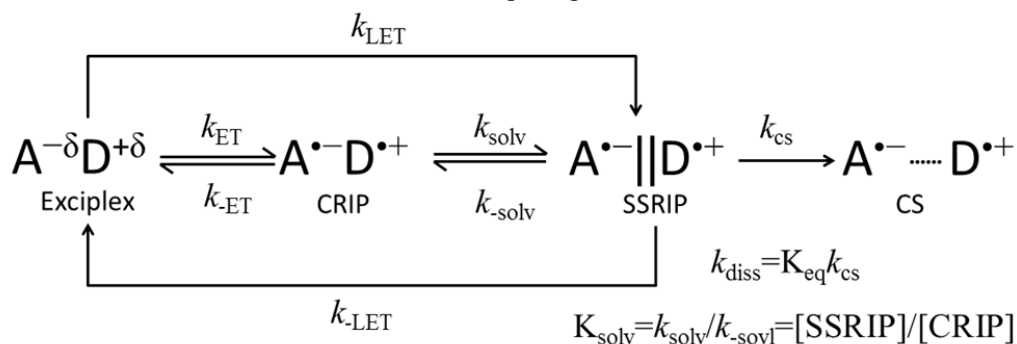
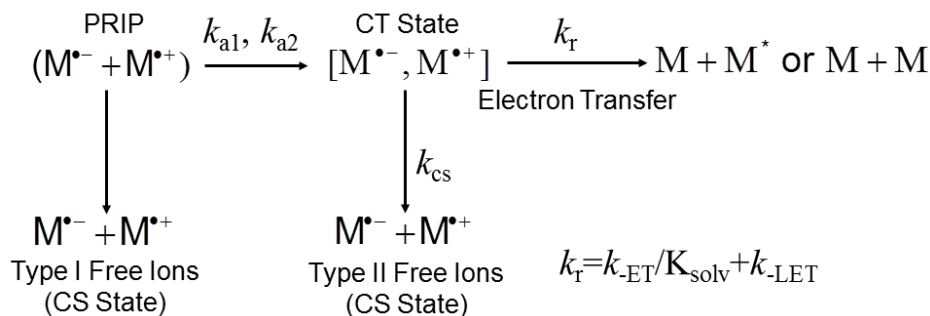


Figure 5.10 The free energy (E) diagrams of charge separation processes for ion pairs created by (a) photoexcitation and (b) pulse radiolysis. CS is charge separation and CT is charge transfer states. PRIP is the primary radical ion pair created by pulse radiolysis. The CT states comprise of contact and solvent separated radical ion pairs.

For pulse radiolysis data, a fitting procedure was developed to extract the geminate recombination rate constant (k_r) and charge separation rate (k_{cs}) based on Scheme 5.2. The potential energy diagram for pulse radiolysis is illustrated in Figure 5.10(b). Based on Scheme 5.1, kinetics of geminate CR for pulse radiolysis is proposed and shown in Scheme 5.2. The primary radical ion pair (PRIP) were created by the electron pulse. From the findings of Chapter 4, PRIP usually escape from each other to become the Type I free ions for PRIP with $r > r_c$. Under influence of the mutual Coulomb attraction, PRIP diffuses together to become CT state, which are comprised of SSRIP and CRIP. The association of PRIP can be described by two exponential function based on the findings in section 4.5.1 of Chapter 4. After CT state forms, the anion recombines with cation via ET reaction with a rate k_r , which is $k_{-ET}/K_{solv} + k_{-LET}$ from Scheme 5.1. In the CT state, the anion and cation may escape from each other to become the Type II free ions. By the definition of CS, the Type I and II free ions are CS state. The decays of Type I and II free ions are described by homogenous recombination rate (k_h), which is not included in Scheme 5.2.

Scheme 5.2 Kinetics of geminate recombination for ions created by pulse radiolysis. PRIP is primary radical ion pairs, CT state is charge transfer state, which consists of solvent separated and contact radical ion pairs, and CS state is charge separated state. k_{a1} and k_{a2} are association rate constants, k_r is geminate recombination rate constant and k_{cs} is the charge separation rate constant.



The fitting procedure extracts k_r and k_{cs} from the data, over the time period from 2 ns to 1 μ s, with F_h^I , k_{a1} and k_{a2} held fixed. The relation between k_r , F_h^II and k_{cs} is

$$F_h^{II} = \frac{k_{cs}}{k_{cs} + k_r} (1 - F_h^I) \quad (5.7),$$

where F_h^I is fraction of the Type I free ions and F_h^{II} is fraction of the Type II free ions. The $F_h^I=0.19$, $k_{a1}=1.16 \times 10^8 \text{ s}^{-1}$ and $k_{a2}=1.61 \times 10^7 \text{ s}^{-1}$ for diffusion controlled recombination were determined by the fitting procedure from data of DMBP shown in Figure 5.2. The fractions for k_{a1} and k_{a2} are 0.64 and 0.17, respectively. By holding F_h^I , k_{a1} and k_{a2} fixed, the lower limits of k_r for DMBP radical ions were found to be $5.0 \times 10^9 \text{ s}^{-1}$. The k_r , k_{cs} and the G_{fi} values of F_n ($n=1-6$) and other small molecules are given in Table 5.3, where $G_{fi}=G_{fi}^I+G_{fi}^{II}$. Because there are almost no Type II free ions forming for ions with diffusion controlled recombination, the G_{fi} values for the Type I free ions is $G_{fi}^I=0.15 \pm 0.02$ per 100 eV in DF, estimated by using TC as a free-ion

indicator from data of DMBP. The G_{fi}^{II} values of $F_n(n=1-6)$ and other small molecules determined by the free-ion indicator are given in Table 5.3.

5.4.2 Influence of the Low Charge Density

Figure 5.11 shows that the free ion yield increases with decreasing charge density. The ion's charge density is represented by the number of the atoms (NA) that contain 80% of the negative charge using Mulliken¹⁰³ charges with hydrogens summed into heavy atoms computed by B3LYP/6-31G(d) in vacuum with the assumption that the charge densities of the anion and the cation are identical. The NA's of $F_n(n=1-6)$ and other small molecules are given in Table 5.3. In Table 5.3, the G_{fi}^{II} values increase with increasing n for $F_n(n=1-3)$ ion pairs, and there is little or no difference of G_{fi}^{II} values for $F_n(n>3)$ ion pairs. No obvious difference in G_{fi}^{II} value between $F_n(n=3-6)$ ion pairs may be due to that the polaron delocalization length in oligofluorenes is 4.3 repeat units⁷⁶ resulting in little or no difference of Coulomb interaction in between $F_n(n=3-6)$ ion pairs. These findings suggest that the enhancement of the free ion yield by charge delocalization leads is due to the weak Coulomb interaction that lets more easily ion escape from the opposite ions to become the free ion.

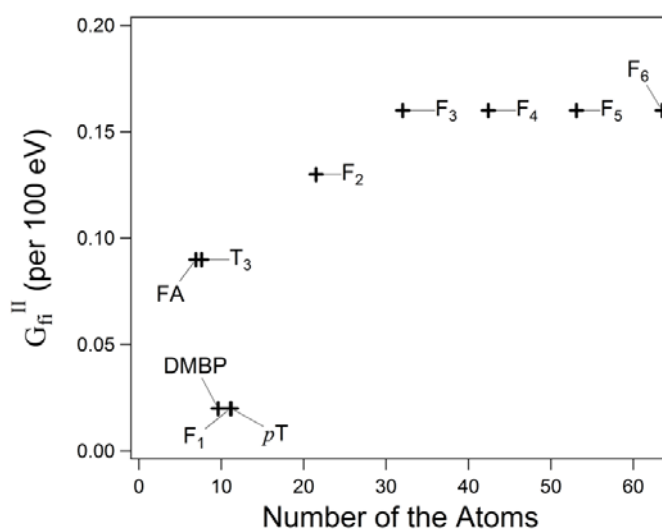


Figure 5.11 A plot of the Type II Free Ion Pair Yield (G_{fi}^{II}) vs. the Number of the Atoms (NA). Relation between charge density and NA is reciprocal.

This thesis also finds that the ion escape probability ($F_{esc}=[Fi^{II}]/[IRIP]$) from photoexcitation of F_3 ion pairs in THF is 0.18 ± 0.02 . Here $[Fi^{II}]$ is the concentration of the Type II free ions, and $[IRIP]$ is the concentration of the IRIPs. Because the ET probability exponentially decreases with increasing distance, formation of the ions by photoexcitation requires that the excited and neutral molecules are close to each other, possibly in contact. Therefore, the ion pairs created by photoexcitation are expected to be CRIPs. The only free ions created by photoexcitation are

Type II. For the ion pairs consisting of 9,10-dicyanoanthracene anions ($\text{DCA}^{\bullet-}$) and hexaethylbenzene cations ($\text{HEB}^{\bullet+}$) created by photoexcitation in THF, Zhou² found that the F_{esc} was 0.06. Charge densities of these ions are higher than those of F_3 ions. The NA's of $\text{DCA}^{\bullet-}$ and $\text{HEB}^{\bullet+}$ are 3.7 and 4.8. The difference of the F_{esc} between this thesis and report of Zhou² strongly suggests that the weak Coulomb interaction caused by low charge density significantly increase the escape probability of the ion.

Based on the observation¹² that the free ions mainly produced from SSRIP in low dielectric constant solvent such as THF, the high population of SSRIPs can increase the free ion yield in low dielectric constant solvent. The SSRIP arises because the ion-dipole interactions between the ions and the solvent molecules with the permanent dipole moments to solvate the ions separately. THF and DF have permanent dipole moments so some IRIPs are CRIPs and other IRIPs are SSRIPs. The equilibrium constant ($K_{\text{solv}} = [\text{SSRIP}]/[\text{CRIP}]$ in Scheme 5.1) between CRIP and SSRIP is determined by the competition between the ion-dipole and Coulomb interactions. The K_{solv} increases with increasing the dipole moment and decreasing the charge density. The r of SSRIP is longer than that of CRIP so the Coulomb interaction in SSRIP is weaker compared with that in CRIP. Therefore, escape probability of ion in SSRIP is higher than that in CRIP. Based on the ET theory (the Marcus theory),³³ the ET rate decreases with increasing r . Therefore, the ET theory predicts that the lifetime of SSRIP is longer than that of CRIP. The ion escape probability of SSRIP is also increased by this long lifetime of SSRIP.

5.4.3 Transformation between CRIP and SSRIP

The F_{esc} from pulse radiolysis and photoexcitation of F_3 ions are different. $[\text{Fi}^{\text{II}}]$ from pulse radiolysis is determined from the different of the free ion concentrations between the diffusion controlled and non-diffusion controlled data shown in Figure 5.5. Because recombination of IRIP is geminate, $[\text{IRIP}]$ from pulse radiolysis is determined from the geminate decay of the diffusion controlled data. The decay of DMBP ion pairs is diffusion controlled, so $[\text{IRIP}]$ from pulse radiolysis determined by a two exponential function from the data is $0.40 \pm 0.18 \mu\text{M}$. The decay of F_3 ion pairs is non-diffusion controlled, so $[\text{Fi}^{\text{II}}]$ from pulse radiolysis determined by a two exponential function from the data is $0.73 \pm 0.09 \mu\text{M}$. Despite of lower ϵ_d of DF compared with THF, the F_{esc} from pulse radiolysis of F_3 ion pairs are 0.52 ± 0.07 in DF which is greater than $F_{\text{esc}} = 0.18 \pm 0.02$ from photoexcitation in THF. Based on the F_{esc} from pulse radiolysis of F_3 ion pairs, the $G_{\text{fi}^{\text{II}}}$ value of F_3 ion pairs is 0.12 per 100 eV, and the G value of F_3 IRIPs is 0.23 per 100 eV. The $[\text{Fi}^{\text{II}}]$ and $[\text{IRIP}]$ from photoexcitation are the free ions concentration and the total concentration of the ions determined by a three exponential function from the data. The fitting results of a three exponential function are given in Table C1 of the Appendix C. For different concentrations of F_3 solutions in THF, the quantum yields of free ions and IRIPs from photoexcitation are given in Table C2 of Appendix C.

Regardless of similar charge density, the F_{esc} from pulse radiolysis and photoexcitation of F_3 ion pairs are different. If the observation¹² that no transformation occurs between CRIP and SSRIP applies to the F_3 ion pairs studied here, this finding signals two things: (1) The transformation from SSRIP to CRIP may be slow. (2) The separation distance distributions of ion pairs from pulse radiolysis and photoexcitation are different. Zhong¹² observed the CRIPs with an average lifetime 48 ns in 1,2-dichloroethane ($\epsilon_d=10.36$) and concluded that no transformation occurred between CRIP and SSRIP over time period 0-100 ns. This conclusion is based on the assumption that the SSRIPs created by photoexcitation in low dielectric constant solvent are mainly due to the long range ET step illustrated in Scheme 5.1. From photoexcitation data in Figure 5.7(a), the average lifetime of F_3 IRIPs in THF is 2 ± 1 ns. From pulse radiolysis data in Figure 5.3, the average lifetime of F_3 IRIPs in DF is 123 ± 7 ns. If the above assumption and the observation² that the free ions are mainly produced from the SSRIPs apply to the present experiments on F_3 then the transformation rate from SSRIP to CRIP in low dielectric constant solvents such as THF and DF is less than $5.0\times 10^6 \text{ s}^{-1}$. Pulse radiolysis creates the ion pairs with large separation distances that become SSRIPs. Photoexcitation mainly creates CRIPs. If the transformation from SSRIP to CRIP is slow then regardless of charge density, free ion yield from pulse radiolysis are greater than that from photoexcitation.

5.4.4 Influence of Charge Density in Electron Transfer Reaction

From Table 5.3, k_r decreases with increasing n . The charge density as reflected in NA decreases with increasing n from Table 5.3. This finding suggests that charge density influences rate of ET reaction. Based on Scheme 5.1, recombination rates of ions in CRIP and SSRIP are related to r . Based on the Marcus theory³⁰ (classical ET theory), formalism of general ET rate (k_{GET}) is:

$$k_{\text{GET}} = \frac{2\pi}{\hbar} V(r) \exp\left[-\frac{(\Delta G^0 + \lambda_s)^2}{4\lambda_s k_B T}\right] \quad (5.8),$$

where $V(r)$ is the electronic coupling term (eq. 2.3.3), λ_s is the solvent reorganization energy and ΔG^0 is the standard free energy change of ET reaction, which may be referred to as charge recombination energy (Δ_{CR}) of ET reaction. The element of electronic coupling matrix $V(R_0)$ is related to the size of the ions. Large ions, which have more complex molecular orbitals compared with small ions, result in lower orbital overlap, and hence have smaller values of V_0 .¹⁴⁰ Gould⁷ reported that k_{ET} decreased with increasing size of D_e (1-3 benzene ring structures) for 9,10-dicyanoanthracene as A_e . With dielectric continuum model, λ_s is:

$$\lambda_s = \frac{q^2}{4\pi\epsilon_0} \left(\frac{1}{d_A} + \frac{1}{d_D} - \frac{1}{r} \right) \left(\frac{1}{n^2} - \frac{1}{\epsilon_d} \right) \quad (5.9),$$

where d_A is the diameter of A_e , d_D is the diameter of D_e , n is refractive index and ϵ_d is the dielectric constant.³³ Δ_{CR} is estimated by:

$$\Delta_{CR} = E_{red}^A - E_{ox}^D - \frac{1}{4\pi\epsilon_0\epsilon_d} \iint d\mathbf{v}_a d\mathbf{v}_b \frac{\rho_a \rho_d}{\gamma^2} \bar{\gamma} - E_p \quad (5.10),$$

where E_{red}^A is the reduction potential of A_e , E_{ox}^D is the oxidation potential of D_e , ρ_a is the charge density of A_e , ρ_d is the charge density of D_e , \mathbf{v}_a is the volume of A_e and \mathbf{v}_b is the volume of D_e , γ is the distance illustrated in Figure 5.12 and E_p is the energy of product state. The possible product states of the ET reaction are singlet or triplet excited states and the ground state. For RIP consisting of high charge density ions such as 1,2,4,5-tetracyanobenzene (TCB) as A and *p*-xylene (*p*Xy) as D_e , the solvation energies of CRIP and SSRIP also affect Δ_{CR} .¹⁴⁶ Chemical structures of TCB and *p*Xy are given in Appendix A. In DF, this solvation energy difference between CRIP and SSRIP are ~ 150 meV in DF ($\epsilon_d=4.33$) and ~ 60 meV in THF ($\epsilon_d=7.58$). These energy differences are estimated by solvation energy terms of the empirical equations, $\Delta_{CRIP}=0.56 \text{ eV}(1/\epsilon_d)+0.003 \text{ eV}$ and $\Delta_{SSRIP}=1.52 \text{ eV}(1/\epsilon_d)-0.064 \text{ eV}$, which are from eq. (4) and (5) found in this reference.¹⁴⁶ Δ_{CRIP} and Δ_{SSRIP} are the solvation energies of CRIP and SSRIP, respectively. Solvation energy decreases with decreasing size of the molecule from the Onsager model¹⁷⁴ for CRIP and the Born model¹⁷⁵ for SSRIP. For ions in which charges are well delocalized over the whole molecule, the charge density of the ion is reciprocal to the size of molecule. In this chapter, RIPs usually consists of low charge density ions compared with *p*Xy and TCB. Therefore, the influence of solvation energy difference between CRIP and SSRIP in Δ_{CR} is negligible.

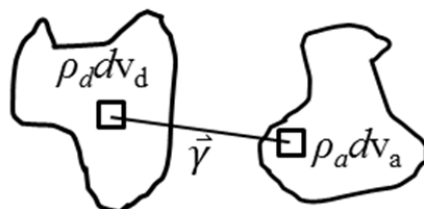


Figure 5.12 Schematic diagram for calculating Coulomb potential energy between two irregular charged objects. ρ_a is charge density of the acceptor and ρ_d is charge density of the donor. \mathbf{v}_a is volume of the acceptor and \mathbf{v}_d is the volume of the donor.

From Figure 5.13, k_r of $F_n(n=1-3)$ ion pairs decrease with increasing NA's. This finding supports the prediction of the Marcus theory that ET rate of SSRIP is smaller than that of CRIP. Low charge density ion prefers to pair with the opposite-ion as SSRIP based on the CRIP-SSRIP picture with the correction from section 4.5.4 of Chapter 4. For $F_n(n=4-6)$ ion pairs, k_r slightly decreases with increasing NA's, which supports the statement from the above section (section 5.4.2) that populations of SSRIPs are almost identical for $F_n(n=3-6)$ ion pairs.

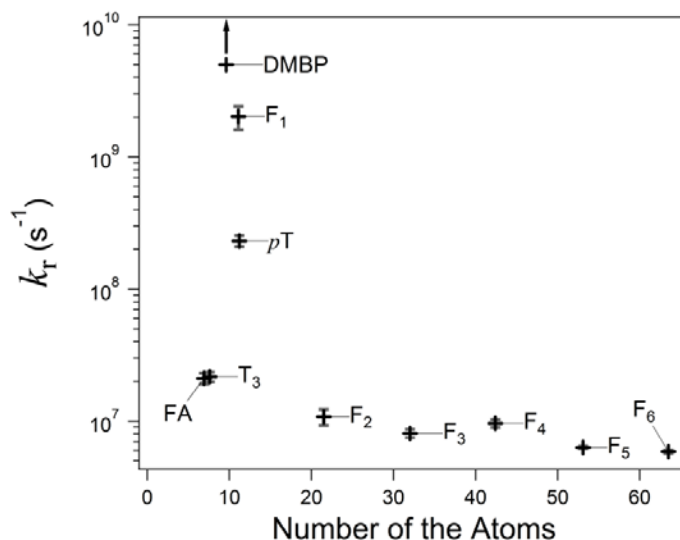


Figure 5.13 A plot of geminate recombination rate (k_r) vs. the Number of the Atoms (NA). Relation between charge density and NA is reciprocal. The up arrow means the lower limit.

From Figure 5.13, terthiophene (T₃) and fluoranthene (FA) ion pairs are smaller than DMBP ion pairs in k_r even through that charge densities of T₃ and FA ions are higher than that of DMBP ions. This finding may be due to small $V(R_0)$ of eq. 2.3.5 for T₃ and FA ion pairs because molecular orbitals of T₃ and FA ions are more complex than that of DMBP ions. Therefore, the lifetimes of T₃ and FA ion pairs are longer than that of DMBP ion pairs. The Type II free ion pair yield possibly increases due to increase lifetime of RIP therefore G_{fi}^{II} of T₃ and FA ion pairs are greater than that of DMBP ion pairs.

Kinetic trace from pulse radiolysis of F₃ ion pairs shown in Figure 5.3 much slower decays compared with that from photoexcitation shown in Figure 5.7(a) at early time. Based on Scheme 5.1, geminate RIPs created by photoexcitation are mainly CRIP. IRIPs created by pulse radiolysis comprise of CRIP and SSRIP. The Marcus theory³³ proposes that rate of ET reaction is faster in CRIP compared with SSRIP. Our findings from Figure 5.3 and 5.7(a) suggest that IRIPs of F₃ created by pulse radiolysis are mainly SSRIP and agree with the above predication of the Marcus theory.

5.4.5 Potential Energy of RIP

The data from photoexcitation of F₃ in Figure 5.7 shown two results: (1) Photoexcitation successfully created F₃ radical ions in THF. (2) $^3F_3^*$ were generated from homogenous recombination of F₃ ion pairs. These findings suggest that the potential energy of the CT state is above the free energy of the triplet excited states (E_T) and below the free energy of the singlet excited states (E_S). The above results also agree with the free energy diagram illustrated in Figure 5.10(a) for photoexcitation. The free energy of RIP can be estimated by eq. (5.10) with

$E_p=0$ eV, $r=0.3$ and 0.7 nm for CRIP and SSRIP, respectively.¹⁰ For the free energy of free ions (E_{FI}), r is usually assumed to be infinite¹⁰ so $E_{FI}=|E_{red}-E_{ox}|$. The relation of the free energies between free ions and RIP is $E_{FI}>E_{SSRIP}>E_{CRIP}$ because the Coulomb potential energies of RIP increase with increasing r . E_{SSRIP} and E_{CRIP} are the free energies of SSRIP and CRIP, respectively. For $F_n(n=1-6)$, the Coulomb potential energies estimated by eq. (5.4) are given in Table 5.5 with face-to-face $F_n(n=1-6)$ ion pairs. An example for face-to-face F_2 ion pair is in Figure C1 of Appendix C. From Table 5.2 and 5.5, both E_{CRIP} and E_{SSRIP} are lower than E_S given in Table 5.2 for $F_n(n=1-6)$ ion pairs in THF.

Table 5.5 The Coulomb potential energies of CRIP and SSRIP relative to that of free ions for $F_n(n=1-6)$ in 2,3-dihydrobenzofuran (DF) and tetrahydrofuran (THF).

Name	^a DF ($\epsilon_d=4.33$)				^a THF ($\epsilon_d=7.58$)			
	^b $\Delta CRIP$	^c E_{CRIP}	^d $\Delta SSRIP$	^e E_{SSRIP}	^b $\Delta CRIP$	^c E_{CRIP}	^d $\Delta SSRIP$	^e E_{SSRIP}
F ₁	-0.804 V	3.527 V	-0.386 V	3.945 V	-0.459 V	3.872 V	-0.248 V	4.083 V
F ₂	-0.604 V	3.072 V	-0.337 V	3.339 V	-0.345 V	3.331 V	-0.212 V	3.464 V
F ₃	-0.492 V	2.960 V	-0.297 V	3.155 V	-0.281 V	3.171 V	-0.184 V	3.268 V
F ₄	-0.419 V	2.943 V	-0.265 V	3.097 V	-0.239 V	3.123 V	-0.163 V	3.199 V
F ₅	-0.367 V	2.884 V	-0.241 V	3.010 V	-0.210 V	3.041 V	-0.147 V	3.104 V
F ₆	-0.337 V	2.920 V	-0.223 V	3.034 V	-0.193 V	3.064 V	-0.136 V	3.121 V

^aFor calculating the Coulomb potential energies of $F_n(n=1-6)$ ion pairs, the assumption is that charges evenly distribute in each carbon atom. The geometries of RIP are face-to-face stacking. An example of face-to-face stacking RIP is given in Figure C1 of Appendix C. The $E_{FI}=|E_{red}-E_{ox}|$ calculated by redox potentials are given in Table 5.2, where E_{ox} of $F_n(n=1-6)$ are measured by electrochemistry methods with supporting electrolyte. The actual E_{FI} , E_{CRIP} and E_{SSRIP} values are greater than the values given in this table (see text). ^bThe Coulomb potential energy of CRIP is estimated by $r=0.3$ nm.¹⁰ ^cThe Potential energy of CRIP estimated by $E_{FI}-\Delta CRIP$. ^dThe Coulomb potential energy of SSRIP is estimated by $r=0.7$ nm.¹⁰ ^eThe Potential energy of SSRIP estimated by $E_{FI}-\Delta SSRIP$.

From data of photoexcitation in Figure 5.7(a), F_3 ion pairs can be created by photoexcitation that suggests lower E_{CRIP} of F_3 compared with the singlet excited states (E_S) of F_3 . This finding suggests that the Coulomb attraction of RIP significantly reduces E_{FI} of F_3 to below E_S of F_3 . Therefore, the E_{CRIP} of F_3 is below E_S of F_3 . From data of photoexcitation in Figure 5.7(b), there are growths of $^3F_3^*$ corresponding to homogenous decays of F_3 ion pairs in THF. This finding suggests that the potential energies of CRIP and SSRIP are higher than that of triplet excited states (E_T) for F_3 .

From data of pulse radiolysis in Figure 5.3 and 5.8, there is no growth of $^3F_n^*(n=3-6)$ corresponding to homogenous decays of $F_n(n=3-6)$ ion pairs in DF. These observations conflict the findings from data of photoexcitation in Figure 5.7 that there are growths of $^3F_3^*$ corresponding to homogenous decays of F_3 ion pairs in THF. This confliction may be due to that

growth of ${}^3F_3^*$ corresponding to homogenous recombination of F_3 ion pairs in Figure 5.8 is concealed by the triplet-triplet annihilation (TTA) of ${}^3F_3^*$. Large amount of ${}^3F_3^*$ are instantly created by pulse radiolysis via triplet excitation energy transfer (reaction 5.6b) and direct excitation to F_3 by the electron pulse. From 2 ns absorbance of ${}^3F_3^*$ in Figure 5.8, pulse radiolysis creates $\sim 2.8 \mu\text{M}$ of ${}^3F_3^*$ in DF based on ϵ of ${}^3F_3^*$, $1.0 \times 10^5 \text{ M}^{-1}\text{cm}^{-1}$ at 640 nm.¹⁷⁶ With ϵ of F_3 ions given in Table 5.1, the concentrations of F_3 free ion pairs from data of pulse radiolysis in Figure 5.3 is $0.45 \mu\text{M}$. Therefore, the TTA of ${}^3F_3^*$ is capable of competing with homogenous recombination of F_3 ion pairs for data of pulse radiolysis in Figure 5.8. Based on the above reason, growths of ${}^3F_n^*$ ($n=4-6$) corresponding to homogenous decays of F_n ($n=4-6$) ion pairs may also be concealed by the TTA for data of pulse radiolysis in Figure 5.8.

The transient emission from pulse radiolysis of F_n ($n=2-6$) in Figure 5.9 show no delayed fluorescence corresponding to recombination of F_n ($n=2-6$) ion pairs. Because the lifetime of ${}^1F_1^*$ is 10 ns,¹⁵³ it is difficult to distinguish between delayed fluorescence and intrinsic fluorescence. Based on the data from pulse radiolysis of DMBP ion pairs in Figure 5.6, triplet excited states yield of the ion recombination is 0.98 ± 0.02 in DF. These findings suggest that E_{CRIP} and E_{SSRIP} are above E_T and below E_S , which is in agreement with the findings from photoexcitation data of F_3 in THF; it also agrees with potential energy diagram illustrated in Figure 5.10(b) for pulse radiolysis. E_{CRIP} and E_{SSRIP} of F_1 are possibly below the E_S of F_1 based on the estimations given in Table 5.5.

In Table 5.4, the fluorescence lifetimes (τ_f) of F_n ($n=2-6$) determined by single exponential function from the pulse radiolysis data in Figure 5.9 are longer than the reported lifetimes of ${}^1F_n^*$ ($n=2-6$) given in Table 5.2. This slightly long lifetime may be due to two mechanisms: (1) Recombination of F_n^{*+} ($n=2-6$) with e_s^- . (2) Singlet excitation energy transfer from DF (reaction 5.6a). Cherenkov radiation created by electron pulse can also create singlet excited molecules. Because the duration of Cherenkov radiation is dependent on the width of the electron pulse, which is much shorter than the lifetimes of ${}^1F_n^*$ ($n=1-6$), τ_f for ${}^1F_n^*$ ($n=1-6$) created by Cherenkov radiation are identical with the lifetimes of the singlet excited state of ${}^1F_n^*$ ($n=1-6$) given in Table 5.2.

The actual E_{FI} is higher than the E_{FI} estimated by the redox potentials measured by electrochemistry methods in polar solvents such as dichloromethane (DCM) with supporting electrolyte. Connelly and Geiger⁹⁷ reported that E_{ox} of ferrocene in THF ($\epsilon_d=7.58$) was 100 meV higher than that in DCM ($\epsilon_d=8.93$). Bao¹⁷⁷ reported that E_{ox} of ferrocene varied ~ 520 meV over a range from 1 to 100 mM of supporting electrolyte, tetrabutylammonium tetrafluoroborate, in DCM. From Born model,¹⁷⁵ solvation energy of ion increases with increasing ϵ_d and decreasing the size of ion. Because the sizes of F_n ($n=2-6$) are larger than ferrocene, the actual E_{ox} of F_n ($n=2-6$) in THF may be $\sim 200-300$ meV higher than E_{ox} of F_n ($n=2-6$) given in Table 5.2. E_{ox} of F_n ($n=2-6$) were measured by the cyclic voltammetry method in DCM with 100 mM of tetrabutylammonium hexafluorophosphate.¹⁵⁵

5.5 Conclusion and Summary

In DF solution, the kinetic analyses for diffusion controlled data suggest two things: (1) The average time length for geminate radical ion pair to diffuse together to become intimate radical ion pair (IRIP) is $\sim 9 \pm 1$ ns. (2) The G_{fi}^I value of free ions in DF is 0.15 ± 0.02 per 100 eV estimated by the free-indicator method and the first time to report that of value in author's best knowledge.

The free ion yield increases with decreasing the charge density. This chapter finds that the Type II free ion yields (the G_{fi}^{II} values) from pulse radiolysis increase with decreasing the charge density in DF. These findings suggest that the enhancement of the free ion yield by charge delocalization is due to the weak Coulomb interaction caused by the low charge density in the ion pair. This thesis finds that the F_{esc} from photoexcitation of F_3 ion pairs is 0.18 ± 0.02 in THF. Scheme 5.1 and Figure 5.10(a) show that photoexcitation only creates IRIPs, and most IRIPs is contact radical ion pair (CRIP). Therefore, the free ions created by photoexcitation are the Type II. For the ion pairs had 9,10-dicyanoanthracene anions and hexaethylbenzene cations created by photoexcitation, Zhou² found that the F_{esc} was 0.06 in THF. These two ions which are high charge density compared with F_3 ion pairs. The difference between the F_{esc} from this thesis and report of Zhou² supports that the weak Coulomb interaction can significantly increase the escape probability of the ion.

This chapter finds that F_{esc} from pulse radiolysis and photoexcitation of F_3 ion pairs are different. If the observation¹² that no transformation from SSRIP to CRIP applied on the F_3 ion pairs, the F_3 ion pairs created by pulse radiolysis have higher free ion yield compared with those created by photoexcitation because the SSRIPs have the weak Coulomb interaction that lets more easily ion escape probability. Pulse radiolysis creates ion pairs with a separation distance distribution so the most the ion pairs become SSRIPs. From the general mechanism for formation of the ion pairs by photoexcitation, most ion pairs created by photoexcitation are expected to be CRIPs. The ET theory predicts that the ET rate exponentially decreases with increasing r , so the lifetime of the SSRIP is longer than that of CRIP. This long lifetime of SSRIP also increases the escape probability of the ion.

The Coulomb potential is crucial to the free energy of RIP (E_{RIP}). Data from photoexcitation in THF strongly suggest that $E_S > E_{RIP} > E_T$. Here E_S is the free energy of the lowest singlet state and E_T is the free energy of the lowest triplet state. From data of pulse radiolysis, the fact that no $^1F_n^*$ ($n=2-6$) is generated by F_n ($n=2-6$) ion recombination in DF shows that $E_S > E_{RIP}$. It is also important to notice that the free energy of the free ion pair (E_{FI}) may be underestimated if this energy is estimated by the redox potentials measured in a polar solvent with a supporting electrolyte. Regardless of the actual E_{FI} , the realistic Coulomb potential energy is capable of decreasing E_{FI} to below E_S .

To conclude, in this chapter have four major findings: (1) This chapter is the first report of the G_{fi} value of free ions in DF, 0.15 ± 0.02 per 100 eV. (2) In low dielectric constant solvent, charge delocalization enhances the free ion yield. (3) In low dielectric constant solvents such as THF and DF, transformation rate from SSRIP to CRIP is less than $5.0 \times 10^6 \text{ s}^{-1}$. (4) The Coulomb potential significantly changes the free energy of RIP. There are two unsolved puzzles: (1) In DF solution, no growth of ${}^3F_n^*$ ($n=3-6$) absorptions corresponding to geminate ion recombination of $F_n(n=1-6)$ ion pairs was observed in pulse radiolysis data. (2) Geminate F_3 ion pairs created by photoexcitation in THF have much fast recombination with each other compared with geminate F_3 ions created by pulse radiolysis in DF. The last puzzle may be due to that most geminate F_3 ion pairs created by photoexcitation is CRIPs which have greater ET rate compared with the ET rate of SSRIP. Nevertheless, further investigations for these two puzzles are a possible future work.

Chapter 6. Energies of Radical Anions Measured by Electron Transfer Equilibria Method

6.1 Introduction

Pulse radiolysis provides an alternative way to study one-electron redox potentials of molecules using bimolecular electron transfer equilibria method. This technique is particularly useful to study molecules that have either a high redox potential or an unstable in their ionic state. Pulse radiolysis is capable of rapidly reducing or oxidizing the donor molecule without working electrode. In pulse radiolysis, molecules are reduced by solvated electrons and oxidized by radical cations of solvent. For combination of pulse radiolysis with the equilibria method, the advantages are: (1) Measurements can be made in less polar solvents such as tetrahydrofuran (THF). (2) The available potential range wider than that of electrochemical methods without supporting electrolyte and working electrode. Marasas⁸⁸ combined pulse radiolysis and the equilibria method to successfully estimate the energy difference between benzene radical anion and solvated electron (e_s^-) in THF.

The disadvantages of the electrochemistry methods to measure redox potential are mainly due to working electrode and supporting electrolyte. An ideal working electrode would be an ideal polarizable electrode (IPE) at which no charge transfer across electrode-solution interface regardless of the applied voltage, which is crucial to electrochemical methods such as cyclic voltammetry.⁹⁴ Because there is, unfortunately, no real IPE, supporting electrolytes such as tetrabutylammonium hexafluorophosphate (TBAPF₆) are employed to ensure homogeneous and near-zero electric field across the interface. Therefore, the available potential range is dependent on the working electrode and supporting electrolytes. However, under some conditions such as high concentration of supporting electrolyte and structural change of electrode-solution interface, absorption and desorption of molecules can occur and require additional applied voltage to reduce or oxidize the molecule of interest.

This chapter reports reduction potentials (E_{red}) for unstable radical anions such as oligo(9,9-dihexyl)fluorenes anions ($F_n^{\bullet-}$, $n=1-10$) found to be unstable by Chi¹⁵⁵ and high E_{red} molecules such as 2,4-dimethylpent-3-one (DMP) with the combination of pulse radiolysis and the bimolecular electron transfer equilibria. The major finding of this chapter, which E_{red} decreases with increasing repeat units (n), is due to an entropic contribution from increasing the possible configurations of the polaron in oligomers for F_n ($n \geq 5$).

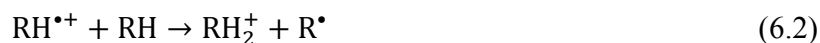
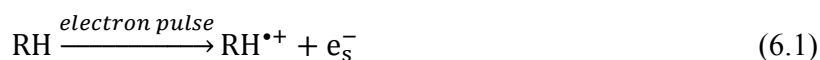
6.2 Experiments

Solutions were prepared under argon atmosphere with purified THF and placed in quartz spectrophotometric cells with 2 or 0.5 cm path lengths. Chemicals were used as received without further purification. Structures for chemicals used in this chapter are given in Appendix A. Synthesis of F_n ($n=1-10$) were described in detail elsewhere.⁷⁵ For pulse radiolysis, 15 ps, 9 MeV

electron pulse was provided by Laser Electron Accelerator Facility (LEAF) at Brookhaven National Laboratory.⁵² The short pulse of high energy electrons ionized THF molecules to create e_s^- and a corresponding number of solvent cations. In THF, the cations decompose into radicals and solvated protons. The radical anions are formed due to e_s^- attaching to solute molecules. These reactions are measured and accounted for in the interpretation of the measurements. The probe light source is a Xenon arc lamp and probe wavelengths were selected by optical interference filter with 10 or 40 nm band width. Optical detectors are a silicon (EG&G FND-100, 2 ns response time) or an InGaAs (Germanium Power Devices GAP-500L, 2 ns response time) photodiodes. The signals were collected with LeCroy 8620A, 640Zi or HRO 66Zi digitizing oscilloscopes.

6.3 Bimolecular Electron Transfer Equilibria Method

In a given solvent, pulse radiolysis creates e_s^- , a powerful reducing agent. The radiation chemistry in THF solution is:



where RH is THF, RH_2^+ is the solvated proton and M is the solute molecule. For molecules such as trimethylphenylsilane (TMPS) and 2,4-dimethylpentan-3-one (DMP), which are difficult to reduce by electrochemical methods, their E_{red} were estimated from the electron capture (EC) reaction (reaction 5.3), where the K_{eq} of this reaction is:

$$K_{eq} = \frac{[M^{\bullet-}]}{[M][e_s^-]} \quad (6.4).$$

In THF, e_s^- has a broad absorption band spanning from the visible to near-infrared and its spectrum and extinction coefficient is known.¹⁷⁸ Therefore, $[e_s^-]$ and $[M^{\bullet-}]$ can be estimated by observing the kinetic trace of e_s^- at a wavelength where there is no absorption of $M^{\bullet-}$.

When a sufficient concentration of electron donor (D_e) is present, e_s^- are mainly captured by D_e to become $D_e^{\bullet-}$. Sufficient here means that D_e captures the majority of e_s^- despite the presence of the electron acceptor (A_e). After e_s^- is captured by D_e , the reactions in THF are:





From K_{eq} for the electron transfer (ET) reaction (reaction 6.6), the E_{red} of A_e can be estimated with the E_{red} of D_e and *vice versa*. K_{eq} of reaction (6.6) is expressed as:

$$K_{eq} = \frac{[A^{\bullet-}][D]}{[A][D^{\bullet-}]} \quad (6.8),$$

where concentrations of $A_e^{\bullet-}$ and $D_e^{\bullet-}$ can be estimated from kinetic traces of $D_e^{\bullet-}$ at wavelengths where only $D_e^{\bullet-}$ absorbs based on the relative extinction coefficient of $D^{\bullet-}$ to e_s^- .

With K_{eq} of reactions (6.3) and (6.6), the standard free energy change (ΔG^0) for both reactions are calculated by:

$$\Delta G^0 = -RT \ln(K_{eq}) \quad (6.9),$$

where R is the gas constant and T is temperature. To obtain E_{red} from ΔG^0 , for molecules which E_{red} are difficultly determined by electrochemical methods, E_{red} is estimated by:

$$E_{red}(M) = (E(e_s^-) - \Delta G^0) / 1 e \quad (6.10),$$

where $E(e_s^-)$ is the energy level of e_s^- in THF, -3.34 eV, based on K_{eq} of reaction (6.3) with benzene being $0.45 M^{-1}$ reported by Marasas⁸⁸ and E_{red} of benzene, -3.38 V (vs. SCE).⁹⁶ With K_{eq} of reaction (6.6) and E_{red} of D , E_{red} of A is calculated by:

$$E_{red}(A) = E_{red}(D) - \frac{\Delta G^0}{1 e} \quad (6.11).$$

6.4 Results

An example of estimating K_{eq} for reaction (6.3) of TMPS is given in Figure 6.1. Comparing the $\text{TMPS}^{\cdot-}$ absorption spectra shown in Figure 6.1(a) with e_s^- absorption spectrum in THF¹⁷⁸ suggests that $\text{TMPS}^{\cdot-}$ has no obvious absorptions from 1000-1600 nm but a little absorption in the visible, $\lambda < 600$ nm. From kinetic traces of TMPS solution in THF shown in Figure 6.1(b) and similar data, $K_{\text{eq}}=33.2 \text{ M}^{-1}$ and $k_{\text{ET}}=1.5 \times 10^{10} \text{ M}^{-1} \text{ s}^{-1}$.

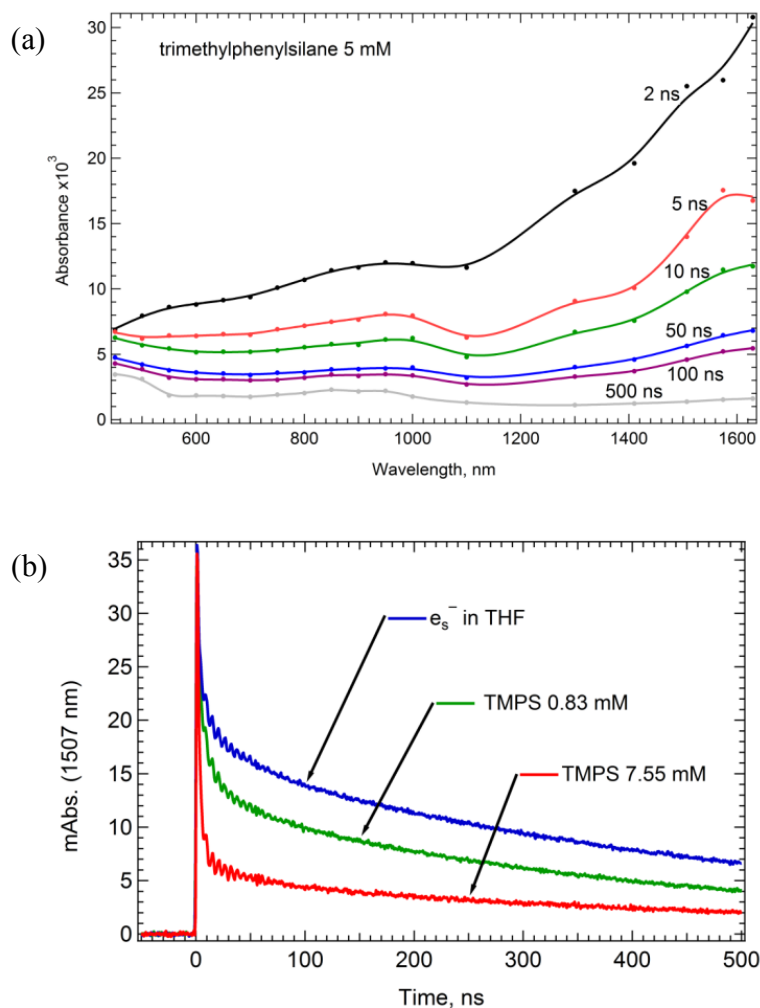


Figure 6.1 (a) Transient spectra of trimethylphenylsilane radical anions (TMPS) in THF with 5 mM of TMPS. (b) Kinetic traces at 1507 nm in THF without and with TMPS.

To estimate K_{eq} between phenanthrene (Phe) and F_1 , Phe was used as A_e and F_1 was used as D_e with 10 mM of sodium tetraphenylborate (NaBPh_4) in THF. The purpose of NaBPh_4 is to convert $F_1^{\cdot-}$ into $(\text{Na}^+, F_1^{\cdot-})$ ion pairs, which have relatively long lifetimes as shown in Figure 6.2, so that most electrons can transfer from $F_1^{\cdot-}$ to Phe. From Figure 6.2 and similar data, $K_{\text{eq}}=700$ and the

bimolecular electron transfer (ET) rate constant is $k_{ET}=2.0\times 10^9\text{ M}^{-1}\text{ s}^{-1}$, for ET from $F_1^{\bullet-}$ to Phe. Based on the E_{red} of Phe⁸⁵ measured by an electrochemical method, the E_{red} of F_1 in THF is calculated by equation (6.11). The E_{red} of $F_n(n=2-4)$ in THF were determined by the above method with less than 5 mM of sodium hexafluorophosphate (NaPF_6). For F_n ($n=5-10$) and *p*-terphenyl (*p*T), their E_{red} were estimated by using E_{red} of trans-stilbene⁸⁰ (ES) as a reference without electrolyte. For tetraphenylmethane (TPM), the E_{red} was estimated by using fluorobenzene (FBz) as references. From Figure 6.3 showing examples of estimating E_{red} for F_8 and TPM by combination of pulse radiolysis and the bimolecular electron transfer equilibria methos, K_{eq} of $\text{ES}^{\bullet-} + F_8 \leftrightarrow \text{ES}^{\bullet-} + F_8^{\bullet-}$ is 357 and K_{eq} of $\text{FBz}^{\bullet-} + \text{TPM} \leftrightarrow \text{FBz} + \text{TPM}^{\bullet-}$ is 62 and; k_{ET} from $\text{ES}^{\bullet-}$ to F_8 is 1.1×10^{10} and k_{ET} from $\text{FBz}^{\bullet-}$ to TPM is $5.0\times 10^{10}\text{ s}^{-1}$. The E_{red} of these molecules in THF are given in Table 6.1, where E_{red} of $F_n(n=1-10)$ are seen to increase with increasing the number of the repeat units (n).

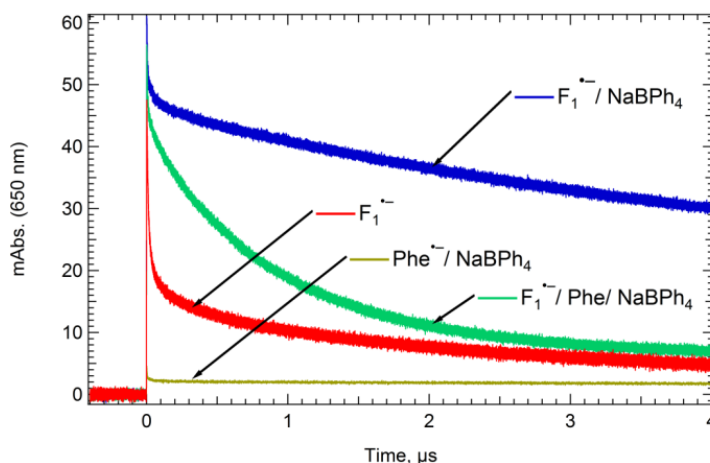


Figure 6.2 Kinetic traces at 650 nm of $F_1^{\bullet-}$ with and without phenanthrene (Phe) in THF, where the concentrations are 100 mM F_1 , 100 mM F_1 + 0.8 mM Phe and 48 mM Phe in THF solutions containing 10 mM of sodium tetraphenylborate (NaBPh_4). $F_1^{\bullet-}$ without NaBPh_4 (red), 100 mM of F_1 decays much faster than $F_1^{\bullet-}$ with NaBPh_4 (blue).

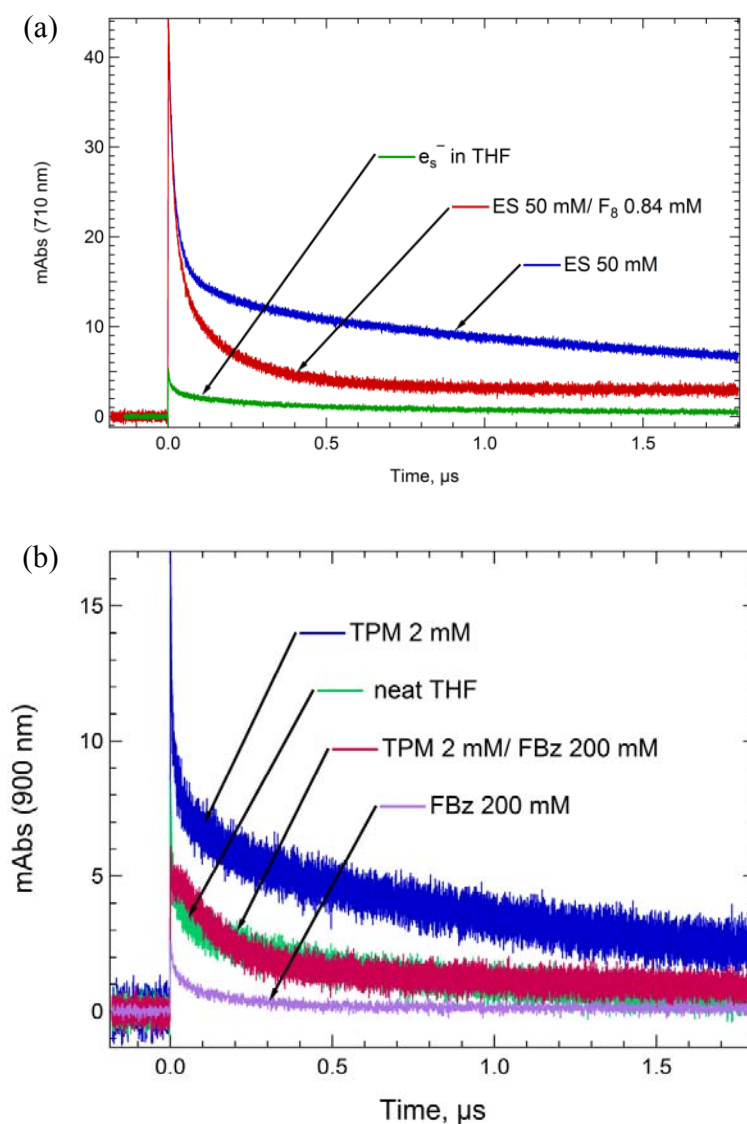


Figure 6.3 Kinetic traces of (a) solvated electrons (e_s^-) and *trans*-stilbene (ES) with and without F_8 at 710 nm, and (b) e_s^- and tetraphenylmethane (TPM) with and without fluorobenzene (FBz) at 900 nm in THF. ES and FBz were used as the electron donor for capturing e_s^- without electrolyte. E_{red} of F_8 was estimated by using E_{red} of ES as a reference, and E_{red} of TPM was estimated by using E_{red} of FBz as references; K_{eq} of the electron transfer reactions were determined by the bimolecular electron transfer equilibria method.

Table 6.1 Reduction Potentials (E_{red}), Equilibrium Constants (K_{eq}), and Bimolecular Electron Transfer Rate Constants (k_{ET}).

	Reactions	E_{red} (V vs. SCE)	$[D_e]/[A_e]$ (mM)	k_{ET} ($M^{-1}s^{-1}$)	K_{eq}
F ₁	^a F ₁ ⁻ +Phe \leftrightarrow F ₁ +Phe ⁻	-2.531 (± 0.016) ^j	100/0.2-20	2.0×10^9	645(± 218)
F ₂	^b Phe ⁻ +F ₂ \leftrightarrow Phe+F ₂ ⁻	-2.238 (± 0.004) ^j	10/0.033-1.67	7.9×10^8	130(± 21)
F ₃	^b F ₂ ⁻ +F ₃ \leftrightarrow F ₂ +F ₃ ⁻	-2.124 (± 0.020) ^j	5/0.025-0.13	2.1×10^9	86(± 16)
F ₄	^b F ₂ ⁻ +F ₄ \leftrightarrow F ₂ +F ₄ ⁻	-2.073 (± 0.008) ^j	0.5/0.025-0.13	1.4×10^9	444(± 150)
	^c ES ⁻ +F ₄ \leftrightarrow ES+F ₄ ⁻	-2.075 (± 0.012) ^k	10/0.95-2.6	3.5×10^9	12(± 6)
F ₅	^c ES ⁻ +F ₅ \leftrightarrow ES+F ₅ ⁻	-2.013 (± 0.012) ^k	50/0.2-1.48	6.1×10^9	141(± 61)
F ₆	^c ES ⁻ +F ₆ \leftrightarrow ES+F ₆ ⁻	-1.999 (± 0.011) ^k	50/0.1-0.74	8.3×10^9	241(± 101)
F ₇	^c ES ⁻ +F ₇ \leftrightarrow ES+F ₇ ⁻	-1.999 (± 0.012) ^k	50/0.1-0.84	8.1×10^9	247(± 112)
F ₈	^c ES ⁻ +F ₈ \leftrightarrow ES+F ₈ ⁻	-1.992 (± 0.015) ^k	50/0.1-0.84	1.1×10^{10}	357(± 189)
F ₉	^c ES ⁻ +F ₉ \leftrightarrow ES+F ₉ ⁻	-1.979 (± 0.012) ^k	50/0.05-0.366	1.5×10^{10}	523(± 216)
F ₁₀	^c ES ⁻ +F ₁₀ \leftrightarrow ES+F ₁₀ ⁻	-1.977 (± 0.012) ^k	50/0.05-0.385	9.7×10^9	589(± 274)
^d TPM	^c FBz ⁻ +TPM \leftrightarrow FBz+TPM ⁻	-3.103 (± 0.020) ^l	20-200/2	5.0×10^{10}	62(± 20)
^e DMP	^c e _s ⁻ +DMP \leftrightarrow DMP ⁻	-3.222 (± 0.015) ^m	0.001/0.41-7.69	3.2×10^{10}	100(± 44) M ⁻¹
^f TMPS	^c e _s ⁻ +TMPS \leftrightarrow TMPS ⁻	-3.271(± 0.036) ^m	0.0008/0.167-7.55	1.5×10^{10}	33.2(± 25.8) M ⁻¹
ⁱ TP	^c TP ⁻ +ES \leftrightarrow TP+ES ⁻	-2.306(± 0.002) ^j	0.1-1/49	5.8×10^{10}	760(± 55)

^aWith 10 mM of Sodium Tetrphenylborate in THF. ^bWith less than 5 mM of Sodium Hexafluorophosphate in THF. ^cWithout Supporting Electrolyte. ^dTetraphenylmethane ^e2,4-dimethylpentan-3-one ^fTrimethylphenylsilane ^g1,4-bis(trimethylsilyl)benzene ^h1,4-bis(trifluoromethyl)benzene ⁱ*p*-terphenyl ^jUsed phenanthrene (Phe) as a reference. The E_{red} of Phe is -2.363 V (vs. SCE) in dimethylformamide (DMF) based on ΔE_{red} between perylene and phenanthrene found in reference⁸⁵ with E_{red} of perylene found in reference.⁸⁰ ^kUsed *trans*-Stilbene (ES) as a reference. The E_{red} of ES is -2.136 (vs. SCE) in DMF.⁸⁰ ^lUsed fluorobenzene (FBz) as reference. The E_{red} of FBz is -3.207 V (vs. SCE) in THF based on $\Delta E_{\text{red}}(\text{FBz}-\text{benzene})=0.173$ V in THF found in this reference,⁸⁸ where E_{red} of benzene is -3.38 V (vs. SCE).⁹⁶ ^mUsed solvated electrons as a reference; The energy level of e_s⁻ is -3.34 V (vs. SCE) in THF based on data of Table 3 found in reference⁸⁸ with the E_{red} of FBz from Table 4.3 of Chapter 4.

6.5 Discussion

E_{red} were measured for: (1) anions such as $F_n^{\bullet-}$ ($n=1-10$) that were not stable enough to be measured by electrochemical methods and (2) anions such as $\text{TMPS}^{\bullet-}$ with high E_{red} . The discussion will focus on the E_{red} of the oligofluorenes as they are the major subject of this thesis.

Chi¹⁵⁵ reported that the oxidation potential (E_{ox}) of F_n ($n=2-7$) decreased with increasing n , similar to studies on oligothiénylenevinylenes.¹⁷⁹ From Figure 6.4, there are two findings: (1) the E_{red} of F_n ($n=1-10$) increase with increasing n , where data was fitted to $E_{\text{red}} = -1.91 - 0.63(1/n)$ V (vs. SCE) as shown in Figure 6.4, and (2) the E_{red} of F_n ($n=1-10$) shows a continued moderate increase for $n \geq 5$. These findings agree with suggestions of Chi¹⁵⁵ that E_{red} of oligofluorenes increase with increasing n showing mirror image behavior to E_{ox} . This behavior of E_{red} and E_{ox} is due to symmetric bonding and anti-bonding molecular orbitals of conjugated oligomers predicted by molecular orbital theory and equal solvation energies (ΔG_{sol}^0) of the resulting anion and cation, which can be roughly estimated by the Born model:

$$\Delta G_{\text{sol}}^0 = -\frac{Ze^2}{2r} \left(1 - \frac{1}{\epsilon_d}\right) \quad (6.12)$$

where r is radius of the ion, Z is number of charges and ϵ_d is the dielectric constant.

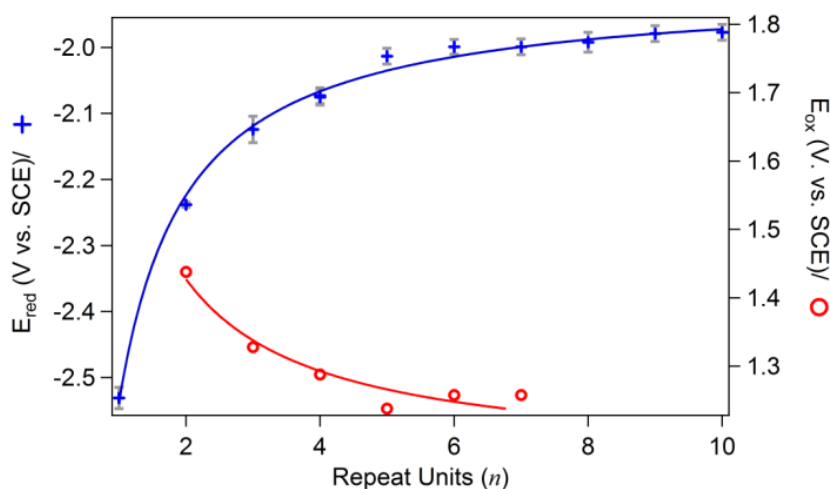


Figure 6.4 A plot of the redox potential of F_n ($n=1-10$) vs. repeat units (n), where E_{red} is reduction potential and E_{ox} is oxidation potential. The E_{ox} of F_n ($n=2-7$) are taken from Table 1 of this reference¹⁵⁵ are reported vs. AgNO_3/Ag and converted into vs. SCE with E_{ox} of ferrocene, 0.232 V (vs. AgNO_3/Ag)¹⁵⁵ and 0.53 V (vs. SCE).⁹⁷ Fit results are $E_{\text{ox}} = 1.16 + 0.53(1/n)$ and $E_{\text{red}} = -1.91 - 0.63(1/n)$, which are red and blue lines, respectively.

For F_n ($n \geq 5$), the reduction potentials, E_{red} , gradually becoming more positive may be due to an entropic contribution, discussed below. Regardless of entropic contributions, E_{red} measured by electrochemistry methods can be written as:¹⁸⁰

$$E_{\text{red}} = (E. A. + \Delta G_{\text{sol}}^0 - \phi) / 1 e \quad (6.13)$$

where E.A. is the electron affinity in gas phase and ϕ is the Fermi level of the reference electrode. ΔG_{sol}^0 of $F_n^{\cdot-}$ ($n \geq 5$) are almost identical with each other because delocalized length of polaron for oligofluorenes is 4.3 repeat units as reported by Zaikowski.⁷⁶ Therefore, differences of E_{red} are due to difference of E.A. for F_n ($n \geq 5$). For conjugated oligomer, the E.A. is related to the energy of the singly occupied molecular orbital (SOMO) as illustrated in Figure 6.5. For $F_n^{\cdot-}$ ($n=4-10$), absorption energies of the P_2 band reported by Zaikowski⁷⁶ and given in Table 6.2 indicate no obvious n dependence of P_2 absorption energy, which suggests energies of SOMO for $F_n^{\cdot-}$ ($n=5-10$) are almost identical.

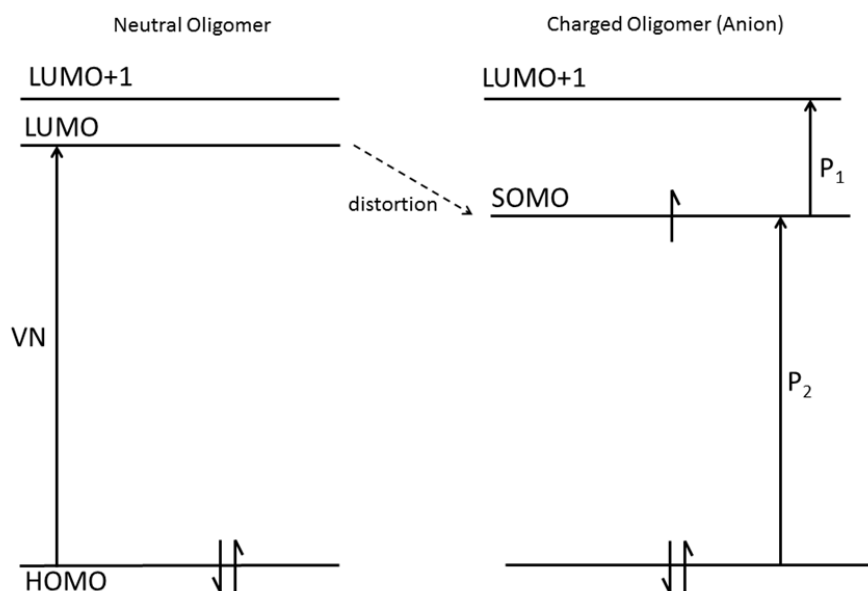


Figure 6.5 Molecular orbital diagram for neutral and charged conjugated oligomers. For the anion of conjugated oligomers, SOMO is due to that additional electron distorts the energy level of LUMO. SOMO is the singly occupied molecular orbital, LUMO is the lowest unoccupied molecular orbital, and HOMO is the highest occupied molecular orbital. The P_1 and P_2 are absorption bands of polaron. The VN is the vestigial neutral band in neutral conjugated oligomers.

Table 6.2 List of Absorption Energies of P₂ Bands and Entropic Contributions ($-\Delta ST$) for F_n^{•-} (n=5-10).

	^a P ₂ (eV)	^b $-\Delta ST$ (meV)
F ₅	2.076	-24
F ₆	2.075	-33
F ₇	2.065	-40
F ₈	2.064	-45
F ₉	2.054	-49
F ₁₀	2.054	-53

^aThe values of absorption energies are taken from Figure 6 of this reference.⁷⁶ ^bEntropic contribution based on the bead model¹⁸¹ (see text) at $T=298$ K with delocalized polaron length, $n_p=4.3$ repeat units.⁷⁶

For E_{red} of F_n(n=5-10), an expected entropic contribution suggested by Zaikowski⁷⁶ is configuration entropy, $k_B \ln(\Omega)$, where Ω describes the number of independent ways in which one polaron can be arranged in oligomers. Kaufman¹⁸¹ suggested that such entropic contributions affected the E_{red} of polyacetylene. For estimating the configuration entropy, a simple model¹⁸¹ treating the polaron as a spherical bead with diameter n_p repeat units, the delocalized length, and the oligomers as a chain with length n repeat units is applied to estimate the entropy (S):

$$S = k_B \left[\ln \left(n_p \cdot \frac{\rho^\rho}{(\rho-1)^{\rho-1}} \right) - 1 \right] \quad (6.14),$$

where $\rho=n/n_p$ with $n_p=4.3$ repeat units.⁷⁶ Based on the bead model, the entropic contributions ($-\Delta ST$) of F_n (n=5-10) given in Table 6.2 suggest 29 meV difference of E_{red} between F₅ and F₁₀. This difference is close to our finding, 36 meV difference of E_{red} between F₅ and F₁₀, from Table 6.1. Therefore, small E_{red} differences among F_n ($n \geq 5$) are due to the entropic contribution.

6.6 Summary

The combination of pulse radiolysis and the bimolecular electron transfer (BET) equilibria method successfully estimated K_{eq} of the electron transfer (ET) and electron capture (EC) reactions. Pulse radiolysis is capable of creating solvated electrons, a highly reactive reducing agent, in a given solvent. The BET equilibria method is a good technique to estimate the K_{eq} of the ET and EC reactions for a molecule which ion has short lifetime. The relative E_{red} of F_n(n=1-10), TPM and TP were estimated with the K_{eq} of ET reactions based on the E_{red} of the reference molecules. The relative E_{red} for molecules such as TMPS that is difficult to reduce by the typical electrochemistry methods were estimated based on the K_{eq} of the EC reaction of the molecules and the energy level of e_s^- in THF.

The E_{red} of F_n (n=5-10) gradually become more positive with increasing the number of the repeat units (n) that is due to entropic contribution from the number of possible configurations for

stabilizing the polaron in oligofluorenes. The bead model¹⁸¹ that treats the polaron as a sphere with a radius (n_p), which is the delocalized polaron length, and polymer as a string with a finite length, which is n , was employed to estimate the entropic contribution to the E_{red} of oligofluorenes. The polaron delocalization length is 4.3 repeat units in oligofluorenes.⁷⁶ The configuration entropies of F_n ($n=5-10$) estimated by the bead model are close to the experimental configuration entropies. This finding suggests that the bead model is a fairly good and simple model to estimate the entropic contribution to the E_{red} of the polymers.

Knowledge of K_{eq} between the electron donor and acceptor is important to establish the ladder of reduction potentials. Once the ladder is established, the ladder can be a tool to quickly estimate the E_{red} of molecule with pulse radiolysis. By observing the transient absorbance, if there is any, for anions of molecules, the sign of ΔE_{red} between the target molecule and a molecule given by the ladder can be determined. Therefore, E_{red} of the target molecules can be estimated with known E_{red} of molecules. The advantage of the reduction potential ladder is the capability of measuring E_{red} in a given solvent without supporting electrolyte and working electrode.

Chapter 7 Summary

In media with low dielectric constants (ϵ_d) such as tetrahydrofuran (THF, $\epsilon_d=7.58$) and 2,3-dihydrobenzofuran (DF, $\epsilon_d=4.33$), the enhancement of the free ion yield by charge delocalization was systematically studied. This enhancement was demonstrated by using oligo(9,9-dihexyl)fluorenes (F_n , $n=1-6$) ions in which charge densities decreased with increasing the number of the repeat units (n). This thesis examines free ions of two types, which are referred to as the Type I and II free ions. The Type I free ion is an ion that escapes from an ion pair in which the initial separation distance (r_i) is comparable to or longer than the Onsager radius (r_c). The Type II free ion is an ion that escapes from an intimate radical ion pair (IRIP) in which separation distance (r) is short allowing the ions to come into contact. This thesis finds that the Type I free ion yields (the G_{fi}^I values) were $G_{fi}^I=0.69\pm 0.06$ per 100 eV in THF (Chapter 4) and $G_{fi}^I=0.15\pm 0.02$ per 100 eV in DF (Chapter 5). This G_{fi}^I value of free ions in THF is close to the reported G_{fi} values of free ions, 0.205~0.72 per 100 eV, in THF.^{61, 67, 113-117} In author's best knowledge, this thesis is the first report of the G_{fi} value of free ions in DF.

In contrast to the Type I free ion yield that depends only on properties of the solvent⁶⁹ regardless of ion's charge density (Chapter 4), this thesis finds that the Type II free ion yields increase with decreasing the charge density. This increase occurs because the weak Coulomb interaction caused by low charge density lets the ions more easily escape from each other. The electrostatic calculations in Table 5.5 (p.69) predict that the strength of the Coulomb interaction decreases with decreasing charge density. From section 5.4.2 (p.64), the ion escape probability $F_{esc}=[Fi^{II}]/[IRIP]$ is 0.18 ± 0.02 for ($F_3^{\bullet-}, F_3^{\bullet+}$) ion pairs formed by photoexcitation in THF. Here $[Fi^{II}]$ is the concentration of the Type II free ions, and $[IRIP]$ is the concentration of the IRIPs. Because the electron transfer (ET) probability exponentially decreases with increasing distance, formation of the ions by photoexcitation requires that the excited and neutral molecules are close to each other, possibly in contact. Therefore, most ion pairs created by photoexcitation are expected to be born as contact radical ion pairs (CRIPs). The only free ions created by photoexcitation are Type II. For ion pairs consisting of 9,10-dicyanoanthracene anions and hexaethylbenzene cations which had higher charge densities compared with F_3 ions, Zhou² reported that F_{esc} from photoexcitation in THF was 0.06. The difference between F_{esc} from this thesis and the report of Zhou² strongly suggests that the weak Coulomb interaction caused by the low charge density significantly increases the escape probability of the ion. Beside the conclusion^{2, 72, 143, 147-148, 182} that the F_{esc} from photoexcitation depends on the dielectric constant of solvent, this thesis finds that the ion escape probability also depends on charge density.

Findings in this thesis that delocalized charges enhance the ion escape probability in low dielectric constant media can help to improve the energy efficiency of a bulk heterojunction (BHJ) solar cell, which is limited by the free ion yield.^{135, 183} The range of ϵ_d is 3-4 for conjugated polymers such as poly(3-hexyl)thiophenes, a typical material for the BHJ solar cell. In the BHJ solar cell, many groups^{134, 149, 184-186} observed rapid (< 20 ps) dissociations of the

excitons into free ions; they concluded that before localization of the excitons induced by structural relaxation, these rapid dissociations were due to the weak Coulomb interaction in the highly delocalized excitons based on theoretical computations. Compared with the exciton delocalization size in the BHJ solar cell estimated by the electronic structures calculations, the degrees of charge delocalization for the $F_n(n=1-6)$ ions in organic solvent are well defined. By increasing the number of the repeat units, this thesis clearly demonstrates that enhancement of the free ion yield by charge delocalization that leads to the weak Coulomb interaction.

Chapter 5 finds that escape yields, F_{esc} , from pulse radiolysis and photoexcitation of F_3 ion pairs are different. From Section 5.4.3 (p.65), F_{esc} from pulse radiolysis of F_3 ion pairs in DF is 0.52 ± 0.07 . This is much larger than $F_{\text{esc}} = 0.18 \pm 0.02$ from F_3 ion pairs produced by photoexcitation in THF, even though the ϵ_d of THF is larger. While experiments in this thesis did not resolve the reason for this difference, reports in the literature¹² suggest a possible interpretation. Zhong¹² reported that no transformation occurred between CRIP and SSRIP in 1,2-dichloroethane ($\epsilon_d = 10.36$). Pulse radiolysis creates ion pairs with large separation distances that become SSRIPs. Photoexcitation creates mainly CRIPs. If the observation¹² that no transformation occurs between CRIP and SSRIP applies to the F_3 ion pairs studied here, then F_3 ion pairs created by pulse radiolysis would escape more easily because the SSRIP has weaker Coulomb interaction. Based on the ET theory (the Marcus theory),³³ the ET rate decreases with increasing r . Therefore, the theory predicts that the lifetime of SSRIP are longer than that of CRIP. This long lifetime of SSRIP also increases the escape probability of the ion. Because the proton transfer (PT) requires a short (< 0.2 nm) distance, the diffusion-controlled data from pulse radiolysis in THF (Chapter 4) imply that the transformation from SSRIP to CRIP occurs and challenge Zhong's report.¹² A possible future work is to thoroughly investigate this transformation in THF.

While SSIPs are almost certainly involved in the experiments in this thesis, the existence of SSRIP in the BHJ solar cell is debatable. Because most conjugated polymers are nonpolar, the BHJ solar cell may have no ion-dipole interaction between the charge carriers and the conjugated polymers to stabilize the charge transfer (CT) state as the SSRIP. In the BHJ solar cell, the CT states with long separation distance (3-4 nm) found by Barker¹⁸⁵ at 10 K are possibly due to a properly blend morphology of the order and disorder phases. This morphology leads electrons and holes to rapidly diffuse apart in the BHJ solar cell.¹⁸⁷ However, stabilization of the SSRIP-like CT state in the BHJ solar cell is possible by the solid-state solvation effect.¹⁸⁸ This effect is that the induced dipole moments of nonpolar polymers caused by the electric field generated by electrons and holes solvate the electrons and holes as the ions solvated by the solvent molecules with permanent dipole moments.

The Coulomb potential is a crucial determinant of the free energy of the RIP and the charge recombination energy (Δ_{CR} in equation 5.10) in low dielectric constant medium. The photoexcitation data in Figure 5.7(b) and pulse radiolysis data in Figure 5.9 suggest that

$E_S > E_{RIP} > E_T$. Here E_S is the free energy of the lowest singlet excited state, E_{RIP} is the free energy of the RIP and E_T is the free energy of the lowest triplet excited state. This finding suggests that the Coulomb potential significantly changes the free energy of the RIP. From equation 5.10, the Coulomb potential also changes Δ_{CR} . Because of the separation distance difference between CRIP and SSRIP, Δ_{CR} of CRIP and SSRIP are different.

For the diffusion-controlled recombination in THF and DF, this thesis reports the average time of the geminate recombination. From the kinetic analyses in section 4.5.1 (p.38), geminate radical anions and solvated protons take an average of 8 ± 1 ns to diffuse together to become intimate ion pairs in THF. Based on the above finding and higher viscosity of DF ($\eta = 1.97 \pm 0.06$ cP) compared with that of THF ($\eta = 0.48$ cP), the 9 ± 1 ns geminate decays of 4,4'-dimethylbiphenyl ions in Figure 5.6 (a) are possibly diffusion controlled. For those ions with diffusion controlled recombination in THF and DF, the effectively geminate recombination rate constants are $> 5.0 \times 10^9$ s⁻¹. The 8 ± 1 and 9 ± 1 ns required for the ions to diffuse together in THF and DF limit observation of faster rates.

In Chapter 4, a wide variety of PT rate constants (k_{PT}) in the radical ion pairs provides opportunities to examine models,^{38-41, 45-49, 130-132} which discuss k_{PT} in terms of ΔG^0 , $C(Q,S)$ and E_R . Here ΔG^0 is the standard free energy change for the PT reaction, $C(Q,S)$ is the protonic coupling term, and E_R is the reorganization energy of PT. In contrast to the observations¹²⁷⁻¹²⁸ that a bell shape correlation of the PT rate with ΔG^0 for the protonation at C and O atoms, the correlation of the effectively geminate PT rate constant with ΔG^0 shown in Figure 4.6 is poor. However, Edwards¹²⁹ found no theoretical basis for an inverted region for PT and proposed that decreases of rates at high driving force might be due to other factors. No PT reaction of the C accepting anions was found to be diffusion controlled, but many PT reactions to the O accepting anions are. These findings may reflect large variations in E_R , which is usually larger for protonation at C atoms. In general, this thesis finds that k_{PT} depends on two factors: (1) the degree of charge delocalization in the anion and (2) type of atom receiving the proton. In author's best knowledge, the measurements of the E_{red} of F_n ($n=5-10$) in this thesis are the first measurements. Chi¹⁵⁵ suggested that oligofluorene radical anions were too unstable to measure by the electrochemistry methods. With bimolecular electron transfer equilibria method and pulse radiolysis, the relative E_{red} were measured for molecules such as F_n ($n=5-10$) that molecules whose radical anions are too unstable for the electrochemistry methods such as tetraphenylmethane that is difficult to reduce by the electrochemistry methods. Two advantages of this technique are (1) a wider potential range compared with the electrochemistry methods and (2) no requirement of the working electrode and supporting electrolyte.

For F_n ($n=5-10$), the reduction potentials, E_{red} , gradually become more positive with increasing the number of the repeat units (n). The polaron delocalization length is 4.3 repeat units in oligofluorenes⁷⁶ so the entropy contribution from the number of possible configurations for stabilizing the polaron in oligofluorenes reflects in the E_{red} of F_n ($n=5-10$). The entropic

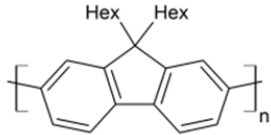

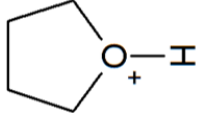
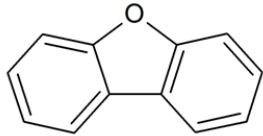
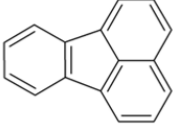
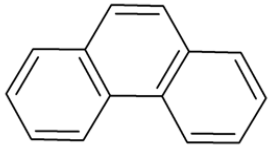
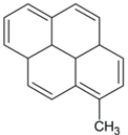
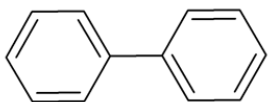
contributions to the E_{red} of F_n ($n=5-10$) were estimated by a bead model¹⁸¹ which treats the polaron as a sphere with a radius of 4.3 repeat units and the polymer as a string with a finite length. Comparison between estimated and experimental entropic contributions to the E_{red} of F_n ($n=5-10$) suggests that the bead model is a fairly good and simple model to estimate the entropic contribution.

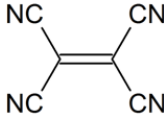

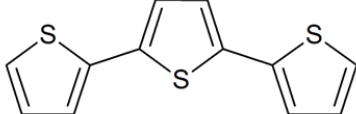
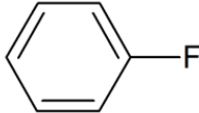


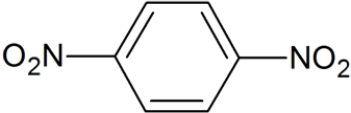
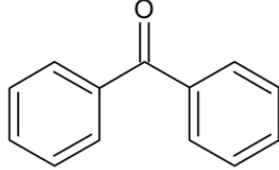
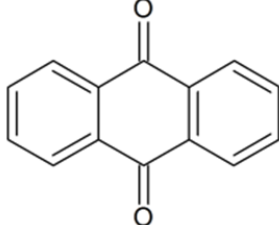
To conclude, the key findings of this thesis are:

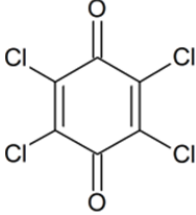
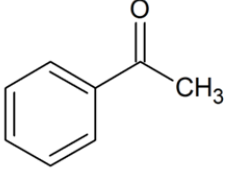
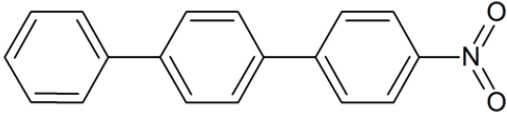
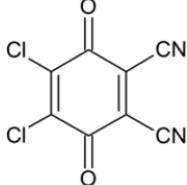
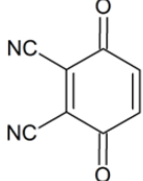
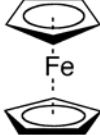
- (1) The G_{fi}^1 value in DF is 0.15 ± 0.02 per 100 eV. This finding is important to future works of radiation chemistry carried in DF.
- (2) The low charge density significantly increases the free ion yield in low dielectric constant medium. A new concept to design a material for the BHJ solar cell is that the material can rapidly delocalize electrons and holes to increase the free ion yield.
- (3) Chapter 5 finds that the F_{esc} from pulse radiolysis and photoexcitation of F_3 ion pairs are different. If the observation¹² that no transformation occurs between CRIP and SSRIP applies to the F_3 ion pairs, it implies that the high population of SSRIPs can enhance the free ion yield.
- (4) In low dielectric constant solvents, the free energy and Δ_{CR} of the ion pair are significantly changed by the Coulomb potential. For estimating the product of the ET reaction (reaction 5.4), the free energies of the RIPs are crucial.
- (5) For the ions with diffusion controlled recombination, the average lifetimes of IRIPs are 8 ± 1 ns in THF and 9 ± 1 ns in DF. These findings are important to study the kinetics of diffusion controlled reactions in THF and DF.
- (6) The rate of the PT reaction depends on ion's charge density and the type of atom receiving proton. These findings help to understand the kinetics of the PT reactions.
- (7) This thesis is the first report of the E_{red} of F_n ($n=5-10$). These findings are important to application of the organic optoelectronic devices.
- (8) For F_n ($n=5-10$), the E_{red} gradually become more positive with increasing n . This gradual change of E_{red} can be interpreted by the entropic contribution from the number of the possible configurations for stabilizing a polaron in oligofluorenes to the E_{red} .

Appendix A. Chemical Structures

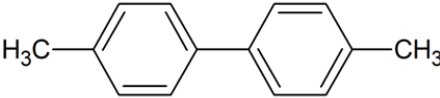
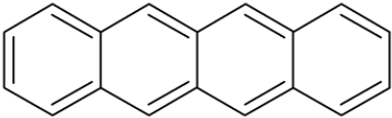
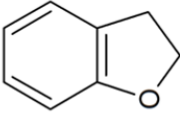

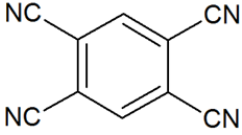
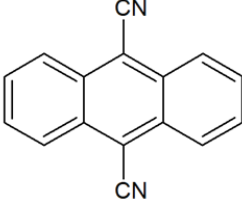
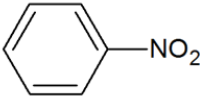
A1. Chemical Structures in Chapter 4.

Name	Chemical Structures
oligo(9,9-dihexyl)fluorenes, (F _n , n=1-10)	
Tetrahydrofuran (THF)	
Solvated Proton	
dibenzofuran (DBF)	
fluoranthene (FA)	
phenanthrene (Phe)	
1-methylpyrene (MePy)	
biphenyl (BP)	

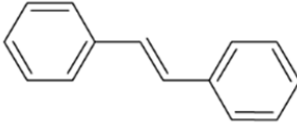
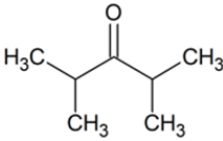
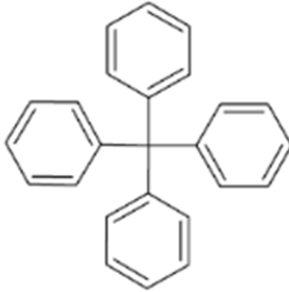
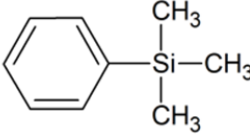
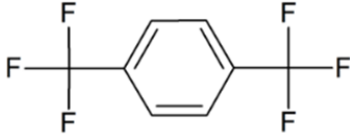
Name	Chemical Structures
tetracyanoethylene (TCNE)	
<i>p</i> -terphenyl (<i>p</i> T)	
terthiophene (T_3)	
fluorobenzene (FBz)	
<i>o</i> -terphenyl (<i>o</i> T)	
4-cyano-4'- <i>n</i> -pentyl- <i>p</i> -terphenyl (CNTP)	
<i>p</i> -dinitrobenzene (DNB)	
benzophenone (BPhO)	
anthraquinone (AQ)	

Name	Chemical Structures
tetrachloro- <i>p</i> -benzoquinone (Cl ₄ BQ)	
acetophenone (AO)	
4-nitro- <i>p</i> -terphenyl (NTP)	
2,3-dichloro-4,5-dicyano- <i>p</i> -benzoquinone (DDQ)	
2,3-dicyano- <i>p</i> -benzoquinone (DCNBQ)	
ferrocene (Fc)	

A2. Chemical Structures in Chapter 5.

Name	Chemical Structures
4,4'-dimethylbiphenyl (DMBP)	
tetracene (TC)	
2,3-dihydrobenzofuran (DF)	
<i>p</i> -xylene (<i>p</i> Xy)	
1,2,4,5-tetracyanobenzene (TCB)	
9,10-dicyanoanthracene	
Nitrobenzene (NBz)	

A3. Chemical Structures in Chapter 6.

Name	Chemical Structures
<i>trans</i> -stilbene (ES)	
2,4-dimethylpentan-3-one (DMP)	
tetraphenylmethane (TPM)	
trimethylphenylsilane (TMPS)	
1,4-bis(trifluoromethyl)benzene (TFMBz)	

Appendix B. Supporting Information for Chapter 4

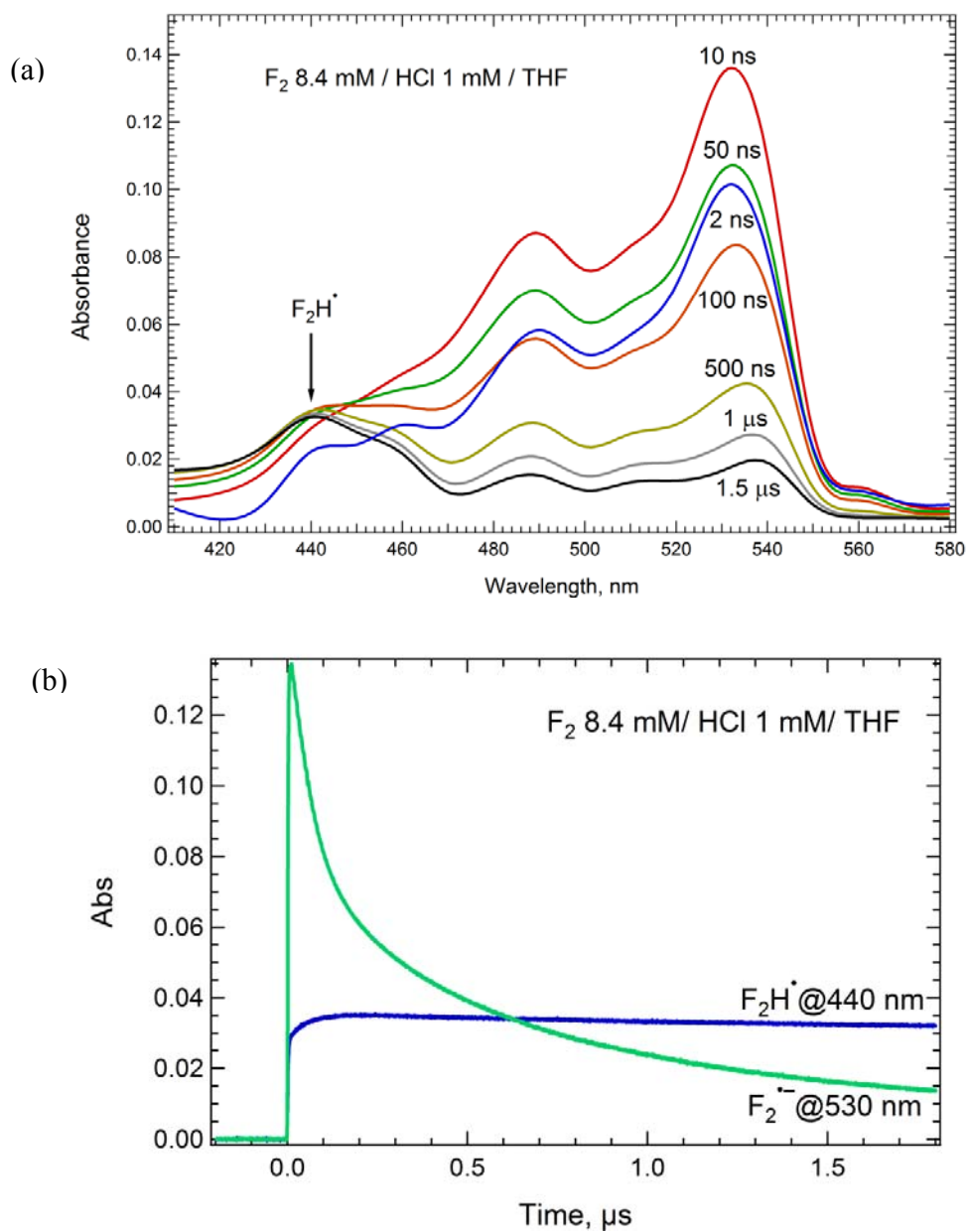


Figure B1. (a) Transient absorption spectra of F_2H^\bullet in THF with 8.4 mM of F_2 and 1 mM of HCl, where $F_2^{\bullet-}$ is converted to F_2H^\bullet by proton transfer. (b) Kinetic traces of F_2H^\bullet and $F_2^{\bullet-}$ in THF.

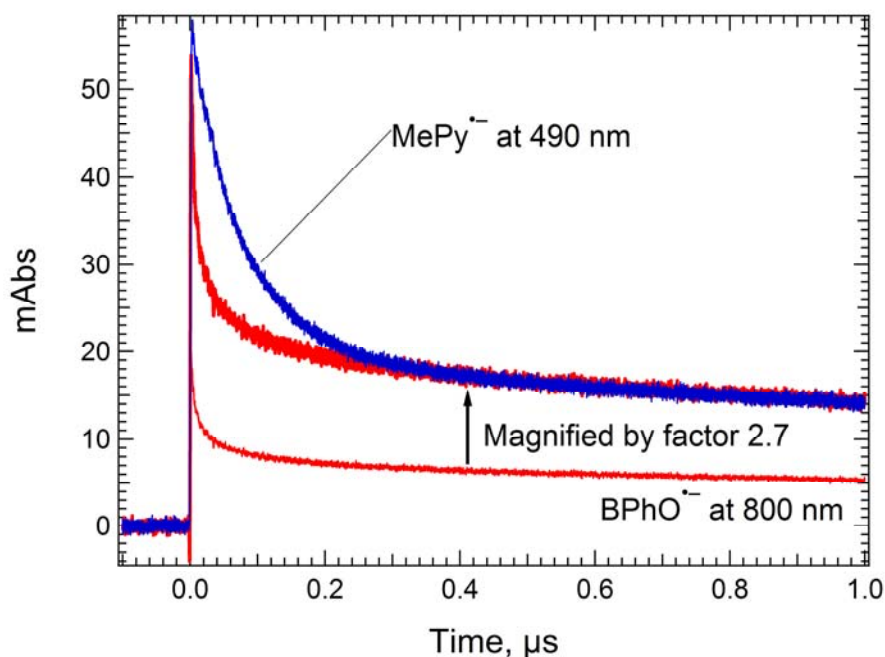


Figure B2. Kinetic traces of benzophenone radical anion ($\text{BPhO}^{\bullet-}$) at 800 nm and 1-methylpyrene radical anions ($\text{MePy}^{\bullet-}$) at 490 nm in THF with $[\text{BPhO}] = 50$ mM and $[\text{MePy}] = 40$ mM, respectively. From Figure 4 and 5, F_h of $\text{BPhO}^{\bullet-}$ and $\text{MePy}^{\bullet-}$ are almost identical. The extinction coefficient (ϵ) of $\text{MePy}^{\bullet-}$ at 490 nm in THF is estimated based on the ϵ of $\text{BPhO}^{\bullet-}$ at 800 nm, which is $9.0 \times 10^3 \text{ M}^{-1}\text{cm}^{-1}$ given in the section S2 of this supporting information. Absorbance of homogenous recombination for $\text{BPhO}^{\bullet-}$ at 800 nm is magnified by factor 2.7 to match that for $\text{MePy}^{\bullet-}$ at 490 nm so ϵ of $\text{MePy}^{\bullet-}$ is $2.43 \times 10^4 \text{ M}^{-1}\text{cm}^{-1}$ at 490 nm in THF.

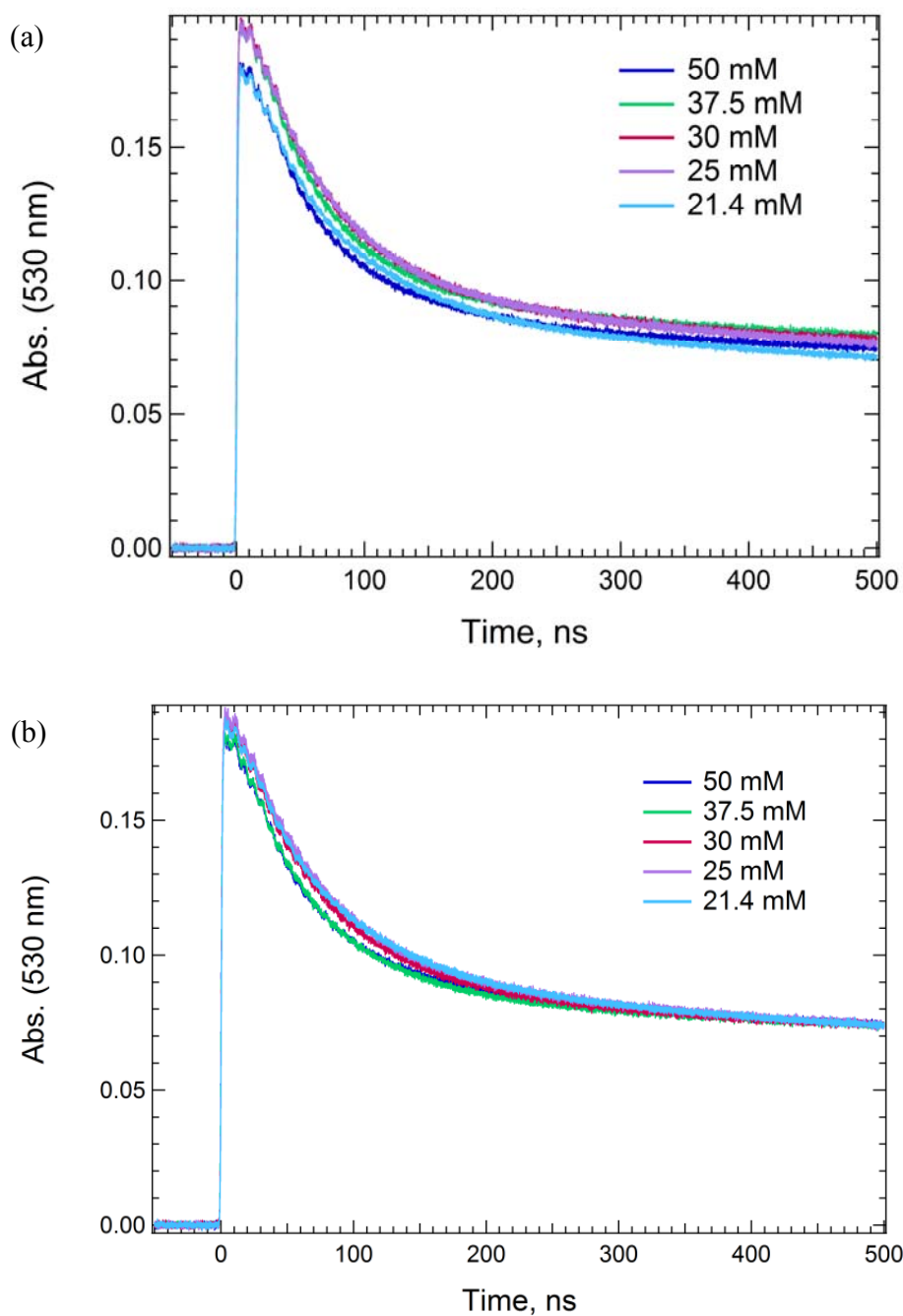


Figure B3. Kinetic traces of $F_2^{\bullet-}$ in THF with 21.4-50 mM of F_2 (a) Without normalization and (b) With normalization to match the absorbances at 400-500 ns to that of 50 mM of F_2 as standard, scaling traces for 21.4-37.5 mM by factors of 1.04, 0.97, 0.95 and 0.93, respectively. Because of non-diffusion controlled recombination of $F_2^{\bullet-}$ with solvated protons, F_2 is a good reference for observing the number of the captured electrons by different concentrations. From comparisons of normalized absorbance at 2 ns between 21.4-50 mM of F_2 , different concentration of F_2 capture similar numbers of electrons within 1%.

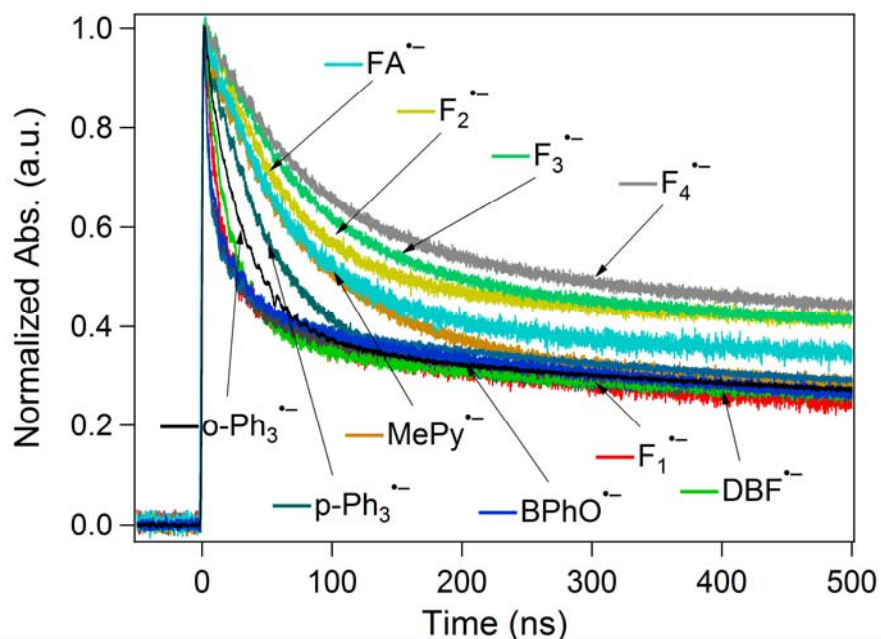


Figure B4. Normalized kinetic traces for radical anions of benzophenone (BPhO 50 mM at 800 nm), fluoranthene (FA 60 mM at 450 nm), 1-methylpyrene (MePy 40 mM at 490 nm), dibenzofuran (DBF 50 mM at 680 nm), *p*-terphenyl (*p*T 50 mM at 950 nm), *o*-terphenyl (*o*T 50 mM at 600 nm), F₁ (50 mM at 650 nm), F₂ (30 mM at 530 nm), F₃ (30 mM at 570 nm) and F₄ (20 mM at 570 nm) without the correction for triplet-triplet absorption for FA and F_n(n=2-4). Normalization factors were 14.7, 30.1, 17.4, 27.0, 9.53, 15.6, 16.3, 8.4, 3.3 and 8.2, respectively. The observation wavelengths and extinction coefficients of anions are given in Table 1.

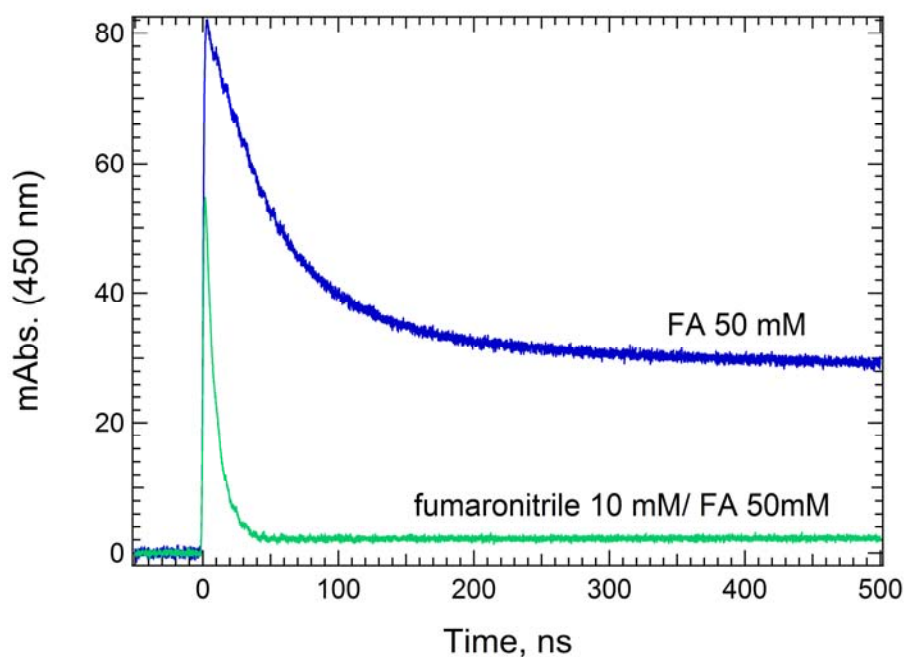


Figure B5. Kinetic traces of fluoranthene anions (FA^-) with and without 10 mM of fumaronitrile (FN) show that $^3\text{FA}^*$ absorbance is 3.8% of of the peak FA^- absorbance at 450 nm in THF. Because the reduction potential (E_{red}) of FA, -1.78 V (vs. SCE)⁸⁵, is more negative than that of FN, -1.30 V (vs. SCE),¹⁸⁹ FA^- will transfer electrons to FN. Therefore, fast decay of kinetic trace for FA with FN is due to electron transfer, and $^3\text{FA}^*$ is the only species to absorb light after ~50 ns. From the kinetic traces of FA without and with FN, we estimate the ratio of absorbance between FA^- and $^3\text{FA}^*$ at 450 nm based on absorbance of FA^- at 2 ns, 81 mO.D., and absorbance of $^3\text{FA}^*$ at 100 ns, 3 mO.D.

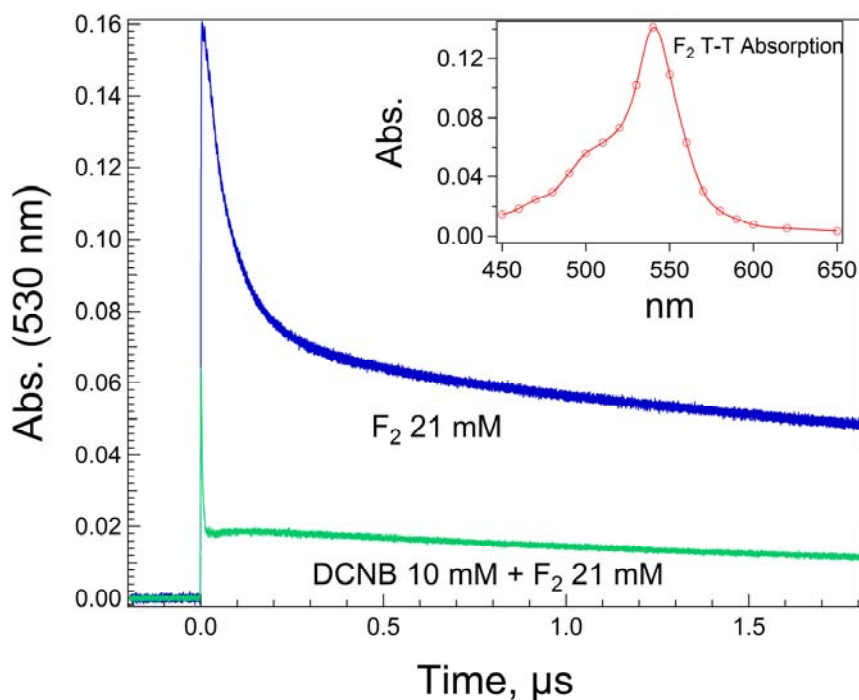


Figure B6. Kinetic traces of $F_2^{\bullet-}$ at 530 nm in THF with and without *p*-dicyanobenzene (DCNB) show that $^3F_2^*$ absorbance is 3.1% of $F_2^{\bullet-}$ absorbance. The insert shows the absorption spectrum of $^3F_2^*$ in *p*-xylene. Because the reduction potential (E_{red}) of F_2 , -2.33 V (vs. SCE),⁷⁶ is more negative than E_{red} of DCNB, -1.52 V (vs. SCE),¹⁹⁰ electrons will transfer from $F_2^{\bullet-}$ to DCNB. Therefore, fast decay of kinetic trace for F_2 with DCNB is due to electron transfer, and $^3F_2^*$ is the only species to absorb light after ~100 ns. Lifetime of $^3F_2^*$ is ~3 ms⁵⁵ so the slow decay of kinetic trace for F_2 with DCNB is due to decay of $DCNB^{\bullet-}$. An extrapolated $^3F_2^*$ absorbance, 5.3 mO.D., is constant term (A_0) for two exponentials function, $A_0 + A_1 \exp(-k_1 t) + A_2 \exp(-k_2 t)$, determined from kinetic trace of F_2 with DCNB. The ratio of absorbance between $F_2^{\bullet-}$ and $^3F_2^*$ at 530 nm is estimated by the above $^3F_2^*$ absorbance and $F_2^{\bullet-}$ absorbance of $F_2^{\bullet-}$ kinetic trace without DCNB at 2 ns, 0.16 O.D.

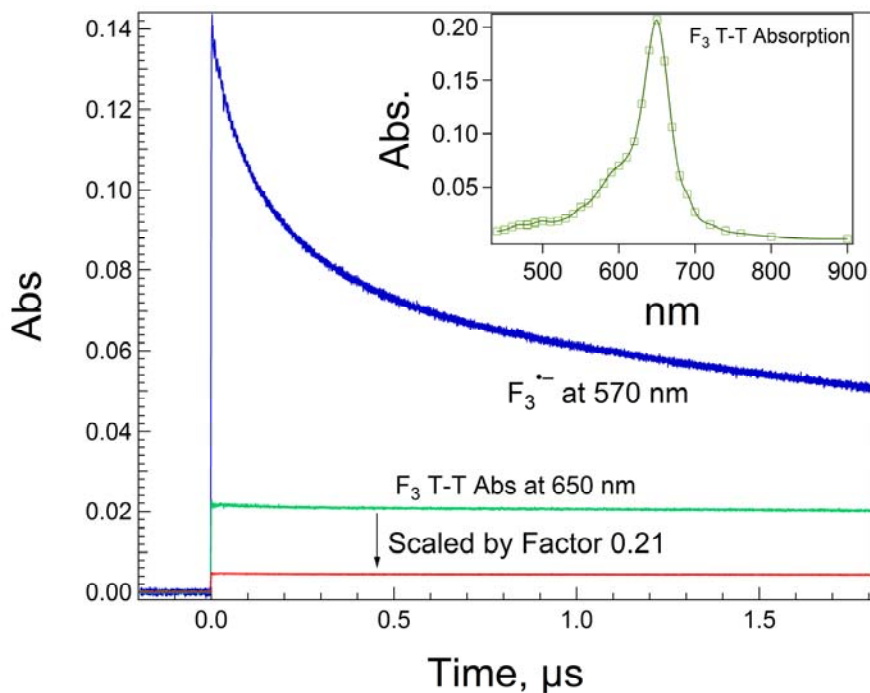


Figure B7. Kinetic traces of F_3^- and ${}^3F_3^*$ collected at 570 nm and 650 nm, respectively, show that absorbance of ${}^3F_3^*$ is $\sim 3.3\%$ of F_3^- absorbance at 570 nm at $t=2$ ns in THF with $[F_3]=20$ mM. The inset is absorption spectrum of ${}^3F_3^*$ in *p*-xylene, and it shows that A_{570}/A_{650} is 0.21, where A_λ is absorbance of ${}^3F_3^*$ at wavelength λ . ${}^3F_3^*$ absorbance at 2 ns at 570 nm is estimated by the above A_{570}/A_{650} with F_3^- absorbance at 570 nm at 2 ns.

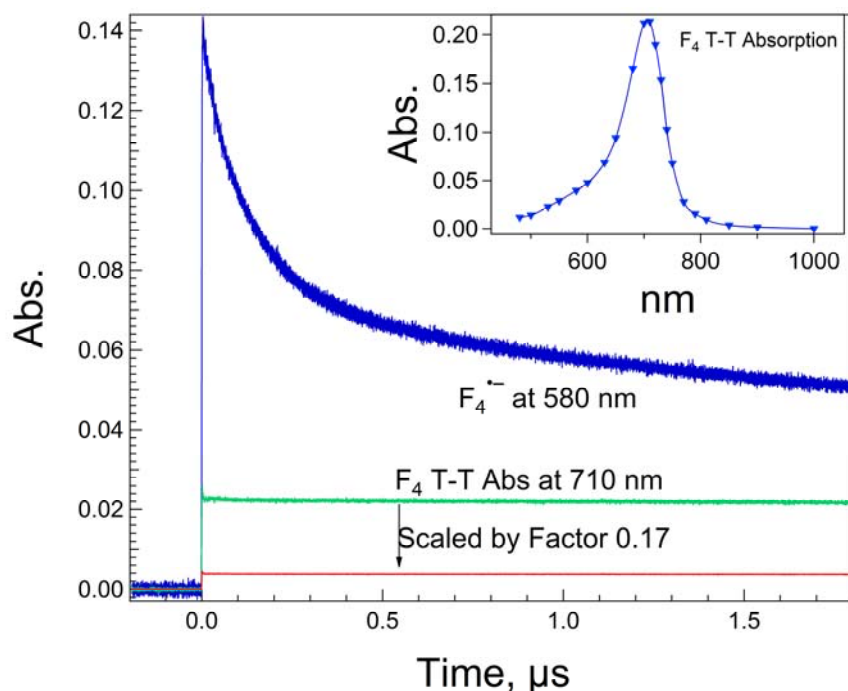


Figure B8. Kinetic Traces of $F_4^{\bullet-}$ and ${}^3F_4^*$ collected at 580 nm and 710 nm, respectively, show that absorbance of ${}^3F_4^*$ is $\sim 3.1\%$ of $F_4^{\bullet-}$ absorbance at 580 nm at $t=2$ ns in THF with $[F_4]=20$ mM. The inset is absorption spectrum of ${}^3F_4^*$ in *p*-xylene, and it shows that A_{580}/A_{710} is 0.17, where A_λ is absorbance of ${}^3F_4^*$ at wavelength λ . ${}^3F_4^*$ absorbance at 2 ns at 580 nm is estimated by the above A_{580}/A_{710} with $F_4^{\bullet-}$ absorbance at 580 nm at 2 ns.

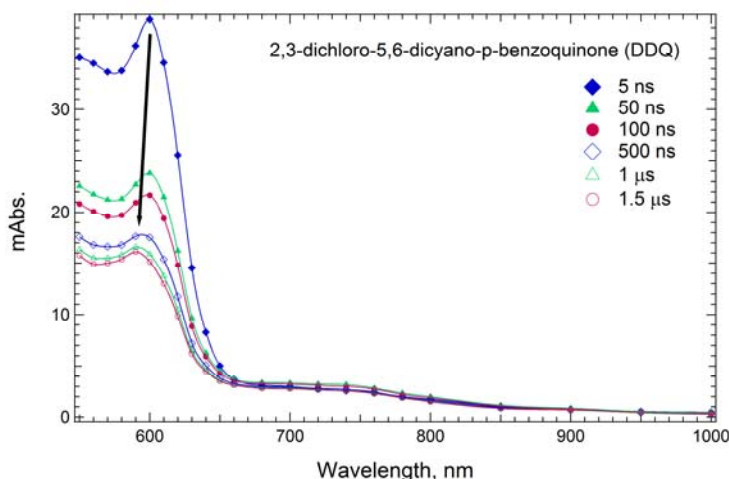


Figure B9. Transient spectra of 2,3-dichloro-5,6-dicyano-*p*-benzoquinone radical anion ($DDQ^{\bullet-}$) in THF with $[DDQ]=50$ mM shows that the absorption maximum of $DDQ^{\bullet-}$ shifts from 600 nm at 5 ns to between 590 and 600 nm with increasing time. Based on time scale of occurrence, after ~ 100 ns, for the above shifts of the spectra, these shifts may be due to reaction of impurities with $DDQ^{\bullet-}$. The small absorption band between 700-800 nm is possibly due to semiquinone radicals of DDQ produced by proton transfer reaction.

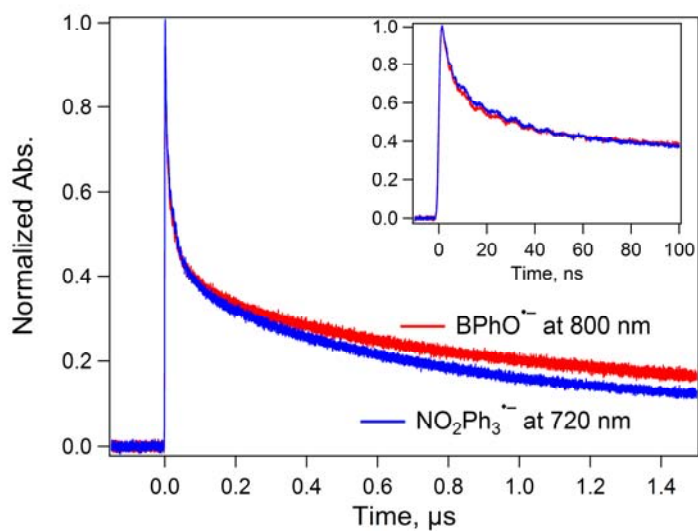


Figure B10. Normalized kinetic traces of benzophenone anion ($\text{BPhO}^{\bullet-}$) and 4-nitro-*p*-terphenyl anion ($\text{NTP}^{\bullet-}$) in THF with 50 mM of BPhO and NTP, respectively, show that geminate decay of $\text{NTP}^{\bullet-}$ similar to that of $\text{BPhO}^{\bullet-}$, with an $\sim 8 \pm 1$ ns average decay time, indicating is diffusion controlled recombination. The normalization factors of kinetic traces for $\text{BPhO}^{\bullet-}$ and $\text{NTP}^{\bullet-}$ are 14.7 and 24.6, respectively.

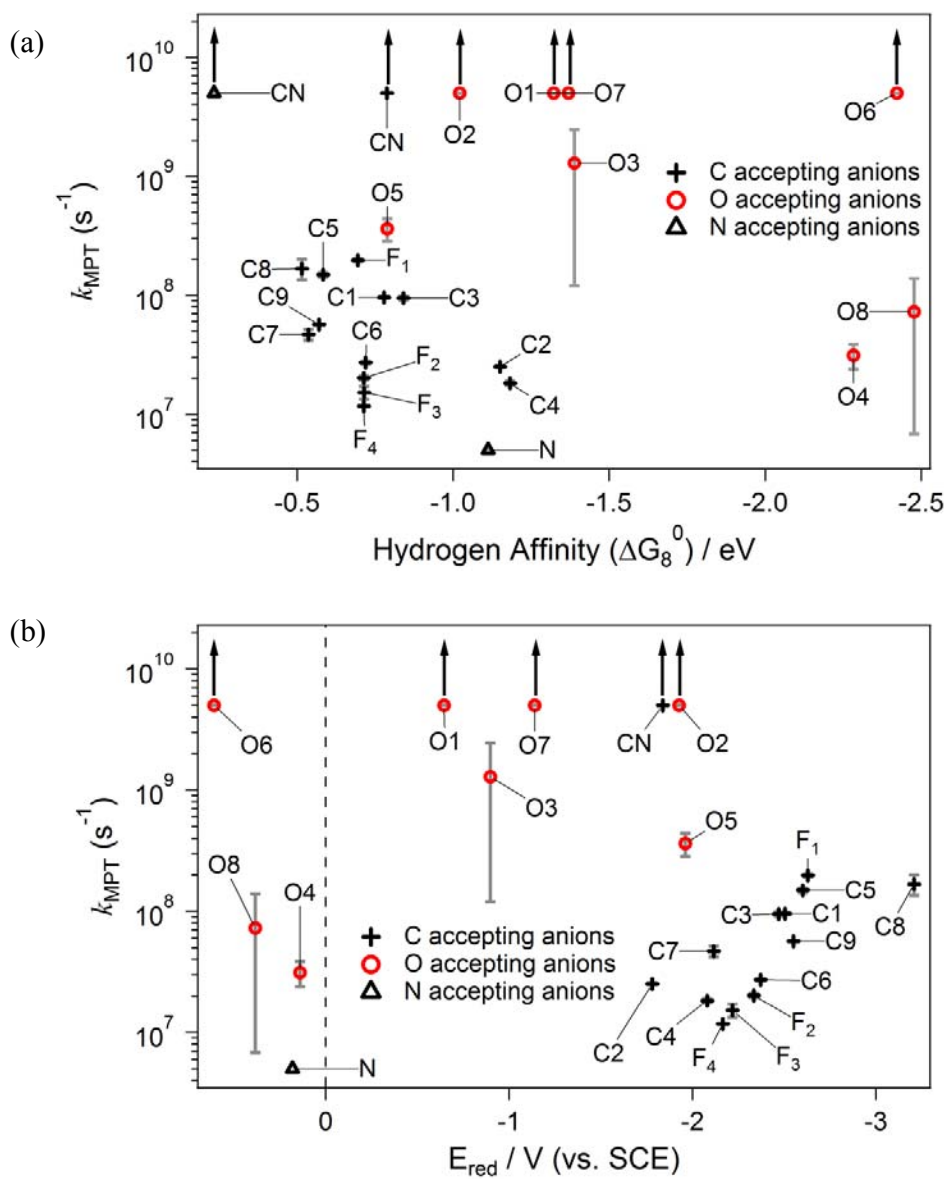


Figure B11. Plots of k_{MPT} vs. (a) Hydrogen Affinity (ΔG_8^0) and (b) Reduction Potential (E_{red}). The up arrows mean the lower limit of k_{MPT} , and symbols are given in Table 4.3.

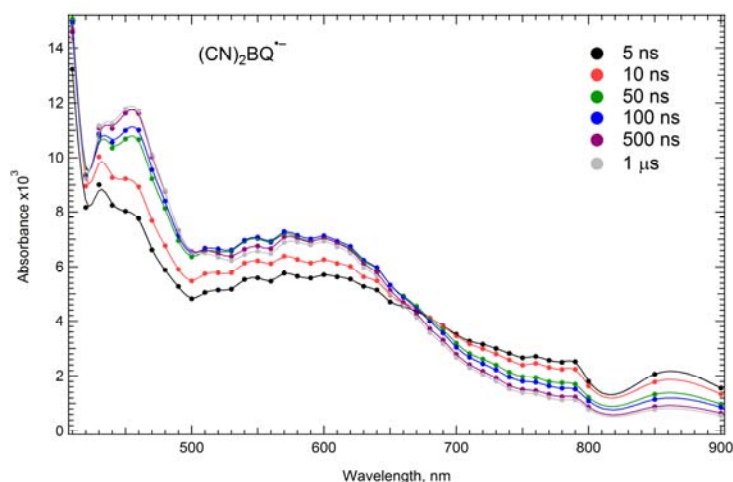


Figure B12. Transient spectra of 2,3-dicyano-*p*-benzoquinone anion, $(\text{CN})_2\text{BQ}^{\bullet-}$, in THF with 50 mM of $(\text{CN})_2\text{BQ}$. Electronic absorption band for radical anions of *p*-benzoquinone and its derivatives are broader and slightly red shifted compared with their semiquinone radicals in aqueous solutions.¹⁹¹ Time-dependent density functional theory with B3LYP/6-31G(d) in THF with the polarizable continuum model indicated that computed absorption bands of $(\text{CN})_2\text{BQ}^{\bullet-}$ and semiquinone radical of $(\text{CN})_2\text{BQ}$ are well overlapped, with the absorption band of $(\text{CN})_2\text{BQ}^{\bullet-}$ somewhat broader. The observed spectra are consistent with such broad, partly overlapped spectra. The decays of absorbance from 680 to 800 nm are due to recombination of $(\text{CN})_2\text{BQ}^{\bullet-}$ with solvated protons, and growths of absorbance from 420 to 650 nm are due to formation of semiquinone radicals of $(\text{CN})_2\text{BQ}$.

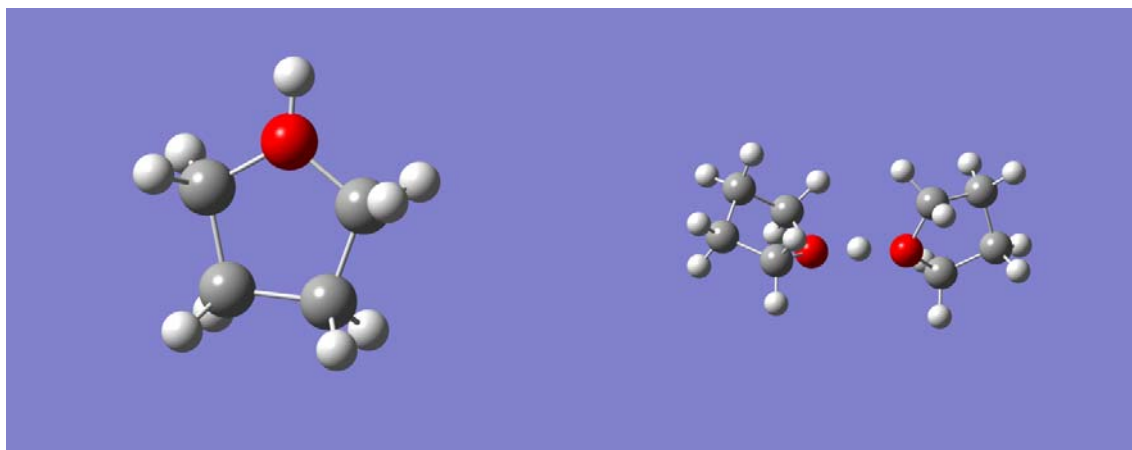


Figure B13. Chemical structures for solvated proton complexes, where protons are stabilized by one THF (Left) or two THF (Right) molecules. The above structures are optimized by B3LYP/6-31G(d) in THF with polarizable continuum model (PCM) and basis set superposition error (BSSE).

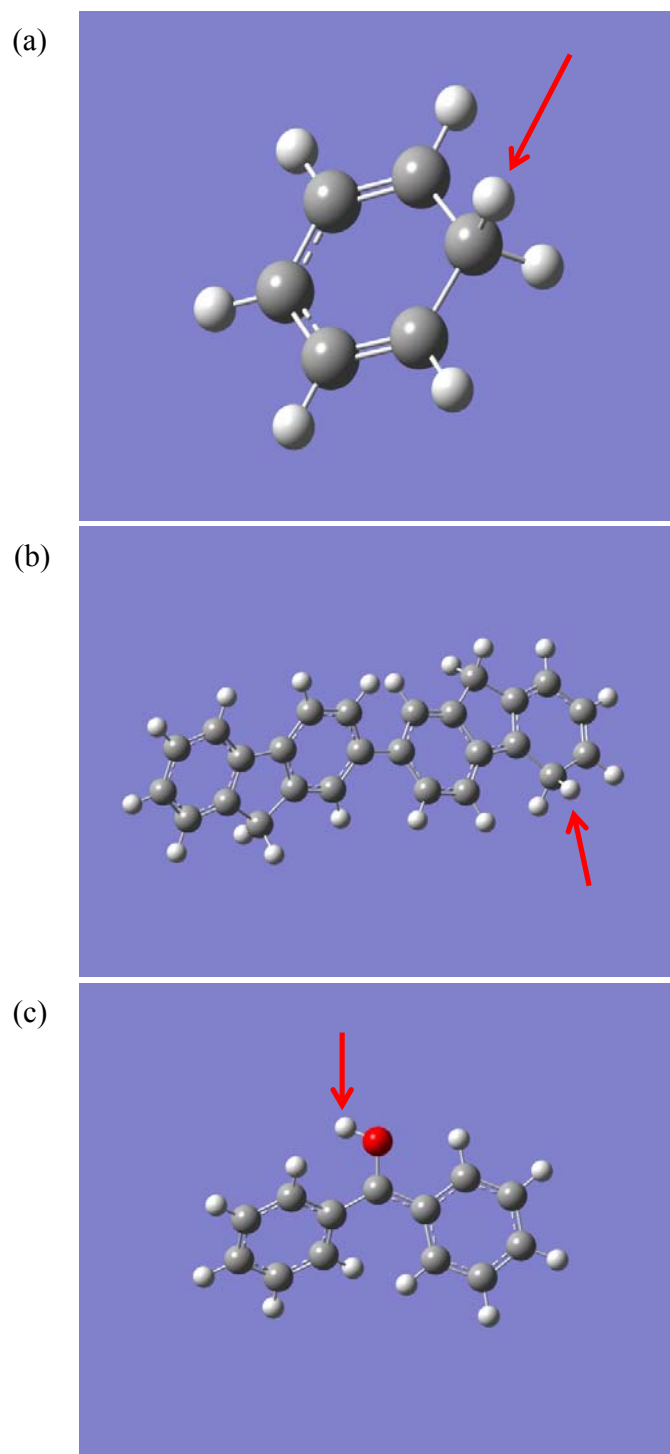


Figure B14. Images of optimized geometries for (a) benzene-H radical, BzH^\bullet , (b) $\text{F}_2\text{H}^\bullet$ and (c) benzophenone ketyl radical, BPhOH^\bullet . The red arrows point out the extra hydrogen atom. Optimizations of geometry were computed by B3LYP/6-31G(d) in THF with polarizable continuum model. The extra hydrogens of $\text{F}_2\text{H}^\bullet$ and BzH^\bullet are tetrahedral around the attachment points.

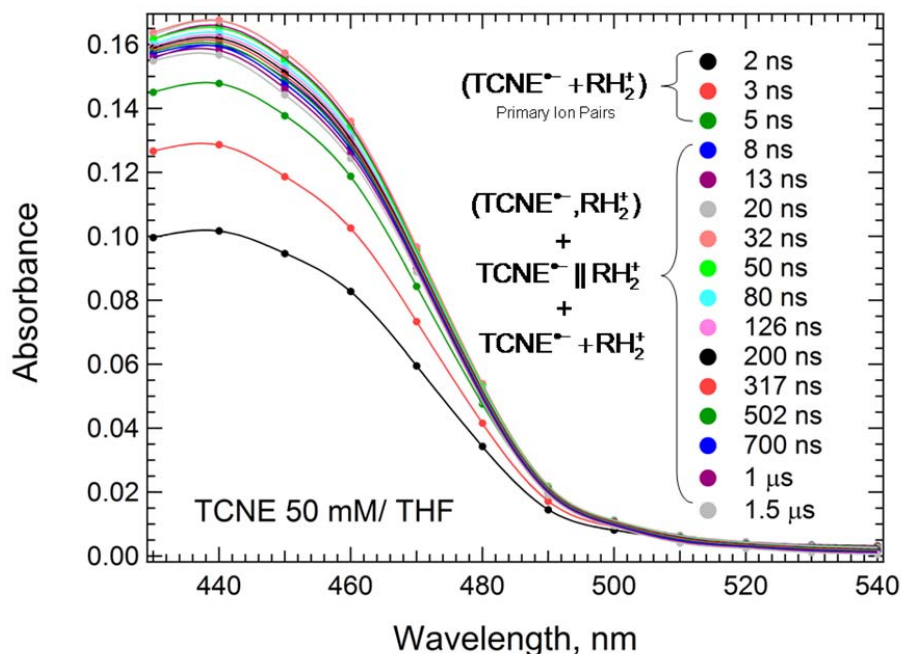


Figure B15. Transient spectra of tetracyanoethylene-solvated proton ($\text{TCNE}^{\bullet-}\text{-RH}_2^+$) ion pairs in THF with 50 mM of TCNE. Geminate primary ion pairs, $\text{TCNE}^{\bullet-} + \text{RH}_2^+$, at a variety of distances, may combine to form $(\text{TCNE}^{\bullet-}, \text{RH}_2^+)$ contact radical ion pairs (CRIP) and $\text{TCNE}^{\bullet-} \parallel \text{RH}_2^+$ solvent separated radical ion pairs (SSRIP). There are also $\text{TCNE}^{\bullet-} + \text{RH}_2^+$ free ions. Growth of $\text{TCNE}^{\bullet-}$ in the first few ns may be due to reaction of solvated electrons with TCNE, reported to proceed with a rate of $2.12 \times 10^{10} \text{ M}^{-1} \text{ s}^{-1}$,¹⁹² which is well below diffusion controlled. There is no decay of $\text{TCNE}^{\bullet-}$ and no difference between primary ion pairs, CRIP, SSRIP and free ions in absorption range 430-540 nm. According to kinetic traces of $\text{BPhO}^{\bullet-}$, primary ion pairs become CRIP, SSRIP and free ions in THF after ~ 8 ns.

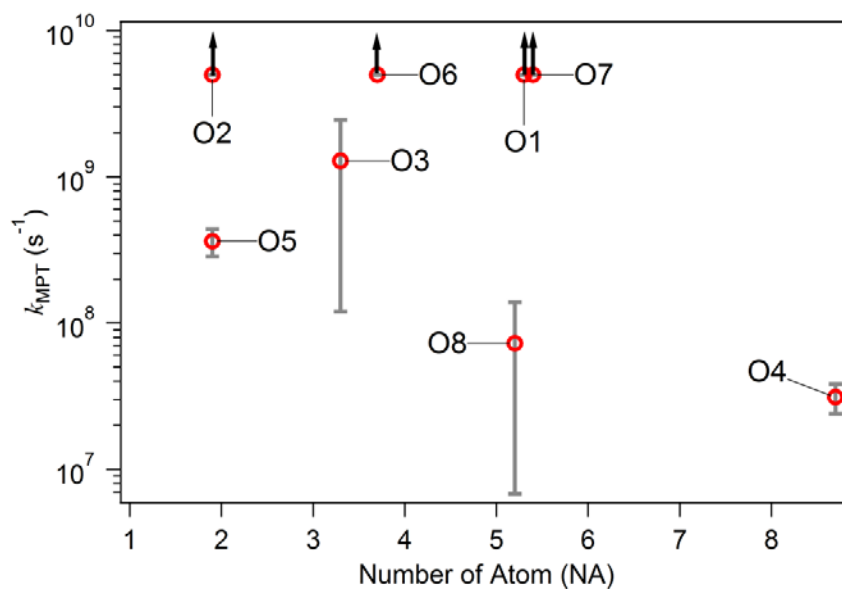


Figure B16. A plot of k_{MPT} vs. the Number of Atoms (NA) for the oxygen accepting anions, where the up arrows mean the lower limit. The symbols are given in Table 4.3.

B1. Extinction coefficients of radical anions of benzophenone and oligofluorenes ($F_n^{\cdot-}$, $n=1-4$)

With an internal reference, Na-solvated electrons ion pair, (Na^+, e_s^-), in which $\epsilon=2.4 \times 10^4 \text{ M}^{-1}\text{cm}^{-1}$ at 890 nm in THF,¹¹⁵ the extinction coefficients (ϵ) of benzophenone radical anions ($BPhO^{\cdot-}$) and oligofluorenes radical anions ($F_n^{\cdot-}$, $n=1-4$) in THF were estimated. Sodium tetraphenylborate ($NaBPh_4$) was employed to provide Na^+ to form (Na^+, e_s^-) had lifetime $\sim 2 \mu\text{s}$ ¹¹⁵ so e_s^- could attach to $BPhO$ and F_n ($n=1-4$) before recombination of e_s^- with solvated protons and THF radical cation. Na^+ also extends the lifetimes of $BPhO^{\cdot-}$ and $F_n^{\cdot-}$ ($n=1-4$) so $[BPhO^{\cdot-}]$ and $[F_n^{\cdot-}$ ($n=1-4$)] are almost identical with concentration of (Na^+, e_s^-) after electrons completely transfer from (Na^+, e_s^-) to $BPhO$ and F_n ($n=1-4$) during the observation time period.

In THF solutions, the ϵ of $BPhO^{\cdot-}$ and $F_n^{\cdot-}$ ($n=1-4$) were estimated by pulse radiolysis with 10 mM of $NaBPh_4$, and concentrations of $BPhO$ and F_n ($n=1-4$) are 0.5, 0.4, 0.3, 0.2 and 0.2 mM. Based on the dissociation equilibrium constant of $NaBPh_4$, 8.52×10^{-5} ,¹⁰⁹ in THF at 298 K, 10 mM of $NaBPh_4$ provides $\sim 938 \mu\text{M}$ of free Na^+ . Bockrath¹¹⁵ reported that Na^+ reacted with e_s^- with a rate constant $7.90 \times 10^{11} \text{ M}^{-1}\text{s}^{-1}$, which was faster than electron attachment rate constants of $BPhO$ and F_n ($n=1-4$) given in Table 1. Most e_s^- attaches first to Na^+ in the first ~ 2 ns followed by electron transfer from (Na^+, e_s^-) to solutes. From Figure B17 (a), kinetic traces of (Na^+, e_s^-) at 890 nm with and without 0.5 mM of $BPhO$ show that electrons completely transfer from (Na^+, e_s^-) to $BPhO$ after 1 μs . The kinetic trace of $BPhO^{\cdot-}$ at 700 nm with $NaBPh_4$ shows that the lifetime of $BPhO^{\cdot-}$ is extended by Na^+ . Therefore, ϵ of $BPhO^{\cdot-}$ at 700 nm is $9.0 \times 10^3 \text{ M}^{-1}\text{cm}^{-1}$ estimated from ratio of absorbance between 2 ns and 2 μs with the assumption that numbers of (Na^+, e_s^-) and $BPhO^{\cdot-}$ are identical. ϵ of $F_n^{\cdot-}$ ($n=1-4$) were estimated by the same method described in the above.

The presence of Na^+ may shift the absorption bands of radical anions in THF so transient spectra of $F_n^{\cdot-}$ ($n=2-4$) given in Figure 4.2 are compared to reported transient spectra of $F_n^{\cdot-}$ ($n=2-4$)⁷⁶ created by using sodium biphenyl to reduce F_n ($n=2-4$) in THF. The above comparisons show that no obvious absorption band shift at observation wavelengths of $F_n^{\cdot-}$ ($n=2-4$) in the presence of Na^+ . From Figure B17 (b), $F_1^{\cdot-}$ absorption at 650 nm is shifted slightly by Na^+ in THF. Transient absorption spectra of $BPhO^{\cdot-}$ with and without $NaBPh_4$ shown in Figure B17(c) indicate that Na^+ shifts the absorption band of $BPhO^{\cdot-}$ from 800 to 700 nm in THF. From Figure B17(c), oscillator strengths (f) of $BPhO^{\cdot-}$ with and without $NaBPh_4$ from 600 to 1000 nm are 0.4176 and 0.4817, respectively; f of the former one is $\sim 86.7\%$ of that of the latter one. The above comparison suggests that these two absorption spectra are contributed by the same absorption band of $BPhO^{\cdot-}$. Therefore, the ϵ of $BPhO^{\cdot-}$ at 700 and 800 nm are identical.

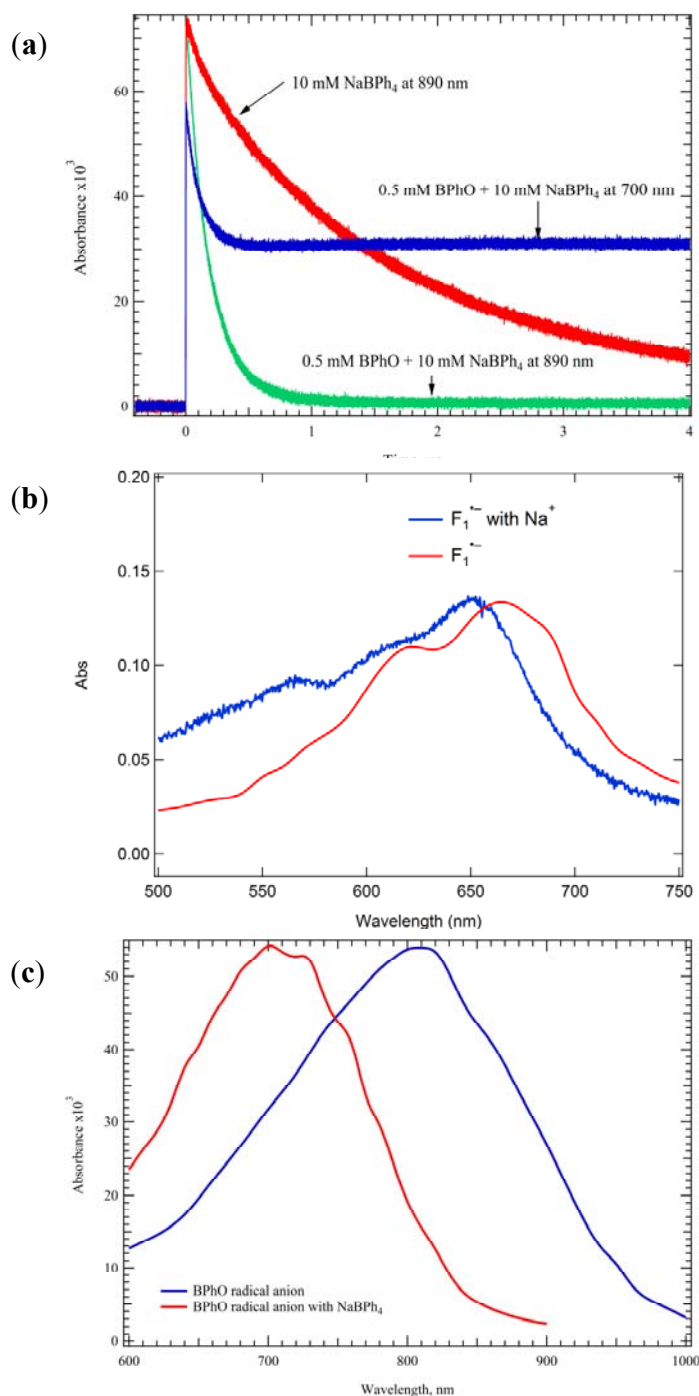
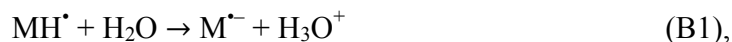


Figure B17. (a) The kinetic traces at 890 nm are for 10 mM of sodium tetraphenylborate (NaBPh₄) with and without 0.5 mM of benzophenone (BPhO) and at 700 nm for 10 mM of NaBPh₄ with 0.5 mM of BPhO. (b) Transient spectra of $F_1^{\cdot-}$ and $(F_1^{\cdot-}, Na^+)$ in THF. The $F_1^{\cdot-}$ is the 10 ns transient spectrum given in Figure 4.2, and the $(F_1^{\cdot-}, Na^+)$ is for F_1 reduced by sodium biphenyl. (c) Transient spectra of BPhO $^{\cdot-}$ were collected in THF with and without 10 mM of NaBPh₄.

B2. Estimation for Difference of Hydrogen Atom Affinity ($\Delta\Delta G_8^0$)

In water, the MH^\bullet radicals undergo acid dissociation:



where MH^\bullet is the product of the proton transfer reaction (reaction 4.4a), $M^{\bullet-}$ is radical anion. The standard free energy change (ΔG^0) of reaction B1 can be estimated from pKa of MH^\bullet . In water, the above reaction can be separated into four parts, which are:



where reaction B2 is the hydrogen dissociation reaction. The standard free energy change (ΔG^0) of acid dissociation reaction is sum of ΔG^0 from reaction B2 to B5. Because this reaction is the reverse reaction of the hydrogen atom attachment reaction (reaction 4.8), the hydrogen atom affinity (ΔG_8^0) is the $-\Delta G^0$ of the reaction B2. Based on the experimental values of ΔG^0 for reactions B3 to B5, an experimental value of ΔG_8^0 in water can be estimated. ΔG^0 of reaction B3 is estimated by E_{red} subtracting liquid Fermi-level of the reference electrode. The liquid Fermi-level of SCE is -4.71 V.⁹⁸ ΔG^0 of reaction B4 is 13.61 eV⁹⁹ and ΔG^0 of reaction B5 is 0.65 eV.¹⁹³⁻¹⁹⁴ Based on pKa and E_{red} in water, the hydrogen atom affinity (ΔG_8^0 from reaction 4.8) is estimated by equation B6:

$$\Delta G_8^0 = RT \ln(10^{-pK_a}) - (E_{red} - 4.71) - 13.61 - 0.65 \text{ eV} \quad (B6),$$

where R is the gas constant and T is temperature.

The uncertainty of ΔG_8^0 is roughly estimated to be ~ 0.3 eV. In water, the calculated ΔG_8^0 difference ($\Delta\Delta G_8^0$) between benzophenone (BPhO) and anthraquinone (AQ) is 0.308 eV. Based on calculations of ΔG_8^0 described in the section 4.4, the calculated ΔG_8^0 of BPhO and AQ are -1.001 and -1.309 eV in water. The experimental $\Delta\Delta G_8^0$ between BPhO and AQ is 0.5 eV in water. The experimental ΔG_8^0 of BPhO and AQ are -8.913 and -9.413 eV in water. These values are estimated by equation B6 with the reported pKa's and E_{red} of BPhO and AQ in water. In water, the reported pKa's of BPhO and AQ are 9.25 and 5.3 ,¹⁰² and the reported E_{red} (vs. SCE) of BPhO and AQ are -1.184 ^{102,195} and -0.45 V.¹⁹⁶ The difference between the calculated and experimental $\Delta\Delta G_8^0$ is 0.192 eV in water.

B3. Measuring the Maximum Observed $G(t)$ and G_{fi} Values of Benzophenone Radical Anions

The $G(t)$ value of benzophenone radical anions ($\text{BPhO}^{\bullet-}$) in THF is estimated by equation B7 with the $G(t)$ value of solvated electrons (e_s^-) in standard solution, which is 20 vol% of methanol, 80 vol% of water and 0.1 M of NaOH.

$$G_b = \frac{G_{\text{std}} \epsilon_{\text{std}} \rho_{\text{THF}} A_b}{\epsilon_b \rho_{\text{std}} A_{\text{std}}} \quad (\text{B7}),$$

where G_b is the $G(t)$ values of $\text{BPhO}^{\bullet-}$ in THF, G_{std} is the $G(t)$ value of e_s^- in the standard solution, A_b is absorbance of $\text{BPhO}^{\bullet-}$ in THF, A_{std} is absorbance of e_s^- in the standard solution and other constants are given in Table B1.

Table B1. Constants for equation B7: extinction coefficients of solvated electrons (ϵ_e) in standard solution, extinction coefficient of benzophenone radical anion (ϵ_b), density (ρ) of standard solution and THF.

	ϵ_e ($\text{M}^{-1}\text{cm}^{-1}$)	ϵ_b ($\text{M}^{-1}\text{cm}^{-1}$) ^c	ρ (g/cm^3)
^a Std.	^b 2.30×10^4 at 760 nm		1.0075
THF			0.8892
Benzophenone		7.90×10^3 at 760 nm	

^aStandard Solution ^bPersonal communication with Dr. Andrew Cook from Chemistry Department of Brookhaven National Laboratory. ^cEstimated from transient absorption spectra without NaBPh_4 in Figure B17(b) with ϵ of benzophenone radical anion, $9.00 \times 10^3 \text{ M}^{-1}\text{cm}^{-1}$ at 700 nm in THF.

The maximum observed $G(t)$ values of $\text{BPhO}^{\bullet-}$ in THF with 50, 100 and 200 mM of BPhO are determined by the following procedures from kinetic traces of $\text{BPhO}^{\bullet-}$ in Figure B18(a) and (b) collected by optical fiber single shot⁵³ (OFSS) with 5 ps of response time. For 50 mM of BPhO in THF, the G_{max} value of $\text{BPhO}^{\bullet-}$ is 2.41 per 100 eV determined by equation B7 with maximum absorbance of $\text{BPhO}^{\bullet-}$ at 280 ps from kinetic trace for 50 mM of BPhO in Figure B18(a), A_{std} at 5 ps from kinetic trace of e_s^- in Figure B18(b) and extrapolated the $G(t=0)$ value of e_s^- in the standard solution, 3.87 per 100 eV.¹⁹⁷ The maximum observed $G(t)$ values of $\text{BPhO}^{\bullet-}$ for 100 mM BPhO is 2.79 per 100 eV and that of 200 mM BPhO is 3.16 per 100 eV. These maximum observed $G(t)$ values are determined by the same method described in the above. The maximum absorbance and $G(t)$ values of 50, 100 and 200 mM are given in Table B2.

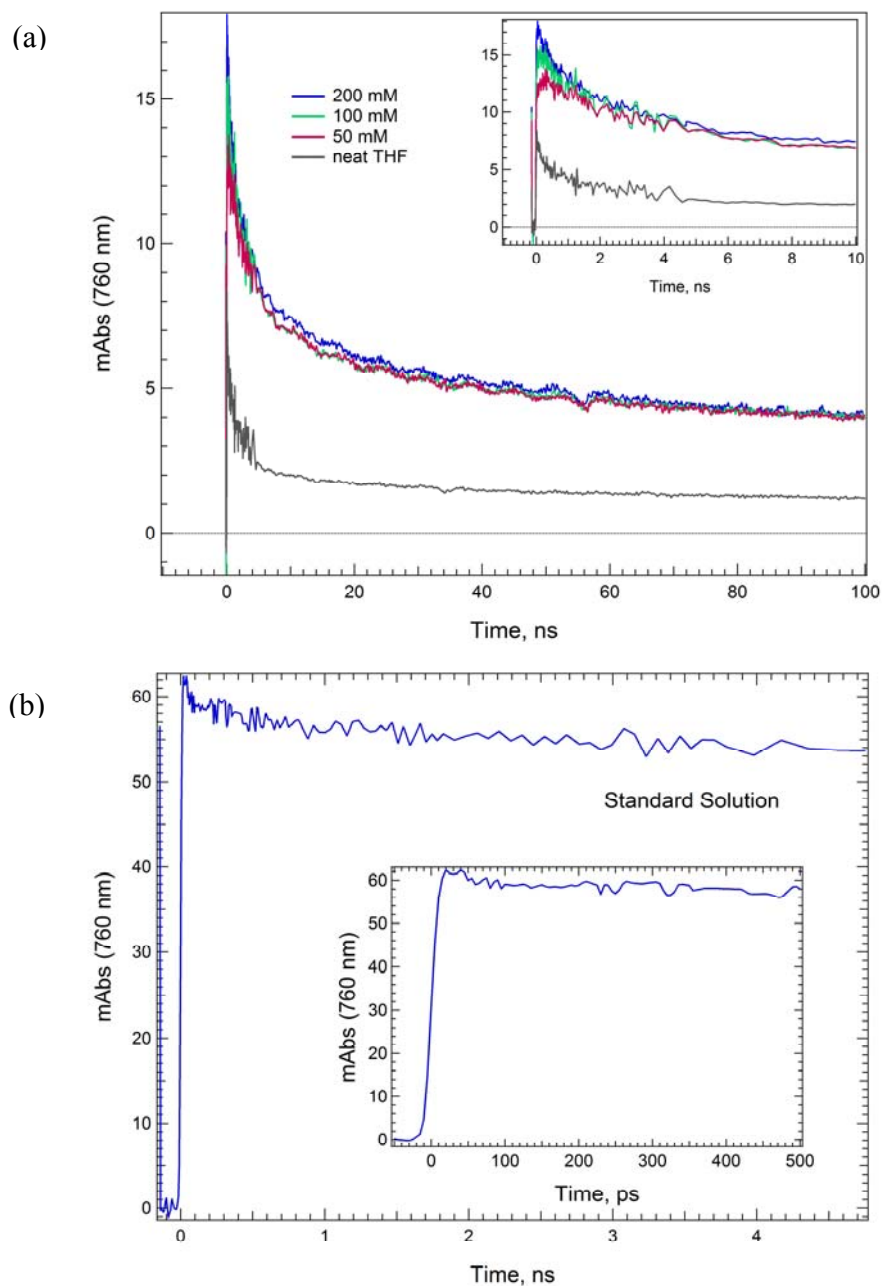


Figure B18. (a) Kinetic traces of neat THF and BPhO⁻ in THF solution with 50, 100 and 200 mM of BPhO collected by optical fiber-based single shot (OFSS).⁵³ (b) Kinetic trace of solvated electron in the standard solution collected by OFSS.⁵³ The standard solution is water with 0.1 M of NaOH and 20 vol% of methanol.

Table B2. List for concentrations of benzophenone, transient absorbance (A_b) of $\text{BPhO}^{\bullet-}$ at 760 nm in THF and the maximum $G(t)$ values of $\text{BPhO}^{\bullet-}$ per 100 eV.

Conc. (mM)	A_b	$^aG(t)$
200	0.017	3.16 (60 ps)
100	0.015	2.79 (150 ps)
50	0.013	2.41 (280 ps)

^aUnit is per absorbing 100eV.

The G_{fi} value of free ions is $G_{max}F_h$, where F_h is the fraction of homogenous recombination. From data in Figure B18(a), the absorbance of $\text{BPhO}^{\bullet-}$ are almost identical after 1 ns in 50, 100 and 200 mM of BPhO solutions that suggest nearly identical the G_{fi} and $G(t > 1 \text{ ns})$ values of $\text{BPhO}^{\bullet-}$ in different concentration of BPhO solution. Therefore, the G_{fi} value of $\text{BPhO}^{\bullet-}$, 0.69 per 100 eV, was determined from data shown in Figure B19, where $[\text{BPhO}] = 50 \text{ mM}$. Kinetic trace in Figure B19 was collected by photodiode (EG&G FND-100, 2 ns response time). Therefore, the $G(t=2 \text{ ns})$ value is the G_{max} for estimation of the G_{fi} value of $\text{BPhO}^{\bullet-}$. Based on ratio of absorbance between 280 ps and 2 ns, the $G(t=2 \text{ ns})$ value of $\text{BPhO}^{\bullet-}$ is 1.92 per 100 eV with $G(t=280 \text{ ps})$ value of $\text{BPhO}^{\bullet-}$ from kinetic traces for 50 mM of BPhO. From kinetic trace in Figure B19, F_h is 0.36 determined by three exponentials function from data shown in Figure B19, time range from 2 ns to 1.8 μs .

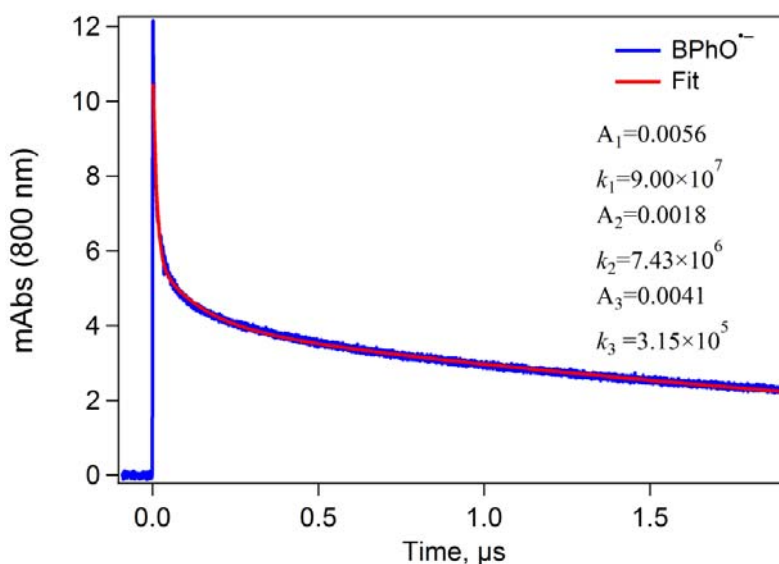


Figure B19. Kinetic trace of benzophenone radical anions ($\text{BPhO}^{\bullet-}$) was collected by transient digitalization with photodiode (EG&G FND-100, 2 ns response time) in THF with 50 mM of BPhO. The fraction of free ion (F_h) is $A_3/(A_1+A_2+A_3)$ from fitting results of a three exponential function, $A_1 \exp(-k_1 t) + A_2 \exp(-k_2 t) + A_3 \exp(-k_3 t)$, over the time period from 2 ns to 1.8 μs , where A_i ($i=1-3$) are absorbances for each exponential decay.

B4. The Fraction of Captured Electrons for Benzophenone (BPhO)

The electrons created by the pulse radiolysis can be captured by a “step capture”¹¹⁸⁻¹²¹ processes and electron attachment. The “step capture” is a mechanism that presolvated electrons instantly captured by solute.¹¹⁸⁻¹¹⁹ The step captured fraction of the electrons (F_{ps}) for BPhO can be estimated by:

$$F_{ps} = 1 - \exp(-q[s]) \quad (\text{B8}),^{120-121}$$

where $[s]$ is the concentration of BPhO, and q is the quencher coefficient. For BPhO, we use $q=11.5 \text{ M}^{-1}$ from measurement on biphenyl¹¹⁸ to calculate F_{ps} because sizes of BPhO and biphenyl are similar. The solvated electrons (e_s^-) are the electrons solvated by solvent molecules and surviving from the step capture. In other words, the e_s^- fraction of the electrons is $1-F_{ps}$. The kinetic trace of e_s^- in THF shown in Figure B20, indicates that $\sim 75\%$ of e_s^- decay geminately with rate $4.55 \times 10^8 \text{ s}^{-1}$ (k_{gd}) and $\sim 25\%$ of e_s^- decay homogenously with rate $3.15 \times 10^7 \text{ s}^{-1}$ (k_{hd}). The capture e_s^- fraction of the electrons (F_s) for BPhO can be estimated by:

$$F_s = \left(0.75 \cdot \frac{k_{att}[s]}{k_{att}[s] + k_{gd}} + 0.25 \cdot \frac{k_{att}[s]}{k_{att}[s] + k_{hd}} \right) \cdot (1 - F_{ps}) \quad (\text{B9}),$$

where k_{att} is the attachment rate constant, $6.4 \times 10^{10} \text{ M}^{-1} \text{ s}^{-1}$, given in Table 4.1. The fractions of captured electrons of 50, 100 and 200 mM of BPhO are given in Table B3.

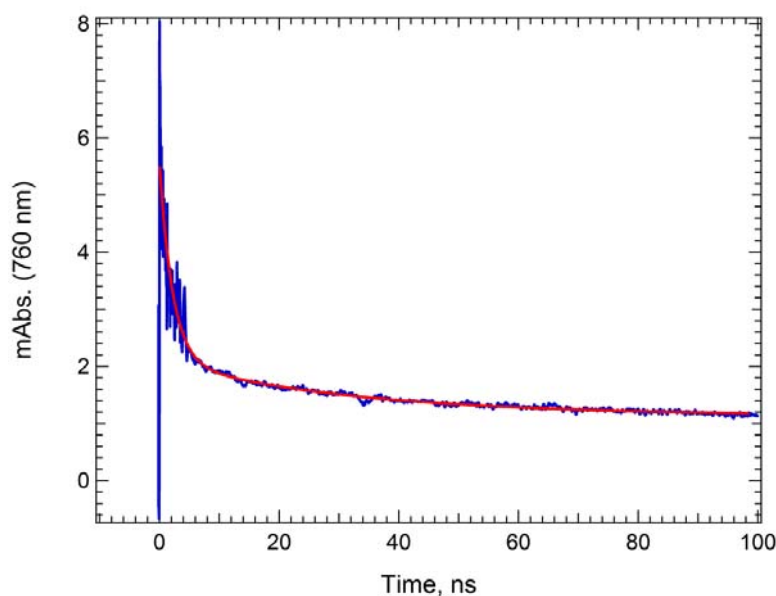


Figure B20. Kinetic trace of e_s^- at 760 nm in THF collected by OFSS.⁵³ The red line is the fit of double-exponential function, $A_0 + A_1 \exp(-k_{gd}t) + A_2 \exp(-k_{hd}t)$, where $k_{gd}=4.55 \times 10^8 \text{ s}^{-1}$ and $k_{hd}=3.15 \times 10^7 \text{ s}^{-1}$.

Table B3. Estimated fractions of the step-captured electrons (F_{ps}), solvated electrons captured by electron attachment (F_s) and total fraction of electrons (F_{tot}) captured by benzophenone (BPhO) with different concentrations.

Conc.	^a F_{ps}	^b F_s	^c F_{tot}
200 mM	0.898	0.099	0.997
100 mM	0.683	0.300	0.983
50 mM	0.437	0.509	0.946

^aCalculated by equation B8 and see text ^bCalculated by equation B9 and see text ^c $F_{tot}=F_{ps}+F_s$

Appendix C. Supporting Information for Chapter 5.

Table C1 Fitting Results of a Three-Exponential and a Two-Exponential Functions for 20 and 40 mM F₃ Solutions at 640 and 1500 nm.

Conc.		20 mM	40 mM
^{a,c} 1500 nm	^a k_{d1} (s ⁻¹)/A ₁ (O.D.)	5.18(±0.03)×10 ⁸ / 0.0103	5.01(±0.01)×10 ⁸ / 0.0132
	^a k_{d2} (s ⁻¹)/A ₂ (O.D.)	1.02(±0.07)×10 ⁷ / 0.0015	2.26(±0.11)×10 ⁷ / 0.0025
	^a k_{d3} (s ⁻¹)/A ₃ (O.D.)	1.32(±0.02)×10 ⁵ / 0.0026	2.49(±0.02)×10 ⁵ / 0.0035
^{b,c} 640 nm	^b k_{g1} (s ⁻¹)	^b -2.85(±0.02)×10 ⁷	^b -2.99(±0.01)×10 ⁷
	^b k_{g2} (s ⁻¹)	^b -1.63(±0.01)×10 ⁶	^b -2.12(±0.01)×10 ⁶

^aFit by a three exponential function, $A_1 \exp(-k_{d1}t) + A_2 \exp(-k_{d2}t) + A_3 \exp(-k_{d3}t)$, where A_i ($i=1-3$) are absorbance for each exponential decay. ^bFitting results of a two exponential function to the data. The growth rates are k_{g1} and k_{g2} , where minus signs mean growth of kinetic traces. ^cBecause the data of 5 and 10 mM F₃ solutions shown in Figure 5.7(a) are small and noisy, the fitting results may be not reliable. Therefore, no fitting results is available.

Table C2. Free Ion Yield of F₃ from Photoexcitation in THF

Conc.	20 mM	40 mM
^a Free Ion Yield	0.18±0.02	0.18±0.02

^aFrom the fitting results of a three exponential function in Table C1, the free ion yield is $A_3/(A_1+A_2+A_3)$. A_i ($i=1-3$) are absorbance for each exponential decay. Based on the uncertainty of extinction coefficients, the uncertainty of the free ion yield is estimated.

Table C3. F₃ Ion Pairs created by Photoexcitation in THF.

[F ₃] (mM)	40	20	^e 10	^e 5
^a [IRIP] (μM)	2.3	1.4	0.3	N/A
^b Φ	0.051	0.0031	0.0067	N/A
^c k_{Biq} (M ⁻¹ s ⁻¹)	1.48×10 ⁹	2.00×10 ⁹	8.13×10 ⁸	N/A
^d [F _i ^{II}] (μM)	0.41	0.25	N/A	N/A

^aConcentration of Intimate Radical Ion Pairs (IRIPs). Scheme 5.1 and Figure 5.10 (a) show that photoexcitation only creates IRIPs, and most IRIPs are contact radical ion pair. ^bQuantum Yield of Forming F₃ Ion Pairs. Because extinction coefficients (ϵ) of quaterthiophene (T₄) and T₄ triplet excited states ($^3T_4^*$) and triplet quantum yield (Φ_T) of T₄ are well known, T₄ is used to estimate the total number of photons. From this publication,²⁴ the ϵ of T₄ and $^3T_4^*$ are 3.00×10⁴ M⁻¹cm⁻¹ at 397 nm and 5.50×10⁴ M⁻¹cm⁻¹ at 600 nm, and Φ_T of T₄ is 0.7. ^cBimolecular quenching rate constant for that excited F₃ molecules are quenched by neutral F₃ molecules. ^dConcentration of the Type II Free Ions. [F_i^{II}] are calculated by [IRIP] and the free ion yields from Table C1. ^eBecause the data of 5 and 10 mM F₃ solutions in Figure 5.7(a) are small and noisy, only [IRIP] of 10 mM data is estimated.

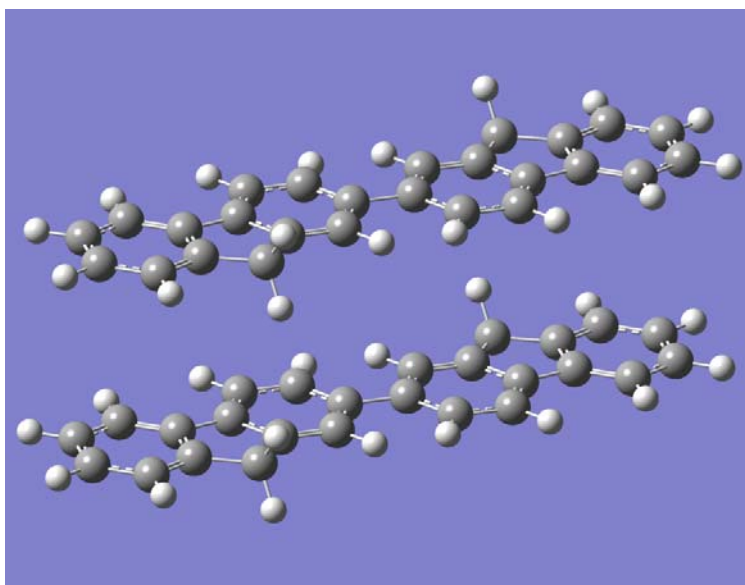


Figure C1 An example of face-to-face stacking radical ion pair for F_2 .

C1. Estimation of Extinction Coefficients for Tetracene Radical Anion and Cation, Oligofluorene Radical Cations, F_n^{*+} ($n=1-6$).

With biphenyl radical anion ($BP^{\bullet-}$) as an internal reference, tetrabutylammonium hexafluorophosphate ($TBAPF_6$) as a stabilizer to extend lifetimes of the anions and a proper concentration gradient $[BP] \gg [TC]$, the anion extinction coefficient (ϵ_a) of tetracene anion ($TC^{\bullet-}$) is estimated in THF. After solvated electrons created by pulse radiolysis in THF, BP captures most solvated electrons to become $BP^{\bullet-}$. From the reduction potential (E_{red}) of BP given in Table 4.3 and E_{red} of TC given in Table 5.2, the electrons will transfer from $BP^{\bullet-}$ to TC. Because $TBAPF_6$ extends lifetimes of the anions, the electrons will completely transfer from $BP^{\bullet-}$ to TC before $BP^{\bullet-}$ recombining with the solvated protons. After the complete electron transfer, $TBAPF_6$ also prevent $TC^{\bullet-}$ from recombining with the solvated protons. Therefore, $[BP^{\bullet-}]$ and $[TC^{\bullet-}]$ are almost identical over the observation time period. With ϵ_a of $BP^{\bullet-}$, $1.25 \times 10^4 \text{ M}^{-1}\text{cm}^{-1}$ at 650 nm,¹¹⁸ the ϵ_a of $TC^{\bullet-}$ at 830 nm can be estimated.

ϵ_a of $TC^{\bullet-}$ at 830 nm is estimated by pulse radiolysis in THF solution with 1 mM of TC, 50 mM of BP and 10 mM of $TBAPF_6$. After the ionization (reaction 4.1), high concentration BP captures most solvated electrons. From kinetic traces of BP at 650 nm shown in Figure C2, 80% of $BP^{\bullet-}$ determined by a two exponential function have lifetimes longer than 1.9 μs . Based on ϵ_a of $BP^{\bullet-}$ at 650 nm and 80% of the 2 ns absorbance from kinetic trace of TC mixed with BP at 650 nm shown in Figure C2, $[BP^{\bullet-}]$ is ca. 1.68 μM . From kinetic trace of TC mixed with BP at 830 nm shown in Figure C2, the electrons completely transfer from $BP^{\bullet-}$ to TC after 0.5 μs , and lifetime of $TC^{\bullet-}$ is also longer than 1.9 μs . Based on 1 μs absorbance at 830 nm and the assumption that $[TC^{\bullet-}] = 1.68 \mu\text{M}$, the estimated ϵ_a of $TC^{\bullet-}$ is $1.61 \times 10^4 \text{ M}^{-1}\text{cm}^{-1}$ at 830 nm.

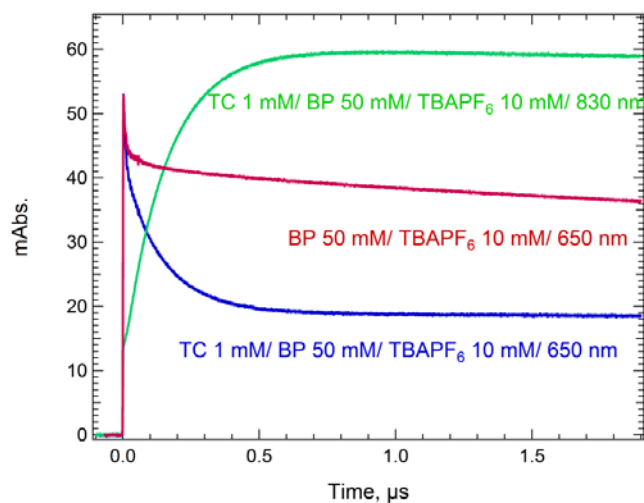


Figure C2 Kinetic traces of biphenyl (BP, 50 mM) with and without tetracene (TC, 1 mM) at 650 nm and TC (1 mM) with BP (50 mM) at 830 nm in THF solution with 10 mM of tetrabutylammonium hexafluorophosphate (TBAPF₆). The path lengths of the cells are 20 mm.

The cation extinction coefficient (ϵ_c) of TC⁺⁺ is estimated in nitrobenzene (NBz) with BP as an internal reference and a concentration gradient [BP]>[TC]. In NBz, pulse radiolysis rapidly creates solvated electrons and NBz^{•+} so solute molecules will be reduced by solvated electrons and oxidized by NBz^{•+}. The E_{red} of NBz is -0.485 V^{198,199} (vs. SCE), and it is below the E_{red} of TC given in Table 5.2 and the E_{red} of BP given in Table 4.3. The electrons will transfer from TC^{•-} and BP^{•-} to NBz quickly so only cations of TC and BP are remaining. With [BP]>[TC], BP will be oxidized by NBz^{•+} much faster than TC kinetically. The oxidation potential of BP, 1.95 V (vs. SCE),²⁰⁰ is higher than that of TC given in Table 5.2 so the holes will transfer from a BP^{•+} to a TC. With ϵ_c of BP^{•+}, $1.45 \times 10^4 \text{ M}^{-1}\text{cm}^{-1}$ at 680 nm,¹⁵² the ϵ_c of TC^{•+} can be estimated.

ϵ_c of TC^{•+} is estimated in NBz solution with 1 mM of TC and 5 mM of BP. Kinetic traces of TC (1 mM) at 680 and 830 nm in NBz solution with 5 mM of BP are shown in Figure C3. After electron pulse, high concentration BP are oxidized by NBz^{•+}. Because NBz is polar solvent, most ions created by pulse radiolysis is free ion. Therefore, most ion recombination in NBz is homogenous, bimolecular. 1 mM of TC is capable of capture most homogenous BP^{•+}. From kinetic trace of BP at 680 nm, a two exponential function estimate that 90% of BP^{•+} are homogenous. Based on the 90% of 2 ns absorbance at 680 nm from kinetic trace of BP, the concentration of BP^{•+} is ~0.30 μM . Kinetic trace of TC with BP at 830 nm suggests that hole transfer from BP^{•+} to TC is complete after 4 μs . Based on 4 μs absorbance at 830 nm from data of TC with BP, ϵ_c of TC^{•+} is $3.87 \times 10^4 \text{ M}^{-1}\text{cm}^{-1}$ estimated with the assumption that [TC^{•+}]=0.30 μM . ϵ_c of F_n^{•+} (n=1-6) are also estimated in NBz with 5 mM of BP by the same method described in the above.

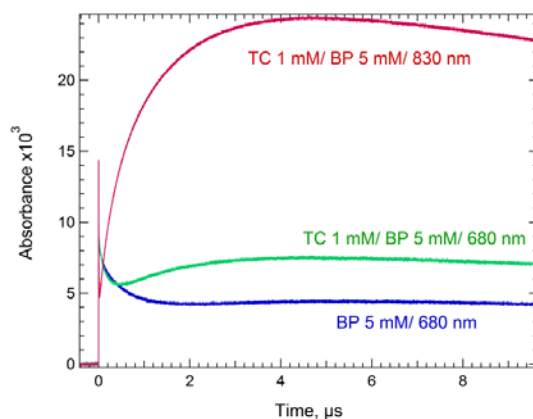


Figure C3 Kinetic traces of tetracene (TC, 1 mM) with and without biphenyl (BP, 5 mM) at 680 and 830 nm and BP (5 mM) at 680 nm in nitrobenzene solution. The path lengths of the cells are 20 mm.

To estimate uncertainty for ϵ_c estimated in NBz solution with ϵ_c of BP^{*+} as internal reference, tri(p-tolyl)amine (TTA) is applied. Based on ϵ_c of BP^{*+} , estimated ϵ_c of TTA^{*+} is $3.13 \times 10^4 \text{ M}^{-1} \text{ cm}^{-1}$ at 670 nm where concentrations of TTA and BP are 1 and 5 mM, respectively. Comparison between this estimated value and reported ϵ_c of TTA^{*+} , $2.75 \times 10^4 \text{ M}^{-1} \text{ cm}^{-1}$ at 670 nm,²⁰¹ gives ~13% of uncertainty.

References

1. Onsager, L., Initial Recombination of Ions. *Phys. Rev.* **1938**, *54*, 554.
2. Zhou, J.; Shah, R. P.; Findley, B. R.; Braun, C. L., Long Distance Photoinduced Electron Transfer in Solutions: A Mechanism for Producing Large Yields of Free Ions by Electron Transfer Quenching. *J. Phys. Chem. A* **2001**, *106*, 12-20.
3. Zhou, J.; Findley, B. R.; Teslja, A.; Braun, C. L.; Sutin, N., Ion Pairs from Photoexcited, "Random" Electron Donors and Acceptors: □ Alkylbenzenes and Tetracyanoethylene. *J. Phys. Chem. A* **2000**, *104*, 11512-11521.
4. Scott, T. W.; Braun, C. L., Picosecond Geminate Charge Recombination: The Dependence of Reaction Kinetics on Initial Pair Separation. *Chem. Phys. Lett.* **1986**, *127*, 501-504.
5. Gould, I. R.; Farid, S., Dynamics of Bimolecular Photoinduced Electron-Transfer Reactions. *Acc. Chem. Res.* **1996**, *29*, 522-528.
6. Todd, W. P.; Dinnocenzo, J. P.; Farid, S.; Goodman, J. L.; Gould, I. R., Efficient Photoinduced Generation of Radical Cations in Solvents of Medium and Low Polarity. *J. Am. Chem. Soc.* **1991**, *113*, 3601-2.
7. Lewis, F. D.; Bedell, A. M.; Dykstra, R. E.; Elbert, J. E.; Gould, I. R.; Farid, S., Photochemical Generation, Isomerization, and Oxygenation of Stilbene Cation Radicals. *J. Am. Chem. Soc.* **1990**, *112*, 8055-8064.
8. Weller, A.; Staerk, H.; Treichel, R., Magnetic-Field Effects on Geminate Radical-Pair Recombination. *Faraday Discussions of the Chemical Society* **1984**, *78*, 271-278.
9. Weller, A., Mechanism and Spindynamics of Photoinduced Electron Transfer Reactions. *Z. Phys. Chem.* **1982**, *130*, 129-138.
10. Weller, A., Photoinduced Electron Transfer in Solution: Exciplex and Radical Ion Pair Formation Free Enthalpies and Their Solvent Dependence. *Z. Phys. Chem.* **1982**, *130*, 129.
11. Weller, A., Singlet and Triplet Exciplex. In *The Exciplex*, Gordon, M.; Ware, W. R., Eds. Academic Press Inc: 1974; p 23.
12. Zhong, C.; Zhou, J.; Braun, C. L., Solvent-Separated Radical Ion Pairs and Free Ion Yields. 1. Effect of Temperature on Free Ion Formation in Solution. *J. Phys. Chem. A* **2004**, *108*, 6842-6849.
13. Dielectric constant of 2,3-dihydrobenzofuran is assuming to be similar to that of 1-methoxybenzene (anisole) because of similarity between two molecules in chemical structures.
14. Eiben, K., Solvated and Stabilized Electrons in Radiation-Chemical Processes. *Angew. Chem.* **1970**, *9*, 619-632.
15. Debye, P., Reaction Rates in Ionic Solutions. *Trans. Electrochem. Soc.* **1942**, *82*, 265-272.
16. Hong, K. M.; Noolandi, J., Solution of the Time-Dependent Onsager Problem. *J. Chem. Phys.* **1978**, *69*, 5026-5039.
17. Hong, K. M.; Noolandi, J., Solution of the Smoluchowski Equation with a Coulomb Potential. I. General Results. *J. Chem. Phys.* **1978**, *68*, 5163-5171.
18. Rice, S. A.; Butler, P. R.; Pilling, M. J.; Baird, J. K., A Solution of the Debye--Smoluchowski Equation for the Rate of Reaction of Ions in Dilute Solution. *J. Chem. Phys.* **1979**, *70*, 4001-4007.
19. Flannery, M. R., Analytical Solution of the Debye-Smoluchowski Equation for Geminate and Homogeneous Recombination and for Fluorescence Quenching. *Phys. Rev. A* **1982**, *25*, 3403-3406.

20. Noolandi, J., Theory of Time-Dependent Geminate Recombination. *J. Electrostat.* **1982**, *12*, 13-25.
21. Noolandi, J., Theory of Electron-Hole Transport in Amorphous Materials. In *Kinetics of Nonhomogenous Processes*, Freeman, G. R., Ed. JOHN WILEY & SONS: 1987; p 465.
22. Buhning, W., Schrodinger Equation with Inverse Fourth-Power Potential, a Differential Equation with 2 Irregular Singular Points. *J. Math. Phys.* **1974**, *15*, 1451-1459.
23. Born, M.; Oppenheimer, R., Zur Quantentheorie Der Molekeln. *Annalen der Physik* **1927**, *389*, 457-484.
24. Becker, R. S.; Seixas de Melo, J.; Maçanita, A. L.; Elisei, F., Comprehensive Evaluation of the Absorption, Photophysical, Energy Transfer, Structural, and Theoretical Properties of A-Oligothiophenes with One to Seven Rings. *J. Phys. Chem.* **1996**, *100*, 18683-18695.
25. Newton, M. D., Quantum Chemical Probes of Electron-Transfer Kinetics: The Nature of Donor-Acceptor Interactions. *Chem. Rev. (Washington, DC, U. S.)* **1991**, *91*, 767-792.
26. Brédas, J.-L.; Beljonne, D.; Coropceanu, V.; Cornil, J., Charge-Transfer and Energy-Transfer Processes in π -Conjugated Oligomers and Polymers: □ A Molecular Picture. *Chem. Rev. (Washington, DC, U. S.)* **2004**, *104*, 4971-5004.
27. Miller, J. R.; Beitz, J. V.; Huddleston, R. K., Effect of Free Energy on Rates of Electron Transfer between Molecules. *J. Am. Chem. Soc.* **1984**, *106*, 5057-5068.
28. Condon, E., A Theory of Intensity Distribution in Band Systems. *Phys. Rev.* **1926**, *28*, 1182.
29. Franck, J.; Dymond, E. G., Elementary Processes of Photochemical Reactions. *Trans. Faraday Soc.* **1926**, *21*, 536-542.
30. Condon, E. U., Nuclear Motions Associated with Electron Transitions in Diatomic Molecules. *Phys. Rev.* **1928**, *32*, 858-872.
31. Marcus, R. A., On the Theory of Oxidation-Reduction Reactions Involving Electron Transfer. I. *J. Chem. Phys.* **1956**, *24*, 966-978.
32. Marcus, R. A., Theoretical Relations among Rate Constants, Barriers, and Broensted Slopes of Chemical Reactions. *J. Phys. Chem.* **1968**, *72*, 891-899.
33. Marcus, R. A., Electron Transfer Reactions in Chemistry. Theory and Experiment. *Rev. Mod. Phys.* **1993**, *65*, 599.
34. Bixon, M.; Jortner, J., Non-Arrhenius Temperature Dependence of Electron-Transfer Rates. *J. Phys. Chem.* **1991**, *95*, 1941-1944.
35. Jortner, J., Temperature Dependent Activation Energy for Electron Transfer between Biological Molecules. *J. Chem. Phys.* **1976**, *64*, 4860-4867.
36. Sumi, H.; Marcus, R. A., Dynamical Effects in Electron Transfer Reactions. *J. Chem. Phys.* **1986**, *84*, 4894-4914.
37. Jortner, J.; Bixon, M., Intramolecular Vibrational Excitations Accompanying Solvent-Controlled Electron Transfer Reactions. *J. Chem. Phys.* **1988**, *88*, 167-170.
38. Hammes-Schiffer, S., Mixed Quantum/Classical Dynamics of Hydrogen Transfer Reactions. *J. Phys. Chem. A* **1998**, *102*, 10443-10454.
39. Hurley, M. M.; Hammes-Schiffer, S., Development of a Potential Surface for Simulation of Proton and Hydride Transfer Reactions in Solution: Application to NADH Hydride Transfer. *J. Phys. Chem. A* **1997**, *101*, 3977-3989.
40. Hammes-Schiffer, S.; Tully, J. C., Proton Transfer in Solution: Molecular Dynamics with Quantum Transitions. *J. Chem. Phys.* **1994**, *101*, 4657-4667.

41. German, E. D.; Kuznetsov, A. M.; Dogonadze, R. R., Theory of the Kinetic Isotope Effect in Proton Transfer Reactions in a Polar Medium. *J. Chem. Soc., Faraday Trans. 2* **1980**, *76*, 1128-1146.
42. Bruniche-Olsen, N.; Ulstrup, J., Quantum Theory of Kinetic Isotope Effects in Proton Transfer Reactions. *J. Chem. Soc., Faraday Trans. 1* **1979**, *75*, 205-226.
43. Levich, V. G.; Dogonadze, R. R.; German, E. D.; Kuznetsov, A. M.; Kharkats, Y. I., Theory of Homogeneous Reactions Involving Proton Transfer. *Electrochim. Acta* **1970**, *15*, 353-367.
44. Dogonadze, R. R.; Kuznetsov, A. M.; Levich, V. G., Theory of Hydrogen-Ion Discharge on Metals: Case of High Overvoltages. *Electrochim. Acta* **1968**, *13*, 1025-1044.
45. Borgis, D.; Hynes, J. T., Curve Crossing Formulation for Proton Transfer Reactions in Solution. *J. Phys. Chem.* **1996**, *100*, 1118-1128.
46. Staib, A.; Borgis, D.; Hynes, J. T., Proton Transfer in Hydrogen-Bonded Acid-Base Complexes in Polar Solvents. *J. Chem. Phys.* **1995**, *102*, 2487-2505.
47. Borgis, D.; Hynes, J. T., Dynamical Theory of Proton Tunneling Transfer Rates in Solution: General Formulation. *Chem. Phys.* **1993**, *170*, 315-346.
48. Borgis, D.; Hynes, J. T., Molecular-Dynamics Simulation for a Model Nonadiabatic Proton Transfer Reaction in Solution. *J. Chem. Phys.* **1991**, *94*, 3619-3628.
49. Borgis, D. C.; Lee, S.; Hynes, J. T., A Dynamical Theory of Nonadiabatic Proton and Hydrogen Atom Transfer Reaction Rates in Solution. *Chem. Phys. Lett.* **1989**, *162*, 19-26.
50. Zener, C., Non-Adiabatic Crossing of Energy Levels. *Proceedings of the Royal Society of London. Series A* **1932**, *137*, 696-702.
51. Migliore, A.; Polizzi, N. F.; Therien, M. J.; Beratan, D. N., Biochemistry and Theory of Proton-Coupled Electron Transfer. *Chem. Rev. (Washington, DC, U. S.)* **2014**, *114*, 3381-3465.
52. Wishart, J. F.; Cook, A. R.; Miller, J. R., The Leaf Picosecond Pulse Radiolysis Facility at Brookhaven National Laboratory. *Rev. Sci. Instrum.* **2004**, *75*, 4359-4366.
53. Cook, A. R.; Shen, Y., Optical Fiber-Based Single-Shot Picosecond Transient Absorption Spectroscopy. *Rev. Sci. Instrum.* **2009**, *80*, 073106.
54. Onsager, L., Deviations from Ohm's Law in Weak Electrolytes. *J. Chem. Phys.* **1934**, *2*, 599-615.
55. Goliber, T. E.; Perlstein, J. H., Analysis of Photogeneration in a Doped Polymer System in Terms of a Kinetic Model for Electric-Field-Assisted Dissociation of Charge-Transfer States. *J. Chem. Phys.* **1984**, *80*, 4162-4167.
56. Braun, C. L., Electric Field Assisted Dissociation of Charge Transfer States as a Mechanism of Photocarrier Production. *J. Chem. Phys.* **1984**, *80*, 4157-4161.
57. Bell, I. P.; Rodgers, M. A. J.; Burrows, H. D., Kinetic and Thermodynamic Character of Reducing Species Produced on Pulse Radiolysis of Acetonitrile. *J. Chem. Soc., Faraday Trans. 1* **1977**, *73*, 315-326.
58. Burrows, H. D.; Greatorex, D.; Kemp, T. J., Solute Radical Cation Yields in the Pulse Radiolysis of Solutions of Aromatic Amines in Chlorinated Hydrocarbons. *J. Phys. Chem.* **1972**, *76*, 20-26.
59. Braun, C. L.; Scott, T. W., Picosecond Measurements of Time-Resolved Geminate Charge Recombination. *J. Phys. Chem.* **1983**, *87*, 4776-4778.
60. Jou, F. Y.; Dorfman, L. M., Pulse Radiolysis Studies. XXI. Optical Absorption Spectrum of the Solvated Electron in Ethers and in Binary Solutions of These Ethers. *J. Chem. Phys.* **1973**, *58*, 4715-4723.

61. Shaede, E. A.; Kurihara, H.; Dorfman, L. M., Observation of Initial Ion-Pairs in Pulse-Irradiated Weakly Polar Liquids. *Int. J. Rad. Phys. Chem.* **1974**, *6*, 47-54.
62. Keene, J. P.; Kemp, T. J.; Salmon, G. A., Effect of Solvent on Spectra Produced by Pulse Radiolysis of Solutions of Organic Electron Scavengers. *Proc. R. Soc. London, Ser. A* **1965**, *287*, 494-509.
63. Kemp, T. J.; Roberts, J. P.; Salmon, G. A.; Thompson, G. F., Pulse Radiolysis of Solutions of Amines of Low Ionization Potential. *J. Phys. Chem.* **1968**, *72*, 1464-1470.
64. Tagawa, S.; Washio, M.; Kobayashi, H.; Katsumura, Y.; Tabata, Y., Picosecond Pulse Radiolysis Studies on Geminate Ion Recombination in Saturated Hydrocarbon. *Radiat. Phys. Chem.* **1983**, *21*, 45-52.
65. Yoshida, Y.; Tagawa, S.; Washio, M.; Kobayashi, H.; Tabata, Y., Picosecond Pulse Radiolysis on Geminate Ion Recombination and Formation of Solute Excited State in Liquid Cyclohexane. *Int. J. Rad. Appl. Instrum. C* **1989**, *34*, 493-496.
66. Yoshida, Y.; Tagawa, S.; Kobayashi, H.; Tabata, Y., Study of Geminate Ion Recombination in a Solute-Solvent System by Using Picosecond Pulse Radiolysis. *Int. J. Rad. Appl. Instrum. C* **1987**, *30*, 83-87.
67. de Waele, V.; Sorgues, S.; Pernot, P.; Marignier, J.-L.; Monard, H.; Larbre, J.-P.; Mostafavi, M., Geminate Recombination Measurements of Solvated Electron in THF Using Laser-Synchronized Picosecond Electron Pulse. *Chem. Phys. Lett.* **2006**, *423*, 30-34.
68. Martini, I. B.; Barthel, E. R.; Schwartz, B. J., Mechanisms of the Ultrafast Production and Recombination of Solvated Electrons in Weakly Polar Fluids: Comparison of Multiphoton Ionization and Detachment Via the Charge-Transfer-to-Solvent Transition of Na⁻ in THF. *J. Chem. Phys.* **2000**, *113*, 11245-11257.
69. van den Ende, C. A. M.; Luthjens, L. H.; Warman, J. M.; Hummel, A., Geminate Ion Recombination in Irradiated Liquid CCl₄: As Observed by Means of Microwave and Optical Absorption Pulse Radiolysis and Compared with Calculations Based on a Single Ion Pair Model. *Radiat. Phys. Chem.* **1982**, *19*, 455-466.
70. Mataga, N.; Okada, T.; Kanda, Y.; Shioyama, H., Behavior of Radical Ion Pairs Produced by Photoinduced Electron Transfer in Polar Solutions : Their Dynamics in Picosecond-Hundred Nanosecond Regime. *Tetrahedron* **1986**, *42*, 6143-6148.
71. Vauthey, E., Direct Measurements of the Charge-Recombination Dynamics of Geminate Ion Pairs Formed Upon Electron-Transfer Quenching at High Donor Concentration. *J. Phys. Chem. A* **2000**, *105*, 340-348.
72. Masuhara, H.; Mataga, N., Ionic Photodissociation of Electron Donor-Acceptor Systems in Solution. *Acc. Chem. Res.* **1981**, *14*, 312-318.
73. Asaoka, S.; Takeda, N.; Iyoda, T.; Cook, A. R.; Miller, J. R., Electron and Hole Transport to Trap Groups at the Ends of Conjugated Polyfluorenes. *J. Am. Chem. Soc.* **2008**, *130*, 11912-11920.
74. Tran-Thi, T. H.; Koulkes-Pujo, A. M., Electron and Organic Radical Anion Solvation. Pulse Radiolysis of Tetrahydrofuran and Its Solutions of N-Methylacetamide or Pyrrolidone. *J. Phys. Chem.* **1983**, *87*, 1166-1169.
75. Sreearunothai, P.; Asaoka, S.; Cook, A. R.; Miller, J. R., Length and Time-Dependent Rates in Diffusion-Controlled Reactions with Conjugated Polymers. *J. Phys. Chem. A* **2009**, *113*, 2786-2795.

76. Zaikowski, L.; Kaur, P.; Gelfond, C.; Selvaggio, E.; Asaoka, S.; Wu, Q.; Chen, H.-C.; Takeda, N.; Cook, A. R.; Yang, A., et al., Polarons, Bipolarons, and Side-by-Side Polarons in Reduction of Oligofluorenes. *J. Am. Chem. Soc.* **2012**, *134*, 10852-10863.
77. Wasserberg, D.; Dudek, S. P.; Meskers, S. C. J.; Janssen, R. A. J., Comparison of the Chain Length Dependence of the Singlet- and Triplet-Excited States of Oligofluorenes. *Chem. Phys. Lett.* **2005**, *411*, 273-277.
78. Tsierkezos, N., Investigation of the Electrochemical Reduction of Benzophenone in Aprotic Solvents Using the Method of Cyclic Voltammetry. *J. Solution Chem.* **2007**, *36*, 1301-1310.
79. Shida, T., *Electronic Absorption Spectra of Radical Ions*. Elsevier Science: 1998.
80. Pedersen, S. U.; Bo Christensen, T.; Thomasen, T.; Daasbjerg, K., New Methods for the Accurate Determination of Extinction and Diffusion Coefficients of Aromatic and Heteroaromatic Radical Anions in N,N-Dimethylformamide. *J. Electroanal. Chem.* **1998**, *454*, 123-143.
81. Somma, E.; Loppinet, B.; Chi, C.; Fytas, G.; Wegner, G., Static and Dynamic Solution Properties of Monodisperse Oligofluorenes. *PCCP* **2006**, *8*, 2773-2778.
82. Hayamizu, K.; Aihara, Y.; Arai, S.; Garcia, Pulse-Gradient Spin-Echo ^1H , ^7Li , and ^{19}F NMR Diffusion and Ionic Conductivity Measurements of 14 Organic Electrolytes Containing $\text{LiN}(\text{SO}_2\text{CF}_3)_2$. *J. Phys. Chem. B* **1999**, *103*, 519-524.
83. Frisch, M. J.; Trucks, G. W.; Schlegel, H. B.; Scuseria, G. E.; Robb, M. A.; Cheeseman, J. R.; Scalmani, G.; Barone, V.; Mennucci, B.; Petersson, G. A., et al. *Gaussian 09*, Revision B.01; Gaussian Inc.: Wallingford, CT, 2009.
84. Gerdil, R.; Lucken, E. A. C., A Polarographic and Spectroscopic Study of Dibenzothiophene and Some of Its Isologs. *J. Am. Chem. Soc.* **1966**, *88*, 733-737.
85. Streitwieser, A.; Schwager, I., A Molecular Orbital Study of the Polarographic Reduction in Dimethylformamide of Unsubstituted and Methyl-Substituted Aromatic Hydrocarbons. *J. Phys. Chem.* **1962**, *66*, 2316-2320.
86. Shriver, D. F.; Smith, D. E.; Smith, P., Reduction Potentials and Electronic Structures of Phenyl-Substituted Borazines. *J. Am. Chem. Soc.* **1964**, *86*, 5153-5160.
87. Meerholz, K.; Heinze, J., Multiple Reversible Electrochemical Reduction of Aromatic Hydrocarbons in Liquid Alkylamines. *J. Am. Chem. Soc.* **1989**, *111*, 2325-2326.
88. Marasas, R. A.; Iyoda, T.; Miller, J. R., Benzene Radical Ion in Equilibrium with Solvated Electrons. *J. Phys. Chem. A* **2003**, *107*, 2033-2038.
89. Shalev, H.; Evans, D. H., Solvation of Anion Radicals: Gas-Phase Versus Solution. *J. Am. Chem. Soc.* **1989**, *111*, 2667-2674.
90. Prince, R. C.; Gunner, M. R.; Dutton, P. L., *In Function of Quinones in Energy Conserving Systems*. Academic Press: New York, 1982.
91. Connors, T. F.; Rusling, J. F.; Owlia, A., Determination of Standard Potentials and Electron-Transfer Rates for Halobiphenyls from Electrocatalytic Data. *Anal. Chem.* **1985**, *57*, 170-174.
92. Hansen, R. L.; Toren, P. E.; Young, R. H., Nitro-p-terphenyls. II. The Relation between Charge-Transfer Properties and Polarographic Oxidation and Reduction Potentials. *J. Phys. Chem.* **1966**, *70*, 1653-1657.
93. Gross-Lannert, R.; Kaim, W.; Olbrich-Deussner, B., Electron Delocalization in Molecule-Bridged Polymetallic Systems. Unique Neutral Complexes of TCNE or TCNQ and up to Four Organometallic Fragments $(\text{C}_5\text{R}_5)(\text{CO})_2\text{Mn}$. *Inorg. Chem.* **1990**, *29*, 5046-5053.

94. Bard, A. J.; Faulkner, L. R., *Electrochemical Methods: Fundamentals and Applications*. Wiley: 2001; p Cover.
95. Marasas, R. A.; Iyoda, T.; Miller, J. R., Benzene Radical Ion in Equilibrium with Solvated Electrons. *J. Phys. Chem. A* **2003**, *107*, 2033-2038.
96. Kukharenko, S. V.; Strelets, V. V., One-Electron Cryoelectrochemical Reduction of Benzene. *Soviet Electrochemistry* **1988**, *24*, 1271-1272.
97. Connelly, N. G.; Geiger, W. E., Chemical Redox Agents for Organometallic Chemistry. *Chem. Rev.* **1996**, *96*, 877-910.
98. Ruoff, R. S.; Kadish, K. M.; Boulas, P.; Chen, E. C. M., Relationship between the Electron Affinities and Half-Wave Reduction Potentials of Fullerenes, Aromatic Hydrocarbons, and Metal Complexes. *J. Phys. Chem.* **1995**, *99*, 8843-8850.
99. Wagman, D. D.; Evans, W. H.; Parker, V. B.; Schumm, R. H.; Halow, I.; Bailey, S. M.; Churney, K. L.; Nuttall, R. L., The Nbs Tables of Chemical Thermodynamic Properties *J. Phys. Chem. Ref. Data, Suppl. 1* **1982**, *11*.
100. Bartmess, J. E., Thermodynamics of the Electron and the Proton. *J. Phys. Chem.* **1994**, *98*, 6420-6424.
101. Berho, F.; Rayez, M.-T.; Lesclaux, R., UV Absorption Spectrum and Self-Reaction Kinetics of the Cyclohexadienyl Radical, and Stability of a Series of Cyclohexadienyl-Type Radicals. *J. Phys. Chem. A* **1999**, *103*, 5501-5509.
102. Rao, P. S.; Hayon, E., Redox Potentials of Free Radicals. I. Simple Organic Radicals. *J. Am. Chem. Soc.* **1974**, *96*, 1287-1294.
103. Mulliken, R. S., Electronic Population Analysis on LCAO-MO Molecular Wave Functions. I. *J. Chem. Phys.* **1955**, *23*, 1833-1840.
104. Chan, L. L.; Smid, J., Contact and Solvent-Separated Ion Pairs of Carbanions. V. The Role of Solvent Structure in Alkali Ion Solvation. *J. Am. Chem. Soc.* **1968**, *90*, 4654-4661.
105. Ellingsen, T.; Smid, J., Contact and Solvent-Separated Ion Pairs of Carbanions. VI. Conductivities and Thermodynamics of Dissociation of Fluorenyl Alkali Salts in Tetrahydrofuran and Dimethoxyethane. *J. Phys. Chem.* **1969**, *73*, 2712-2719.
106. Esch, T. E. H.; Smid, J., Studies of Contact and Solvent-Separated Ion Pairs of Carbanions. I. Effect of Temperature, Counterion, and Solvent. *J. Am. Chem. Soc.* **1966**, *88*, 307-318.
107. Hogen-Esch, T. E.; Smid, J., Solvent-Separated Ion Pairs of Carbanions. *J. Am. Chem. Soc.* **1965**, *87*, 669-670.
108. Hogen-Esch, T. E.; Smid, J., Studies of Contact and Solvent-Separated Ion Pairs of Carbanions. II. Conductivities and Thermodynamics of Dissociation of Fluorenyllithium, -Sodium, and -Cesium. *J. Am. Chem. Soc.* **1966**, *88*, 318-324.
109. Bhattacharyya, D. N.; Lee, C. L.; Smid, J.; Szwarc, M., Studies of Ions and Ion Pairs in Tetrahydrofuran Solution. Alkali Metal Salts of Tetraphenylboride. *J. Phys. Chem.* **1965**, *69*, 608-611.
110. Carvajal, C.; Tölle, K. J.; Smid, J.; Szwarc, M., Studies of Solvation Phenomena of Ions and Ion Pairs in Dimethoxyethane and Tetrahydrofuran. *J. Am. Chem. Soc.* **1965**, *87*, 5548-5553.
111. Hogen-Esch, T. E., Ion-Pairing Effects in Carbanion Reactions. In *Adv. Phys. Org. Chem.*, Gold, V., Ed. Academic Press: London, 1978; Vol. 15.
112. Bartczak, W. M.; Hummel, A., Computer Simulation Study of Spatial Distribution of the Ions and Electrons in Tracks of High-Energy Electrons and the Effect on the Charge Recombination. *J. Phys. Chem.* **1993**, *97*, 1253-1255.

113. Beaumont, D.; Rodgers, M. A. J., Pulse Radiolysis Studies of Ion Association. *Trans. Faraday Soc.* **1969**, *65*, 2973-2980.
114. Baxendale, J. H.; Beaumont, D.; Rodgers, M. A. J., Electrons, Ions and Excited States in the Pulse Radiolysis of Tetrahydrofuran. *Trans. Faraday Soc.* **1970**, *66*, 1996-2003.
115. Bockrath, B.; Dorfman, L. M., Pulse Radiolysis Studies. XXII. Spectrum and Kinetics of the Sodium Cation-Electron Pair in Tetrahydrofuran Solutions. *J. Phys. Chem.* **1973**, *77*, 1002-1006.
116. Dodelet, J.-P.; Freeman, G. R., Electron Mobilities and Ranges in Liquid Ethers: Ion-Like and Conduction Band Mobilities. *Can. J. Chem.* **1975**, *53*, 1263-1274.
117. Kadhum, A. A. H.; Salmon, G. A., Electron Scavenging in the Gamma-Radiolysis of Tetrahydrofuran. *Radiat. Phys. Chem.* **1984**, *23*, 67-71.
118. Saeki, A.; Kozawa, T.; Ohnishi, Y.; Tagawa, S., Reactivity between Biphenyl and Precursor of Solvated Electrons in Tetrahydrofuran Measured by Picosecond Pulse Radiolysis in near-Ultraviolet, Visible, and Infrared. *J. Phys. Chem. A* **2007**, *111*, 1229-1235.
119. Cook, A. R.; Sreearunothai, P.; Asaoka, S.; Miller, J. R., Sudden, "Step" Electron Capture by Conjugated Polymers. *J. Phys. Chem. A* **2011**, *115*, 11615-11623.
120. Wolff, R. K.; Aldrich, J. E.; Penner, T. L.; Hunt, J. W., Picosecond Pulse Radiolysis. V. Yield of Electrons in Irradiated Aqueous Solution with High Concentrations of Scavenger. *J. Phys. Chem.* **1975**, *79*, 210-219.
121. Lam, K. Y.; Hunt, J. W., Picosecond Pulse Radiolysis—VI. Fast Electron Reactions in Concentrated Solutions of Scavengers in Water and Alcohols. *Int. J. Rad. Phys. Chem.* **1975**, *7*, 317-338.
122. Slates, R. V.; Szwarc, M., Dissociative Equilibria in the Systems Aromatic Hydrocarbon⁻, Na⁺ <-> Radical Anion⁻ + Na⁺. *J. Phys. Chem.* **1965**, *69*, 4124-4131.
123. Schuler, R. H.; Infelta, P. P., Lifetime Distribution Function for Geminate Ion Pairs and Its Importance to the Kinetics of Ionic Reactions in the Radiolysis of Hydrocarbon Solutions. *J. Phys. Chem.* **1972**, *76*, 3812-3823.
124. Yoshida, Y.; Tagawa, S.; Tabata, Y., Initial Distribution Function of the Electron and the Positive Hole in Liquid Cyclohexane Determined by the Geminate Recombination Data and the Smoluchowski Equation. *Radiat. Phys. Chem.* **1984**, *23*, 279-283.
125. Saeki, A.; Kozawa, T.; Yoshida, Y.; Tagawa, S., Study on Geminate Ion Recombination in Liquid Dodecane Using Pico- and Subpicosecond Pulse Radiolysis. *Radiat. Phys. Chem.* **2001**, *60*, 319-322.
126. Okamoto, K.; Kozawa, T.; Saeki, A.; Yoshida, Y.; Tagawa, S., Subpicosecond Pulse Radiolysis in Liquid Methyl-Substituted Benzene Derivatives. *Radiat. Phys. Chem.* **2007**, *76*, 818-826.
127. Andrieux, C. P.; Gamby, J.; Hapiot, P.; Savéant, J.-M., Evidence for Inverted Region Behavior in Proton Transfer to Carbanions. *J. Am. Chem. Soc.* **2003**, *125*, 10119-10124.
128. Heeb, L. R.; Peters, K. S., Further Evidence of an Inverted Region in Proton Transfer within the Benzophenone/Substituted Aniline Contact Radical Ion Pairs; Importance of Vibrational Reorganization Energy. *J. Phys. Chem. A* **2006**, *110*, 6408-6414.
129. Edwards, S. J.; Soudackov, A. V.; Hammes-Schiffer, S., Driving Force Dependence of Rates for Nonadiabatic Proton and Proton-Coupled Electron Transfer: Conditions for Inverted Region Behavior. *J. Phys. Chem. B* **2009**, *113*, 14545-14548.
130. German, E. D.; Kuznetsov, A. M., Dependence of the Hydrogen Kinetic Isotope Effect on the Reaction Free Energy. *J. Chem. Soc., Faraday Trans. 1* **1981**, *77*, 397-412.

131. Kiefer, P. M.; Hynes, J. T., Nonlinear Free Energy Relations for Adiabatic Proton Transfer Reactions in a Polar Environment. I. Fixed Proton Donor Acceptor Separation. *J. Phys. Chem. A* **2002**, *106*, 1834-1849.
132. Kiefer, P. M.; Hynes, J. T., Kinetic Isotope Effects for Nonadiabatic Proton Transfer Reactions in a Polar Environment. 1. Interpretation of Tunneling Kinetic Isotopic Effects. *J. Phys. Chem. A* **2004**, *108*, 11793-11808.
133. Clarke, T. M.; Durrant, J. R., Charge Photogeneration in Organic Solar Cells. *Chem. Rev. (Washington, DC, U. S.)* **2010**, *110*, 6736-6767.
134. Grancini, G.; Maiuri, M.; Fazzi, D.; Petrozza, A.; Egelhaaf, H. J.; Brida, D.; Cerullo, G.; Lanzani, G., Hot Exciton Dissociation in Polymer Solar Cells. *Nat. Mater.* **2013**, *12*, 29-33.
135. Heeger, A. J., 25th Anniversary Article: Bulk Heterojunction Solar Cells: Understanding the Mechanism of Operation. *Adv. Mater. (Weinheim, Ger.)* **2014**, *26*, 10-28.
136. Gould, I. R.; Farid, S., Radiationless Decay in Exciplexes with Variable Charge Transfer. *J. Phys. Chem. B* **2007**, *111*, 6782-6787.
137. Gould, I. R.; Boiani, J. A.; Gaillard, E. B.; Goodman, J. L.; Farid, S., Intersystem Crossing in Charge-Transfer Excited States. *J. Phys. Chem. A* **2003**, *107*, 3515-3524.
138. Gould, I. R.; Young, R. H.; Mueller, L. J.; Farid, S., Mechanisms of Exciplex Formation. Roles of Superexchange, Solvent Polarity, and Driving Force for Electron Transfer. *J. Am. Chem. Soc.* **1994**, *116*, 8176-87.
139. Gould, I. R.; Noukakis, D.; Gomez-Jahn, L.; Young, R. H.; Goodman, J. L.; Farid, S., Radiative and Nonradiative Electron Transfer in Contact Radical-Ion Pairs. *Chem. Phys.* **1993**, *176*, 439-56.
140. Gould, I. R.; Ege, D.; Moser, J. E.; Farid, S., Efficiencies of Photoinduced Electron-Transfer Reactions: Role of the Marcus Inverted Region in Return Electron Transfer within Geminate Radical-Ion Pairs. *J. Am. Chem. Soc.* **1990**, *112*, 4290-4301.
141. Murrell, J. N., Molecular Complexes and Their Spectra. Ix. The Relationship between the Stability of a Complex and the Intensity of Its Charge-Transfer Bands I. *J. Am. Chem. Soc.* **1959**, *81*, 5037-5043.
142. Beens, H.; Knibbe, H.; Weller, A., Dipolar Nature of Molecular Complexes Formed in the Excited State. *J. Chem. Phys.* **1967**, *47*, 1183-1184.
143. Mataga, N.; Kanda, Y.; Asahi, T.; Miyasaka, H.; Okada, T.; Kakitani, T., Mechanisms of the Strongly Exothermic Charge Separation Reaction in the Excited Singlet State. Picosecond Laser Photolysis Studies on Aromatic Hydrocarbon-Tetracyanoethylene and Aromatic Hydrocarbon-Pyromellitic Dianhydride Systems in Polar Solutions. *Chem. Phys.* **1988**, *127*, 239-248.
144. Mataga, N.; Asahi, T.; Kanda, Y.; Okada, T.; Kakitani, T., The Bell-Shaped Energy Gap Dependence of the Charge Recombination Reaction of Geminate Radical Ion Pairs Produced by Fluorescence Quenching Reaction in Acetonitrile Solution. *Chem. Phys.* **1988**, *127*, 249-261.
145. Koch, M.; Letrun, R.; Vauthey, E., Exciplex Formation in Bimolecular Photoinduced Electron-Transfer Investigated by Ultrafast Time-Resolved Infrared Spectroscopy. *J. Am. Chem. Soc.* **2014**.
146. Arnold, B. R.; Farid, S.; Goodman, J. L.; Gould, I. R., Absolute Energies of Interconverting Contact and Solvent-Separated Radical-Ion Pairs. *J. Am. Chem. Soc.* **1996**, *118*, 5482-5483.
147. Asahi, T.; Mataga, N., Charge Recombination Process of Ion Pair State Produced by Excitation of Charge-Transfer Complex in Acetonitrile Solution. Essentially Different Character

- of Its Energy Gap Dependence from That of Geminate Ion Pair Formed by Encounter between Fluorescer and Quencher. *J. Phys. Chem.* **1989**, *93*, 6575-6578.
148. Vauthey, E.; Parker, A. W.; Nohova, B.; Phillips, D., Time-Resolved Resonance Raman Study of the Rate of Separation of a Geminate Ion Pair into Free Ions in a Medium Polarity Solvent. *J. Am. Chem. Soc.* **1994**, *116*, 9182-9186.
149. Bakulin, A. A.; Rao, A.; Pavelyev, V. G.; van Loosdrecht, P. H. M.; Pshenichnikov, M. S.; Niedzialek, D.; Cornil, J.; Beljonne, D.; Friend, R. H., The Role of Driving Energy and Delocalized States for Charge Separation in Organic Semiconductors. *Science* **2012**, *335*, 1340-1344.
150. Hapiot, P.; Lagrost, C.; Le Floch, F.; Raoult, E.; Rault-Berthelot, J., Comparative Study of the Oxidation of Fluorene and 9,9-Disubstituted Fluorenes and Their Related 2,7'-Dimers and Trimer. *Chem. Mater.* **2005**, *17*, 2003-2012.
151. Viscosity of 2,3-dihydrobenzofuran is measured by oscillating piston viscometer at room temperature, 298 K.
152. Merkel, P. B.; Luo, P.; Dinnocenzo, J. P.; Farid, S., Accurate Oxidation Potentials of Benzene and Biphenyl Derivatives Via Electron-Transfer Equilibria and Transient Kinetics. *J. Org. Chem.* **2009**, *74*, 5163-5173.
153. Perkampus, H.-H.; Sandeman, I.; Timmons, C. J., *DMS UV Atlas of Organic Compounds*. Verlag Chemie, Weinheim; Butterworths, London, England, 1966-1971; Vol. I-V.
154. Chi, C.; Im, C.; Wegner, G., Lifetime Determination of Fluorescence and Phosphorescence of a Series of Oligofluorenes. *J. Chem. Phys.* **2006**, *124*, 024907(1-8).
155. Chi, C.; Wegner, G., Chain-Length Dependence of the Electrochemical Properties of Conjugated Oligofluorenes. *Macromol. Rapid Commun.* **2005**, *26*, 1532-1537.
156. Schumacher, S.; Ruseckas, A.; Montgomery, N. A.; Skabara, P. J.; Kanibolotsky, A. L.; Paterson, M. J.; Galbraith, I.; Turnbull, G. A.; Samuel, I. D. W., Effect of Exciton Self-Trapping and Molecular Conformation on Photophysical Properties of Oligofluorenes. *J. Chem. Phys.* **2009**, *131*, 154906.
157. Catherall, C. L. R.; Palmer, T. F.; Cundall, R. B., Chemiluminescence from Reactions of Bis(Pentachloro-Phenyl)Oxalate, Hydrogen Peroxide and Fluorescent Compounds. Role of the Fluor and Nature of Chemielectronic Process(es). *J. Chem. Soc. Faraday Trans. 2* **1984**, *80*, 837-849.
158. Boens, N.; Qin, W.; Basarić, N.; Hofkens, J.; Ameloot, M.; Pouget, J.; Lefèvre, J.-P.; Valeur, B.; Gratton, E.; vandeVen, M., et al., Fluorescence Lifetime Standards for Time and Frequency Domain Fluorescence Spectroscopy. *Anal. Chem.* **2007**, *79*, 2137-2149.
159. Marchetti, A. P.; Kearns, D. R., Investigation of Singlet-Triplet Transitions by the Phosphorescence Excitation Method. Iv. The Singlet-Triplet Absorption Spectra of Aromatic Hydrocarbons. *J. Am. Chem. Soc.* **1967**, *89*, 768-777.
160. Davis, A. P.; Fry, A. J., Experimental and Computed Absolute Redox Potentials of Polycyclic Aromatic Hydrocarbons Are Highly Linearly Correlated over a Wide Range of Structures and Potentials. *J. Phys. Chem. A* **2010**, *114*, 12299-12304.
161. Abdel-Shafi, A. A.; Wilkinson, F., Charge Transfer Effects on the Efficiency of Singlet Oxygen Production Following Oxygen Quenching of Excited Singlet and Triplet States of Aromatic Hydrocarbons in Acetonitrile. *J. Phys. Chem. A* **2000**, *104*, 5747-5757.
162. Thulstrup, E. W.; Nepras, M.; Dvorák, V.; Michl, J., Excited Singlet States of Fluoranthene: Linear Dichroism, Polarized Fluorescence Excitation, and Anodic Oxidation of the Aminofluoranthenes. *J. Mol. Spectrosc.* **1976**, *59*, 265-285.

163. Nepomnyashchii, A. B.; Ono, R. J.; Lyons, D. M.; Bielawski, C. W.; Sessler, J. L.; Bard, A. J., Electrochemistry and Electrogenerated Chemiluminescence of Thiophene and Fluorene Oligomers. Benzoyl Peroxide as a Coreactant for Oligomerization of Thiophene Dimers. *Chem. Sci.* **2012**, *3*, 2628-2638.
164. Rentsch, S.; P. Yang, J.; Paa, W.; Birckner, E.; Schiedt, J.; Weinkauff, R., Size Dependence of Triplet and Singlet States of α -oligothiophenes. *Phys. Chem. Chem. Phys.* **1999**, *1*, 1707-1714.
165. Reyftmann, J. P.; Kagan, J.; Santus, R.; Morliere, P., Excited State Properties of α -Terthienyl and Related Molecules. *Photochem. Photobiol.* **1985**, *41*, 1-7.
166. Suga, K.; Ohkubo, K.; Fukuzumi, S., Selective Oxygenation of 4,4'-Dimethylbiphenyl with Molecular Oxygen, Catalyzed by 9-Phenyl-10-Methylacridinium Ion Via Photoinduced Electron Transfer. *J. Phys. Chem. A* **2005**, *109*, 10168-10175.
167. Rembaum, A.; Eisenberg, A.; Haack, R.; Landel, R. F., Equilibria between Metallic Sodium and Aromatic Hydrocarbons. *J. Am. Chem. Soc.* **1967**, *89*, 1062-1066.
168. Berlman, I. B., *Handbook of Fluorescence Spectra of Aromatic Molecules*. Academic Press: New York, 1971.
169. Wilkinson, F.; Abdel-Shafi, A. A., Mechanism of Quenching of Triplet States by Molecular Oxygen: \square Biphenyl Derivatives in Different Solvents. *J. Phys. Chem. A* **1999**, *103*, 5425-5435.
170. Odom, S. A.; Parkin, S. R.; Anthony, J. E., Tetracene Derivatives as Potential Red Emitters for Organic LEDs. *Org Lett* **2003**, *5*, 4245-4248.
171. Berlman, I. B., *Handbook of Fluorescence Spectra of Aromatic Molecules*. Academic Press: New York, 1965.
172. McGlynn, S. P.; Azumi, T.; Kasha, M., External Heavy-Atom Spin—Orbital Coupling Effect. V. Absorption Studies of Triplet States. *J. Chem. Phys.* **1964**, *40*, 507-515.
173. Naik, D. B.; Dey, G. R.; Kishore, K.; Moorthy, P. N., Studies of the Triplet State of Biphenyl Derivatives by Nanosecond Pulse Radiolysis. *Journal of Photochemistry and Photobiology A: Chemistry* **1992**, *68*, 337-342.
174. Onsager, L., Electric Moments of Molecules in Liquids. *J. Am. Chem. Soc.* **1936**, *58*, 1486-1493.
175. Born, M., Volumen Und Hydratationswärme Der Ionen. *Z. Physik* **1920**, *1*, 45-48.
176. Personal communication with Dr. Andrew Cook from Chemistry Department of Brookhaven National Laboratory.
177. Bao, D.; Millare, B.; Xia, W.; Steyer, B. G.; Gerasimenko, A. A.; Ferreira, A.; Contreras, A.; Vullev, V. I., Electrochemical Oxidation of Ferrocene: A Strong Dependence on the Concentration of the Supporting Electrolyte for Nonpolar Solvents. *J. Phys. Chem. A* **2009**, *113*, 1259-1267.
178. Mostafavi, M.; Lampre, I., An Overview of Solvated Electrons: Recent Advances. In *Recent Trends in Radiation Chemistry*, Wishart, J. F.; Rao, B. S. M., Eds. World Scientific: 2010.
179. Elandaloussi, E. H.; Frère, P.; Richomme, P.; Orduna, J.; Garin, J.; Roncali, J., Effect of Chain Extension on the Electrochemical and Electronic Properties of π -conjugated Soluble Thienylenevinylene Oligomers. *J. Am. Chem. Soc.* **1997**, *119*, 10774-10784.
180. Parker, V. D., Problem of Assigning Values to Energy Changes of Electrode Reactions. *J. Am. Chem. Soc.* **1974**, *96*, 5656-5659.

181. Kaufman, J. H.; Chung, T. C.; Heeger, A. J., Fundamental Electrochemical Studies of Polyacetylene. *J. Electrochem. Soc.* **1984**, *131*, 2847-2856.
182. Arnold, B. R.; Atherton, S. J.; Farid, S.; Goodman, J. L.; Gould, I. R., Combined Application of Picosecond Transient Absorption and Emission Measurements in Studies of Radical-Ion Pair Dynamics. *Photochem. Photobiol.* **1997**, *65*, 15-22.
183. Dou, L.; You, J.; Hong, Z.; Xu, Z.; Li, G.; Street, R. A.; Yang, Y., 25th Anniversary Article: A Decade of Organic/Polymeric Photovoltaic Research. *Adv. Mater. (Weinheim, Ger.)* **2013**, *25*, 6642-6671.
184. Howard, I. A.; Etzold, F.; Laquai, F.; Kemerink, M., Nonequilibrium Charge Dynamics in Organic Solar Cells. *Adv. Eng. Mater.* **2014**, *4*, 1301743(1-9).
185. Barker, A. J.; Chen, K.; Hodgkiss, J. M., Distance Distributions of Photogenerated Charge Pairs in Organic Photovoltaic Cells. *J. Am. Chem. Soc.* **2014**, *136*, 12018-12026.
186. Chen, K.; Barker, A. J.; Reish, M. E.; Gordon, K. C.; Hodgkiss, J. M., Broadband Ultrafast Photoluminescence Spectroscopy Resolves Charge Photogeneration Via Delocalized Hot Excitons in Polymer:Fullerene Photovoltaic Blends. *J. Am. Chem. Soc.* **2013**, *135*, 18502-18512.
187. Ma, W.; Yang, C.; Gong, X.; Lee, K.; Heeger, A. J., Thermally Stable, Efficient Polymer Solar Cells with Nanoscale Control of the Interpenetrating Network Morphology. *Adv. Funct. Mater.* **2005**, *15*, 1617-1622.
188. Madigan, C. F.; Bulović, V., Solid State Solvation in Amorphous Organic Thin Films. *Phys. Rev. Lett.* **2003**, *91*, 247403.
189. Jones, G.; Griffin, S. F.; Choi, C. Y.; Bergmark, W. R., Electron Donor-Acceptor Quenching and Photoinduced Electron Transfer for Coumarin Dyes. *J. Org. Chem.* **1984**, *49*, 2705-2708.
190. Legros, B.; Vandereecken, P.; Soumillion, J. P., Electron Transfer Photoinduced from Naphtholate Anions: Anion Oxidation Potentials and Use of Marcus Free Energy Relationships. *J. Phys. Chem.* **1991**, *95*, 4752-4761.
191. Patel, K. B.; Willson, R. L., Semiquinone Free Radicals and Oxygen. Pulse Radiolysis Study of One Electron Transfer Equilibria. *J. Chem. Soc., Faraday Trans. 1* **1973**, *69*, 814-825.
192. Kadhum, A. A. H.; Salmon, G. A., Reactivity of Solvated Electrons in Tetrahydrofuran. *J. Chem. Soc., Faraday Trans. 1* **1986**, *82*, 2521-2530.
193. Hine, J.; Weimar, R. D., Carbon Basicity Ia. *J. Am. Chem. Soc.* **1965**, *87*, 3387-3396.
194. Taft, R. W.; Wolf, J. F.; Beauchamp, J. L.; Scorrano, G.; Arnett, E. M., Solvent Effects of Water and Fluorosulfuric Acid on Proton Transfer Equilibria and the Energies of Solvation of Gaseous Onium Ions. *J. Am. Chem. Soc.* **1978**, *100*, 1240-1249.
195. In Ref. 100, no reference electrode is given for reduction potential of benzophenone (BPhO). Reduction potential of BPhO in water is calculated with difference of reduction potentials between anthraquinone (AQ) and BPhO from Ref. 100 and reduction potential (vs. SCE) of AQ from Ref 187 in water.
196. Hayano, S.; Fujihira, M., The Effect of Water on the Reduction Potentials of Some Aromatic Compounds in the DMF-Water System. *Bull. Chem. Soc. Jpn.* **1971**, *44*, 2051-2055.
197. Personal Communication with Dr. Andrew Cook from Chemistry Department of Brookhaven National Laboratory.
198. Smith, W. H.; Bard, A. J., Electrochemical Reactions of Organic Compounds in Liquid Ammonia. II. Nitrobenzene and Nitrosobenzene. *J. Am. Chem. Soc.* **1975**, *97*, 5203-5210.

199. Reduction potential (E_{red}) of nitrobenzene was reported versus Ag/Ag ion in anhydrous liquid ammonia with 0.1 M KCl as supporting electrolyte. Based on Ag/Ag ion = -0.045 vs SCE from reference 93.
200. Guirado, G.; Fleming, C. N.; Lingenfelter, T. G.; Williams, M. L.; Zuilhof, H.; Dinnocenzo, J. P., Nanosecond Redox Equilibrium Method for Determining Oxidation Potentials in Organic Media. *J. Am. Chem. Soc.* **2004**, *126*, 14086-14094.
201. Takeda, N.; Asaoka, S.; Miller, J. R., Nature and Energies of Electrons and Holes in a Conjugated Polymer, Polyfluorene. *J. Am. Chem. Soc.* **2006**, *128*, 16073-16082.